Study of Doping & Functionalization of Graphene Quantum Dots for Sensing and Optoelectronic Applications

A Thesis Submitted to
Indian Institute of Technology Guwahati
For the Degree of

Doctor of Philosophy

By

Ruma Das

Department of Physics
Indian Institute of Technology Guwahati
Guwahati-781039, India

August 2020

Dedicated to

.....My beloved Parents and Brother

Department of Physics
Indian Institute of Technology Guwahati
Guwahati-781039, India

STATEMENT

The work contained in the thesis entitled "**Study of Doping & Functionalization of Graphene Quantum Dots for Sensing and Optoelectronic Applications**" has been carried out by me at Indian Institute of Technology Guwahati under the supervision of **Prof. P. K. Giri**, Professor, Department of Physics, Indian Institute of Technology Guwahati. This work has not been submitted elsewhere for the award of any degree.

Ruma Das

Roll No. - **156121010**

Senior Research Fellow
Department of Physics
Indian Institute of Technology Guwahati
Guwahati-781039, India

Prof. P. K. Giri
Professor
Department of Physics
Indian Institute of Technology Guwahati
Guwahati-781039, India
Phone: ***+91 361 2582703****, Fax:* ***+91 361 2690762***
Email: ***giri@iitg.ac.in***

CERTIFICATE

This is to certify that the work contained in the thesis entitled "***Study of Doping & Functionalization of Graphene Quantum Dots for Sensing and Optoelectronic Applications***" has been carried out by **Ms. Ruma Das** at Indian Institute of Technology Guwahati under my supervision. This work has not been submitted elsewhere for the award of any degree.

Prof. P. K. Giri
Thesis supervisor

ACKNOWLEDGEMENT

The entire PhD journey would not have been possible without the constant help, support and encouragement of many people. Here I take this opportunity to acknowledge them.

The first person who deserves to be mentioned is my supervisor Prof. P. K. Giri, without whom this PhD journey would not have even started. I owe my sincerest gratitude to him for giving me the opportunity to work under his guidance. His fruitful discussion, kind support, constant encouragement and useful suggestions made the completion of my PhD possible. His vast knowledge and strong technical expertise have helped me in getting an excellent background in the semiconductor technology, identifying the opportunities in this field and preparing for the challenges. I am thankful for giving me the complete freedom in my work and providing the essential arrangements, laboratory facilities and moral support throughout my PhD work to achieve the goal.

I express my sincere gratitude to my Doctoral Committee members, Dr. Uday Narayan Maiti (Chairman), Prof. Dilip Pal, and Prof. V. Manivannan for their regular review of my work, constructive criticism and valuable suggestions.

I am thankful to our Head of the Department of Physics, other faculty members of Physics, members of the Central Instruments Facilities and Centre for Nanotechnology for providing me a research friendly environment with up-to-date research facilities. I am immensely grateful to Indian Institute of Technology Guwahati for providing the fellowship, good accommodation in this beautiful campus and having pleasant working environment. A special thanks to the scientific/technical officers, Dr. Sidananda Sarma, Indrajit Talukdar, Kaustubh Acharya, Chandan Borgohain, Dr. Kula K. Senapati, and Madhurjya Borah for their help and co-operation to complete my work. Junior technical superintendent Ashim Malakar, Sujit Deb, and Milan Mahadani deserve a special mention who helped in the characterization of my samples. I am also thankful to Central Workshop, Department of Mechanical Engineering for the fabrication of essential components used in my experimental setup. I would like to thank specially Prof. Minoru Fujii, Dr. Sugimoto from Kobe University, Japan, Dr. Wolfgang Theis and A. J. Pattison from University of Birmingham, UK for providing the opportunity to use some of their laboratory facilities.

Life in the lab have always been exciting due to the amazing labmates that I was fortunate to have. I should not forget to mention a few of them. I express my sincere gratitude to my

seniors Dr. Ramesh Ghosh and Dr. Kamal Kumar Paul for their constant help throughout my whole PhD journey. I would like to thank Dr. Biswajit Choudhury, Dr. Jitendra Kumar, Dr. Sk. Md. Obaidullah, Dr. Rajender Gone. Thanks to my labmates Dr. Sumana Paul, Somorjit, Larionette, Joydip, Sumaiya, Abhilasha, Tarik, Koushik, Ravinder, Abdul, and Tadasha for their support and help to bring the thesis in reality.

I should not forget to mention Sasmita di, Sanjib da, Sayandeep, Sumit, Manvendra, Swapan, Anisha, Srijita and Sheuly for their support in my PhD.

Last but not the least my acknowledgements to my father Haradhan Das and mother Madhabi Das without whose support and encouragement this journey would not have been possible at all for me. I am immensely thankful to my brother Dr. Indranil Das for his support in each and every step. I am highly grateful to Somnath Das sir (School teacher), whose constant motivation has enabled me to pursue higher studies.

Ruma Das

IIT Guwahati

CONTENTS

SYNOPSIS

Graphene, a two-dimensional (2D) lattice of sp^2-hybridized carbon with zero bandgap, attracted intensive research interest due to its extraordinary electronic, optical, mechanical, and thermal properties. However, zero bandgap nature limits its applications as light-active material in the optoelectronics and photo science field. The conversion of the graphene to graphene quantum dots (GQDs) with the quantum confinement effect (QCE) and the edge effect is considered as one of the most effective approaches for its bandgap engineering. Among several extraordinary properties of GQDs, photoluminescence (PL) is an outstanding feature of GQDs, which can be easily tailored by controlling their size and shape, doping elements, and modifying the surfaces and edges states. As a consequence of their special structure and unique properties, GQDs are establishing themselves as promising and useful emerging materials for various applications in recent time.

The GQDs often show excitation-wavelength dependent PL emission. However, the tuning of the PL intensity at a particular excitation is still challenging. Along with the interaction mechanism, we show that the functionalization of undoped GQDs (U-GQDs) with single walled carbon nanotubes (SWCNTs) shows the tunability of PL intensity of U-GQDs at a fixed excitation energy.

Despite of considerable research effort in the fabrication of GQDs by various methods to tune their photophysical properties, the effects of the reacting mediums/solvents in the photophysical properties of GQDs are not well studied. Moreover, despite a decade of studies, the origin of PL emission of GQDs still remains controversial, as multiple factors, such as QCE, extrinsic states, impurities, doped atoms, functionalization, etc., contribute to the PL spectrum. Our study focuses on the change of the structural and optical properties of GQDs synthesized in different reacting mediums and a conclusive explanation of the origin of their fluorescence signal on the basis of functionalization and doping with controlled experiments. Here, we deal with three different types of GQDs: U-GQDs, nitrogen-doped GQDs (N-GQDs), and sulfur-doped GQDs (S-GQDs), among which N-GQDs show the highest PL yield along with some interesting properties for further applications in various fields. We use N-GQDs as efficient surface-enhanced Raman spectroscopy (SERS) substrate and light convertor for the fabrication of liquid phase white LED. Due to the large surface area and an enormous number of accessible edges of GQDs, they are used as efficient SERS substrate for detecting target molecules. As a consequence of the SERS enhancement, the charge/energy transfer from

GQDs to target molecules was highlighted as a chemical enhancement (CM). Even though there are plenty of ways for charge/energy transfer process, such as Förster resonant energy transfer (FRET), chemical interaction, electrostatic interaction, band-alignment, etc., there is no clarity on the individual contribution to SERS performance, as it is challenging to isolate the type of interaction, charge transfer, and their individual contributions to the SERS enhancement. For the first time, we show the individual contribution of FRET and π–π interaction in the SERS effect with rhodamine-B (RhB) target on N-GQDs substate by controlled experiments.

When two semiconducting materials with different bandgap form a hybrid structure, a certain band bending at their interface may cause charge transfer depending on their band positions. Interestingly, we observe that the hybrid structure of graphene oxide (GO), the precursor material for GQDs growth, with tungsten disulfide quantum dots (WS_2 QDs) (WS_2/GO) efficiently detects dopamine (DA) in pM level in human serum with 10^4 times higher sensitivity than that of the bare WS_2 QDs. Being an important neurotransmitter and one of the controllers of central nervous system, metabolism, cardiovascular, renal, and hormonal systems in the human body, sensitive and selective detection of DA is essential to diagnosis DA dysfunction related disease like Huntington's disease, Parkinson's disease, schizophrenia, etc. In this sensing process, fluorescence intensity of WS_2/GO hybrid is quenched by following a non-linear nature, which is explained by the combine effect of linear Stern-Volmer model and charge transfer model, for the first time. Moreover, from the comparative studies of DA sensing with WS_2/GO and WS_2/GQDs hybrid, we conclude that higher sensing efficiency of WS_2/GO hybrid is due to higher charge transfer from WS_2 QDs to DA with GO mediator with the consequence of higher probability of π–π interaction between GO sheets and DA.

Currently, noble metal nanoparticles (NP) like Au, Ag, Pt, Pd etc., are extensively studied in various fields due to their unique surface plasmon resonance (SPR) effect. In practice, the optical properties of doped or undoped GQDs are manipulated by the incorporation of the compatible plasmonic NPs for the improvement of their optoelectronic properties. For the first time, we report in-situ grown fluorescent N-GQDs engineered with plasmonic Au NPs (Au@N-GQDs) as optical fluorescence sensors (bio-sensor and metal ion sensors) along with high-speed photodetectors. In the bio-sensor, the sensing of DA with Au@N-GQDs is explained, for the first time, by the formation of a core-shell structure. In another application, metal ion Fe^{3+} is detected by the quenching of fluorescence intensity of Au@N-GQDs in a wide concentration range (0.001-10 μM) following a non-linear nature, which strongly deviates from

the known models of static/dynamic quenching. Surprisingly, for the case of such non-linear nature in fluorescence based sensing, the linear region was only considered to explain the sensing mechanism to date. For the first time, we propose a new model of quenching process by considering the charge transfer dynamics and Langmuir's law of adsorption to explain this non-linear nature in a wide range of concentrations.

For the fabrication of high-speed photodetectors, various kinds of charge-transporting layers are used. To achieve the best performance of the fabricated device, the optimizations of the various parameters such as layer thickness, the orientation of the layers, etc., are very complicated as well as time-consuming process. In our work, Au@N-GQDs is utilized for the fabrication of the high-speed photodetector without using any conducting or charge transporting layer in the device with better performance.

This thesis presents a systematic study on the controlled synthesis of doped and functionalized GQDs and its heterostructure for tunable photophysical and optoelectronic properties with the applications as biological and environmental sensors, LED, and fast photodetection. We believe that these studies are very significant to advance our understanding of the multifunctional optoelectronic and sensing applications of GQDs, which is a low cost and abundant material. The thesis is presented in seven chapters and a brief account of the different chapters are summarized below:

Chapter 1 presents a brief overview of the recent advances in growth strategies, important properties, and the potential utilization of GQDs and their heterostructures in various sensing, bio-imaging, energy storage, optoelectronics, and photocatalysis applications. Recent progress and the lacunae on the GQDs based heterostructures with plasmonic metal nanoparticles, semiconducting materials, etc., for sensing, optoelectronic applications are presented towards the end. The motivation and focus of the present thesis are presented at the end.

Chapter 2 elucidates on the tuning of the PL intensity of undoped GQDs and understanding the interaction mechanism of GQDs and SWCNTs. At very low concentrations of SWCNTs, PL intensity of U-GQDs is enhanced, while at higher concentrations, systematic quenching of PL intensity is observed. It is explained that at very low concentration of SWCNTs, the fluorescence intensity of U-GQDs is first enhanced due to the improved dispersion and higher absorption caused by the metallic SWCNTs, while at higher concentration of SWCNTs, the PL intensity of U-GQDs is quenched by the combined effect of the complex formation and the reduction of the radiative sites of U-GQDs following a non-linear Stern–Volmer model.

Chapter 3 presents the controlled synthesis of doped and functionalized GQDs by a top-down method using GO as the precursor material. By changing the reacting solvents, here we synthesize U-GQDs, N-GQDs, and S-GQDs. With a comparative study of the structural and optical properties of different types of GQDs, the origin of PL peaks is elucidated. Further, we demonstrate N-GQDs as an efficient SERS substrate with an enhancement factor of 3.2×10^3 with 10^{-4} M RhB target, which is able to detect as low as 10^{-10} M RhB. For the first time, we point out the individual contributions of FRET and CM in the SERS process by controlled experiments. Finally, N-GQDs combined with RhB is utilized to fabricate a liquid phase white LED with CIE coordinate (0.30, 0.34).

Chapter 4 demonstrates a cost-effective ultrahigh sensitive biomolecule sensor with a hybrid system of GO and WS_2 QDs (WS_2/GO) for the pM level detection of DA with high selectivity. Van der Waals interaction between WS_2 QDs and GO as well as the defect states and functional groups help in the formation of WS_2/GO hybrid with the consequence of the excited states charge transfer from WS_2 to GO, resulting in the quenching of PL intensity of WS_2 QDs. Later, WS_2/GO hybrid is used as a fluorescence-based sensor for the selective detection of DA as low as 10 pM, which is superior to the earlier reports. The nature of the change of the PL intensity of WS_2/GO hybrid with the presence of DA is observed to follow a combined model of linear Stern-Volmer equation and nonlinear charge transfer model. Due to the aromatic structures of both GO and DA, DA is adsorbed efficiently on GO sheets by the strong $\pi-\pi$ interaction, which assists in the charge transfer from WS_2 QDs to DA leading to the strong quenching of PL intensity of WS_2 QDs. Finally, the newly developed sensor is successfully implemented for the detection of DA in the human serum sample and the Brahmaputra river water with satisfactory recovery, which establishes this sensor as an efficient bio-sensor and environmental sensor.

Chapter 5 discusses a rapid, facile, and label-free sensing strategy for the detection of DA in the real-life samples by employing Au@N-GQDs heterostructure along with mechanistic insights into the sensing mechanism. The strong blue fluorescence of Au@N-GQDs is drastically quenched upon addition of DA in a neutral medium by the unique core-shell complex formation as well as electron transfer. The presence of Au NPs in Au@N-GQDs accelerates the quenching process (~14 fold higher than bare N-GQDs) by the formation of stable dopamine-o-quinone (DQ) in this present detection scheme. This sensing scheme is also successively applied to trace spiked DA in the human serum sample and the Brahmaputra river water sample with satisfactory recovery (95-112%).

In **Chapter 6,** we present the exceptional optoelectronic property of N-GQDs decorated Au nanoparticles (Au@N-GQDs). The as-prepared Au@N-GQDs heterostructure shows more than one order of magnitude enhancement in the fluorescence intensity as compared to that of the bare N-GQDs due to hot electron generation and improved absorption in N-GQDs by local field enhancement and the modification of the edge functional groups. Due to the selective coordination to Fe^{3+} ions, the fluorescence of Au@N-GQDs is further used for the ultrahigh sensitive detection of Fe^{3+} (<1 nM) by fluorescence quenching with a non-linear nature. To explain the nature of this quenching process, a new model is developed by considering the charge transfer dynamics and Langmuir's law of adsorption, which deviates from the well-known static/dynamic quenching models. Au@N-GQDs based fluorescence sensor is successfully implemented for the detection of the spiked Fe^{3+} ions in different water samples and the human serum sample with satisfactory recovery.

Additionally, due to the high absorption in the UV-Vis-NIR region and high charge density with long life excitons, Au@N-GQDs are utilized as a high-speed photodetector with ~10^4 times faster response than that of bare N-GQDs. This is caused by the transfer of hot electrons along with the tunneling of the electrons from Au NPs to N-GQDs as well as the reduction of the defect in N-GQDs by the incorporation of Au NPs. The Au@N-GQDs based photodetector possesses a high responsivity of ~1.36 A/W and a remarkably high external quantum efficiency of ~292.2%.

Chapter 7 presents the summary and highlights of the contributions of the present thesis. Future scope of work on the hybrid and doped GQDs for the sensing, energy, and broadband photodetection applications are presented at the end.

LIST OF PUBLICATIONS:

A. *In Peer-Reviewed Journals:*

1. Ruma Das, Gone Rajender, and P. K. Giri, 'Anomalous Fluorescence Enhancement and Fluorescence Quenching of Graphene Quantum Dots by Single-Walled Carbon Nanotubes'. ***Phys. Chem. Chem. Phys.*** 20, 4527–4537 (2018).

2. Ruma Das, Kamal Kumar Paul, and P. K. Giri, 'Mechanistic Insight into the Highly Sensitive and Selective Dual Mode Detection of Dopamine by N-doped Graphene-Quantum-Dot-Decorated Au Nanoparticles'. ***Appl. Surf. Sci.*** 490, 318–330 (2019).

3. Ruma Das, Sumaiya Parveen, Abhilasha Bora, and P. K. Giri, 'Origin of High Photoluminescence Yield and High SERS Sensitivity of Nitrogen-Doped Graphene Quantum Dots'. ***Carbon*** 160, 273–286 (2020).

4. Ruma Das, Hiroshi Sugimoto, Minoru Fujii, and P. K. Giri, 'Quantitative understanding of charge transfer mediated Fe^{3+} sensing and fast photoresponse by N-doped graphene quantum dots decorated on plasmonic Au nanoparticles'. ***ACS Appl. Mater. Interfaces*** 12, 4755–4768 (2020).

5. Ruma Das, Abhilasha Bora, and P. K. Giri, 'Quantitative Understanding of the Ultra-Sensitive and Selective Detection of Dopamine using Graphene Oxide/WS_2 Quantum Dot Hybrid'. ***J. Mater. Chem. C*** 8, 7935–7946 (2020).

6. Ramesh Ghosh, Ruma Das, P. K. Giri, 'Label-free Glucose Detection over a Wide Dynamic Range by Mesoporous Si Nanowires Array based on Anomalous Photoluminescence Enhancement'. ***Sens. Actuator B-Chem.*** 260, 693–704 (2018).

7. Ramesh Ghosh, Joydip Ghosh, Ruma Das, Larionette P.L. Mawlong, Kamal Kumar Paul, and P. K. Giri, 'Multifunctional Ag nanoparticle decorated Si nanowires for sensing, photocatalysis and light emission applications'. ***J. Colloid Interface Sci.*** 532, 464–473 (2018).

8. Sumaiya Parveen, Kamal Kumar Paul, Ruma Das, and P. K. Giri, 'Large exciton binding energy, high photoluminescence quantum yield and improved photostability of organo-metal halide hybrid perovskite quantum dots grown on a mesoporous titanium dioxide template'. ***J. Colloid Interface Sci.*** 539, 619–633 (2019).

9. Abhilasha Bora, Larionette P. L. Mawlong, Ruma Das, and P. K. Giri, 'Understanding the excitation wavelength-dependent spectral shift and large exciton binding energy of tungsten disulfide quantum dots and its interaction with single-walled carbon nanotubes'. ***J. Colloid Interface Sci.*** 561, 519–532 (2020)

B. *Conference Papers Presented:*

1. Ruma Das, Ramesh Ghosh and P. K. Giri, '*Effect of Ball Milling on the Photophysical Properties of Nanodiamond*', Recent Advances in Nanoscience and Nanotechnology **(NCRANNT-2016)**, *NEHU, Shillong, India, September 8–9, 2016.*

2. Ruma Das, Gone Rajender and P. K. Giri, '*Study of Fluorescence Enhancement and Fluorescence Quenching of Graphene Quantum Dots by Single Walled Carbon Nanotubes in Aqueous Medium*', International Conference on Advanced Nanomaterials and Nanotechnology **(ICANN-2017)**, *IIT Guwahati, Assam, India, December 18–21, 2017.*

3. Ruma Das and P. K. Giri, '*Fluorescence Based Comparative Study of Interaction of Perylene with Nitrogen Doped Graphene Quantum Dots and Graphene Oxide Sheets*', International Conference on Optoelectronic and Nano Materials for Advanced Technology **(icONMAT-2019)**, *Cochin University of Science and Technology, Kerala, India, January 3–5, 2019.*

4. Ruma Das, and P. K. Giri, 'Fluorescence based comparative study of interaction of perylene with nitrogen doped graphene quantum dots and graphene oxide sheets'. ***AIP Conference Proceedings.*** Vol. 2082. No. 1. AIP Publishing LLC (2019).

5. Ruma Das and P. K. Giri, '*Quantitative Analysis of the Charge Transfer Mediated Fe^{3+} Sensing in nM level with Nitrogen-Doped Graphene-Quantum-Dots Decorated on Plasmonic Au Nanoparticles*', International Conference on Advanced Nanomaterials and Nanotechnology **(ICANN-2019)**, *IIT Guwahati, Assam, India, December 18–21, 2019.*

6. Ruma Das and P. K. Giri, '*Fast Photoresponse by Nitrogen-Doped Graphene-Quantum-Dots Decorated on Plasmonic Au Nanoparticles*', International Conference on Nano Science and Technology **(ICONSAT-2020)**, *S. N. Bose Center, Kolkata, March 5–7, 2020.*

C. *Workshops Attended:*

1. *'National Workshop on Advanced Probing Techniques in TEM', IIT Guwahati, 15–16 February, 2016.*
2. *'3rd National Workshop on MEMS/NEMS and Theranostic devices (NWNTD)', IIT Guwahati 21–23 March, 2017.*
3. 'Advance Microscopy and imaging Techniques', *IIT Guwahati, 18–20 April, 2017.*

LIST OF ABBREVIATIONS

Abbreviation	***Description***
FESEM	Field Emission Scanning Electron Microscopy
EDX	Energy-dispersive X-ray
TEM	Transmission Electron Microscopy
FETEM	Field Emission Transmission Electron Microscopy
STEM	Scanning Transmission Electron Microscopy
HRTEM	High Resolution Transmission Electron Microscopy
XRD	X-ray Diffraction
XPS	X-ray Photoelectron Spectroscopy
FTIR	Fourier Transform Infrared Spectroscopy
UV-Vis	Ultraviolet-Visible
NIR	Near Infrared
PL	Photoluminescence
PLE	Photoluminescence Excitation
TRPL	Time resolved Photoluminescence
FWHM	Full width at half maxima
QCE	Quantum confinement effect
QD	Quantum dot
GO	Graphene oxide
GQD	Graphene quantum dot
CNT	Carbon nanotube
DMF	Dimethylformamide
DMSO	Dimethyl sulfoxide
DA	Dopamine
QY	Quantum yield
FRET	Förster resonant energy transfer
N_A	Avogadro number
CIE	Commission International d'Eclairage
WLED	White light emitting diode
SERS	Surface enhanced Raman spectroscopy

SPR	Surface plasmon resonance
BWF	Breit–Wigner–Fano
LOD	Limit of detection

Chapter 1

Introduction

Functional materials based on the allotropes of carbon have attracted a great deal of attention since the discovery of fullerenes in 1985.[1] Graphene, a two dimensional (2D) sheet of a hexagonal lattice with sp^2-hybridized carbon and zero bandgap, has been at the center stage due to its various exceptional properties, such as high electrical and thermal conductivity, high charge carrier mobility, thermal transparency, mechanical strength and so on.[2-8] However, a zero bandgap nature of graphene, caused by the unusual overlapping of the valence band and the conduction band at the same Dirac point, limits its optical applications due to the low optical absorption, short carrier lifetime, etc.[2, 6, 9] As zero bandgap is the characteristic of the defect-free infinite-dimensional graphene only, a finite bandgap can be brought about in graphene by altering its electronic structure with the restriction of the dimensions and introducing defects within its lattice structure.[1, 10] Nevertheless, due to the infinite exciton Bohr radius of graphene, any finite size or shape of graphene sheet can exhibit quantum confinement effect (QCE) along with many interesting properties, which are different from their 2D counterpart.[10, 11] When the graphene sheet is restricted from all directions to the nanoscale dimension, it is known as graphene quantum dot (GQD).[1, 2, 7] Interestingly, the electrical and optical properties of GQDs can be tuned significantly depending on its size, shape, and edge structure. By additional structural engineering through the hybrid structure formation, functionalization, doping, and defect creation, the characteristic properties of GQDs are tuned selectively through different chemical and physical processes.[10, 12] The unique merits of GQDs such as QCE,[10, 13] strong, broad and tunable photoluminescence (PL) spectrum,[14-16] high surface to volume ratio,[8] easy bandgap modification,[7, 10] abundant active sites (edge states, functional groups, and defects),[16, 17] capability of heterostructure formation,[18-20] water solubility,[17, 21] high photostability[12] and biocompatibility[1, 22] opened up immense opportunities for various advanced applications in optical sensing,[23-26] optoelectronics,[7, 17, 27, 28] energy harvesting,[29, 30] and numerous medical issues[1, 31, 32]. In this chapter, a brief review of the important features of GQDs (morphological and optical), methodologies of various synthesis processes of GQDs, doping, functionalization, and the formation of GQDs based heterostructure are presented. The recent advancements of the applications of GQDs and their heterostructures in the sensing (metal ions, biomolecules, chemical, etc.), optoelectronics (photodetector, LED, solar cell, etc.), energy storage

devices (supercapacitor, battery, etc.) and bio-medical (bio-imaging, drug delivery, etc.) are discussed shortly. At the end of this chapter, the unresolved issues and challenges, along with the focus of the present thesis and the outline of the present thesis are deliberated.

1.1. Morphology and Structure of GQDs

GQDs are one of the emerging derivatives of graphene, classified as zero-dimensional (0D) semiconducting material with lateral size <10 nm.[12] GQDs own a graphene core with sp^2 hybridized carbon and an enormous number of oxygen functional groups at their edge sites as well as on the basal planes.[14, 15, 33] Among them, epoxy (–COC–) groups are located mainly on the basal plane of GQDs and hydroxyl (–OH), carbonyl (–HC=O), carboxyl (–COOH), etc., groups are attached at the edge sites of GQDs.[14, 16] Typically, GQDs are of circular/elliptical shape, but the variation of the shape of GQDs from circular to polygonal was reported experimentally.[10, 34-36] The size and shape of GQDs can be modified by controlling synthesis conditions, such as the reaction time, temperature, reacting medium, etc.[14, 37] For the synthesis of GQDs, graphene sheet is mainly cut into two different crystallographic directions leading to two types of edge structures of GQDs, namely armchair and zigzag.[10, 38] **Fig 1.1** shows the armchair and zigzag edges in GQDs. Kim et

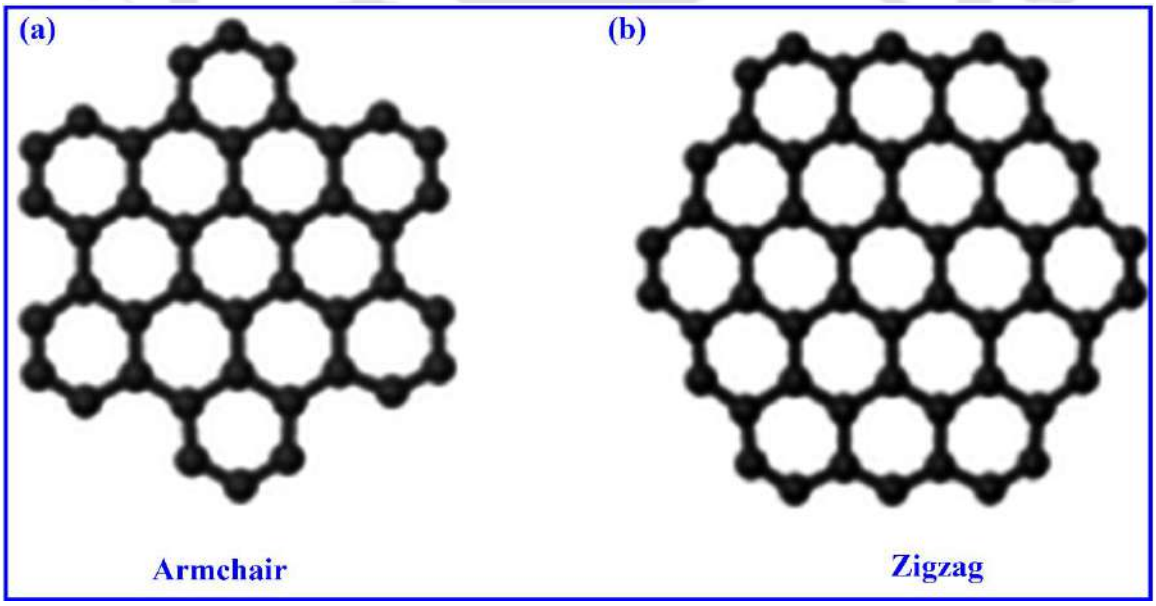

Fig. 1.1. GQD with (a) armchair and (b) zigzag edges. Adopted from Ref.[38]

al. reported that both zigzag and armchair edges are observed in circular/elliptical shaped GQDs while the dominating contribution of the armchair edges is observed in polygonal-shaped GQDs.[35]

Moreover, GQDs with zigzag edges exhibit a higher bandgap than that of the armchair edges.[10] Usually, GQDs are crystalline in nature with a six-fold symmetry,[37] while the presence of defects or doping may break the symmetry due to the change of the lattice spacing. In crystalline GQDs, (002), (100), (110) planes are generally observed. Among them, (002) planes correspond to the graphitic planes of GQDs with a lattice spacing of ~0.32–0.34 nm and other planes of GQDs arise due to the attachment of the functional groups.[39-41] Peng et al. reported that the interlayer spacing of (002) planes in GQDs is of ~0.403 nm due to the presence of a high density of oxygen functional groups.[42] The nature of crystallinity, edge state, and defects in GQDs are usually characterized by D and G bands in the Raman spectrum.[43] The G band at ~1580 cm^{-1} in GQDs arises from the in-plane phonon vibration of C=C graphitic carbon, and the D band at ~1350 cm^{-1} is mainly due to the armchair edge sites.[14, 44] Moreover, the edge structure and functional groups of GQDs play an important role to determine the optical properties of GQDs.[14, 33, 45]

1.2. Optical Properties of GQDs

Since the invention of GQDs, it has been used extensively for the cutting edge research and advanced applications due to their exceptional optical properties.[1, 10, 14, 15, 33] Optical properties of GQDs are mostly analyzed on the basis of UV-vis absorption and PL spectroscopy studies. The UV-vis absorption spectrum of GQDs is explained with two different types of electronic transitions, namely π–π* and n–π* transition. The absorption by GQDs in the region of ~230–270 nm is due to the π–π* transition, which confirms the QCE in GQDs, and an extended tail in the region ~300–600 nm arises from the n–π* transition due to the surface states, defects, functional groups, doping, etc.[10, 33, 46, 47] The UV-vis absorption depends on the optical bandgap of GQDs, which is solely influenced by its intrinsic properties, such as size, shapes, etc., as well as the extrinsic properties, like surface functionalization, doping, and defects.[10, 48] The blue shift of the absorption peak of GQDs are observed with the reduction of the size of GQDs, indicating the QCE effect.[35, 42] The broadening of the absorption spectrum corresponding to n–π* transition was also reported after oxygen functionalization.[14] Notably, the change of the UV-vis absorption of GQDs was also conveyed by the doping effect.[49] Like UV-vis absorption, PL emission is another interesting characteristic property of GQDs. PL is basically the emission of the photons through the relaxation of excitons to the lower energy levels. When GQDs are excited with UV-vis light, depending on their intrinsic properties as well as surface states, PL emission of various colors from

blue to red is observed.[14, 15, 17, 33, 48, 50, 51] Moreover, the colors of PL emission in GQDs are also influenced by the synthesis method, excitation wavelength, solvent, pH, etc.[10, 33] The origin of the PL emission in GQDs is mostly explained by the QCE, i.e., the size of the GQDs.[15, 52] According to the QCE mechanism, with the reduction of the GQDs size, the energy bandgap increases, and consequently, the corresponding PL peak of GQDs shifts towards lower wavelength,[10] as shown in **Fig. 1.2**. Moreover, due to the particle size distribution of GQDs, closely spaced energy states,

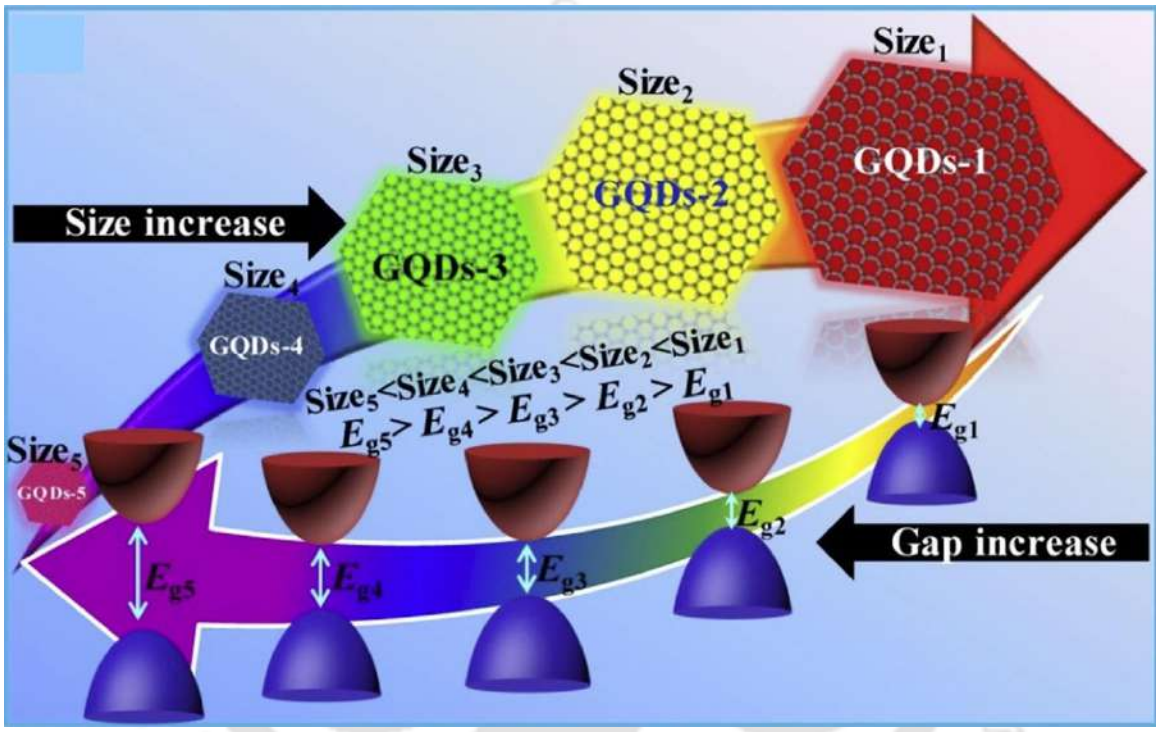

Fig. 1.2. Modulation of the bandgap and the corresponding color of PL emission in GQDs via size variation. Adopted from Ref.[34]

known as intrinsic states, appear within the energy bandgap, is one of the reasons for the excitation dependent PL emission in GQDs.[15, 53] Zhu et al. demonstrated the excitation dependent PL emission in GQDs and they showed that with the variation of the excitation wavelength from 400 to 540 nm, emission peak shifts from ~515–570 nm with a maximum intense peak at ~515 nm.[54] They proposed that the excitation dependent PL of GQDs is caused by the size distribution of GQDs and the surface defects states of GQDs. Moreover, Li et al. claimed that excitation independent PL is achievable with the uniform size and emissive sites of GQDs.[10] The presence of abundant oxygen functional groups in GQDs are assigned as another source of the PL emission in GQDs, which exhibit green PL emission generally. It may be noted that C-O and –OH groups

work as the emissive PL centers in GQDs,[10, 33] while C-O-C and COOH mostly behave as non-radiative sites and trapping centers for carriers.[10, 55, 56] A schematic of the PL emission from different energy levels in GQDs are presented in **Fig. 1.3**. Besides GQDs size and functional

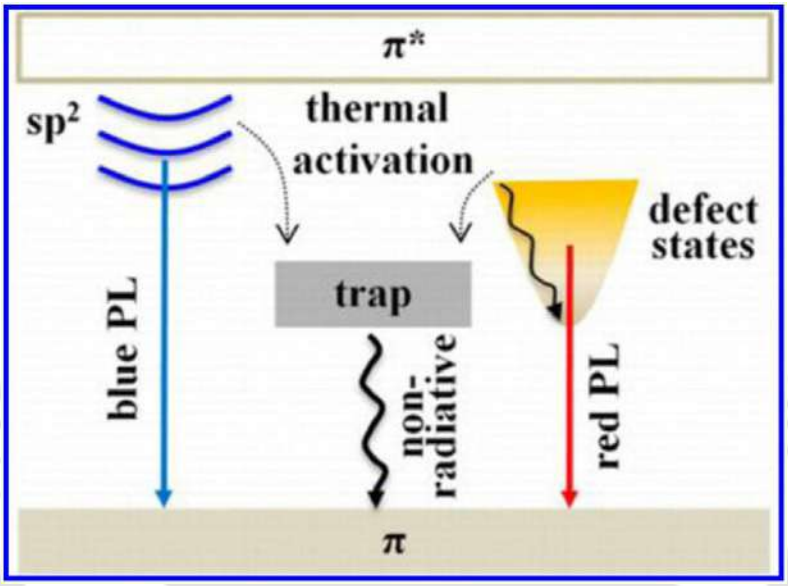

Fig. 1.3. Band structure of GQDs for intrinsic and extrinsic PL emission along with the non-radiative trap center. Adopted from Ref.[33]

groups, edge structures of GQDs also affect the PL emission in GQDs. Gone et al. demonstrated the change of the PL emission spectrum of GQDs by controlling both zigzag and armchair edge states.[14] Additionally, the PL of GQDs is also observed to be sensitive towards the solvent medium, such as dimethylformamide (DMF), tetrahydrofuran (THF), water, acetone, etc., due to the surface passivation of GQDs with the solvents.[54] Moreover, the variation of pH can also alter the PL intensity of GQDs by protonation or deprotonation effect.[10, 54] With the variation of the solvents or pH, the change in the PL intensity of GQDs is mainly due to their surrounding environments that influence the surface states of GQDs.[56] Although the mechanism of the PL emission in GQDs can be explained by the QCE and surface states, some specific details of PL behavior in GQDs are still inconclusive. In addition to the PL emission in GQDs, PL quantum yield (QY) is an important parameter to recognize GQDs as a fluorescent material. QY is defined as the ratio of the number of photons emitted to the number of photons absorbed by the fluorescent material at a particular excitation wavelength. The reported values of the QY of GQDs are observed in the range of ~2.9–83%,[54, 55, 57] which are remarkably high to establish GQDs as a good fluorescent material, particularly for sensing and bioimaging applications. This thesis work mainly deals with the optical

properties of undoped and GQDs, and their heterostructures for various sensing and optoelectronic applications.

1.3. Synthesis of GQDs

Due to the unique optical properties of GQDs and the immense scope for their practical applications in the advanced research field, various chemical and physical synthesis processes have been developed over the last decade. The synthesis strategies of GQDs are categorized into two major classes, specifically the top-down method and bottom-up method.[2, 10, 12] Top-down approach is a simple and cost-effective method for the synthesis of GQDs. In this synthesis method, bulk graphitic precursor materials, such as graphite,[58, 59] graphene sheet (GS),[13, 60] graphene oxide (GO),[14, 54] carbon fiber,[42, 61] carbon nanotubes (CNTs),[59] etc., are cut into a smaller size in nanometer scale through chemical or physical methods, such as hydrothermal/solvothermal method,[2, 14, 54] electrochemical exfoliation,[50, 62] liquid-phase exfoliation,[63, 64] microwave-assisted exfoliation,[65] pulse laser ablation,[66] etc. While top-down synthesis methods follow the size reduction of the graphitic precursor through the oxidation process, the mechanism for bottom-up synthesis is governed by the fusion and carbonization of small organic molecules, and polycyclic aromatic hydrocarbons, like glucose, citric acid, 1,3,6-trinitropyrene, adenosine triphosphate, etc.[12, 17, 27, 67] Pyrolysis,[27, 68] hydrothermal/solvothermal[17] and organic synthesis[1] are mostly used processes in the bottom-up approach for the synthesis of GQDs. A schematic of various methods of GQDs synthesis is presented in **Fig. 1.4**. The top-down approach is facilitated with large scale production of crystalline GQDs with the layered structure and high water solubility with oxygen-containing functional groups at the edge sites.[1, 34] However, the top-down method suffers from uncontrolled size and shape as well as surface functionalization of GQDs and low PL QY. The synthesis of GQDs via bottom-up method provides a controllable size and morphology with high PL QY. Nevertheless, the bottom-up method is time consuming and expensive process with low production yield, and it requires complicated reaction steps and different reaction strategies from different precursors.[12, 69] Moreover, the synthesized GQDs by the bottom-up method are mostly of amorphous nature with small dot size, poor water solubility, and aggregation issues confine their diverse applications in advanced science.[10, 69] Due to the low production cost with the simple synthesis strategy and the promising nature for practical applications, there have been efforts for the modification in the top-down synthesis process of GQDs in a controlled way as well as for the

improvement of their PL QY. Based on the above, the present thesis is focused on the top-down method for the synthesis of GQDs. A brief overview of both synthesis methods is presented below.

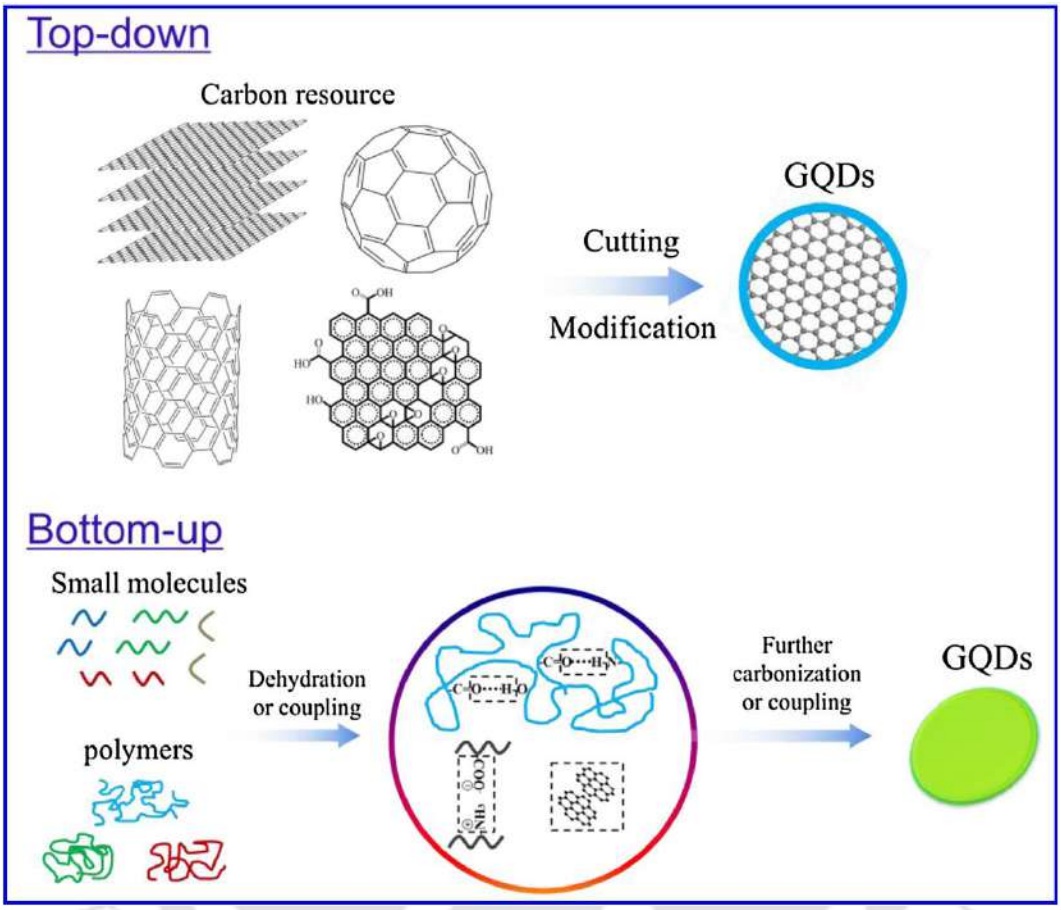

Fig. 1.4. A schematic of the top-down and bottom-up methods for the synthesis of GQDs. Adopted from Ref.[33]

1.3.1. Top-down Methods

Among various processes in the top-down approach, hydrothermal/solvothermal methods are most promising for the synthesis of GQDs on a large scale. In the hydrothermal/solvothermal methods, GQDs are synthesized from the carbon materials under the conditions of high pressure and temperature in the aqueous/solvent medium.[14] Generally, the precursor carbon materials are treated with oxidants, such as strong acid (concentrated sulfuric acid (H_2SO_4), nitric acid (HNO_3)),[13, 14, 42, 60] oxone,[59] hydrogen peroxide (H_2O_2),[70, 71] etc., for the oxidation before the reactions. For the first time, GQDs were synthesized with the hydrothermal method by Pan's group in 2010.[13] In this process, at first the GO, prepared by the modified Hummers' method from graphite powder, was deoxidized in a nitrogen atmosphere to obtain GSs. Then, the GSs were oxidized with concentrated

H_2SO_4 and HNO_3, and subsequently, the GSs were put into the hydrothermal reaction chamber at 200 °C for 10 h in a basic aqueous medium for the synthesis of GQDs. The size of the synthesized GQDs was ~5–13 nm with an average size of ~9.6 nm and 1–2 nm of layer thickness. To explain the mechanism behind the GQDs synthesis from oxidized GSs, they proposed the cutting of C–C line of graphene sheets along with the epoxy groups by the oxidation process, as shown in **Fig. 1.5**. Moreover, they reported a blue emission from the as-synthesized GQDs with PL QY of ~6.9%

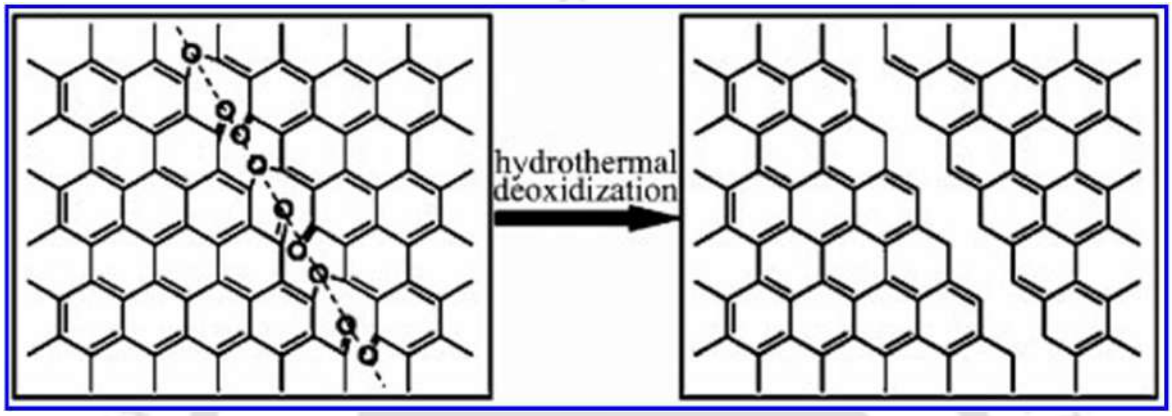

Fig. 1.5. Schematic of the mechanism of hydrothermal cutting graphene sheet by top-down method for the synthesis of GQDs. Adopted from Ref.[13]

mainly due to the free zigzag edge states of GQDs. However, any contribution of the oxygen-rich functional groups in GQDs to the PL QY was ignored. Gone et al. reported the hydrothermal synthesis of GQDs at 200 °C with 12 h and 24 h reaction together with the functionalization of GQDs with poly-ethylene glycol.[14] To explain the growth mechanism, they proposed the formation of quasi-ring type epoxy functional groups on the basal plane of GO, and later these epoxy groups energetically favor to cut the GO sheet into GQDs. Additionally, the origin of PL emission of GQDs was assigned to the zigzag and armchair free edge states and various oxygen functional groups of GQDs. However, no estimation of the PL QY was made in this study. Tetsuka et al. reported the hydrothermal synthesis of functionalized GQDs with an average size of ~2.5 nm from oxidized GSs at 150 °C for 5 h reaction, which exhibits a broad PL emission in the UV-vis region.[60] Though the change of the optical bandgap of amino-functionalized GQDs was explained as a function of primary amine, the mechanism of PL emission was not explained properly. It's noteworthy that due to the high efficiency and wide tunability of PL emission, the functionalized GQDs have been used in several applications. Like the hydrothermal method, a solvothermal method is a useful approach for GQDs synthesis in various solvents like DMF, dimethyl sulfoxide

(DMSO), N-methyl-2-pyrrolidone (NMP), etc.[1, 22, 54, 59] Liu et al. demonstrated the synthesis of GQDs in DMF medium by the nucleophilic reaction.[72] The synthesis of GQDs in DMSO medium in ambient pressure was reported for the edge functionalization of GQDs.[22] However, high pressure and high-temperature reaction in DMSO medium was not attempted in this work. Shin et al. reported an acid free solvothermal synthesis of GQDs with oxone oxidant in DMF medium,[59] where they used various types of carbon materials, such as graphite, CNTs, coal, etc., as precursor materials. With oxone oxidant, the synthesized GQDs were observed to possess blue emission with high PL QY. Even though hydrothermal/solvothermal methods provide large scale production of GQDs, being a chemical process, these approaches barely control the morphology of GQDs, leading to the non-uniform particle size and functionalization. For the synthesis of GQDs with controlled size and shape, exfoliation methods have been used recently.[1, 50] Shinde et al. reported the electrochemical exfoliation of multi-walled CNTs (MWCNTs) for the synthesis of GQDs by controlling their particle size.[62] They also demonstrated green emission from the synthesized GQDs with QY of ~6.3%. Later, by following the same synthesis process, Tan et al. produced red fluorescent GQDs with uniform size (~3 nm) from the graphite precursor.[50] In the electrochemical exfoliation process, first, the applied electric potential in the anode creates the cleavage in the bulk material by the intercalation of the electrolytes between the layers of bulk material and then the cathodic potential reduces the size of the intercalated bulk layers. In this process, the precise control over the applied potential causes selective oxidation of the precursor materials, which leads to the control over the GQDs size.[1] Like the electrochemical exfoliation method, liquid-phase exfoliation is another controlled method for the synthesis of GQDs, where carbonaceous materials are transformed into GQDs by the ultrasonication process. In this case, the vibrations of the solvent molecules in the sonication process provide the required energy for the disintegration of the bulk materials into nano-size particles.[1, 12, 63] Synthesis of GQDs is reported by liquid-phase exfoliation of nano graphite in NMP by ultrasonication, where defects states are controlled nicely.[1] The pulsed laser ablation technique is also used for the selective synthesis of GQDs from MWCNTs.[66] It is noteworthy that oxygenated functional groups are unavoidably attached with GQDs in the oxidative reduction process.[12]

1.3.2. Bottom-up Methods

With the bottom-up approaches, the synthesis of GQDs by the organic synthesis process was reported by a few groups.[1, 11] Among these, Yan et al. reported the synthesis of uniform and tunable

size of colloidal GQDs.[11] However, due to the complicated reaction scheme and low product yield in the organic synthesis process, it lost its feasibility. In this context, the pyrolysis and microwave-assisted synthesis processes attracted immense attention in the bottom-up approach due to the simple synthesis strategy. With the pyrolysis method, GQDs were synthesized from citric acid, which exhibited excitation independent PL emission of blue color with QY of ~9%.[68] Dey et al. produced monodispersed GQDs from citric acid by pyrolysis approach, which exhibited blue PL emission, and the PL emission was tuned from blue to yellow color by controlling the surface functional groups.[27] They proposed that the six-member carbon ring in GQDs are formed by the stepwise carbonization and aggregation of citric acid. Through a facile microwave-assisted hydrothermal method, Tang et al. demonstrated the synthesis of GQDs from glucose, which exhibits deep UV emission with the QY of ~11%.[17] In this synthesis scheme, glucose is first pyrolyzed by the microwaves, and subsequently, GQDs are formed by the nucleation process, as illustrated in **Fig. 1.6**. Though they tried to use the as-synthesized GQDs as a light convertor for

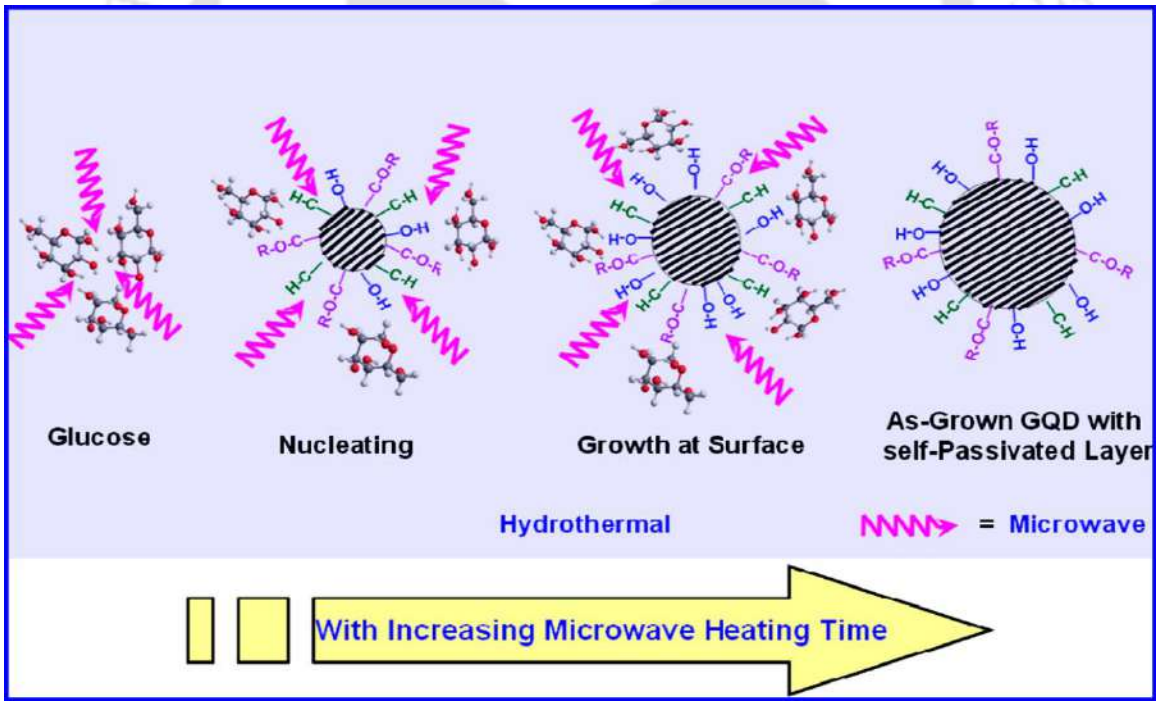

Fig. 1.6. Microwave-assisted synthesis of GQDs by the bottom-up method. Adopted from Ref.[17]

the fabrication of white LED, further modification of GQDs properties can help to achieve a pure white LED. Besides the chemical methods, Lui et al. reported the synthesis of ultra-clean GQDs

by plasma-enhanced chemical vapor deposition (CVD) from methane, which was used for surface-enhanced Raman scattering (SERS) application.[73] It may be noted the authors did not address the PL property of CVD grown GQDs.

1.4. Chemical Doping in GQDs

Since the discovery of GQDs, researchers have invested their efforts in the modification of the bandgap of GQDs with several techniques to make them useful in the UV to NIR region for advanced applications. Doping of heteroatoms in GQDs is one of those techniques, which modulates their chemical, optical and electronic properties enormously. The doping of various heteroatoms and the corresponding changes in the optical properties of GQDs are elaborated here. Heteroatoms that are generally used for the doping in GQDs are nitrogen (N),[49, 74-76] sulfur (S),[77-79] boron (B),[80-82], and phosphorus (P)[83, 84]. Also, potassium (K),[85] selenium (Se),[86] fluorine (F),[87, 88] chlorine (Cl),[89] etc., atoms are used as the dopants in GQDs. In addition, these atoms can be co-doped into GQDs for the improvement of the GQDs properties.[90-93] In general, the type of doping can be categorized into three groups depending on the type of doping atoms, namely single doping, double doping, and multiple doping, as depicted in **Fig. 1.7**. In single doping, only one type of heteroatom is doped in the GQDs lattice. Double doping is characterized by the doping of two different types of atoms in GQDs, and doping of more than two types of different atoms are known as multiple doping.[34] Note that the selection of the doping atoms mostly influences the alteration of the GQDs properties rather than the doping methods. Among various types of heteroatoms, N atom is widely used as a dopant in GQDs because of their ability to be easily doped in graphene lattice due to the comparable size of the N atom and the significant difference in the electronegativity with C atom[91] and moreover, superior properties of N doped GQDs (N-GQDs) for novel applications in various fields. Tang et al. demonstrated the synthesis of N-GQDs in atmospheric pressure at room temperature by mixing glucose solution with ammonia in the aqueous medium, where ammonia works as a catalyst as well as the source of N.[75] In the synthesized N-GQDs, N is incorporated as pyridinic N, pyrrolic N and graphitic N with dominating contribution of pyridinic N. They proposed the formation of new energy levels in the band structure of GQDs as a result of the N doping. Due to the modification of the band structure, they reported some changes in the UV-vis absorption and PL emission spectra. This group claimed that the

presence of N atoms in N-GQDs is the main reason for the tunable optical properties of GQDs. Notably, the reported synthesis process of N-GQDs is highly time-consuming (~14 months), which

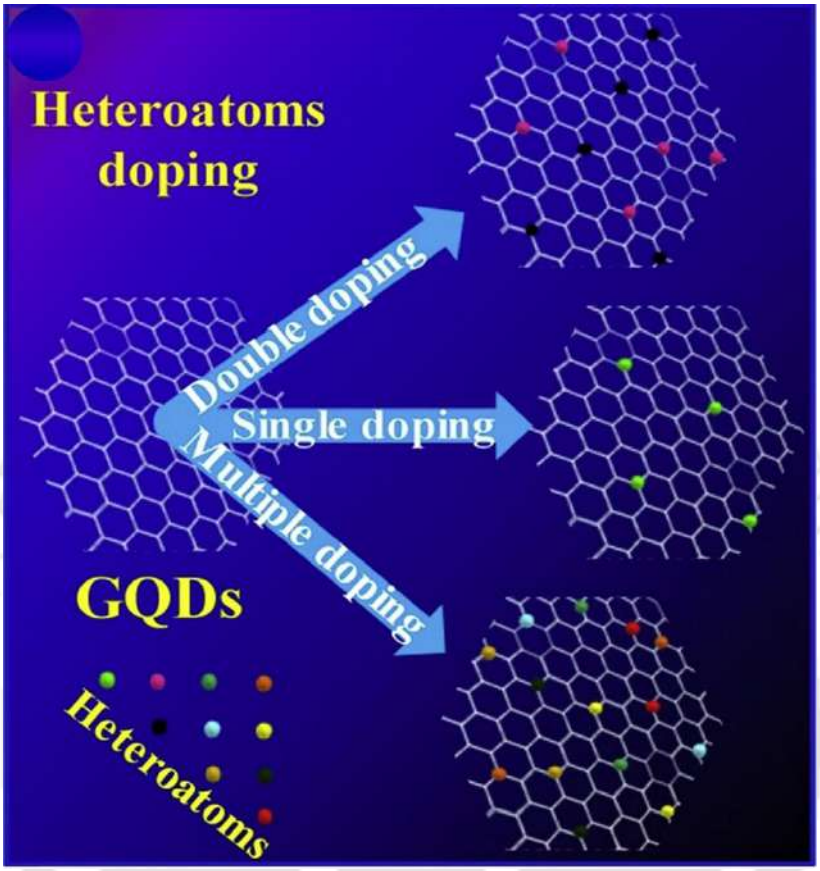

Fig. 1.7. Schematic of three different kinds of doping in GQDs. Adopted from Ref.[34]

is a major disadvantage for large scale synthesis and their applications. Further, N-GQDs, prepared by the hydrothermal method from GO in the presence of ammonia, emit strong blue PL with QY ~24.6%.[94] Liu et al. synthesized biocompatible green fluorescent N-GQDs from GO precursor by the solvothermal method using DMF as the solvent as well as the source of N, and later, they used the as-synthesized N-GQDs as an efficient two-photon probe for bio-imaging.[95] They proposed that the decomposed DMF at high pressure and temperature introduces N doping into GO surface by the nucleophilic ring-opening reaction with the epoxy groups of GO surface. However, the low carrier lifetime (~6.3 ns) in the N-GQDs restrict their applications, and further modification is needed to extend their usages in various optoelectronic applications. Niu et al. reported a significant blue shift of UV-vis absorption and PL emission spectra after N doping.[96] Permatasari et al. demonstrated the synthesis of N-GQDs by the hydrothermal reaction of citric acid and urea,

where urea was used as the N source. They highlighted that the contribution of the delocalized π electrons from pyridinic N to the C system helps to enhance the PL intensity in N-GQDs.[97] Besides the N doping, B doped GQDs (B-GQDs) are also studied to tune the energy bandgap. Li et al. reported the synthesis of B-GQDs by hydrothermally cutting of the B doped graphene sheet.[80] In the synthesis of B-GQDs, the doping sites of B atoms were not understood properly. Though the as-synthesized B-GQDs exhibit excitation wavelength-dependent PL, highly intense PL was observed only in the blue region. Moreover, the origin of PL emission was not addressed properly and there was no information about the PL QY of B-GQDs. Fan et al. reported the electrochemical synthesis of B-GQDs from graphite rod in borax solution, where B-GQDs exhibit blue, green, and yellow emission depending on the surrounding environments.[81] They showed that the environment-dependent PL behavior of B-GQDs results only for the B doping, which facilitates the effective energy transfer from B^{3+} to the graphitic structure. As the size of S atom is much higher than that of the C atom and negligible difference in the electronegativity between S and C, the doping of S atom in GQDs becomes quite difficult. Nonetheless, due to promising applications, researchers have developed various methods to synthesize S-GQDs. Li et al. reported the synthesis of stable blue-green fluorescence S-GQDs by the electrochemical process using graphite as precursor material and sodium p-toluenesulfonate aqueous solution as electrolyte solution as well as the source of S.[78] As compared to undoped GQDs, the as-synthesized S-GQDs exhibit enormous improvement in their chemical and electronic properties by donating the loosely bound valence electrons from S to GQDs network, which facilitates the coordination interaction of S-GQDs with electron-deficient materials. Wang et al. reported the hydrothermal synthesis of S-GQDs by the bottom-up method from durian with the platinum catalyst in a controlled way.[98] In this case, the doped S atoms exist as thiophene-S (-C-S-C-) form in GQDs, which enhanced the stability of S-GQDs along with the high PL QY at ~600 nm. Another hydrothermally synthesized S-GQDs, using 1,3,6-trinitropyrene for C source and 3-mercaptopropionic acid for S source, show blue PL emission with QY of ~9.2% along with the drastic changes in their electronic and chemical properties.[79] For the requirement of the advanced applications, double doping is also developed along with the doping of a single atom, which provides improved properties as compared to single doping. Qu and co-workers reported the synthesis of S, N co-doped GQDs by a simple solvothermal route, where they used thiourea as the source of S and N dopants with a citric acid precursor in DMF medium.[90] Interestingly, the S, N-GQDs shows three prominent absorption

bands at ~338, 467, and 557 nm by covering whole UV-visible region and they produce excitation independent strong PL emission with blue, green and red color with high PL QY (~61%, 45%, and 8%, respectively) within the excitation wavelength ranges of 340–420 nm, 460–540 nm, and 560–620 nm, respectively. It was proposed that the co-existence of three independent luminescent centers, C=O, C=N, and C=S, is the reason for the single excitation band dependent PL emission in S, N co-doped GQDs. As compared to single doped GQDs, this co-doping approach was able to tune the optical properties in the whole UV-vis region efficiently. The multiple doping was reported by Kundu et al., where they reported the co-doping of S, N and F atoms by the microwave heating of MWCNTs precursor in 1-methyl-1-propylpiperidinium bis (trifluoro methylsulfonyl) imide ionic liquid as the source of S, N and F dopants.[91] Due to the interaction of defect clusters and dopants, the as-synthesized S, N, F-GQDs exhibit blue PL emission with QY of ~70%, which is higher than the single or double doped GQDs. The co-doping with other combinations such as B, N-GQDs,[93] P, N-GQDs,[92] N, P, S-GQDs,[99] etc., were also reported. Thus, doping is a very useful tool for the tuning of the optical and electronic properties of GQDs according to the requirements. However, the identification of the doping sites as well as an understanding of the doping mechanism was not addressed in the literature.[80, 90, 91]

1.5. Functionalization of GQDs

As the synthesis processes of GQDs mostly involves chemical approaches, the uncontrolled functionalization is an unavoidable part of GQDs. However, the controlled functionalization in GQDs with strong electron-donating/accepting groups have an appreciable impact on their extrinsic properties, such as optical, chemical, and electronic properties. Jin et al. observed a ~30 nm redshift of the PL emission peak in amine-functionalized GQDs as compared to the bare GQDs.[46] They proposed that the electron-rich amine groups transfer their lone pair electrons to GQDs to enhance the electron density in GQDs, and consequently, the bandgap in functionalized GQDs decreases. The functionalization of GQDs with dopamine (DA) was discussed by Chowdhury and co-workers.[100] The $–NH_2$ group of DA was linked up with –COOH groups on the GQDs surface through the functionalization, and this altered the local chemical property of GQDs enormously. Interestingly, glycine modified GQDs was observed as chemically more active for the interaction with ascorbic acid as compared to GQDs.[101] For the enhancement of the fluorescence intensity of GQDs, GQDs were also reduced by hydrazine hydrate.[21, 102] Thus, like

the doping process, functionalization is also another beneficial approach for the modification of the properties of GQDs. However, the controlled functionalization of GQDs is still a great challenge.

1.6. GQDs Based Heterostructures

Due to the unique optical and electrical properties of GQDs, they have drawn huge attention worldwide for a diverse range of applications. Moreover, the water solubility, chemical stability, and biocompatibility of GQDs are advantageous for cutting-edge research in a variety of fields ranging from optoelectronics to bio-medical applications. Though the presence of abundant functional groups, defects, dopants, and their co-existence are responsible for making GQDs versatile, these factors are recognized as the reasons for poor conductivity of pristine GQDs, which limits the applications of GQDs in electronic devices. To overcome the present challenges and extend the versatility of GQDs, researchers are encouraged to develop the heterostructure (HS) of GQDs, which opens up a new research direction with GQDs for numerous potential applications in optoelectronics, energy storage, photocatalysis, sensing, etc. In GQDs, the presence of abundant oxygen functional groups, defect states, and edge states facilitate to integrate with semiconductors and plasmonic nanoparticles for the HS formation. A variety of semiconductors, such as few-layer molybdenum disulfide (MoS_2),[103] monolayer tungsten diselenide (WSe_2),[104] silicon nanowire (Si NW),[105] zinc oxide (ZnO),[106] etc., were used for the HS formation with GQDs and were utilized in efficient optoelectronics applications depending on the charge transfer mechanism. Titanium dioxide (TiO_2),[18] carbon nitride (C_3N_4),[107] etc. were also engaged in the HS formation with GQDs for catalytic applications. Besides the HS with semiconductors, N-GQDs were widely implemented for the formation of HS with plasmonic gold (Au)[108] and silver (Ag)[109] nanoparticles by the in-situ method for various sensing applications. Besides, GQDs are also used with graphene for the improvement of the performance of the graphene-based photodetectors, where GQDs increase the charge generation as well as charge separation in graphene.[110-112] Importantly, the choice of materials for the formation of HSs with GQDs is essential for the specific usages.

1.7. Applications of Various Type of GQDs and their Heterostructures

GQDs, generally known as graphene derived fluorescent material with various edge sites, abundant oxygen functional groups, defects, dopant, and chemical groups, have the ability to interact with a variety of ions, organic and inorganic molecules, chemicals, metals, semiconductors

and so on. Moreover, exceptional properties of GQDs, such as small size with QCE, high water solubility, photostability, non-toxicity, and moreover, ability to penetrate into living cells exploit them as prospective elements for the advanced applications in sensing, imaging, theranostic, energy storage and so on. Some of the potential applications of GQDs and GQDs based HSs are discussed below. **Fig. 1.8** showcases a library of applications of GQDs in various fields.

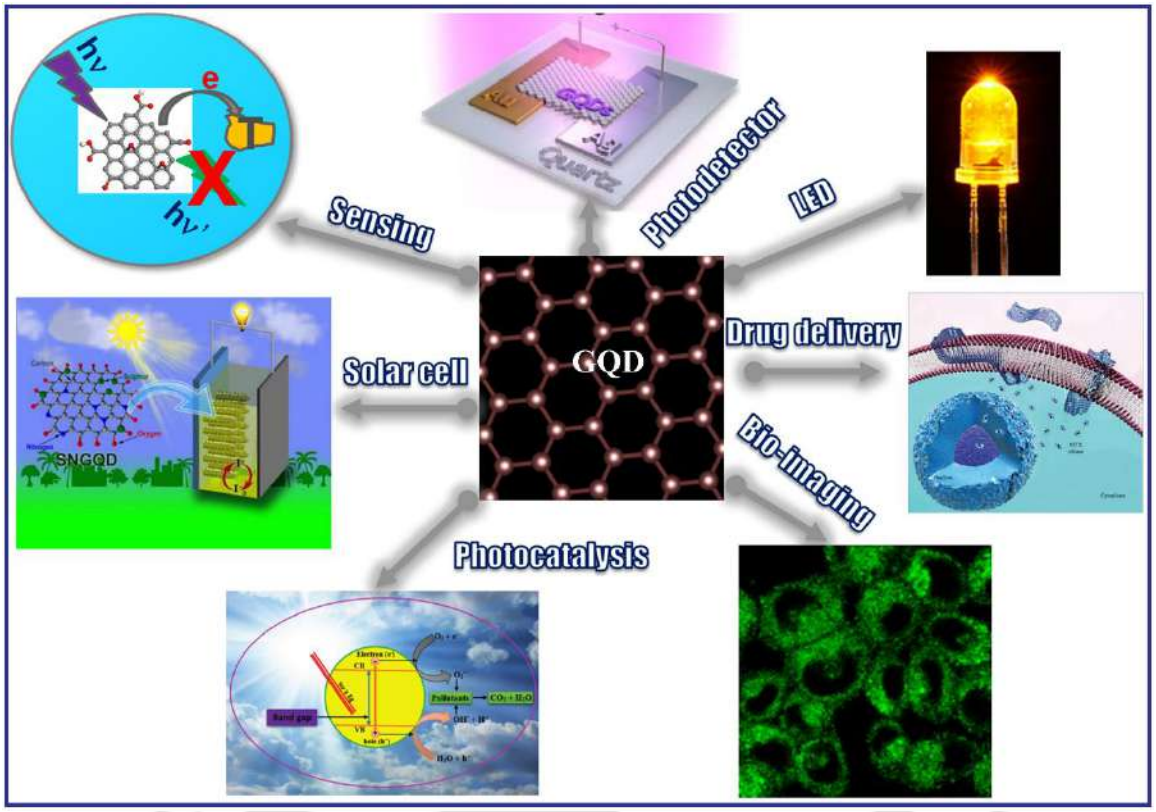

Fig. 1.8. A showcase of various applications of GQDs in different fields. Some parts are adopted from Ref.[1, 7, 95]

1.7.1. Applications as Sensor: Metal Ions, Bio-Molecules and Chemical Sensing

Unique optical and electronic properties of GQDs empower them for the intensive sensing of a variety of analytes by fluorometric method, colorimetric method, electrochemical method, and SERS method. In the fluorometric method, the PL intensity of GQDs change significantly with the presence of analyte due to the charge transfer (CT), energy transfer (ET), Förster resonance energy transfer (FRET) and ground-state complex formation, while the colorimetric method is mainly ascribed by the ground state complex formation resulting to the change of UV-vis absorption spectra. Sensing via the electrochemical method and photocurrent measurement are monitored by the change of the electrical current in the presence of analytes under the applied voltage and the

incident light, respectively. Among these, fluorometric and colorimetric methods are used most widely for sensing applications as these methods are quick, simple, low-cost, due to its easy sample preparation processes. The fluorometric sensing was used extensively for the detection of several heavy metal ions (Hg^{2+}, Pb^{2+}, etc.) including other metal ions (Fe^{3+}, Al^{3+}, Cu^{2+}, etc.), biomolecules (glucose (GL), DA, ascorbic acid (AA), uric acid (UA), hydroquinone (HQ), etc.) and chemicals (2,4,6-trinitrotoluene (TNT), etc.) with GQDs and GQDs based HSs. With GQDs based sensor, the efficient detection of H_2O_2, GL, cysteine (Cys), etc., were also established by the colorimetric process.[113, 114] However, the detection limit could not reach up to the satisfactory level by the colorimetric method. The selective and sensitive detection of H_2O_2 and heavy metal ions (Hg^{2+}) were reported with GQDs based HS by electrochemical method.[108, 115] Moreover, GQDs were used for the detection of numerous numbers of biomolecules and chemicals via the SERS method, where charge transfer from GQDs to the analytes was pointed out as the primary detection mechanism, though the mechanism of SERS enhancement was not addressed properly.[73, 109] A summary of the detecting analytes by different methods with GQDs and their HSs and the corresponding detection mechanism along with the limit of detection (LOD) are tabulated in **Table 1.1**. Even though numerous applications of GQDs and their HSs have been reported, there is huge scope for the improvement of the sensing performance for sophisticated applications. Further, there is a lack of quantitative understanding of the mechanism of sensing in various cases.

1.7.2. Optoelectronic Applications: Photodetector, Light Emitting Diodes and Solar Cell

Along with the exceptional optical properties of GQDs, due to the ultrathin layer and small size in the nanoscale level, GQDs are expected to be suitable for small and compact optoelectronic devices among the new generation smart inventions. GQDs are widely used for the fabrication as well as the development of the most useful optoelectronic devices such as high-performance photodetectors (PDs), light-emitting diodes (LEDs), solar cell, etc.. A brief discussion on the GQD based optoelectronic devices is presented below.

PD is a photo-sensitive diode with Schottky junction or p-n junction, which converts the incident photons into electric current usually under externally applied bias. PDs are intensively used in optical communications, video imaging, real-time monitoring, and so on.[34] Zhang et al. reported

Table 1.1. *Summary of the reported sensing performances of undoped and doped GQDs and their HSs with various analytes.*

Sample	*Detecting Analyte*	*Detecting Method*	*Detection Mechanism*	*Detection Range (μM)*	*LOD (nM)*	*Ref.*
GQDs	Cu^{2+}	Turn off fluorometric	CT	50–150	5.0×10^{4}	116
GQDs	Cu^{2+}		Complex formation	0.2–300	2.3×10^{2}	117
N-GQDs	Cu^{2+}		ET	0.0–35.0	7.2×10^{1}	118
S-GQDs	Ag^{+}		CT	0.1–130.0	3.0×10^{1}	79
S-GQDs	Pb^{2+}		-	0.1–140.0	3.0×10^{1}	119
DA/GQDs	Fe^{3+}		Complexation and oxidation of DA	0.02–2.0	7.6×10^{0}	100
N, S-GQDs	Hg^{2+}		CT and complex formation	0.1–15	1.4×10^{-1}	120
Glycine/GQDs	Ce^{4+}		Complex formation	50–700	5.0×10^{4}	101
N-GQDs	Al^{3+}	Turn on fluorometric	PET and complex formation	0.25–100	1.3×10^{3}	74
RhB derivative/GQDs	Fe^{3+}		Complex formation	0.0–65.0	2.0×10^{1}	121
GQDs/Au NP	Hg^{2+}	Electrochemical	Oxidation	2×10^{-5}–1.5×10^{-3}	2.0×10^{-2}	115
GQDs	HQ	Turn off fluorometric	Oxidation of HQ and CT	0.01–30.0	5.0×10^{0}	122
GQDs	DA		CT	0.01–60.0	8.0×10^{0}	23
GQDs	UA		CT	2–300	5.0×10^{2}	123
Polypyrrole/GQDs	DA		CT	0.005–8	1.0×10^{-2}	124
B-GQDs	GL	Turn on fluorometric	Aggregation	$100–2\times10^{5}$	6.0×10^{4}	80
GQDs/Cu^{2+}	AA		Reduction of Cu^{2+} to Cu^{+}	0.3–10.0	9.4×10^{1}	116
Glycine/GQDs/Ce^{4+}	AA		Reduction of Ce^{4+} to Ce^{3+}	0.03–17.0	2.5×10^{1}	101
Au@r-GQDs/Ag^{+}	Cys	Colorimetric	Aggregation	0.0–5	5.6×10^{0}	114
GQDs/Ag NP	H_2O_2		Reduction	0.1−100	3.3×10^{1}	113
GQDs/Ag NP	GL		Reduction	0.5−400	1.7×10^{2}	113
Au@N-GQDs	H_2O_2	Electrochemical	CT and reduction	$0.25−1\times10^{4}$	1.2×10^{2}	108
GQDs	RB6	SERS	CT	0.001–1.0	1.0×10^{0}	73
Ag@N-GQDs	GL		CT	$1–10^{6}$	1.0×10^{2}	109
GQDs	TNT	Turn off Fluorometric	FRET	$459–2.3\times10^{5}$	2.2×10^{3}	125

the fabrication of high-performance PD in deep UV region with GQDs.[7] However, due to limitation of the absorption of GQDs in the UV region, the performance of pure GQD based PDs cannot be extended into the visible or higher wavelength region. Meanwhile, HSs of GQDs with conventional semiconductor materials, such as Si NWs,[105] Si NPs,[126] ZnO,[106] etc., exhibited the photodetection in the UV-NIR region. Moreover, the high-performance broadband PDs in UV-

vis-NIR region were reported by the 2D HS of GQDs, such as GQDs/MoS_2,[103] N-GQDs/WSe_2,[104] GQDs/graphene,[110, 111] N-GQDs/boron nitride nanosheets/graphene,[112] etc. Nguyen et al. showed that due to the decoration of N-GQDs on monolayer WSe_2, the n-type doping effect improves the PL emission by the neutral exciton emission as well as the photo responsivity in WSe_2.[104] Mihalache et al. reported ~20 time higher photocurrent in GQDs/Si NW core-shell HS based Schottky PD with a remarkable enhancement of the external quantum efficiency as compared to pure Si NWs based PD, where GQDs act as a hole-blocking layer to increase the charge separation.[105] Thus, in these HSs, GQDs behave as an active material for the enhancement of the photocurrent. However, the usages of undoped and doped GQDs in the fabrication of PDs are explored in the literature. Tetsuka et al. reported the N-GQDs/graphene-based PD with the buffer layer of boron nitride nanosheets for the enhancement of the PD performance.[112] For the improvement of the PD performance, the usage of an additional layer is expensive for commercial applications.

As a clean and renewable energy source, the solar cell is another potential application field of GQDs. A solar cell is a photovoltaic device that converts solar light to the electric voltage under self-bias. Diao et al. demonstrated GQDs/Si heterojunctions solar cell with high power conversion efficiency (PCE) of ~12.35%, where GQDs behave as a hole transporting layer to separate the photo-generated electron-hole pairs as well as an electron blocking layer to reduce the recombination.[127] Li et al. reported the usage of GQDs as an electron-accepting layer in the fabrication of P3HT based solar cells with PCE of ~1.28%.[128] Moreover, the GQDs are also used with TiO_2, ZnO, etc., for solar cell applications.[34] Because of the low cost, chemical stability and non-toxicity, GQDs received inclusive attention in solar cell applications as compared to other traditional materials, such as silicon, perovskite, etc.[69]

LED is another optoelectronic device, where GQDs are used as a charge transporting layer or light convertor. Song et al. fabricated GQDs based LED, where GQD layers provide additional carrier transport to increase the radiative recombination, resulting in the overall enhancement of the current density.[129] Tang and co-workers reported the fabrication of white LED by applying a coating of highly fluorescent GQDs on commercial blue LED, where GQDs converted the sharp blue emission of LED to a broad spectrum leading to the white emission.[17] Note that due to the coating of GQDs, the agglomeration causes dramatic quenching of the fluorescence intensity of

GQDs, and consequently, the luminance of the LED is affected badly. Due to the ability of the tuning of the emission color as well as intensity, biocompatibility, chemical stability, low cost, etc., GQDs establish themselves as a potential material in organic and inorganic LED applications.[10, 34]

1.7.3. Photocatalytic Applications

A photocatalysis process is described as a chemical reaction that is accelerated by a catalyst in the presence of light. The photocatalytic process is initiated through the generation of electron/hole pairs by the absorption of the incident light. In the recent situation, this photocatalysis approach is implemented for environmental cleaning as well as renewable energy. For environmental cleaning, TiO_2 has been widely used for dye degradation by the UV light. However, the high bandgap nature of TiO_2 limits its photocatalytic efficiency in the visible region. Thus, to harness the visible spectrum of sunlight, the bandgap of TiO_2 has been modified in various ways such as doping, functionalization, and HS formation. Among them, the formation of HSs with GQDs has drawn huge attention in photocatalytic applications. Gone et al. reported TiO_2/GQDs heterojunction for the enhanced visible-light photocatalysis of methylene blue (MB) by the interfacial charge separation.[18] They demonstrated ~5.2 times higher degradation rate constant for the heterostructure as compared to bare TiO_2. Besides the undoped GQDs, the S, N co-doped GQDs were also used for the enhancement of the photocatalytic activity of TiO_2.[130, 131] Besides TiO_2 based HSs, other materials HSs, such as GQDs/ZnO NWs were also used for the efficient photocatalytic degradation of MB under solar irradiation.[132] Along with the dye degradation, the photocatalytic activity of S, N-GQDs/TiO_2 was used for the water splitting under solar light.[133] The H_2 generation by the photocatalysis of water was also reported with GQDs/C_3N_4 composites.[134]

1.7.4. Energy Storage Applications: Supercapacitor and Battery

In the present era, scientists are giving huge attention to renewable energy sources to meet the increasing energy crisis. Meanwhile, the storage of energy is another important issue. In that context, the supercapacitor and lithium-ion battery (LIB) are highlighted as the potential devices for efficient energy storage.

Owing to the unique structural properties, including high surface area, GQDs have engrossed tremendous research interest in supercapacitors. Zhang et al. demonstrated an ideal electric double-layer capacitance behavior of GQD electrodes.[135] Because of the nanometer size, huge edge sites,

and moreover, the high surface area of GQDs, they exhibit high specific capacitance (SC) (~192.9 F g^{-1} at 100 mV S^{-1}), which is two times higher than that of the graphene electrodes. Additionally, GQDs based capacitor showed excellent stability with long cycle life. Liu et al. demonstrated that as compared to the symmetric electrode with GQDs, the asymmetric electrode-based supercapacitor produces better performance.[136] They reported GQDs/MnO_2 asymmetric electrode micro-supercapacitor with an energy density of ~0.154 μWh cm^{-2} at the current density of 15 μA cm^{-2}, which is two times higher than that of the GQDs/GQDs system.

Due to high efficiency, long cycling life, low weight, high energy density, long term stability, LIB becomes one of the most useful batteries in portable electronics used in daily life. As the performance of LIB strongly depends on their electrode properties, the development of the electrodes is in high demand. Guo and co-workers showed the enhancement of the storage capability of LIB after modification of MoS_2 anode with GQDs.[137] Khan et al. reported the incorporation of N-functionalized GQDs in LIB as a stable charge transporting layer as well as a protecting layer of $Li_4Ti_5O_{12}$ anode from electrolyte for the enhancement of specific capacity and cycling life.[138] The incorporation of GQDs in supercapacitor and LIB may pave the way for next-generation storage devices.

1.7.5. Bio-Medical Applications: Bioimaging and Drug Delivery

GQDs have drawn tremendous attention in biomedical applications, such as bioimaging and drug delivery in living cells.

Bioimaging is an interesting technology used in both research and clinical fields for imaging inside the biological cells by applying selective fluorescent material. Bright fluorescence emission in the visible region along with high photostability, non-toxicity, and biocompatibility are the advantages of GQDs over the conventional mounting dyes for targeted bioimaging in living cells. Peng et al. reported the in vitro imaging of human breast cancer cell lines T47D with green fluorescent GQDs.[42] They got a phase-contrast image of the cancer cells, where the blue-stained nucleus was surrounded by green color. As the low energy excitation is favorable for living cell, doped functionalized GQDs with red emission are enormously used for the bioimaging applications.[139-141]

Free drug delivery to living cells is observed to be passive and inefficient due to the intracellular biologic barriers, whereas the conjugated drug is able to reach inside the cells and particularly to the specific target. Recently GQDs are used for targeted drug delivery in the living cell. Chen and co-workers reported nuclear-targeted drug delivery with GQDs conjugated peptide TAT along with the real-time drug release process.[142] In the drug delivery process, GQDs acted as the drug carriers, and TAT helped for the attachment of the drug to the nucleus of the cell. When the drug was released, the fluorescence signal of GQDs increased due to the inhibition of FRET to the drug, and depending on the change of fluorescence signal, real-time monitoring was possible. GQD conjugated albumin nanoparticles functionalized with hyaluronic acid were efficiently used for the drug delivery in the pancreatic cancer cells, where the green fluorescent GQDs confirmed the presence of albumin nanoparticles.[143] Thus, GQDs exhibit huge potential for bioimaging as well as target-specific drug delivery.

1.8. Unresolved Issues and Challenges

Due to the outstanding structural and optical properties, GQDs have established themselves as a promising material for various potential applications from academics to industry level. Although several studies have been done on the properties of GQDs as well as the applications of GQDs in numerous fields ranging from electronics to biomedical, GQDs are still at the primary stage of research, and there are plenty of unresolved issues and challenges yet to be addressed to meet the future demands. Firstly, controlled and large-scale synthesis of GQDs with predefined properties are still a challenge. Precise location dopants in GQDs and their actual role in tailoring the properties of GQDs are yet to be understood. As a fluorescent material, the PL QY is one of the most important properties of GQDs. GQDs, prepared by the top-down method, can give high production yield, while the PL QY is remarkably low. On the other hand, the bottom-up method exhibits relatively high PL QY, while the production yield is very poor. To fulfill the commercial requirements, along with the high production yield, the achievement of high PL QY is a great challenge in the present research. To date, most of the reported PL emissions in GQDs are of blue to green colors, and few are of yellow to red colors. The extension of the color tunability in the visible-NIR region, along with the tuning of the PL intensity is essential to solving various issues in optical and biomedical applications. Though various features of GQDs such as QCE, functional groups, defects, etc., were pointed out to explain the PL emission, some of these appear

contradictory to each other, and isolating the contributions of each remains a challenge to the researchers. To understand the mechanism of the PL emission as well as to point out the origin of emission centers are the great challenges in the research of GQDs. The usages of GQDs in various fields, such as sensing, optoelectronics, SERS, etc., were reported. In the case of SERS phenomena, multiple factors are involved in the SERS enhancement. To identify the individual contribution of different factors in the SERS process is an important issue for the improvement of the SERS based sensors. Though bare GQDs (un-doped/doped) were used extensively for various sensing applications, there are a lot of scopes to explore their hybrid structure as more efficient sensors. Coming to the optoelectronic field, GQDs are generally used as a charge transporting/ generating layers in the fabrication of electronic devices like PD, LED, solar cell, etc. Moreover, these devices generally use commercially available charge transporting materials. The application of bare GQDs or their hybrid structures in the optoelectronic devices without any commercial charge-transporting layers can open up a new direction in their applications.

1.9. Focus of the Present Thesis

Even though GQDs have garnered a huge research interest in nanoscience and nanotechnology since the last decade, the advancement in GQDs research is hampered by several challenges, especially in the field of GQD based sensors and optoelectronic applications, as discussed above. In the present thesis, we have attempted to synthesis different types of GQDs and their hybrid structures for the advanced sensing applications in various fields of nanoscience along with the investigation of their interesting photophysical properties. The objectives of the present thesis are as follows:

- Interaction of GQDs with single-walled CNTs (SWCNTs) and tuning of the PL intensity of undoped GQDs (U-GQDs) using SWCNTs as a quencher.
- Investigation of the origins of the PL emission in GQDs by the controlled synthesis of un-doped and doped GQDs in different solvents by top-down methods.
- The mechanism and applications of N-GQDs as an efficient SERS substrate for the sensing of rhodamine-B (RhB) and as a light convertor for the fabrication of the liquid phase white LED. In this study, we attempt to isolate the individual contribution of various factors involved in the SERS enhancement by controlled experiments.

- Detection of DA with ultra-high sensitivity by a semiconductor-semiconductor based hybrid structure with GO and tungsten disulfide QDs (GO/WS_2). Moreover, a comprehensive study of the DA sensing with the hybrid structure of GQDs and WS_2 QDs are addressed to find out the reasons behind the ultra-high sensitivity of GO/WS_2 towards DA.
- Metal-semiconductor based hybrid structure of N-GQDs, such as with plasmonic Au NPs (Au@N-GQDs) are investigated for multipurpose applications, such as DA sensor, Fe^{3+} sensor, and a high-speed photodetector.

1.10. Organization of the Thesis

The complete thesis work is presented in seven chapters. In the present chapter (**Chapter 1**), an overview of the various synthesis processes, including their advantages and disadvantages, structural and optical properties, and the diverse applications of various types of GQDs and their hybrid structures along with their limitations are discussed. **Chapter 2** discusses the interaction of undoped GQDs with SWCNTs and tuning of the PL intensity of GQDs by the incorporation of SWCNTs. **Chapter 3** provides a detailed investigation of the origin of PL emission in GQDs by the controlled synthesis of different types of undoped and doped GQDs and their applications as SERS substrate and light convertor. **Chapter 4** presents the formation of a hybrid structure of GO and WS_2 QDs for an ultra-high sensitive detection of DA in the human serum by the fluorometric method. In **Chapter 5**, Au@N-GQDs are implemented for the dual-mode sensing of DA along with the investigation of the sensing mechanism. Au@N-GQDs are further used as Fe^{3+} sensor and fast photodetector in **Chapter 6**. **Chapter 7** summarizes the important findings and outlooks of the present thesis for future works.

References

1. S. Chung, R. A. Revia and M. Zhang, *Adv. Mater.*, 2019, 1904362.
2. Z. Jin, P. Owour, S. Lei and L. Ge, *Curr. Opin. Colloid Interface Sci.*, 2015, **20**, 439-453.
3. A. A. Balandin, *Nat. Mater.*, 2011, **10**, 569-581.
4. Z. Chen, Z. Cheng, J. Wang, X. Wan, C. Shu, H. K. Tsang, H. P. Ho and J. B. Xu, *Adv. Opt. Mater.*, 2015, **3**, 1207-1214.

5. A. C. Ferrari, J. Meyer, V. Scardaci, C. Casiraghi, M. Lazzeri, F. Mauri, S. Piscanec, D. Jiang, K. Novoselov and S. Roth, *Phys. Rev. Lett.*, 2006, **97**, 187401.
6. C.-W. Chiang, G. Haider, W.-C. Tan, Y.-R. Liou, Y.-C. Lai, R. Ravindranath, H.-T. Chang and Y.-F. Chen, *ACS applied materials & interfaces*, 2016, **8**, 466-471.
7. Q. Zhang, J. Jie, S. Diao, Z. Shao, Q. Zhang, L. Wang, W. Deng, W. Hu, H. Xia and X. Yuan, *ACS nano*, 2015, **9**, 1561-1570.
8. J. Sanghwa, R. L. Pinals, D. Bhushan, S. Hayong, K. Ankarao, D. Debika, Q. Wu, H. Moon-Ho, P. Prabir and M. P. Landry, *Sci. Rep.*, 2020, **10**.
9. G. Konstantatos, M. Badioli, L. Gaudreau, J. Osmond, M. Bernechea, F. P. G. De Arquer, F. Gatti and F. H. Koppens, *Nat. Nanotechnol.*, 2012, **7**, 363-368.
10. L. Li, G. Wu, G. Yang, J. Peng, J. Zhao and J.-J. Zhu, *Nanoscale*, 2013, **5**, 4015-4039.
11. X. Yan, X. Cui and L.-s. Li, *J. Am. Chem. Soc.*, 2010, **132**, 5944-5945.
12. Y. Yan, J. Gong, J. Chen, Z. Zeng, W. Huang, K. Pu, J. Liu and P. Chen, *Adv. Mater.*, 2019, **31**, 1808283.
13. D. Pan, J. Zhang, Z. Li and M. Wu, *Adv. Mater.*, 2010, **22**, 734-738.
14. G. Rajender and P. Giri, *J. Mater. Chem. C*, 2016, **4**, 10852-10865.
15. Z. Gan, H. Xu and Y. Hao, *Nanoscale*, 2016, **8**, 7794-7807.
16. S. Wang, I. S. Cole, D. Zhao and Q. Li, *Nanoscale*, 2016, **8**, 7449-7458.
17. L. Tang, R. Ji, X. Cao, J. Lin, H. Jiang, X. Li, K. S. Teng, C. M. Luk, S. Zeng and J. Hao, *ACS Nano*, 2012, **6**, 5102-5110.
18. G. Rajender, J. Kumar and P. Giri, *Appl. Catal. B*, 2018, **224**, 960-972.
19. S. Chen, Y. Quan, Y.-L. Yu and J.-H. Wang, *ACS Biomater Sci Eng*, 2017, **3**, 313-321.
20. L. Deng, L. Liu, C. Zhu, D. Li and S. Dong, *ChemComm*, 2013, **49**, 2503-2505.
21. M. Zhang, L. Bai, W. Shang, W. Xie, H. Ma, Y. Fu, D. Fang, H. Sun, L. Fan and M. Han, *J. Mater. Chem.*, 2012, **22**, 7461-7467.
22. G. Rajender, U. Goswami and P. Giri, *J. Colloid Interface Sci.*, 2019, **541**, 387-398.
23. S. Weng, D. Liang, H. Qiu, Z. Liu, Z. Lin, Z. Zheng, A. Liu, W. Chen and X. Lin, *Sens. Actuator B-Chem.*, 2015, **221**, 7-14.
24. T.-T. Xu, J.-X. Yang, J.-M. Song, J.-S. Chen, H.-L. Niu, C.-J. Mao, S.-Y. Zhang and Y.-H. Shen, *Sens. Actuators B Chem.*, 2017, **243**, 863-872.
25. Y.-X. Qi, M. Zhang, Q.-Q. Fu, R. Liu and G.-Y. Shi, *ChemComm*, 2013, **49**, 10599-10601.
26. S. L. Ting, S. J. Ee, A. Ananthanarayanan, K. C. Leong and P. Chen, *Electrochimica Acta*, 2015, **172**, 7-11.
27. T. Dey, S. Mukherjee, A. Ghorai, S. Das and S. K. Ray, *Carbon*, 2018, **140**, 394-403.
28. K. D. Lee, M. J. Park, D.-Y. Kim, S. M. Kim, B. Kang, S. Kim, H. Kim, H.-S. Lee, Y. Kang and S. S. Yoon, *ACS Appl. Mater. Interfaces*, 2015, **7**, 19043-19049.
29. S. Mondal, U. Rana and S. Malik, *ChemComm*, 2015, **51**, 12365-12368.
30. D. Chao, C. Zhu, X. Xia, J. Liu, X. Zhang, J. Wang, P. Liang, J. Lin, H. Zhang and Z. X. Shen, *Nano Lett.*, 2015, **15**, 565-573.
31. X. Su, C. Chan, J. Shi, M.-K. Tsang, Y. Pan, C. Cheng, O. Gerile and M. Yang, *Biosens. Bioelectron.*, 2017, **92**, 489-495.
32. T. Chen, H. Yu, N. Yang, M. Wang, C. Ding and J. Fu, *J. Mater. Chem. B*, 2014, **2**, 4979-4982.
33. S. Zhu, Y. Song, J. Wang, H. Wan, Y. Zhang, Y. Ning and B. Yang, *Nano Today*, 2017, **13**, 10-14.
34. P. Tian, L. Tang, K. Teng and S. Lau, *Mater. Today Chem.*, 2018, **10**, 221-258.

35. S. Kim, S. W. Hwang, M.-K. Kim, D. Y. Shin, D. H. Shin, C. O. Kim, S. B. Yang, J. H. Park, E. Hwang and S.-H. Choi, *ACS nano*, 2012, **6**, 8203-8208.
36. X. T. Zheng, A. Ananthanarayanan, K. Q. Luo and P. Chen, *Small*, 2015, **11**, 1620-1636.
37. S.-H. Song, M. Jang, H. Yoon, Y.-H. Cho, S. Jeon and B.-H. Kim, *RSC Adv.*, 2016, **6**, 97990-97994.
38. A. V. Vorontsov and E. V. Tretyakov, *Phys. Chem. Chem. Phys.*, 2018, **20**, 14740-14752.
39. M. Li, T. Chen, J. J. Gooding and J. Liu, *ACS Sens.*, 2019, **4**, 1732-1748.
40. R. K. Biroju, G. Rajender and P. Giri, *Carbon*, 2015, **95**, 228-238.
41. Y. Li, Y. Zhao, H. Cheng, Y. Hu, G. Shi, L. Dai and L. Qu, *J. Am. Chem. Soc.*, 2012, **134**, 15-18.
42. J. Peng, W. Gao, B. K. Gupta, Z. Liu, R. Romero-Aburto, L. Ge, L. Song, L. B. Alemany, X. Zhan and G. Gao, *Nano Lett.*, 2012, **12**, 844-849.
43. E. Dervishi, Z. Ji, H. Htoon, M. Sykora and S. K. Doorn, *Nanoscale*, 2019, **11**, 16571-16581.
44. J. Kim, N. Lee, Y. H. Min, S. Noh, N.-K. Kim, S. Jung, M. Joo and Y. Yamada, *ACS Omega*, 2018, **3**, 17789-17796.
45. S. S. Yamijala, A. Bandyopadhyay and S. K. Pati, *Chem. Phys. Lett.*, 2014, **603**, 28-32.
46. S. H. Jin, D. H. Kim, G. H. Jun, S. H. Hong and S. Jeon, *ACS Nano*, 2013, **7**, 1239-1245.
47. R. Ye, Z. Peng, A. Metzger, J. Lin, J. A. Mann, K. Huang, C. Xiang, X. Fan, E. L. Samuel and L. B. Alemany, *ACS Appl. Mater. Interfaces*, 2015, **7**, 7041-7048.
48. X. Hai, J. Feng, X. Chen and J. Wang, *J. Mater. Chem. B*, 2018, **6**, 3219-3234.
49. C. Zhu, S. Yang, G. Wang, R. Mo, P. He, J. Sun, Z. Di, N. Yuan, J. Ding and G. Ding, *J. Mater. Chem. C*, 2015, **3**, 8810-8816.
50. X. Tan, Y. Li, X. Li, S. Zhou, L. Fan and S. Yang, *ChemComm*, 2015, **51**, 2544-2546.
51. Y. Zhao, X. Wu, S. Sun, L. Ma, L. Zhang and H. Lin, *Carbon*, 2017, **124**, 342-347.
52. Z. Gan, X. Wu, G. Zhou, J. Shen and P. K. Chu, *Adv. Opt. Mater.*, 2013, **1**, 554-558.
53. J. Shen, Y. Zhu, C. Chen, X. Yang and C. Li, *ChemComm*, 2011, **47**, 2580-2582.
54. S. Zhu, J. Zhang, C. Qiao, S. Tang, Y. Li, W. Yuan, B. Li, L. Tian, F. Liu and R. Hu, *ChemComm*, 2011, **47**, 6858-6860.
55. S. Yang, J. Sun, X. Li, W. Zhou, Z. Wang, P. He, G. Ding, X. Xie, Z. Kang and M. Jiang, *J. Mater. Chem. A*, 2014, **2**, 8660-8667.
56. S. Zhu, J. Zhang, S. Tang, C. Qiao, L. Wang, H. Wang, X. Liu, B. Li, Y. Li and W. Yu, *Adv. Funct. Mater.*, 2012, **22**, 4732-4740.
57. A. Xu, P. He, T. Huang, J. Li, X. Hu, P. Xiang, D. Chen, S. Yang, G. Wang and G. Ding, *Synth. Met.*, 2018, **244**, 106-112.
58. Z. Luo, G. Qi, K. Chen, M. Zou, L. Yuwen, X. Zhang, W. Huang and L. Wang, *Adv. Funct. Mater.*, 2016, **26**, 2739-2744.
59. Y. Shin, J. Park, D. Hyun, J. Yang, J.-H. Lee, J.-H. Kim and H. Lee, *Nanoscale*, 2015, **7**, 5633-5637.
60. H. Tetsuka, R. Asahi, A. Nagoya, K. Okamoto, I. Tajima, R. Ohta and A. Okamoto, *Adv. Mater.*, 2012, **24**, 5333-5338.
61. B. Guo, K. Yu, H. Li, R. Qi, Y. Zhang, H. Song, Z. Tang, Z. Zhu and M. Chen, *ACS Appl. Mater. Interfaces*, 2017, **9**, 3653-3660.
62. D. B. Shinde and V. K. Pillai, *Chem. Eur. J.*, 2012, **18**, 12522-12528.
63. W. Chen, G. Lv, W. Hu, D. Li, S. Chen and Z. Dai, *Nanotechnol. Rev.*, 2018, **7**, 157-185.

64. F. Liu, M. H. Jang, H. D. Ha, J. H. Kim, Y. H. Cho and T. S. Seo, *Adv. Mater.*, 2013, **25**, 3657-3662.
65. L. L. Li, J. Ji, R. Fei, C. Z. Wang, Q. Lu, J. R. Zhang, L. P. Jiang and J. J. Zhu, *Adv. Funct. Mater.*, 2012, **22**, 2971-2979.
66. S. H. Kang, S. Mhin, H. Han, K. M. Kim, J. L. Jones, J. H. Ryu, J. S. Kang, S. H. Kim and K. B. Shim, *Sci. Rep.*, 2016, **6**, 38423.
67. H. Sun, L. Wu, W. Wei and X. Qu, *Mater. Today*, 2013, **16**, 433-442.
68. Y. Dong, J. Shao, C. Chen, H. Li, R. Wang, Y. Chi, X. Lin and G. Chen, *Carbon*, 2012, **50**, 4738-4743.
69. S. Bak, D. Kim and H. Lee, *Curr. Appl. Phys.*, 2016, **16**, 1192-1201.
70. Q. Liu, J. Zhang, H. He, G. Huang, B. Xing, J. Jia and C. Zhang, *Nanomaterials*, 2018, **8**, 844.
71. R. Tian, S. Zhong, J. Wu, W. Jiang, Y. Shen and T. Wang, *Opt. Mater.*, 2016, **60**, 204-208.
72. S. Khan, A. Gupta, N. C. Verma and C. K. Nandi, *Nano Lett.*, 2015, **15**, 8300-8305.
73. D. Liu, X. Chen, Y. Hu, T. Sun, Z. Song, Y. Zheng, Y. Cao, Z. Cai, M. Cao and L. Peng, *Nat. Commun.*, 2018, **9**, 193.
74. B.-Y. Fang, C. Li, Y.-Y. Song, F. Tan, Y.-C. Cao and Y.-D. Zhao, *Biosens. Bioelectron.*, 2018, **100**, 41-48.
75. L. Tang, R. Ji, X. Li, K. S. Teng and S. P. Lau, *J. Mater. Chem. C*, 2013, **1**, 4908-4915.
76. L. Zhang, D. Peng, R.-P. Liang and J.-D. Qiu, *Anal. Chem.*, 2015, **87**, 10894-10901.
77. X. Li, S. P. Lau, L. Tang, R. Ji and P. Yang, *Nanoscale*, 2014, **6**, 5323-5328.
78. S. Li, Y. Li, J. Cao, J. Zhu, L. Fan and X. Li, *Anal. Chem.*, 2014, **86**, 10201-10207.
79. S. Bian, C. Shen, Y. Qian, J. Liu, F. Xi and X. Dong, *Sens. Actuators B Chem.*, 2017, **242**, 231-237.
80. L. Zhang, Z.-Y. Zhang, R.-P. Liang, Y.-H. Li and J.-D. Qiu, *Anal. Chem.*, 2014, **86**, 4423-4430.
81. Z. Fan, Y. Li, X. Li, L. Fan, S. Zhou, D. Fang and S. Yang, *Carbon*, 2014, **70**, 149-156.
82. X. Hai, Q.-X. Mao, W.-J. Wang, X.-F. Wang, X.-W. Chen and J.-H. Wang, *J. Mater. Chem. B*, 2015, **3**, 9109-9114.
83. Y. Li, S. Li, Y. Wang, J. Wang, H. Liu, X. Liu, L. Wang, X. Liu, W. Xue and N. Ma, *Phys. Chem. Chem. Phys.*, 2017, **19**, 11631-11638.
84. G. Wang, A. Xu, P. He, Q. Guo, Z. Liu, Z. Wang, J. Li, X. Hu, Z. Wang and D. Chen, *Mater. Lett.*, 2019, **242**, 156-159.
85. F. Qian, X. Li, L. Tang, S. K. Lai, C. Lu and S. P. Lau, *AIP Adv.*, 2016, **6**, 075116.
86. S. Yang, J. Sun, P. He, X. Deng, Z. Wang, C. Hu, G. Ding and X. Xie, *Chem. Mater.*, 2015, **27**, 2004-2011.
87. W. Zuo, L. Tang, J. Xiang, R. Ji, L. Luo, L. Rogée and S. Ping Lau, *Appl. Phys. Lett.*, 2017, **110**, 221901.
88. H. Sun, H. Ji, E. Ju, Y. Guan, J. Ren and X. Qu, *Chem. Eur. J.*, 2015, **21**, 3791-3797.
89. X. Li, S. P. Lau, L. Tang, R. Ji and P. Yang, *J. Mater. Chem. C*, 2013, **1**, 7308-7313.
90. D. Qu, Z. Sun, M. Zheng, J. Li, Y. Zhang, G. Zhang, H. Zhao, X. Liu and Z. Xie, *Adv. Opt. Mater.*, 2015, **3**, 360-367.
91. S. Kundu, R. M. Yadav, T. Narayanan, M. V. Shelke, R. Vajtai, P. M. Ajayan and V. K. Pillai, *Nanoscale*, 2015, **7**, 11515-11519.
92. A. Ananthanarayanan, Y. Wang, P. Routh, M. A. Sk, A. Than, M. Lin, J. Zhang, J. Chen, H. Sun and P. Chen, *Nanoscale*, 2015, **7**, 8159-8165.

93. H. Fei, R. Ye, G. Ye, Y. Gong, Z. Peng, X. Fan, E. L. Samuel, P. M. Ajayan and J. M. Tour, *ACS nano*, 2014, **8**, 10837-10843.
94. C. Hu, Y. Liu, Y. Yang, J. Cui, Z. Huang, Y. Wang, L. Yang, H. Wang, Y. Xiao and J. Rong, *J. Mater. Chem. B*, 2013, **1**, 39-42.
95. Q. Liu, B. Guo, Z. Rao, B. Zhang and J. R. Gong, *Nano Lett.*, 2013, **13**, 2436-2441.
96. X. Niu, Y. Li, H. Shu and J. Wang, *Nanoscale*, 2016, **8**, 19376-19382.
97. F. A. Permatasari, A. H. Aimon, F. Iskandar, T. Ogi and K. Okuyama, *Sci. Rep.*, 2016, **6**, 21042.
98. G. Wang, Q. Guo, D. Chen, Z. Liu, X. Zheng, A. Xu, S. Yang and G. Ding, *ACS Appl. Mater. Interfaces*, 2018, **10**, 5750-5759.
99. Y. Xu, S. Wang, X. Hou, Z. Sun, Y. Jiang, Z. Dong, Q. Tao, J. Man and Y. Cao, *Appl. Surf. Sci.*, 2018, **445**, 519-526.
100. A. Dutta Chowdhury and R.-a. Doong, *ACS Appl. Mater. Interfaces*, 2016, **8**, 21002-21010.
101. R. Liu, R. Yang, C. Qu, H. Mao, Y. Hu, J. Li and L. Qu, *Sens. Actuators B Chem.*, 2017, **241**, 644-651.
102. Y. Feng, J. Zhao, X. Yan, F. Tang and Q. Xue, *Carbon*, 2014, **66**, 334-339.
103. C. Chen, H. Qiao, S. Lin, C. M. Luk, Y. Liu, Z. Xu, J. Song, Y. Xue, D. Li and J. Yuan, *Sci. Rep.*, 2015, **5**, 11830.
104. D. A. Nguyen, H. M. Oh, N. T. Duong, S. Bang, S. J. Yoon and M. S. Jeong, *ACS Appl. Mater. Interfaces*, 2018, **10**, 10322-10329.
105. I. Mihalache, A. Radoi, R. Pascu, C. Romanitan, E. Vasile and M. Kusko, *ACS Appl. Mater. Interfaces*, 2017, **9**, 29234-29247.
106. S. Dhar, T. Majumder and S. P. Mondal, *Mater. Res. Bull.*, 2017, **95**, 198-203.
107. G. Rajender, B. Choudhury and P. Giri, *Nanotechnology*, 2017, **28**, 395703.
108. J. Ju and W. Chen, *Anal. Chem.*, 2015, **87**, 1903-1910.
109. J. Ju, W. Liu, C. M. Perlaki, K. Chen, C. Feng and Q. Liu, *Sci. Rep.*, 2017, **7**, 6917.
110. C.-W. Chiang, G. Haider, W.-C. Tan, Y.-R. Liou, Y.-C. Lai, R. Ravindranath, H.-T. Chang and Y.-F. Chen, *ACS Appl. Mater. Interfaces*, 2016, **8**, 466-471.
111. C. O. Kim, S. W. Hwang, S. Kim, D. H. Shin, S. S. Kang, J. M. Kim, C. W. Jang, J. H. Kim, K. W. Lee and S.-H. Choi, *Sci. Rep.*, 2014, **4**, 5603.
112. H. Tetsuka, A. Nagoya and S.-i. Tamura, *Nanoscale*, 2016, **8**, 19677-19683.
113. S. Chen, X. Hai, X.-W. Chen and J.-H. Wang, *Anal. Chem.*, 2014, **86**, 6689-6694.
114. X. Hai, X. Lin, X. Chen and J. Wang, *Sens. Actuator B-Chem.*, 2018, **257**, 228-236.
115. S. L. Ting, S. J. Ee, A. Ananthanarayanan, K. C. Leong and P. Chen, *Electrochim. Acta*, 2015, **172**, 7-11.
116. J.-J. Liu, Z.-T. Chen, D.-S. Tang, Y.-B. Wang, L.-T. Kang and J.-N. Yao, *Sens. Actuators B Chem.*, 2015, **212**, 214-219.
117. F. Wang, Z. Gu, W. Lei, W. Wang, X. Xia and Q. Hao, *Sens. Actuators B Chem.*, 2014, **190**, 516-522.
118. Z. Wang and Z. Fan, *Spectrochim. Acta A Mol. Biomol. Spectrosc.*, 2018, **189**, 195-201.
119. S. Bian, C. Shen, H. Hua, L. Zhou, H. Zhu, F. Xi, J. Liu and X. Dong, *RSC Adv.*, 2016, **6**, 69977-69983.
120. N. T. N. Anh, A. D. Chowdhury and R.-a. Doong, *Sens. Actuators B Chem.*, 2017, **252**, 1169-1178.
121. R. Guo, S. Zhou, Y. Li, X. Li, L. Fan and N. H. Voelcker, *ACS Appl. Mater. Interfaces*, 2015, **7**, 23958-23966.

122. Y. He, J. Sun, D. Feng, H. Chen, F. Gao and L. Wang, *Biosens. Bioelectron.*, 2015, **74**, 418-422.
123. N. Cai, L. Tan, Y. Li, T. Xia, T. Hu and X. Su, *Anal. Chim. Acta*, 2017, **965**, 96-102.
124. X. Zhou, P. Ma, A. Wang, C. Yu, T. Qian, S. Wu and J. Shen, *Biosens. Bioelectron.*, 2015, **64**, 404-410.
125. L. Fan, Y. Hu, X. Wang, L. Zhang, F. Li, D. Han, Z. Li, Q. Zhang, Z. Wang and L. Niu, *Talanta*, 2012, **101**, 192-197.
126. S. Kim, D. H. Shin, J. Kim, C. W. Jang, S. S. Kang, J. M. Kim, J. H. Kim, D. H. Lee, J. H. Kim and S.-H. Choi, *Sci. Rep.*, 2016, **6**, 27145.
127. S. Diao, X. Zhang, Z. Shao, K. Ding, J. Jie and X. Zhang, *Nano Energy*, 2017, **31**, 359-366.
128. Y. Li, Y. Hu, Y. Zhao, G. Shi, L. Deng, Y. Hou and L. Qu, *Adv. Mater.*, 2011, **23**, 776-780.
129. S. H. Song, M. H. Jang, J. Chung, S. H. Jin, B. H. Kim, S. H. Hur, S. Yoo, Y. H. Cho and S. Jeon, *Adv. Opt. Mater.*, 2014, **2**, 1016-1023.
130. H. Tian, K. Shen, X. Hu, L. Qiao and W. Zheng, *J. Alloys Compd.*, 2017, **691**, 369-377.
131. D. Qu, M. Zheng, P. Du, Y. Zhou, L. Zhang, D. Li, H. Tan, Z. Zhao, Z. Xie and Z. Sun, *Nanoscale*, 2013, **5**, 12272-12277.
132. M. Ebrahimi, M. Samadi, S. Yousefzadeh, M. Soltani, A. Rahimi, T.-c. Chou, L.-C. Chen, K.-H. Chen and A. Z. Moshfegh, *ACS Sustain. Chem. Eng.*, 2017, **5**, 367-375.
133. H. Xie, C. Hou, H. Wang, Q. Zhang and Y. Li, *Nanoscale Res. Lett.*, 2017, **12**, 400.
134. Z. Ma, R. Sa, Q. Li and K. Wu, *Phys. Chem. Chem. Phys.*, 2016, **18**, 1050-1058.
135. S. Zhang, L. Sui, H. Dong, W. He, L. Dong and L. Yu, *ACS Appl. Mater. Interfaces*, 2018, **10**, 12983-12991.
136. W. W. Liu, Y. Q. Feng, X. B. Yan, J. T. Chen and Q. J. Xue, *Adv. Funct. Mater.*, 2013, **23**, 4111-4122.
137. J. Guo, H. Zhu, Y. Sun, L. Tang and X. Zhang, *J. Mater. Chem. A*, 2016, **4**, 4783-4789.
138. F. Khan, M. Oh and J. H. Kim, *Chem. Eng. J.*, 2019, **369**, 1024-1033.
139. J. Ge, M. Lan, B. Zhou, W. Liu, L. Guo, H. Wang, Q. Jia, G. Niu, X. Huang and H. Zhou, *Nat. Commun.*, 2014, **5**, 1-8.
140. D. Qu, Z. Sun, M. Zheng, J. Li, Y. Zhang, G. Zhang, H. Zhao, X. Liu and Z. Xie, *Adv. Opt. Mater.*, 2015, **3**, 360-367.
141. M. K. Kumawat, M. Thakur, R. B. Gurung and R. Srivastava, *ACS Sustain. Chem. Eng.*, 2017, **5**, 1382-1391.
142. H. Chen, Z. Wang, S. Zong, P. Chen, D. Zhu, L. Wu and Y. Cui, *Nanoscale*, 2015, **7**, 15477-15486.
143. P. Nigam, S. Waghmode, M. Louis, S. Wangnoo, P. Chavan and D. Sarkar, *J. Mater. Chem. B*, 2014, **2**, 3190-3195.

Chapter 2

Anomalous Photoluminescence Enhancement and Photoluminescence Quenching of Undoped Graphene Quantum Dots by Single-Walled Carbon Nanotubes

In this chapter, we discuss about tuning the photoluminescence (PL) intensity of undoped graphene quantum dot (U-GQDs) through its interaction with single-walled carbon nanotubes (SWCNTs). A detailed investigation of the enhancement and quenching of PL intensity of U-GQDs are presented here over a wide range of concentration of SWCNTs. At a very low concentration of SWCNTs, PL intensity of U-GQDs is observed to be enhanced, while a systematic quenching of PL intensity of U-GQDs is monitored in the high concentration of SWCNTs. Interestingly, the relative change of PL intensity varies linearly with SWCNTs concentration in the low concentration region, while the nature of the Stern-Volmer plot for the latter case is found to be nonlinear, indicating a combined effect of dynamic and static quenching. Due to the improved dispersion and high metallic absorption, PL intensity of U-GQDs first enhances with a very low concentration of SWCNTs, while the PL intensity of U-GQDs is quenched by the composite formation and associated reduction of the radiative sites of U-GQDs in the presence of a high concentration of SWCNTs. We believe that this study provides an essential insight into the tuning of the PL intensity of U-GQDs and the interaction mechanism between U-GQDs and different CNTs, which is important for bioimaging and drug delivery applications.

2.1. Introduction

Room temperature visible PL is one of the most outstanding features of GQDs, which can be easily tailored by controlling their size and shape, doping as well as modifying their surfaces and edges states.[1-6] Besides, GQDs also exhibit low toxicity, robust chemical inertness and good performance in high photostability against photobleaching, excellent water solubility, and biocompatibility as compared to organic dyes and other semiconducting QDs.[1, 7] In this regard, GQDs have been widely used for cellular imaging,[8] energy storage,[9] disease diagnosis, drug delivery[10], and fluorescence bio-sensing since its first synthesis.[11] As compared to the conventional QDs, GQDs have many distinctive optical properties as a fluorescent probe, for example, strong signal

intensity, high PL QY, and tunable size-dependent PL.[5, 8, 12, 13] Due to their novel properties, recently concerted efforts have been made to develop sensors based on turn off and turn on fluorescence of GQDs.[14,15]

Alike GQDs, another fascinating form of carbon/ graphene is SWCNTs, which are formed by a rolled-up graphene sheet.[16] Due to the excellent quenching property of SWCNTs, they have been used for the development of the fluorescence sensors. The fluorescence quenching effects of CNTs were reported for a variety of molecules, such as π-stacked pyrenes and porphyrins,[17, 18] chromophores,[19] commonly used fluorophores like fluorescein, rhodamine 6G, and quinine sulfate,[20] fluorescent QDs like CdSe QDs,[21] CdSe-ZnS QDs,[22] etc.

However, the interaction of undoped GQDs (U-GQDs) and SWCNTs and their effect on the PL intensity of fluorescent U-GQDs has not been addressed yet. In this chapter, the tuning of the PL intensity of U-GQDs is studied with the variation of SWCNTs concentration along with their interaction mechanism.

2.2. Experimental Details

2.2.1. Sample Preparation

2.2.1.1. Synthesis of Graphene Oxide

Herein, graphene oxide (GO) was synthesized from graphite flakes by well-known modified Hummers' method. In a typical synthesis, 3 g expandable graphite flakes (purity 99%) and 1.5 g $NaNO_3$ were mixed with 70 mL concentrated H_2SO_4 (98%, Merck) under continuous stirring for 2 h. Subsequently, 9 g of $KMnO_4$ (Merck) was added slowly in the above mixture with stirring at 4 °C. After the addition of $KMnO_4$, the stirring was continued at 35 °C for 4 h for proper oxidation. After that, Milli-Q water (18.3 MΩ-cm, MQ water) was slowly added to the prepared mixture at 98 °C, and then the solution was quenched with 15 mL of 30% H_2O_2. To remove the unreacted $KMnO_4$ and $NaNO_3$, 60 mL of HCl (35%, Merck) was mixed slowly and kept under stirring for 4 hr. MQ water was added with the mixture to dilute the acidic parts. Finally, the GO was separated from the unreacted flakes and impurities by centrifugation at 10,000 rpm for 10 min in 3 cycles and dried at 100 °C.

2.2.1.2. Synthesis of Undoped GQDs

Undoped GQDs (U-GQDs) were prepared by the top-down method using GO as the precursor. In a typical synthesis process, 600 mg of GO powder was mixed in 40 mL MQ water and sonicated for 30 min for proper dispersion. Then the GO solution was transferred into a Teflon lined autoclave (Berghof, BR-100) and heated at 200 °C for 24 h. After cooling down to room temperature, the solution was centrifuged at 10,000 rpm, and the transparent suspension was collected as U-GQDs.

2.2.2. Sample Preparation for Photoluminescence Tuning of Undoped GQDs

For the tuning of the PL intensity of U-GQDs, U-GQDs aqueous solution (1.0 mg/mL) was mixed with various concentrations of SWCNTs (Sigma-Aldrich, >90%, ~0.7–1.4 nm diameter) ranging from 2–60 μg/mL in 1:2 ratio under ultra-sonication for 15 min. At first, different concentrations of SWCNTs solution was separately prepared in MQ water by proper sonication. In the case of pure SWCNTs, they are insoluble in the aqueous medium. However, we have used defective SWCNTs, and they are observed as reasonably well dispersed in the aqueous medium, as shown in **Fig. 2.1**. **Fig. 2.1(a, b)** show the dispersed SWCNTs in MQ water before and after ultra-sonication (15 min). At the low concentration of SWCNTs, the solution is quite transparent and

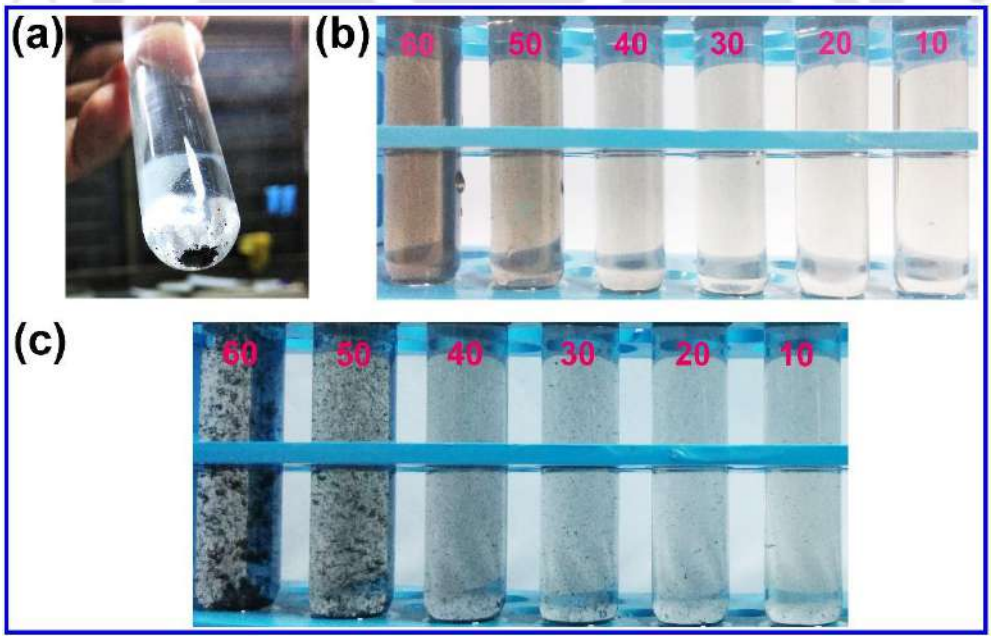

Fig. 2.1. (a) Digital photographs of 0.6 mg SWCNTs in 10 mL MQ water before sonication. Different concentrations of SWCNTs (10–60 μg/mL denoted by 10–60, respectively, from right to left) (b) just after ultra-sonication and (c) 20 mins after ultra-sonication.

clear, implying good dispersion, while at high concentration (60 μg/mL), the solution is less transparent. For the case of 50 μg/mL and 60 μg/mL, the solutions show some kind of agglomeration after 20 min of sonication, as revealed in **Fig. 2.1(c)**. Based on this, the 60 μg/mL solution was not used for the quantitative analysis of PL quenching. However, for the analysis of composite formation and a better understanding of the structural features of the samples at the high concentration, we used 60 μg/mL SWCNTs. It is generally believed that the defects on the sidewall of SWCNTs help in achieving good dispersion of SWCNTs in aqueous medium by ultra-sonication. A mechanical method, ultrasonic treatment, provides high local shear, particularly to the nanotube bundle ends[23], and this may result in the creation of additional defects and thus good dispersion. In the present work, the usage of any stabilizing agent is avoided as they cover up the surfaces of SWCNTs or make some composites with SWCNTs, which affects the direct interaction between U-GQDs and SWCNTs.[24, 25] The sample codes used in this study are denoted as U-GQD/x SW, where x denotes the concentration of SWCNTs in μg/mL. For example, the sample U-GQD/2 SW implies that a fixed concentration of U-GQDs is added with 2 μg/mL SWCNTs solution. PL study was also conducted with different concentrations of U-GQDs (0.25, 0.5, and 2.0 mg/mL).

2.2.3. Characterization Techniques

To study the morphologies and elemental compositions of GO, field emission scanning electron microscope (FESEM, GEMINI 300) attached with an energy-dispersive X-ray (EDX) spectrometer was used. Transmission electron microscopy (TEM), including high-resolution TEM imaging, was carried out using a JEOL-JEM 2010 transmission electron microscope operated at 200 kV. The test samples were obtained by drop-casting the aqueous dispersion on a carbon-coated copper grid of 300 mesh (Pacific Grid, USA), followed by drying at 70 °C. Powder X-ray diffraction (XRD) pattern was recorded with Rigaku RINT 2500 TTRAX-III using Cu K_α radiation with a scanning speed of 3°/min. Raman scattering measurements were performed in a high-resolution Raman spectrometer (LabRam HR800, Jobin Yvon) with 514 nm Ar^+ laser excitation. UV-vis absorption spectra of the samples were recorded using the PerkinElmer spectrophotometer, Lamda 950. The steady-state PL measurements were carried out in a commercial spectrofluorometer (Horiba Jobin Yvon, Fluoromax-4) equipped with a 355 nm diode laser. Time-resolved PL (TRPL) measurements were carried out with the excitation of 375 nm pulse laser by a picosecond time-resolved luminescence spectrometer (FSP920, Edinburg Instruments) with an

instrument response time of ~50 ps. Additionally, fluorescence images of the sample were obtained with a commercial confocal microscope (Zeiss LSM 880) with 355 nm laser excitation.

2.3. Results and Discussion

2.3.1. Morphology Studies

The as-synthesized GO is characterized by FESEM imaging, as shown in **Fig. 2.2(a)**. The FESEM image of GO shows a sheet-like structure with 67% carbon (C) and 33% oxygen (O). Additionally, the spatial distribution of C and O on that GO sheets are also shown in **Fig. 2.2(b, c)** using EDX mapping that confirms the formation of GO, which is further used for the synthesis of U-GQDs.

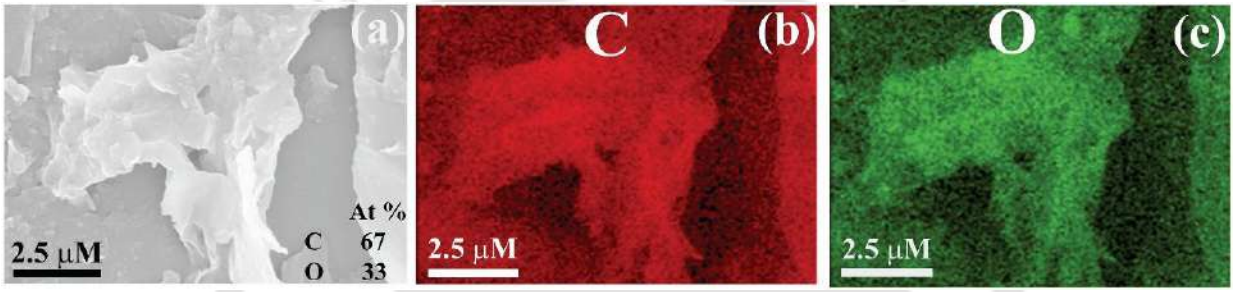

Fig. 2.2. (a) FESEM image of GO with atomic % of elemental compositions in the inset. (b, c) Elemental mapping on the same GO sheets for C and O, respectively.

The morphology of as-synthesized U-GQDs is characterized by TEM and HRTEM analysis, as shown in **Fig. 2.3(a, b)**. The TEM image in **Fig. 2.3(a)** shows the uniform distribution of nearly circular-shaped U-GQDs with an average size of ~3.6 nm. Furthermore, in **Fig. 2.3(b),** the HRTEM image of U-GQDs shows the well-resolved lattice fringes with the interplanar spacing of ~0.26 nm and 0.22 nm corresponding to (002) and (100) planes of graphitic phase, respectively, revealing the crystalline nature of the as-synthesized U-GQDs.[12, 15] **Fig. 2.3(c)** shows the TEM image of pristine SWCNTs, which reveals the presence of defect sites and metal nanoparticles, as indicated by white and pink arrows, respectively. Note that the size of the metal nanoparticles is ~6–7 nm, and these are not uniformly distributed over the length of the SWCNTs. **Fig. 2.3(d)** shows a high magnification TEM image of SWCNT with a diameter of ~1.5 nm. The presence of metal nanoparticles in SWCNTs is further confirmed from the EDX analysis. **Fig. 2.4(a, b)** show the FESEM image and the corresponding EDX spectrum that reveal the presence of C (92.9%), O (6.6 %), cobalt (Co, 0.1 %) and molybdenum (Mo, 0.5%). Thus, the SWCNTs contain a very small

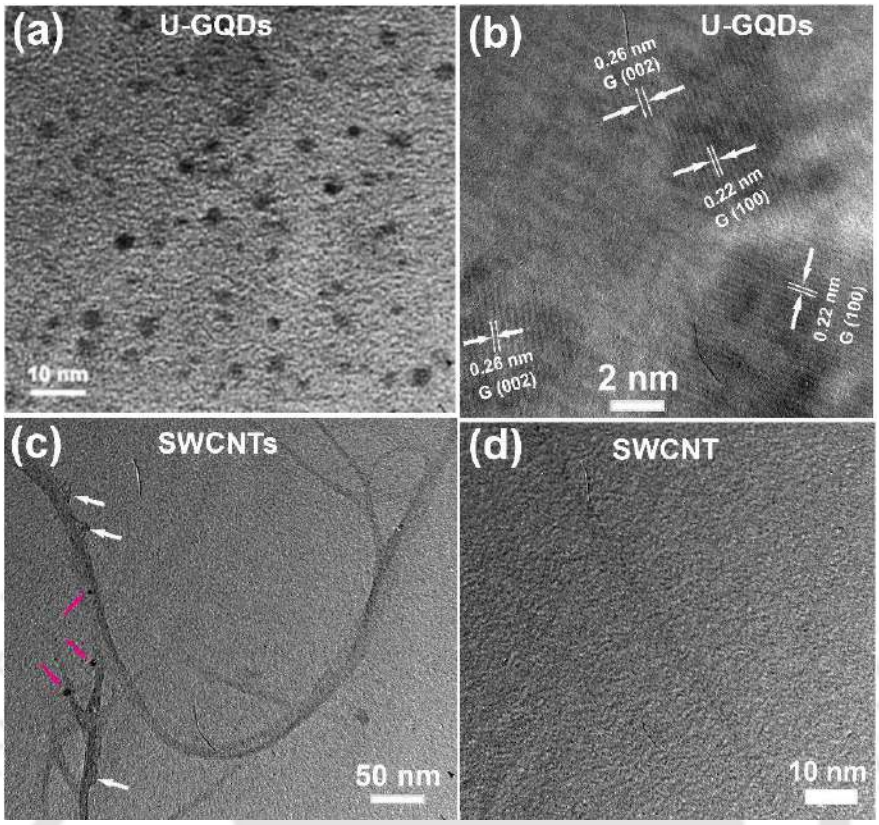

Fig. 2.3. (a) TEM and (b) HRTEM lattice image of U-GQDs. 'G' symbol in (b) represents the graphitic planes. (c, d) Low and high magnified TEM images of SWCNTs.

amount of metallic impurities that arise from the metal catalysts used during the growth of the SWCNTs. Interestingly, after the interaction of U-GQDs with SWCNTs, the morphology of the

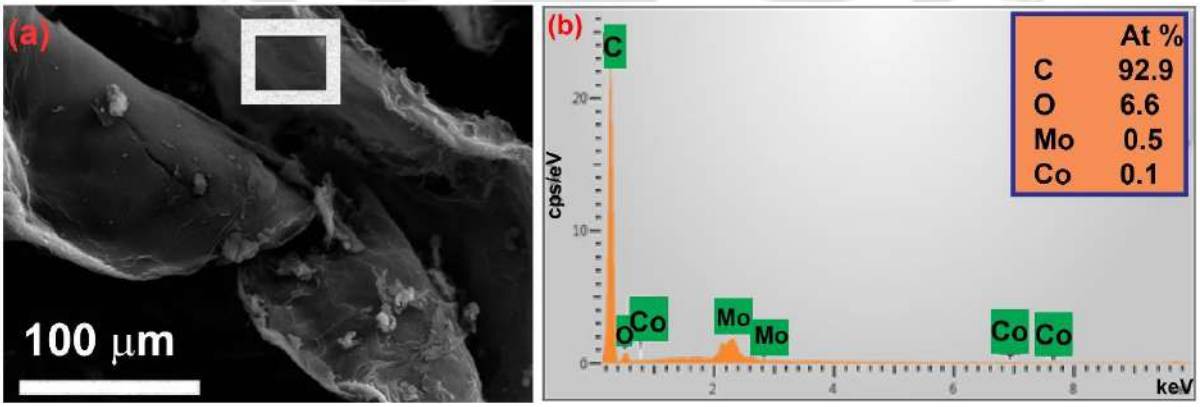

Fig. 2.4. (a) FESEM image of SWCNTs and (b) EDX spectrum of SWCNTs obtained from the square region shown in (a).

composites is observed to be changed for various concentrations of SWCNTs, as presented in **Fig. 2.5**. **Fig. 2.5(a)** shows the HRTEM image of U-GQD/2 SW, where U-GQDs are attached to the

SWCNT walls due to the interaction of U-GQDs and SWCNTs at the low concentration. The particle size distribution of the attached U-GQDs is presented in the inset of **Fig. 2.5(a)**, which reveals an average size of ~3.5 nm, consistent with the particle size of bare U-GQDs. **Fig. 2.5(b)** shows that at a high concentration of SWCNTs, the U-GQDs are sandwiched in between the SWCNT bundle, and it appears in the form of the agglomeration of SWCNTs due to the interaction of U-GQDs with the SWCNTs.

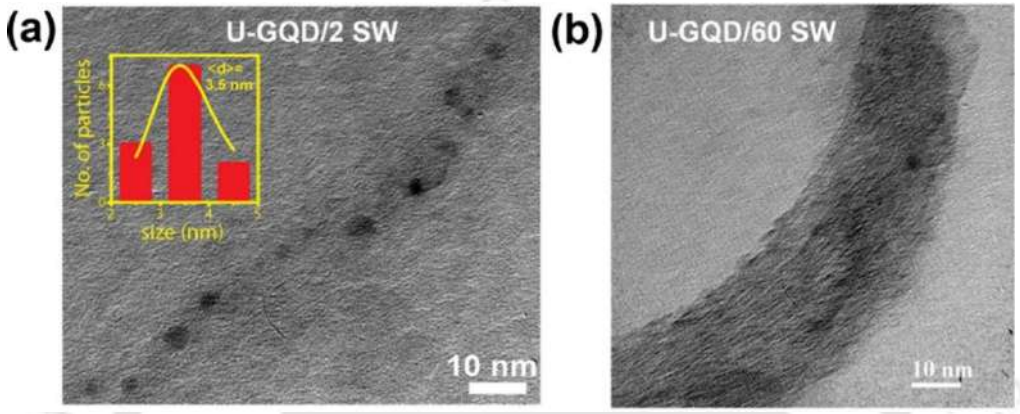

Fig. 2.5. HRTEM images of (a) U-GQDs/2 SW and (b) U-GQDs/60 SW. The inset of (a) shows the histogram of the particle size distribution of U-GQDs on the surface of SWCNTs along with lognormal fitting.

2.3.2. Structural Analysis: XRD and Raman Analysis

To confirm the crystalline structure of U-GQDs, the powder XRD pattern of U-GQDs is presented in **Fig. 2.6**. The diffraction peak at 2θ ~26.1° is attributed to (002) plane of sp^2 hybridized carbon

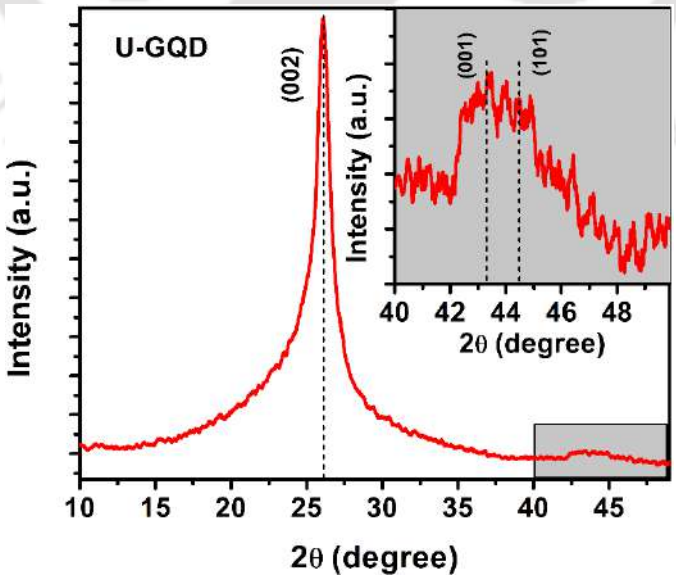

Fig. 2.6. XRD pattern of U-GQDs. The inset presents the enlarged view of the XRD pattern in the range 2θ ~40–50°.

atoms for the highly ordered and crystalline graphitic structure. The inset of **Fig. 2.6** shows the magnified view of the XRD pattern of U-GQDs in the range 2θ ~40–50°, which shows the weak reflections from (100) and (101) planes of U-GQDs.

For further structural analysis of U-GQDs, the Raman spectrum of pristine U-GQDs is presented in **Fig. 2.7(a)**. In U-GQDs, the characteristic D and G bands arise at ~1355 cm^{-1} and 1580 cm^{-1}, respectively. The presence of another band at ~1614 cm^{-1} (D') is attributed to the vacancies and/or

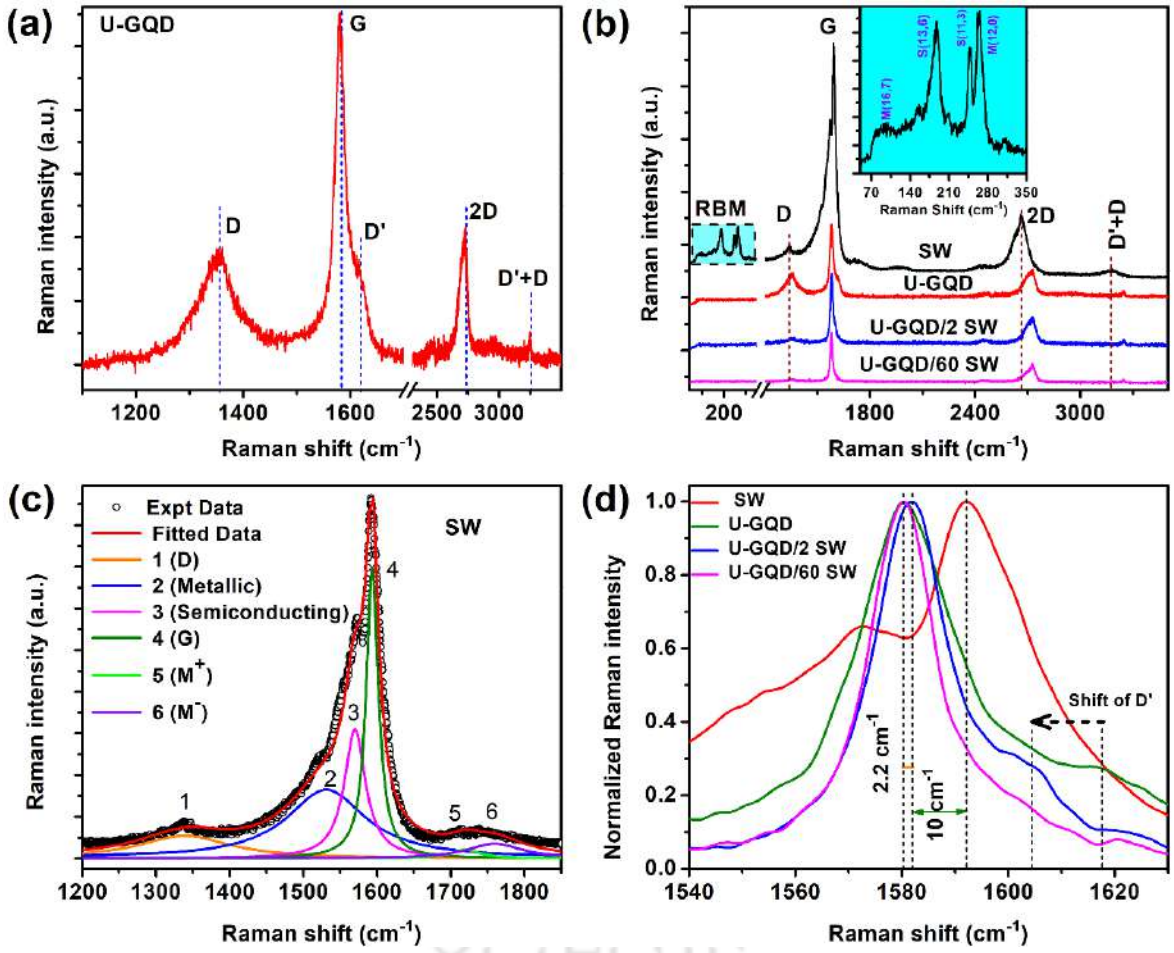

Fig. 2.7. (a) Raman spectrum of pristine U-GQDs. (b) Comparison of the Raman spectra of pristine SWCNTs, U-GQDs, and U-GQDs/SWCNTs composites at two different concentrations of SWCNTs keeping the U-GQDs concentration unchanged. The corresponding inset shows the presence of different chirality in SWCNTs related to the metallic and semiconducting nature of SWCNTs. (c) Deconvoluted Raman spectrum of SWCNTs with one BWF and five Lorentz line shape. (d) Comparison of normalized Raman spectra of G peak for different composite samples, showing the redshift with respect to the pristine SWCNTs spectrum.

pentagonal and octagonal defects, usually referred to as zigzag defects.[26] The Raman band in U-GQDs at ~2723 cm^{-1}, known as the 2D band, originates from the in-plane breathing-like mode of

the carbon rings.[27] The D + D′ band at ~3243 cm^{-1} in U-GQDs is a combined effect of D and D′.[27] In order to understand the change in the structural features of U-GQDs after the formation of the composites with SWCNTs, we performed a comparative study of the Raman spectra of bare SWCNTs, U-GQDs as well as their composites at different SWCNTs concentrations, as shown in **Fig. 2.7(b)**. For SWCNTs, the Raman spectrum shows the clear signature of radial breathing modes (RBM) lying in the region ~92–374 cm^{-1}. The inset of **Fig. 2.7(b)** shows the enlarged view of the RBM in the region ~50–350 cm^{-1} with four prominent peaks at ~154.7 cm^{-1}, 187.3 cm^{-1}, 248.0 cm^{-1}, and 263.8 cm^{-1}. From these RBM, the diameters of SWCNTs are calculated using the empirical formula:[28]

$$\omega_{RBM} = C/d_t \qquad (2.1)$$

where, C =248 for isolated SWCNTs on a SiO_2 substrate, d_t (nm) is the diameter of SWCNT, ω_{RBM} is in cm^{-1}. The value of d_t and the corresponding chirality are presented in **Table 2.1**. The calculated value of

Table 2.1. *Chirality (n, m) of pristine SWCNTs calculated from the RBM. S and M denote the semiconducting and metallic nature of the SWCNTs.*

ω_{RBM} (cm^{-1})	$d_t = 248/\omega_{RBM}$ (nm)	Chirality	
		S (n,m)	M (n,m)
154.7	1.60	-	(16,7)
187.3	1.32	(13,6)	-
248.0	1.00	(11,3)	-
263.8	0.94	-	(12,0)

the diameter of SWCNTs using eqn. (2.1) consistent with the TEM analysis (see **Fig. 2.3(d)**). Additionally, the chirality analysis reveals the metallic nature of SWCNTs along with their semiconducting nature. Chirality (16,7) and (12,0) correspond to the metallic SWCNTs with diameter ~1.60 nm and 0.94 nm, respectively, while, (13,6) and (11,3) are attributed to the semiconducting nature of SWCNTs with diameter ~1.32 nm and 1.00 nm, respectively.[29, 30] The presence of both metallic and semiconducting nature of the pristine SWCNTs are also observed by the deconvolution of Raman spectrums of SWCNTs with five Lorentz peaks and one Breit–Wigner–Fano (BWF) line shape in the range ~1200–1850 cm^{-1}, as shown in **Fig. 2.7(c)**. The Lorentz peaks at ~1339 cm^{-1} and 1593 cm^{-1} correspond to the characteristic D and G bands of SWCNTs, respectively. The BWF line shape fitted peak at ~1531 cm^{-1} (peak 2) corresponds to

metallic SWCNTs[28], and the Lorentzian peak at ~1570 cm^{-1} (peak 3) reveals the presence of semiconducting nature of SWCNTs.[28] Other two weak Raman bands at ~1720 and 1760 cm^{-1} attribute to the presence of M^- and M^+ bands in SWCNTs.[28] The semiconducting and metallic nature of the SWCNTs is further confirmed from the Raman frequency (ω) calculation using the equation:[28]

$$\omega = \omega_0 + \beta/d_t^2 \qquad (2.2)$$

where $\beta = -45.7\ cm^{-1}\ nm^2$ for semiconducting nature and $\beta = -79.5 cm^{-1}\ nm^2$ for metallic nature. In the present case, d_t of SWCNT is =1.5 nm, and ω_0 is the Raman frequency of G band =1593 cm^{-1} from the fitted graph. The calculated values of 'ω' nicely match with the fitted band frequencies of the metallic and semiconducting nature of SWCNTs, i.e., with the value of peak 2 and peak 3, respectively. Also, the first overtone of the D band of SWCNTs appears at ~2661 cm^{-1} (2D band) [31] along with D + D′ band at ~3138 cm^{-1}. Interestingly, after the composite formation with U-GQDs, RBM features of SWCNTs are observed to be disappeared completely from the Raman spectra (see **Fig. 2.7(b)**), confirming the strong attachment U-GQDs with SWCNTs. **Fig. 2.7(d)** represents the normalized Raman spectra of the G band of pristine SWCNTs, U-GQDs, and their composites. The formation of composites of SWCNTs with U-GQDs shows a redshift of the G peak (see **Fig. 2.7(d)**) and the blueshift of D, 2D, and D + D' peaks with respect to SWCNTs (see **Fig. 2.7(b)**). The shifts of defect-related peaks are shown in **Fig. 2.7(b)** with the vertical dashed lines. The shift in the Raman modes confirms the bonding of U-GQDs with SWCNTs. It is clear from **Fig. 2.7(d)** that Raman peak at ~1617 cm^{-1} (D') in U-GQDs is redshifted after the addition of 2 µg/mL SWCNTs, while this band disappears with 60 µg/mL SWCNTs. Similarly, the intensity of D and D' band reduces at a higher concentration of SWCNTs, which is due to a stronger bonding between U-GQDs and SWCNTs in the defects sites. The redshift of G mode in U-GQDs/2 SW (~10 cm^{-1}) is less than that of U-GQDs/60 SW (~12.2 cm^{-1}) with respect to SWCNTs (see **Fig. 2.7(d)**), which indicates that tensile strain is increasing with the SWCNTs concentration and binding becomes stronger.

2.3.3. Optical Analysis

2.3.3.1. UV-vis Absorption Study

Fig. 2.8 shows the UV-vis absorption spectra of bare U-GQDs, SWCNTs, and their composites with U-GQDs. In **Fig. 2.8(a)**, a broad absorption peak of U-GQDs at ~270 nm represents the

characteristic π-π* transition due to sp^2 carbon domains as well as QC effect and an absorption tail extending up to 500 nm corresponds to n-π* transition appears from the functional groups/defects in U-GQDs. The optical bandgap of the U-GQDs is estimated to be ~3.24 eV by Tauc plot, as presented in the inset of **Fig. 2.8(a)**.[13] For the case of SWCNTs, the absorption spectra with SWCNTs concentration 2 μg/mL (2 SW) and 60 μg/mL (60 SW) are presented in **Fig. 2.8(b, c)**, respectively, in the UV- vis-NIR region. **Fig. 2.8(b)** shows a sharp absorption peak at ~273 nm in 2 SW, along with the metallic M11 band in the region ~450–670 nm and the semiconducting S22 bands at ~963 nm and 1157 nm,[32, 33] which confirm the presence of both metallic and

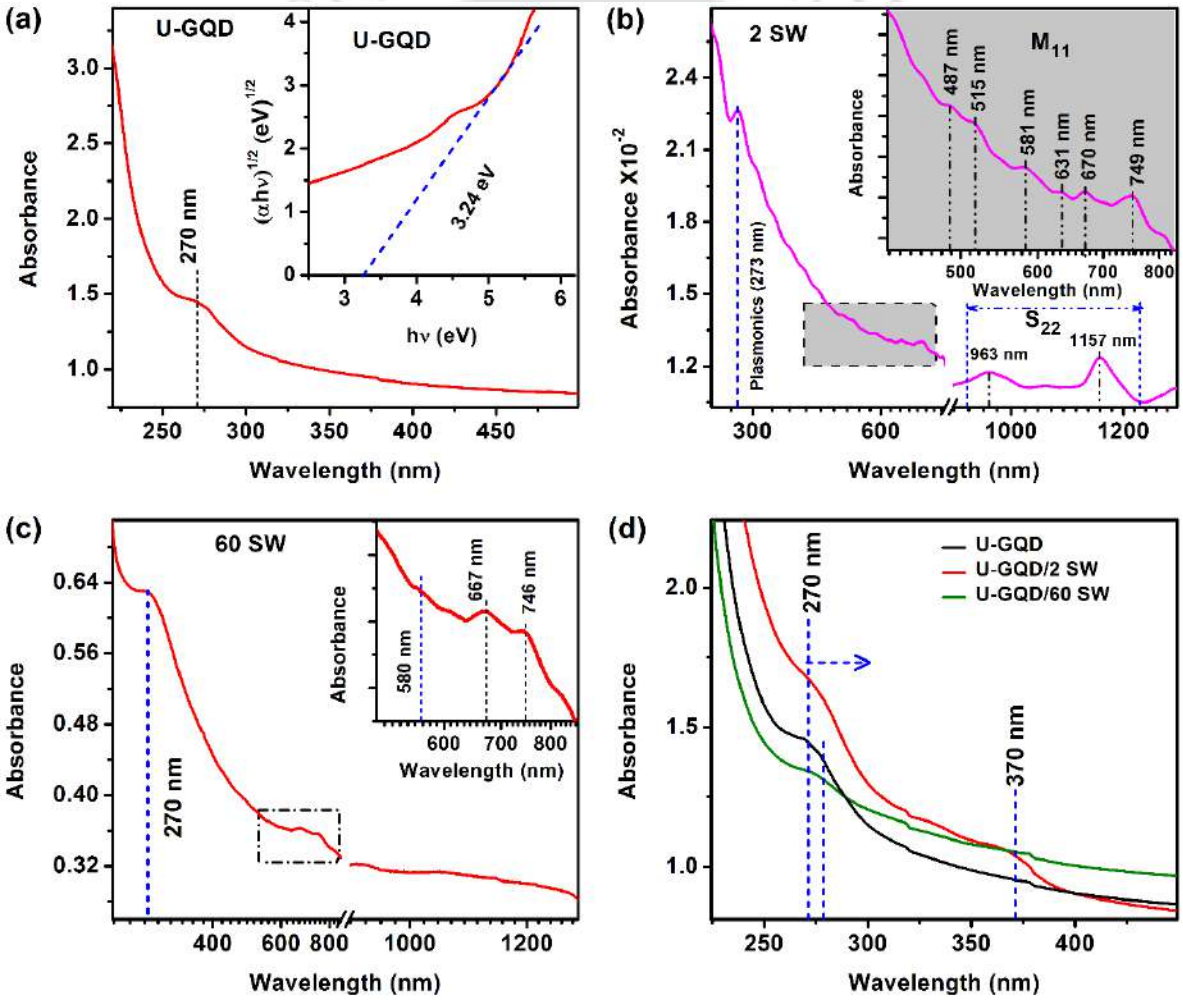

Fig. 2.8. (a) UV absorption spectrum of U-GQDs; the inset shows the Tauc plot exhibiting a bandgap of ~3.24 eV. (b) UV-vis-NIR absorption spectra of pristine SWCNTs solution with the concentration of 2 μg/mL, showing semiconducting peaks in the region 900–1300 nm. The inset shows the metallic peaks in the region 450–670 nm. (c) (c) The absorption spectrum of SWCNTs with concentration 60 μg/mL. The inset shows the metallic peaks in the region 400–830 nm. (d) Comparison of absorption spectra of U-GQDs and U-GQDs/SWCNTs solutions, showing the prominent redshift at a higher SWCNTs concentration with respect to U-GQDs.

semiconducting nature in the used SWCNTs, consistent with Raman analysis. On the other hand, 60 SW in **Fig. 2.8(c)** exhibits a broad absorption band at ~270 nm, together with a small contribution of the M11 band, as shown in the inset. The sharp absorption at ~273 nm is identified as π plasmon resonance peak of SWCNTs.[34] Multiple peaks corresponding to metallic and semiconducting regions are due to the presence of different diameter SWCNTs.[35, 36] Note that the absorption spectrum of SWCNTs is an important tool for assessing their dispersion quality. Bundled SWCNTs exhibit very weak absorption in the wavelength region ~200–1200 nm due to the carrier tunneling effect between the nanotubes.[37] The presence of various absorption peaks in the region ~200–1200 nm for sample 2 SW in **Fig. 2.8(b)** reveals the good dispersion of SWCNTs in the aqueous medium without buddle effect, while the absorption of 60 SW in **Fig. 2.8(c)** demonstrates the presence of aggregation at a higher SWCNTs concentration. Due to the less aggregation at low concentration, the SWCNTs primarily show a metallic nature, while at a higher concentration, aggregated SWCNTs show only the semiconducting behavior.[36] A comparison of the UV-vis absorption spectra of U-GQDs is presented in **Fig. 2.8(d)** before and after the composite formation with SWCNTs at two different concentrations, which show the enhancement and reduction of π-π* absorption at ~273 nm for U-GQDs/2 SW and U-GQDs/60 SW, respectively. At low concentration of SWCNTs, due to their dominant metallic nature, the plasmonic contribution of SWCNTs increases the local incident field on U-GQDs, and subsequently, π-π* absorption of U-GQDs increases in U-GQDs/2 SW composites. On the other hand, the reduction of π-π* absorption intensity in U-GQDs/60 SW, along with the redshift of the absorption peak, endorse the semiconducting nature of SWCNTs. At low concentration of SWCNTs, U-GQDs also prevent SWCNTs from agglomeration by surrounding the SWCNTs, while with the high concentration of SWCNTs, due to the insufficient amount of U-GQDs, SWCNTs agglomerate easily and then SWCNTs start to show semiconducting nature only.[36] Note that the appearance of another absorption band at ~370 nm in only U-GQDs/2 SW is due to the strong metallic contribution of SWCNTs at the low concentration. Since SWCNTs contain highly delocalized π-electrons, they can easily attach with π electron rich U-GQDs through π-π interactions.[20] Additionally, the change of the absorption tail of U-GQDs in the composites indicates that the interaction between U-GQDs and SWCNTs also happens with the functional groups and defect states. **Fig. 2.9** shows a schematic of the attachment of U-GQDs on the surface of SWCNT in two different pathways for U-GQDs/SWCNTs composite formation.

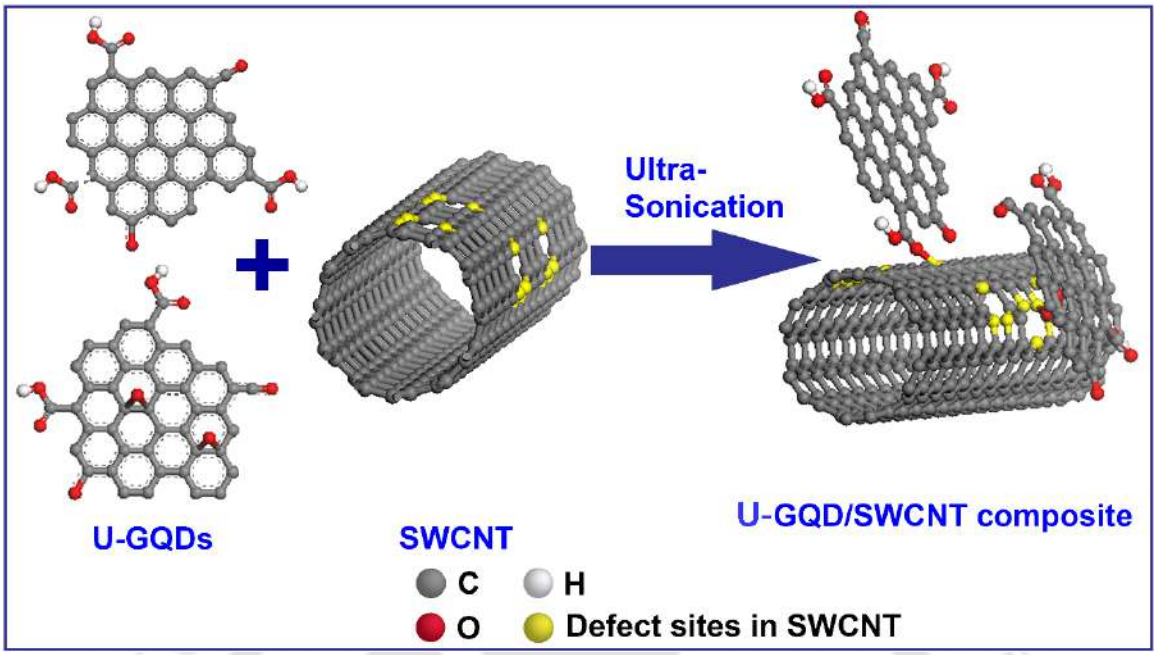

Fig. 2.9. A schematic illustration of the attachment of U-GQDs on the surface of SWCNT.

2.3.3.2. Photoluminescence Study

PL study of U-GQDs was conducted with different excitation wavelengths in the range 300-380 nm using a Xe lamp. **Fig. 2.10(a)** shows the PL spectrum of U-GQDs with 300 nm excitation. The deconvolution of the PL spectrum reveals three peaks with centers at ~385 nm, 427 nm and 480

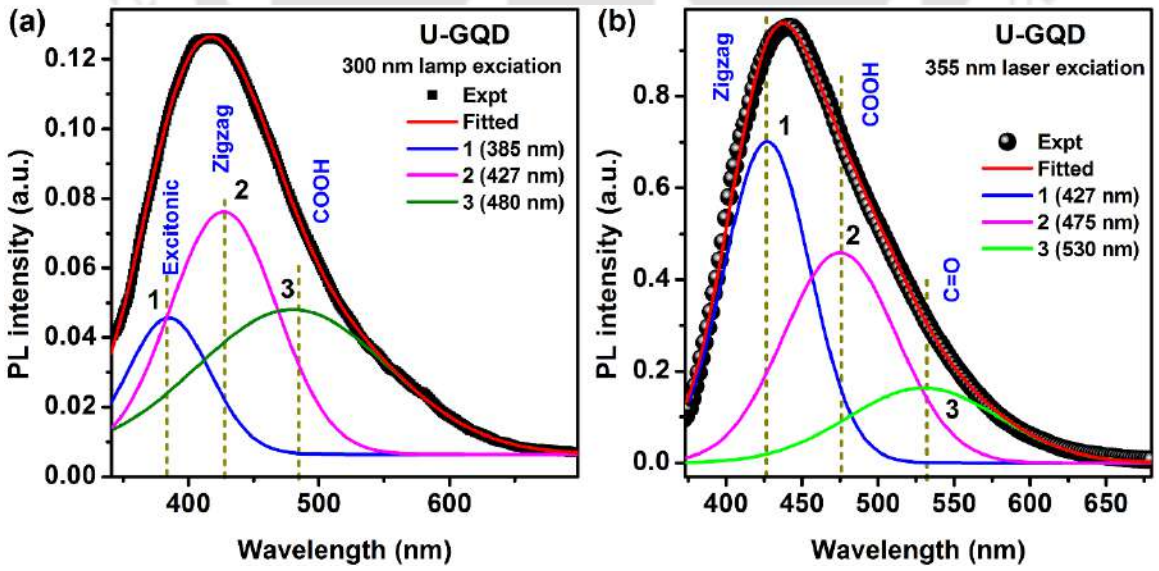

Fig. 2.10. (a) PL spectrum of U-GQDs with 300 nm excitation (Xe lamp). The deconvoluted peaks are shown with solid lines. (b) PL spectrum of U-GQDs with 355 nm laser excitation and its deconvolution with three peaks.

nm. The first peak corresponds to band to band excitonic transition, which is consistent with the absorption spectrum. To understand the origin of the other two peaks, we measured the PL spectrum with 355 nm laser excitation, as shown in **Fig. 2.10(b)**. The deconvoluted PL peak at ~427 nm is due to the contribution of the zigzag edge states, and the other two peaks at ~475 nm and 530 nm are assigned to the COOH and C=O functional groups in U-GQDs.[26] Moreover, the relative PL quantum yield (QY) (ϕ) of the as-synthesized U-GQDs was also measured with 0.05 M quinine sulfate (QS) as a reference fluorophore. The relative PL QY is defined as:

$$\phi = Q_r \frac{A_r I_s \eta^2{}_s}{I_r A_s \eta^2{}_r} \qquad (2.3)$$

where Q_r is the absolute QY of reference (QS). A_s and A_r are the absorbance of the sample and reference, respectively. I_s and I_r are integrated PL intensity of sample and reference, respectively. η_s and η_r are the refractive index of sample and reference, respectively. The value of Q_r of QS is ~0.52[38], and the refractive index of water is 1.33. Here, for aqueous medium, $\eta_s = \eta_r = 1.33$ is used. For U-GQDs, ϕ value is calculated as ~2.4%. In the purpose of tuning of the PL intensity, U-GQDs is further functionalized with SWCNTs. With different concentrations of SWCNTs, the PL intensity of U-GQDs is monitored at ~440 nm under 355 nm laser excitation, as shown in **Fig. 2.11**. The PL spectra of U-GQDs before and after the addition of SWCNTs with concentrations of 2, 4, 6, and 8 µg/mL are presented in **Fig. 2.11(a)**. The nature of the relative change in the PL intensity at low concentration region is observed to follow a linear equation:

$$\frac{I_0}{I} = A + BQ \qquad (2.4)$$

where I_0 and I are the PL intensities of the U-GQDs before and after the addition of SWCNTs, 'Q' is the concentration of SWCNTs, 'A' and 'B' are the constants. The linear fitting of the experimental data gives the values of A =0.51 and B =0.01 mL/µg, as shown in **Fig. 2.11(b)**. In **Fig. 2.11(a),** a redshift of ~5 nm in the PL maxima (~440 nm) of U-GQDs is observed after the addition of SWCNTs, indicating the formation of a composite of U-GQDs with SWCNTs at low concentration of SWCNTs. The enhancement in PL intensity at low concentration region is due to the high absorption at ~370 nm in U-GQDs/2 SW, as observed from **Fig. 2.8(d)**. In addition to the metallic contribution of the SWCNTs, the PL enhancement is also partly due to the improved dispersion of U-GQDs in the aqueous medium with the addition of SWCNTs at low concentration,

despite the extremely low absorbance of the SWCNTs (see **Fig. 2.8(b)**). Note that the value of ϕ is calculated as ~5.5% for U-GQDs/2 SW. **Fig. 2.11(c)** represents the PL spectra of U-GQDs before and after the addition of SWCNTs with a concentration of 10–50 µg/mL, i.e., in the high concentration region. In this high concentration region, PL intensity of U-GQDs is observed to be quenched systematically with increasing concentration of SWCNTs and the PL intensity of

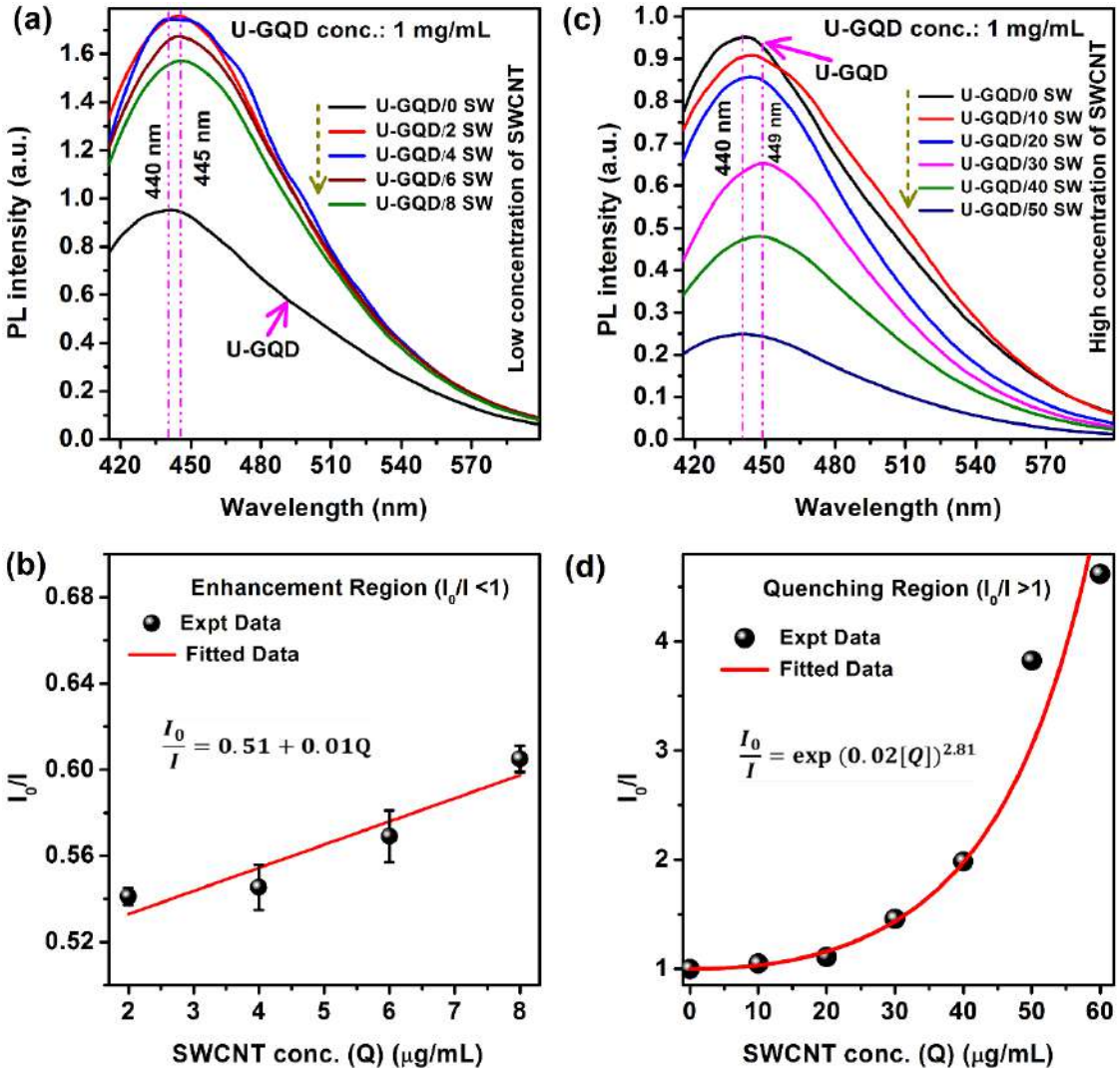

Fig. 2.11. (a) PL spectra of 1.0 mg/ mL concentration of U-GQDs at the low concentration region of SWCNTs (2, 4, 6, and 8 µg/mL) and (b) the corresponding relative change of the PL intensity with SWCNTs concentration. (c) The change of the PL intensity of U-GQDs with the high concentration of SWCNTs (10–50 µg/mL) and (d) the corresponding non-linear Stern–Volmer plot.

is quenched by ~74% with 50 µg/mL SWCNTs. In this region, the nature of PL quenching of U-GQDs shows a non-linear behavior following the equation:[20]

$$\frac{I_0}{I} = \exp(b[Q])^a \qquad (2.5)$$

where 'b' and 'a' are the constants. The fitted values of the constants are b =0.02 mL/μg and a =2.81 (see **Fig. 2.11(d)**). Such a positive deviation from the usual non-linear Stern–Volmer equation is observed when the extent of quenching is large.[20] Due to the strong composite

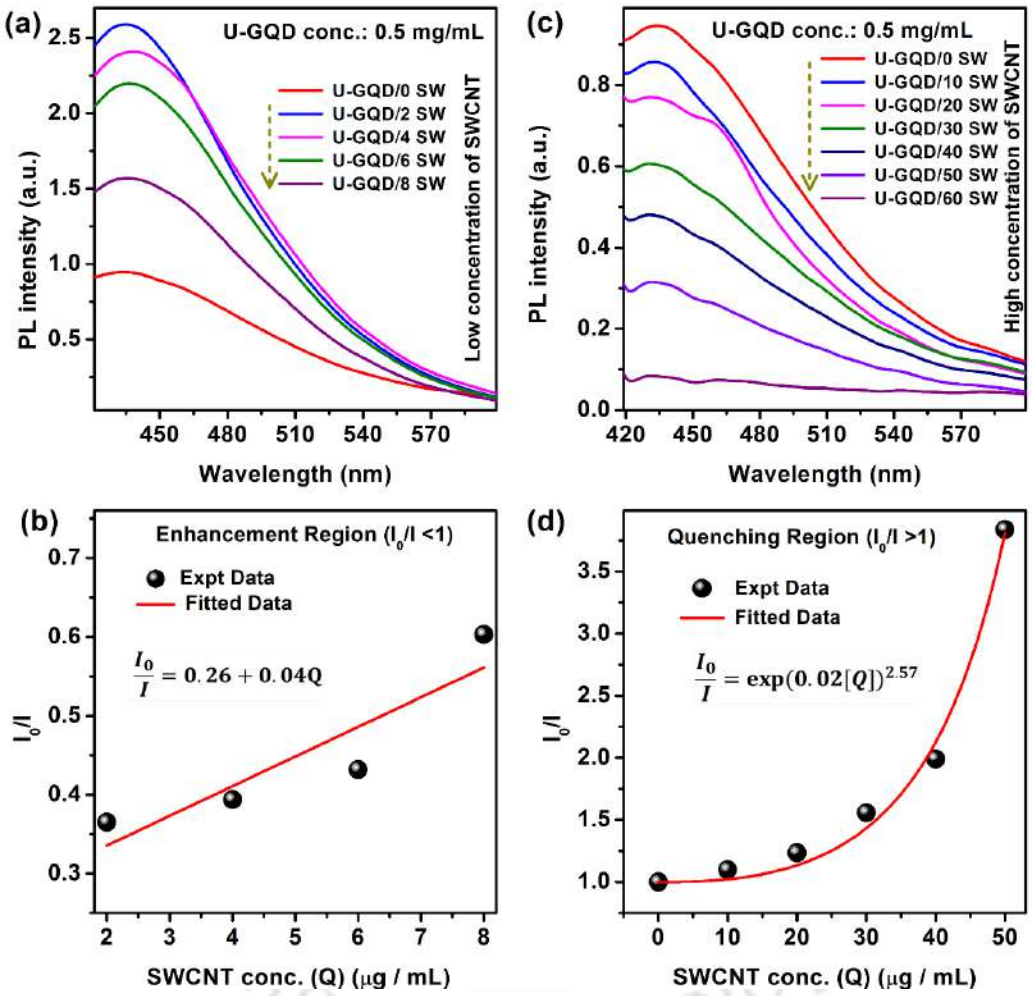

Fig. 2.12. (a) PL spectra of 0.5 mg/ mL concentration of U-GQDs at low concentrations of SWCNTs (2, 4, 6, and 8 μg/mL) and (b) the corresponding relative change of the PL intensity with the SWCNTs concentration. (c) The change of the PL intensity of U-GQDs with the high concentration of SWCNTs (10–50 μg/mL). (d) Nonlinear Stern–Volmer plot at high concentration of SWCNTs.

formation with SWCNTs through the π–π interaction and the functional groups/defects sites, the quenching efficiency is unusually high, and it follows a faster than exponential growth behavior with the combined contributions of dynamic and static quenching. At a high concentration of SWCNTs (≥10 μg/mL), the semiconducting nature of SWCNTs insists on the excited-state charge

transfer from U-GQDs to SWCNTs after the composite formation and thus PL intensity of U-GQDs is quenched due to the reduced recombination. The band position of U-GQDs with the particle size of ~2–7 nm is ~3 eV[13], and that of SWCNTs is ~5 eV[39] with respect to the vacuum level also implies the possibility of charge transfer from U-GQDs to SWCNTs. To test the reproducibility of the above results, the PL spectral analysis is carried out with different concentrations of U-GQDs (0.25, 0.5, and 2 mg/mL). In **Fig. 2.12**, with 0.5 mg/mL of U-GQDs, the tuning of PL intensity is observed with different concentration of SWCNTs by following the similar nature as discussed for 1.0 mg/mL of U-GQDs. **Fig. 2.12(a)** shows the enhancement of PL intensity of U-GQDs with the low concentrations of SWCNTs (<10 μg/mL) and the corresponding relative change of the PL intensity with SWCNTs concentration is observed to follow the linear nature, with the intercept and slope as 0.26 and 0.04 mL/μg, as shown in **Fig. 2.12(b)**. The change in the slope and intercept with the variation of U-GQDs concentration is attributed to the difference in the interaction possibilities. In the high concentration region of SWCNTs (>10 μg/mL), the systematic quenching of the PL intensity of U-GQDs and the corresponding change of the relative PL intensity with SWCNTs are shown in **Fig. 2.12(c, d)**. Further, the effect of concentration of U-GQDs in the tuning of the PL intensity is analyzed in both low and high concentration regions of SWCNTs, as shown in **Fig. 2.13**. With 2 μg/mL SWCNTs, we have observed a systematic increase

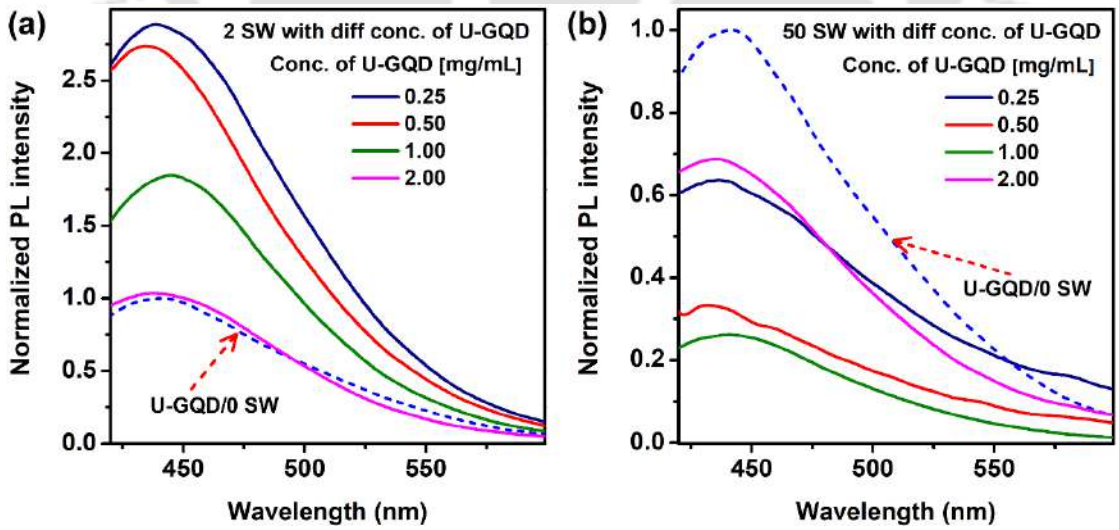

Fig. 2.13. Concentration effect of U-GQDs in the tuning of PL intensity. Normalized PL spectra of different concentrations of U-GQDs with (a) 2 SW and (b) 50 SW. The dashed curve indicates the normalized PL spectrum of bare U-GQDs.

in the PL intensity with the reduction of U-GQDs concentration, and the PL intensity is highest for a U-GQDs concentration of 0.25 mg/mL (see **Fig. 2.13(a)**). Note that each PL spectrum is normalized with its absorption spectrum to account for the concentration effect on the PL intensity of U-GQDs. At a low concentration of U-GQDs, SWCNTs get more open surfaces to interact with the well-separated U-GQDs, and thus, the interaction of U-GQDs and SWCNTs can efficiently increase the local fields on U-GQDs and as a consequence, the PL intensity of U-GQDs increases strongly. On the other hand, 1.0 mg/mL U-GQDs exhibit maximum PL quenching with 50 μg/mL SWCNTs, as presented in **Fig. 2.13(b)**. At a high concentration of U-GQDs, the agglomeration effect in U-GQDs affects the composite formation with SWCNTs due to the limited availability of sites for interaction. Thus, 1 mg/mL concentration of U-GQDs is considered as the optimized concentration of U-GQDs for efficient quenching of the PL intensity.

2.3.3.3. Time-Resolved Photoluminescence Study

In order to understand the charge transfer dynamics in U-GQDs before and after composites formation with SWCNTs, a comparison of the TRPL spectra is presented in **Fig. 2.14**. Each spectrum is fitted with a bi-exponential decay function given by:

$$I(t) = \sum_{i=1}^{2} B_i e^{(-t/\tau_i)} \qquad (2.6)$$

where I(t) is PL intensity at the time 't' and B_i is the fractional intensity corresponding to decay time τ_i. The average excited state lifetime (τ_{avg}) can be calculated by using the following relation:

$$\tau_{avg} = \frac{\sum_{i=1}^{2} B_i \tau_i^2}{\sum_{i=1}^{2} B_i \tau_i} \qquad (2.7)$$

The fitted parameters of the TRPL spectra along with τ_{avg} values of all samples are presented in the inset of **Fig. 2.14**. The average carrier lifetime, τ_{avg} of the pristine U-GQDs, is observed as ~4.79 ns, while that for U-GQDs/50 SW is ~3.44 ns. The reduced lifetime in the composite sample is due to the enhancement of the contribution of fast decay time (τ_1) with the increasing concentration of SWCNTs, and it strongly suggests the non-radiative charge transfer from U-GQDs to SWCNTs.[40] In the steady-state and time-resolved experiments, the PL intensity of U-GQDs is quenched by the presence of a high concentration of SWCNTs, which is an indication for fast and efficient energy trapping at the SWCNTs site. On the other hand, for U-GQDs/2 SW, the increase of τ_{avg} value by ~1.0 ns with respect to bare U-GQDs is due to the increase of radiative

recombination by the high absorption in U-GQDs through the enhancement of the local field with the metallic contribution of SWCNTs.

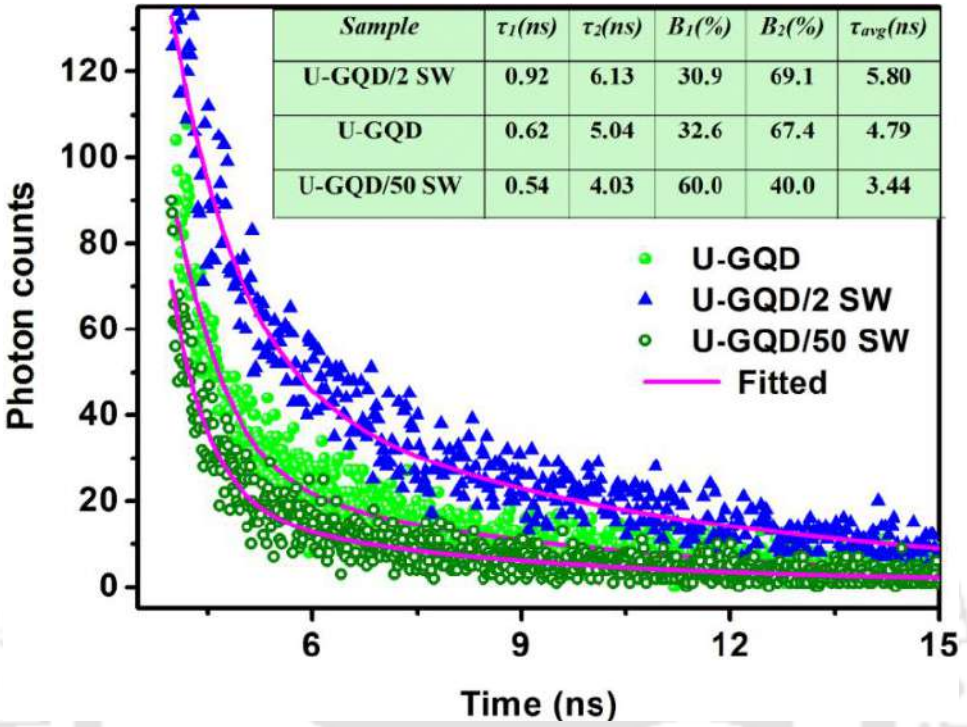

Fig. 2.14. TRPL spectra (symbols) with bi-exponential fit (solid lines) for bare U-GQDs and after addition of 2 μg/mL and 50 μg/mL concentration of SWCNTs. The fitted parameters of the TRPL spectra of all samples are shown in the inset.

2.3.3.4. Confocal Imaging

To understand the anomalous fluorescence activity of U-GQDs before and after the addition of SWCNTs, the fluorescence confocal imaging of bare U-GQDs, pristine SWCNTs, and their composites are shown in **Fig. 2.15**. **Fig. 2.15(a, b)** show that U-GQDs exhibit strong blue fluorescence, while SWCNTs do not show any fluorescence signal. In contrast, the fluorescent images of U-GQDs are distinctly different in U-GQDs/4 SW and U-GQDs/60 SW, as shown in **Fig. 2.15(c, d)**. As compared to the pristine U-GQDs, a brighter fluorescence signal in U-GQDs/4 SW is clearly visible. In contrast, the low fluorescence background in U-GQDs/60 SW evidently demonstrates the strong quenching effect of SWCNTs.

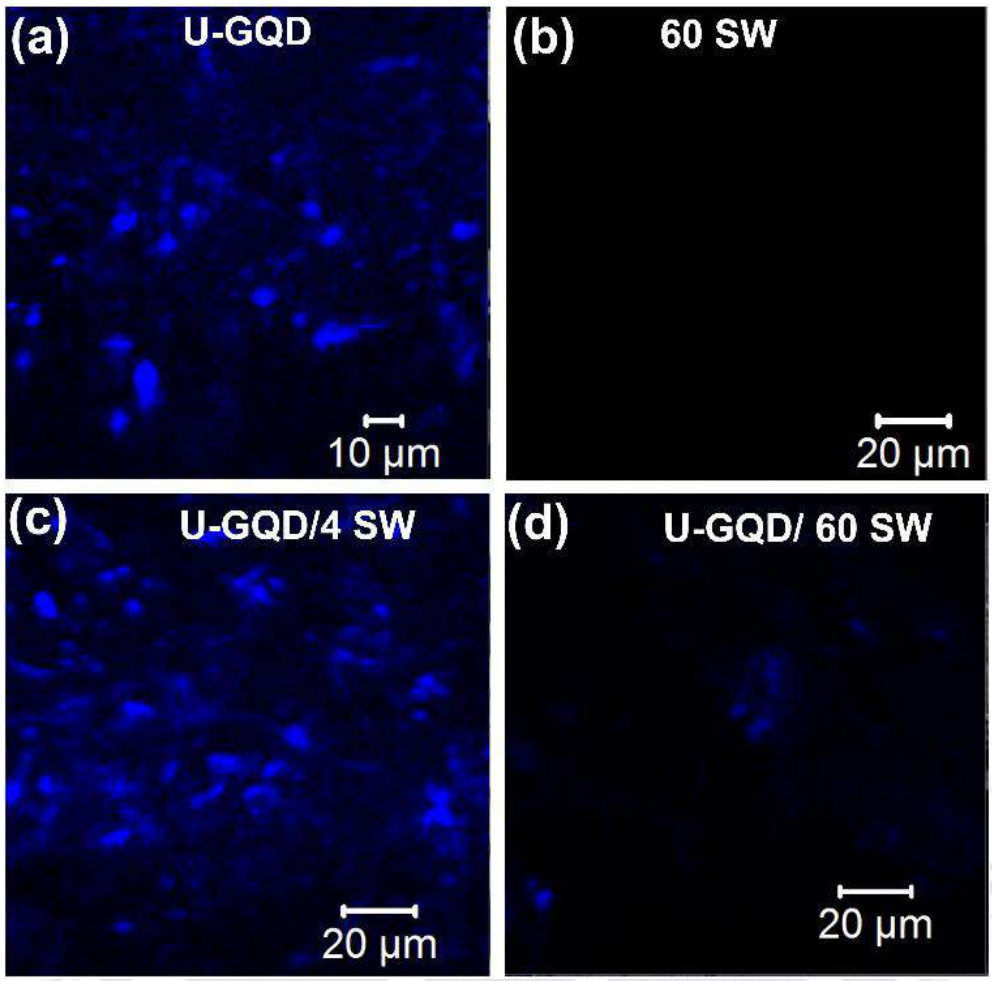

Fig. 2.15. Laser confocal microscopy images of (a)U-GQDs, (b) SWCNTs, (c) U-GQDs/4 SW, and (d) U-GQDs/60 SW composites.

2.4. Summary and Conclusions

In this chapter, the anomalous PL quenching behavior of U-GQDs in the presence of SWCNTs in the aqueous medium has been demonstrated. The important findings of this chapter are summarized below. These results enable us to tune the PL intensity of U-GQDs as well as an insight into the interaction process of U-GQDs with SWCNTs, which are important for biomedical applications.

1. At low concentrations of SWCNTs (2–8 µg/mL), PL intensity of U-GQDs increases linearly, and the maximum PL intensity is achieved with the lowest SWCNTs concentration, i.e., 2 µg/mL.

2. The dominating metallic nature of SWCNTs at low concentration increases the incident local field on the fluorophores U-GQDs by the plasmonic effect, which causes the PL enhancement in U-GQDs.
3. The PL intensity of U-GQDs shows a systematic quenching with SWCNTs in the concentration region of 10–60 μg/mL following a non-linear Stern-Volmer equation with a faster than exponential behavior.
4. At higher concentrations of SWCNTs, the PL quenching of U-GQDs occurs with contributions from both static and dynamic quenching. The π–π interaction between SWCNTs and U-GQDs causes the ground state composite formation leading to the static quenching, and due to the dominating semiconducting behavior of SWCNTs, the excited state charge transfer from U-GQDs to SWCNTs reduces the radiative recombination in U-GQDs resulting in nonlinear Stern-Volmer plot. These results are important for biosensing/ imaging and drug delivery applications.

References

1. L. Li, G. Wu, G. Yang, J. Peng, J. Zhao and J.-J. Zhu, *Nanoscale*, 2013, **5**, 4015-4039.
2. L. Zhang, Z.-Y. Zhang, R.-P. Liang, Y.-H. Li and J.-D. Qiu, *Anal. Chem.*, 2014, **86**, 4423-4430.
3. D. Qu, M. Zheng, P. Du, Y. Zhou, L. Zhang, D. Li, H. Tan, Z. Zhao, Z. Xie and Z. Sun, *Nanoscale*, 2013, **5**, 12272-12277.
4. H. Sun, L. Wu, W. Wei and X. Qu, *Mater. Today*, 2013, **16**, 433-442.
5. G. S. Kumar, R. Roy, D. Sen, U. K. Ghorai, R. Thapa, N. Mazumder, S. Saha and K. K. Chattopadhyay, *Nanoscale*, 2014, **6**, 3384-3391.
6. J. Sun, Y. He and L. Wang, *Anal. Methods*, 2017, **9**, 3525-3530.
7. J. Shen, Y. Zhu, X. Yang and C. Li, *ChemComm*, 2012, **48**, 3686-3699.
8. Z. Wang, H. Zeng and L. Sun, *J. Mater. Chem. C*, 2015, **3**, 1157-1165.
9. Z. Protich, P. Wong and K. Santhanam, *ACS Sustain. Chem. Eng.*, 2016, **4**, 6177-6185.
10. X. Wang, X. Sun, J. Lao, H. He, T. Cheng, M. Wang, S. Wang and F. Huang, *Colloids Surf. B Biointerfaces*, 2014, **122**, 638-644.
11. Y. Li, F. Shi, N. Cai and X. Su, *New J. Chem.*, 2015, **39**, 6092-6098.
12. L. Tang, R. Ji, X. Li, K. S. Teng and S. P. Lau, *Part. Part. Syst. Charact.*, 2013, **30**, 523-531.
13. S. Diao, X. Zhang, Z. Shao, K. Ding, J. Jie and X. Zhang, *Nano Energy*, 2017, **31**, 359-366.
14. N. Cai, L. Tan, Y. Li, T. Xia, T. Hu and X. Su, *Anal. Chim. Acta*, 2017, **965**, 96-102.

15. J.-J. Liu, Z.-T. Chen, D.-S. Tang, Y.-B. Wang, L.-T. Kang and J.-N. Yao, *Sens. Actuator B-Chem.*, 2015, **212**, 214-219.
16. P. Tan, A. Rozhin, T. Hasan, P. Hu, V. Scardaci, W. Milne and A. Ferrari, *Phys. Rev. Lett.*, 2007, **99**, 137402.
17. J. P. Casey, S. M. Bachilo and R. B. Weisman, *J. Mater. Chem.*, 2008, **18**, 1510-1516.
18. R. B. Martin, L. Qu, Y. Lin, B. A. Harruff, C. E. Bunker, J. R. Gord, L. F. Allard and Y.-P. Sun, *J. Phys. Chem. B*, 2004, **108**, 11447-11453.
19. C. F. Chiu, N. Dementev and E. Borguet, *J. Phys. Chem. A*, 2011, **115**, 9579-9584.
20. D. K. Singh, P. K. Iyer and P. K. Giri, *Carbon*, 2012, **50**, 4495-4505.
21. B. Pan, D. Cui, C. S. Ozkan, M. Ozkan, P. Xu, T. Huang, F. Liu, H. Chen, Q. Li and R. He, *J. Phys. Chem. C*, 2008, **112**, 939-944.
22. V. Biju, T. Itoh, Y. Baba and M. Ishikawa, *J. Phys. Chem. B*, 2006, **110**, 26068-26074.
23. L. Vaisman, H. D. Wagner and G. Marom, *Adv. Colloid Interface Sci*, 2006, **128-130**, 37-46.
24. H. Wang, *Curr. Opin. Colloid Interface Sci.*, 2009, **14**, 364-371.
25. R. Bandyopadhyaya, E. Nativ-Roth, O. Regev and R. Yerushalmi-Rozen, *Nano Lett.*, 2002, **2**, 25-28.
26. G. Rajender and P. K. Giri, *J. Mater. Chem. C*, 2016, **4**, 10852-10865.
27. R. Beams, L. G. Cançado and L. Novotny, *J. Condens. Matter Phys.*, 2015, **27**, 083002.
28. M. S. Dresselhaus, G. Dresselhaus, R. Saito and A. Jorio, *Phys. Rep.*, 2005, **409**, 47-99.
29. A. Roch, L. Stepien, T. Roch, I. Dani, C. Leyens, O. Jost and A. Leson, *Synth. Met.*, 2014, **197**, 182-187.
30. J. Maultzsch, H. Telg, S. Reich and C. Thomsen, *Phys. Rev. B*, 2005, **72**, 205438.
31. S. Gupta, A. Scuttler and J. Farmer, *J. Appl. Phys.*, 2010, **107**, 104308.
32. T. Morimoto, S.-K. Joung, T. Saito, D. N. Futaba, K. Hata and T. Okazaki, *ACS nano*, 2014, **8**, 9897-9904.
33. M. Ichida, S. Saito, T. Nakano, Y. Feng, Y. Miyata, K. Yanagi, H. Kataura and H. Ando, *Solid State Commun.*, 2011, **151**, 1696-1699.
34. J.-S. Lauret, C. Voisin, G. Cassabois, C. Delalande, P. Roussignol, O. Jost and L. Capes, *Phys. Rev. Lett.*, 2003, **90**, 057404.
35. J. G. Duque, A. N. G. Parra-Vasquez, N. Behabtu, M. J. Green, A. L. Higginbotham, B. K. Price, A. D. Leonard, H. K. Schmidt, B. Lounis, J. M. Tour, S. K. Doorn, L. Cognet and M. Pasquali, *ACS Nano*, 2010, **4**, 3063-3072.
36. M. Gopannagari and H. Chaturvedi, *Nanoscale*, 2015, **7**, 16590-16596.
37. Y. Shi, L. Ren, D. Li, H. Gao and B. Yang, *J Surf Eng Mater Adv Technol*, 2013, **Vol.03No.01**, 7.
38. A. M. Brouwer, *Pure Appl. Chem.*, 2011, **83**, 2213-2228.
39. G. J. Wang, M. W. Lee and Y. H. Chen, *Photochem. Photobiol.*, 2008, **84**, 1493-1499.
40. P. Yu, X. Wen, Y.-R. Toh, Y.-C. Lee, K.-Y. Huang, S. Huang, S. Shrestha, G. Conibeer and J. Tang, *J. Mater. Chem. C*, 2014, **2**, 2894-2901.

Chapter 3

Origin of High Photoluminescence Yield and High SERS Sensitivity of Nitrogen-Doped Graphene Quantum Dots

In this chapter, the origin of high photoluminescence (PL) quantum yield (QY) and high surface-enhanced Raman scattering (SERS) sensitivity of nitrogen-doped graphene quantum dots (N-GQDs) is investigated by the controlled synthesis of various kind of doped and functionalized GQDs using a solvothermal route. Among different types of doped GQDs, N-GQDs are observed with the highest PL QY of ~34%. The origin of high PL QY in N-GQDs is investigated here in terms of the improvement of the recombination process by the structural and functional modifications in the graphitic planes. Additionally, N-GQDs are demonstrated as an efficient SERS substrate with a remarkably high enhancement factor (EF) of ~3.2×10^3 in the presence of 10^{-4} M Rhodamine B (RhB) target, due to the combined effect of Förster resonant energy transfer (FRET) and chemical enhancement (CM). Furthermore, the individual contributions of FRET and CM factors are isolated by controlling the functional groups of N-GQDs, laser excitations, and target materials. The optimized N-GQDs SERS substrate is exhibited to detect RhB as low as 100 pico-Molar concentration. Finally, N-GQDs combined with RhB are used to fabricate a liquid phase white light-emitting diode (WLED) with a CIE coordinate (0.30, 0.34). The present study not only provides valuable insights into the origin of high PL QY of N-GQDs but also it shows multifunctional applications of N-GQDs such as an efficient sensor and energy device.

3.1. Introduction

In the previous chapter, we have discussed the tuning of the PL intensity of undoped GQDs with the incorporation of SWCNTs, and the undoped GQDs exhibit a PL QY of ~5.5%. However, further improvement in the PL QY of GQDs is essential for practical applications. For the development and alteration of the PL property of GQDs, identification of the radiative sites, and non-radiative sites for PL emission is crucial. GQDs, including doped GQDs, the zero-dimension (0D) derivatives of sp^2-hybridized graphene, are recently developed as fascinating fluorescent materials with diverse applications in various fields including optical sensing, SERS detection, optoelectronic devices, photoscience, bio-imaging and biomedical applications due to their

extraordinary optical and electrical properties.[1-12] Considerable research efforts have been focused on the fabrication of GQDs by various advanced methods, e.g., hydrothermal/ solvothermal treatment, pyrolysis, microwave irradiation, laser ablation, electrochemical etching, chemical ablation, etc.[1, 4, 5, 13, 14] Among different synthesis processes, hydrothermal/ solvothermal methods were reported widely for the synthesis of undoped as well as doped GQDs in a large scale.[1, 14, 15] Recently, the study of the solvent effects on GQDs has attracted much attention.[16, 17] It is notable that the effect of solvents was studied mostly on post-synthesized GQDs, which showed the variation in optical properties of GQDs is mainly due to the screening effect, polarization effect of solvents as well as the modification of surface states of GQDs by the passivation.[16-19] In the reported works, the reacting solvents were chosen mainly to serve the purpose of different types of doping or functionalization.[1, 14, 16] However, there is a lack of understanding in the choice of solvent/dopant for a specific application of GQDs. In this context, we present here a comparative study of GQDs synthesized in different solvents under identical conditions that enables suitable doping of the GQDs and study their corresponding formation mechanism and a critical analysis of the origin of high PL QY and their applications in SERS and light-emitting devices.

SERS, being a sophisticated optical technique, enables label-free and ultra-sensitive detection of biological molecules and chemical species.[3, 20-22] GQDs were recently reported as efficient SERS substrate for detecting target molecules due to their large specific surface areas and additionally accessible edges, which results in further effective adsorption of target molecules.[3, 23] However, there is no clarity on the individual contribution of different factors, such as chemical enhancement (CM) and electromagnetic enhancement factors, affecting the contributions to SERS performance, as it is challenging to classify the type of interactions, charge transfer, and their individual contributions in the SERS enhancement. It is essential to understand the contribution of each process to engineer the SERS performance of GQDs for ensuing applications. Herein, the controlled synthesis of undoped GQDs (U-GQDs), N-GQDs, and sulfur-doped GQDs (S-GQDs) are elucidated through the growth by the solvothermal route by using graphene oxide (GO) as precursor material. Through the study of the structural and optical properties of different types of GQDs, the origin of high PL QY and high SERS sensitivity of N-GQDs are investigated here. Further, we identify and isolate the individual contribution of FRET and CM in the SERS process by controlled experiments. Finally, N-GQDs combined with RhB is utilized to fabricate the liquid phase WLED.

3.2. Experimental Details

3.2.1. Sample Preparation

3.2.1.1. Synthesis of Graphene Oxide

In the present work, GO was synthesized by a well-known modified Hummers' method, as discussed in **Chapter 2, Section 2.2.1.1**. In brief, 3 g graphite flakes were mixed with 70 mL concentrated H_2SO_4 under continuous stirring in the present of 1.5 g $NaNO_3$. After 2h stirring, 9 g of $KMnO_4$ was added slowly in the above mixture inside an ice bath. After that, MQ water was slowly added to the prepared mixture at 98 °C, and then the solution was quenched with 15 mL of 30% H_2O_2. Finally, the GO was separated from the unreacted flakes and impurities by centrifugation.

3.2.1.2. Synthesis of undoped GQDs

Undoped GQDs (U-GQDs) were prepared by the top-down method using GO as the precursor, as discussed in **Chapter 2, Section 2.2.1.2**. Briefly, 600 mg of GO powder was dispersed in 40 mL MQ water and sonicated for 30 min for proper dispersion and then the solution was heated at 220 °C for 12 h into a Teflon lined autoclave. After that, the transparent suspension was collected as U-GQDs.

3.2.1.3. Synthesis of Nitrogen-doped GQDs

Nitrogen-doped GQDs (N-GQDs) were synthesized by a solvothermal route in dimethylformamide (DMF, 99%, Sigma-Aldrich) solvent with the GO as a precursor. Typically, 600 mg of GO powder was dispersed in 40 mL DMF with sonication for 30 min. Then the GO solution was transferred into the Teflon lined autoclave and heated at 220 °C for 7h. After cooling down at room temperature, the solution was centrifuged at 10,000 rpm to collect the yellow suspension of N-GQDs. To optimize the synthesis of N-GQDs with different N-content, different amounts of GO (200, 600, 800 mg) was added in a fixed amount (40 mL) of DMF and reacted at discussed above.

3.2.1.4. Synthesis of Sulfur-doped GQDs

Sulfur-doped GQDs (S-GQDs) was synthesized top-down method in dimethyl sulfoxide (DMSO, Sigma-Aldrich) solvent. In brief, 600 mg of GO powder was mixed with 40 mL of DMSO under ultra-sonication. After that, GO solution was heated at 220 °C for 7h into the Teflon lined autoclave. Finally, the suspension part was collected as S-GQDs.

A schematic of the synthesis process of various types of GQDs in different mediums and the features of the resulting products is shown in **Fig. 3.1**.

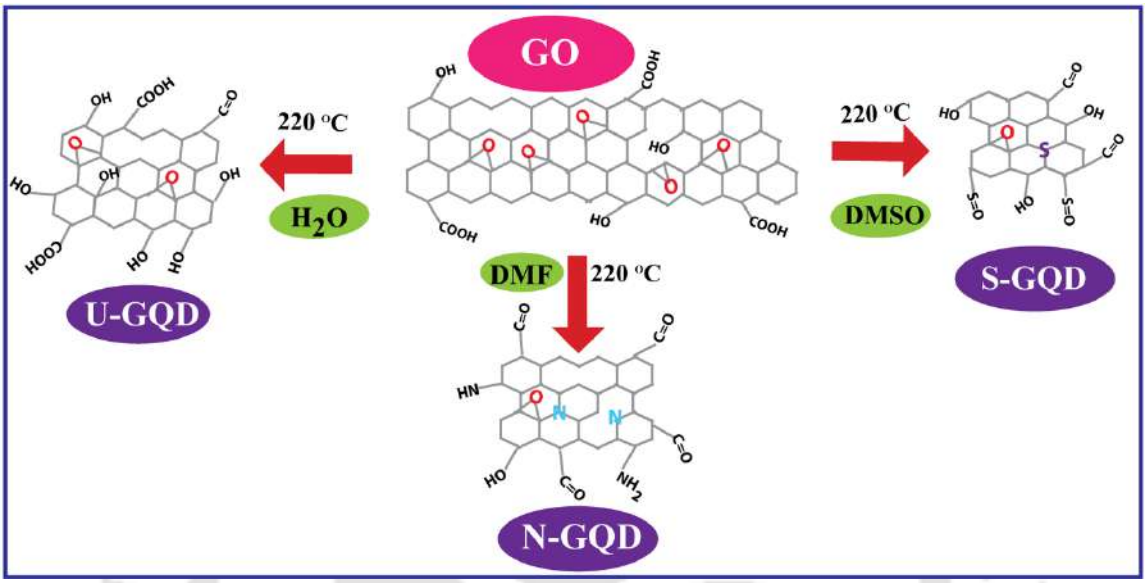

Fig. 3.1. Reaction scheme of different types of GQDs with various solvents and the chemical features of the resulting products.

3.2.2. SERS Detection

The efficiency of undoped and doped GQDs as SERS substrates was monitored with Si (100) substrate coated with 0.2 mg/mL solution of GQDs in MQ water for each sample. The solutions of dye molecules, e.g., RhB and methyl blue (MB), were arranged with different concentrations in methanol. 10 μL of GQDs solution was first drop cast on cleaned Si substrate at a constant temperature, 70 °C. After the complete drying of the GQDs solution, 20 μL of dye solution was dropped on top of the GQD-coated Si substrate and used for SERS detection.

3.2.3. Fabrication of Liquid Phase White LED

N-GQDs were used as light converting material for the fabrication of liquid phase WLED. Commercially procured low-cost UV LED (~396 nm) was put into a culture tube containing N-GQDs solution (0.4 mg/mL) and sealed with a glass slip to obtain a liquid phase LED. The same arrangement was implemented with the addition of 50 μM RhB solution in N-GQDs solution with a volume ratio of 1:5 for improvement of the purity of the white light.

3.2.4. Characterization Techniques

The details of the characterization techniques (TEM, Raman, UV-vis, PL, and TRPL) used to study the systems were described in **Chapter 2, Section 2.2.3**. Additionally, high-angle annular dark-field (HAADF) images were obtained using a scanning transmission electron microscope (STEM) in aberration-correction mode (JEM 2100F, 200 kV) for high-resolution imaging of few samples. Atomic force microscopy (AFM) (Cypher, Oxford Instruments) image was acquired in non-contact mode. X-ray photoelectron spectroscopy (XPS) measurement was carried out using a PHI X-tool automated photoelectron spectrometer (ULVAC-PHI, Japan) with an Al Kα X-ray beam (1486.6 eV) at a beam current of 20 mA for the analysis of the chemical compositions and chemical environment. The shift in the binding energy of various material was corrected using the C 1s spectrum at 284.8 eV as the reference value.[24] The Raman scattering measurements were performed in a high-resolution Raman spectrometer (LabRam HR800, Jobin Yvon) with different laser excitations: 488, 514 and 633 nm. A 100X objective lens focused the laser beam with a spot size of ~1μm in diameter. The acquisition time was 20 s for collecting the SERS spectrum. Fourier transform infrared spectroscopy (FTIR) measurements were executed in PerkinElmer, Spectrum BX spectrophotometer in the reflectance mode. For XRD, FTIR, and Raman measurements, samples were drop cast on Si (100) wafer, followed by drying at 70 °C. UV-vis absorption spectra of the samples were recorded using the PerkinElmer spectrophotometer, Lamda 950. The steady-state PL measurements were carried out in a commercial spectrofluorometer (Horiba, Fluoromax-4) equipped with a Xe lamp source. Low temperature (80–300 K) PL measurements were carried out using a 405 nm laser excitation and a liquid nitrogen-cooled optical cryostat (Optistat DNV, Oxford Instruments) with the sample kept in the vacuum. Electroluminescence (EL) signal was acquired with the same spectrofluorometer using an external power supply. Time-resolved PL (TRPL) measurements were carried out with the excitation of A 405 nm laser source by a picosecond time-resolved luminescence spectrometer (FSP920, Edinburg Instruments) with an instrument response time of ~50 ps. The vacuum annealing was carried out in a quartz chamber for 2 h at different temperatures (~200, 400, and 600 °C) under 2.5×10^{-2} mbar base pressure.

3.3. Results and Discussion

3.3.1. Morphology Studies

To study the morphology of various types of GQDs, **Fig. 3.2(a-c)** shows the typical plan-view TEM images and the size distributions of as-prepared U-GQDs, N-GQDs, and S-GQDs with the histogram in the respective insets. For U-GQDs, the average size is obtained as ~4.0 nm by lognormal fitting, as shown in the inset of **Fig. 3.2(a)**. **Fig. 3.2(b)** shows the HAADF TEM image

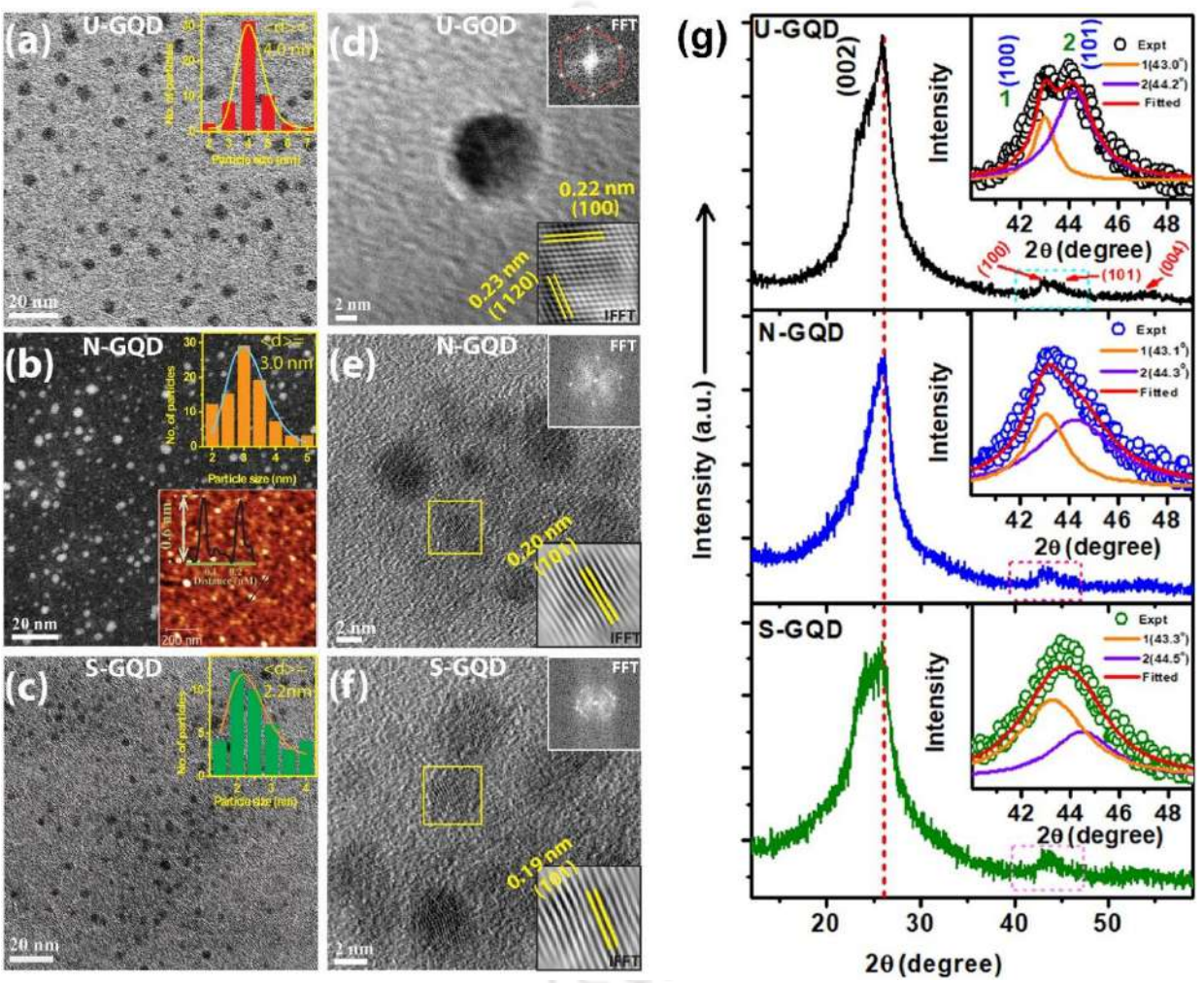

Fig. 3.2. TEM images of (a) U-GQDs, (b) N-GQDs, and (c) S-GQDs, where, U-GQDs and S-GQDs are presented with bright-field images and N-GQDs with dark-field images. The upper insets show the particle size distribution of the respective samples. The lower inset in (b) shows the AFM image of N-GQDs with a height profile revealing the monolayer thickness of GQDs. (d) The HRTEM lattice image of one of U-GQDs; the upper inset shows the 2D FFT image of U-GQD with hexagonal lattice structure, and the lower inset shows the IFFT image of the U-GQD. (e, f) HRTEM images of N-GQDs and S-GQDs, respectively; The upper inset in each case shows the 2D FFT image, and the lower inset shows the IFFT image of selected particle marked with yellow square. (g) Powder XRD pattern of undoped and doped GQDs. The inset in each case shows the deconvoluted peak in the range 2θ ~40–50°. The vertical dashed line indicates the position of (002) peak in different samples.

of N-GQDs, and the upper inset shows the size distribution of N-GQDs with an average size of ~3.0 nm. The lower inset of **Fig. 3.2(b)** shows the AFM image and the corresponding height profile of N-GQDs, revealing their thickness as ~0.6 nm corresponding to monolayer graphene oxide.[25] The bright-field TEM image of S-GQDs in **Fig. 3.2(c)** shows an average particle size of ~2.2 nm. Thus, the average size of GQDs gradually decreases with doping in the order of U-GQDs, N-GQDs, and S-GQDs. The HRTEM images of different GQDs in **Fig. 3.2(d-f)** exhibit the well-resolved lattice fringes confirming their crystalline nature. The 2D fast Fourier transform (FFT) pattern of the U-GQDs in the inset of **Fig. 3.2(d)** shows a standard six-fold symmetry of synthesized U-GQDs. Further, the inverse FFT (IFFT) of the HRTEM image of the selected area (yellow square) reveals the clear lattice fringes. The lattice spacing of ~0.23 nm corresponding to (1120) hcp planes[26] of U-GQDs and ~0.22 nm for (100) planes[1] shows the high crystalline nature of the as-grown U-GQDs. The 2D FFT pattern of N-GQDs and S-GQDs in the inset of **Fig. 3.2(e, f)** show the gradual destruction of hexagonal structure with an approach towards amorphous nature after the doping of N or S atoms.[27] The IFFT image of N-GQDs shows an interplanar spacing of ~0.20 nm in (101) direction, while it is ~0.19 nm in S-GQDs, which could be due to the compressive strain in S-GQDs.

3.3.2. Structural Analysis

3.3.2.1. XRD and XPS Analysis

The XRD pattern of undoped and doped GQDs are recorded to study the structural changes due to doped atoms in GQDs. In each case, a strong diffraction peak corresponding to (002) graphitic planes appear together with few weak peaks corresponding to (100), (101), and (004) planes, as indicated in **Fig. 3.2(g)**. The (002) diffraction peak at 2θ ~26.0° is attributed to the presence of sp^2 hybridized carbon in the basal plane of U-GQDs.[28] Interestingly, the lowering of the 2θ values for the doped GQDs (N-GQDs and S-GQDs) indicates the expansion of interplanar spacing in the basal planes. The formation of GQDs in DMF and DMSO may dope N and S, respectively, in the sp^2 domains, and thus carbon atoms could be replaced with N or S atoms, which could modify the interplanar spacing. For a detailed analysis of the changes in the doping/defect induced planes in different GQDs, the XRD peak is deconvoluted with two Lorentz peaks in the range 2θ ~40–50°, as shown in the corresponding inset of **Fig. 3.2(g)**. The deconvoluted peaks named as 1 and 2 in each sample correspond to (100) and (101) planes, respectively. Note that the interplanar spacing of both (100) and (101) planes reduce after doping with N and S atoms. Also, the increase in

FWHM of the deconvoluted peaks after doping could be due to the attachment of excessive functional groups or the creation of defects in graphitic structures, which may cause a compressive strain along the (100) and (101) planes of the doped GQDs.

An overview of the chemical composition of different samples is observed from the XPS survey scan shown in **Fig. 3.3(a)**. Along with the presence of C 1s and O 1s peaks, the appearance of N 1s peak in N-GQDs, and S 2p, S 2s peaks in S-GQDs confirm the doping of N and S atoms for the

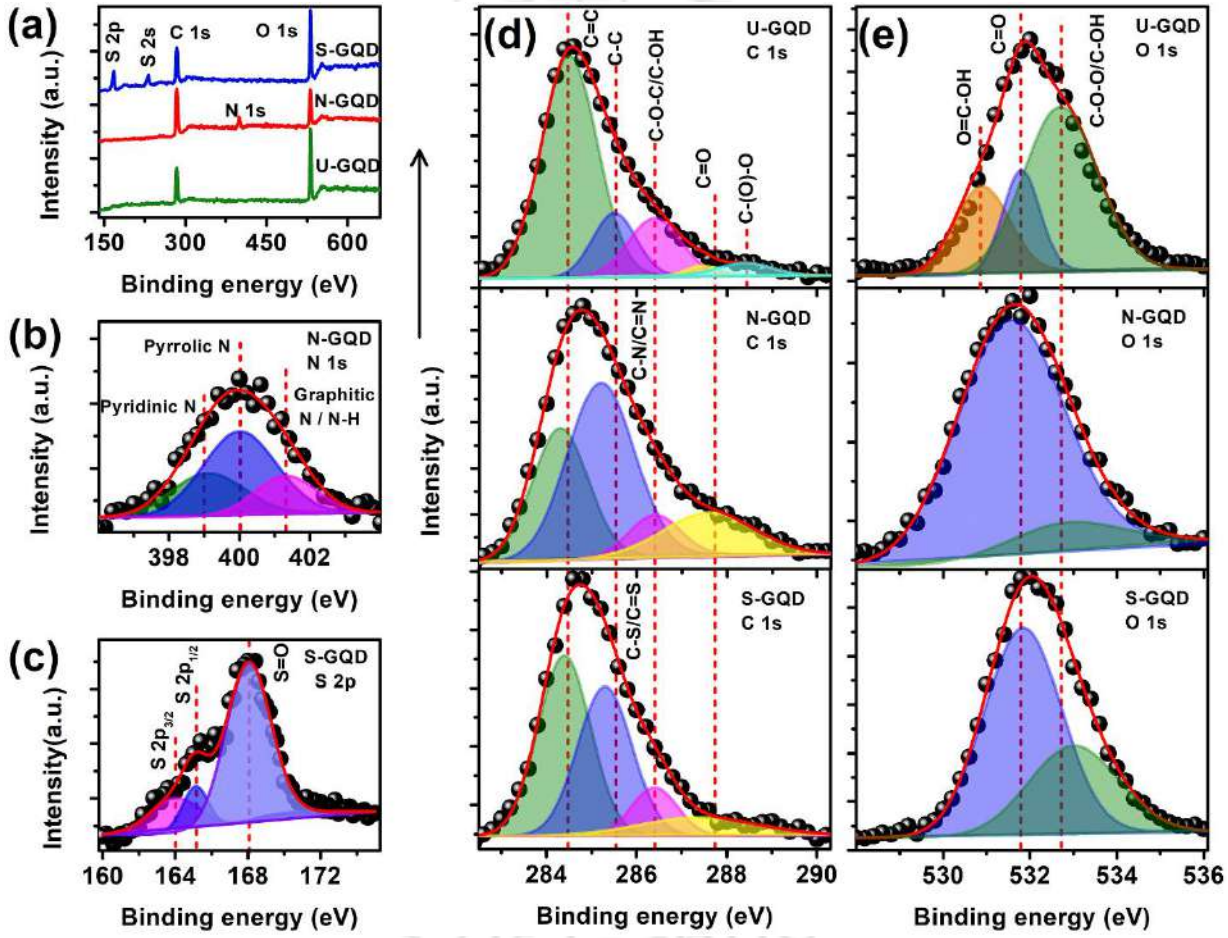

Fig. 3.3. (a) The survey scan XPS spectra for U-GQDs, N-GQDs, and S-GQDs. (b, c) High-resolution N 1s and S 2p XPS spectra of N-GQDs and S-GQDs, respectively. (d, e) Comparison of the C 1s and O 1s XPS spectra for various types of GQDs. The symbols represent the experimental data, and the solid lines indicate the fitted curves in each case. The vertical dashed lines indicate the respective peak positions in different samples.

reaction in DMF and DMSO medium, respectively. The XPS analysis on N-GQDs and S-GQDs show the concentration of N and S as 7.9% and 16.9%, respectively. Based on the XPS analysis, the ratio of carbon to oxygen content (C/O) is 1.85, 3.60, and 1.69 in U-GQDs, N-GQDs, and S-GQDs, respectively, which reveals that O content is much less in N-GQDs as compared to the

other samples. Next, the high-resolution N 1s spectrum is deconvoluted to determine the different types of doped N, as shown in **Fig. 3.3(b)**. The peak position of deconvoluted curves of the N 1s spectrum in N-GQDs (see **Table 3.1**) indicates the presence of pyridinic-N, pyrrolic-N, and graphitic-N/N-H.[15, 29] Note that the high percentage of pyrrolic-N in N-GQDs is due to the reaction tendency of DMF with the epoxy-functional groups of GO to form tertiary N.[29] On the other hand, the S 2p XPS spectrum of S-GQDs shows two peaks located at ~163.9 eV and 165.1 eV (see **Fig. 3.3(c)**), which are identified as $2p_{3/2}$ and $2p_{1/2}$ states of thiophene-S (-C-S-C-), due to spin-orbit coupling.[28] The peak located at ~168.0 eV is due to the oxide S as the S=O group.[28, 29] The oxide S in S-GQDs acquires ~71% of the total sulfur content, indicating that most of S atoms exist as

Table 3.1. *Details of the deconvoluted high-resolution XPS spectra of U-GQDs, N-GQDs, and S-GQDs.*

Sample	*Spectrum*	*Peak position (eV)*	*Peak identity*	*% of contribution*	*Remarks*
U-GQDs	C1s	284.5	C=C	64	High
		285.5	C-C	14	Low
		286.4	C-OH/C-O-C	16	High
		287.4	C=O	2	Low
		288.4	C-(O)-O	4	Low
N-GQDs	C 1s	284.3	C=C	30	Low
		285.2	C-N/C=N	47	Extra
		286.4	C-OH/C-O-C	8	Low
		287.4	C=O	15	High
	N 1s	399.1	Pyridinic-N	27	N-doping
		400.0	Pyrrolic-N	53	
		401.3	Graphitic-N/ -NH	20	
S-GQDs	C 1s	284.4	C=C	43	Moderate
		285.3	C-S/C=S	37	Extra
		286.4	C-OH/C-O-C	10	Moderate
		287.4	C=O	10	Moderate
	S 2p	163.9	$2p_{3/2}$	18	S-doping
		165.1	$2p_{1/2}$	11	
		168	S=O	71	

S=O functional group in S-GQDs. Thus, the doped sulfur in S-GQDs exists in two configurations: thiophene sulfur and oxide sulfur. Note that inside the autoclave, the DMF decomposes to electron-donating dimethylamine and carbon monoxide.[30] Dimethylamine, being a nucleophilic center, causes a nucleophilic ring-opening reaction with the unstable epoxy groups of GO and extracts

smaller sp^2 domains from the large GO sheets and simultaneously bonds with the aromatic ring to form N-GQDs.[30] Thus, the DMF can mainly introduce N content in N-GQDs as confirmed from the N 1s spectrum, and it helps to reduce O content by cutting of GO sheets into smaller sp^2 domains. In contrast, for the case of DMSO, S and O can act as a nucleophile towards soft and hard electrophiles, respectively. Thus, in the nucleophilic ring-opening reaction of GO, the epoxy group being a soft electrophile is mainly affected by S center, and thus S-O functional groups are directly attached at the edge sites, which enhances the O content in S-GQDs. Note that water being a polar protic environment, it does not process any nucleophilic reaction. Mainly, the equilateral epoxy groups on the basal plane of GO create such a high strain that leads to the creation of fault lines and cracks in GO sheets.[31] Further, by the consecutive unzipping processes, circular-shaped U-GQDs are formed. The deconvolution of C 1s spectra of different types of GQDs are presented in **Fig. 3.3(d)** and the summary of the changes of various states with doping in different samples is presented in **Table 3.1**. The presence of graphitic sp^2 hybridized carbon (C=C), sp^3 hybridized carbon (C-C), together with various oxygen functional groups (C-OH/C-O-C, C-(O)-O) are identified in U-GQDs. Interestingly, for the case of N-GQDs and S-GQDs, the reduction of the binding energy of C=C is observed as a result of the doping in the graphitic network with subsequent enhancement of the localization of electronic charge distribution in the sp^2 domains. Moreover, the deconvoluted peaks at ~285.2 eV and 285.3 eV correspond to C-N/C=N and C-S/C=S states in N-GQDs and S-GQDs, respectively,[29] and that confirm the successful doping in respective samples. The maximum redshift of the binding energy of sp^3 carbon in N-GQDs endorses a higher electronic charge in C-N/C=N states. Note that the maximum contribution of C=C in U-GQDs is attributed to the high crystallinity, while the dominating contribution of sp^3 carbon in N-GQDs and S-GQDs implies their disordered characteristics. To be more precise about various oxygen functional groups of different samples, O 1s spectra are also deconvoluted, as presented in **Fig. 3.3(e)**. Due to O=C-OH group, a peak at ~530.9 eV is observed in U-GQDs,[32] while there is no such peak in doped GQDs, consistent with the C 1s spectra. DMSO works as a mild oxidant, and thus in the DMSO medium, the oxidation of hydroxyl groups to carbonyl can take place at high pressure and temperature reaction. Compared with U-GQDs, the reduction of C-OH/C-O-C functional groups and the enhancement of C=O groups for both N-GQDs and S-GQDs may be due to the conversion of hydroxyl to carbonyl groups or higher number of ring-opening reaction with epoxy groups.

3.3.2.2. Raman and FTIR Spectral Analysis

The extent of the disorder, degree of crystallinity, and doping induced changes in GQDs are investigated by Raman spectroscopy. The comparative Raman spectra of different types of GQDs are presented in **Fig. 3.4(a)** and the characteristics D, G, and 2D band positions are indicated by the vertical dashed lines. **Fig. 3.4(b)** shows the deconvolution of the Raman spectra in the region 1060–1650 cm^{-1} with Gaussian peaks and one BWF peak. The details of the peak parameters are presented in **Table 3.2**. The characteristic G band at ~1604 cm^{-1} in U-GQDs arises from the in-plane phonon vibration of sp^2 carbon. The redshift of G band with ~11 cm^{-1} and 18 cm^{-1} in N-GQDs and S-GQDs, respectively, with respect to U-GQDs, indicate the creation of tensile strain

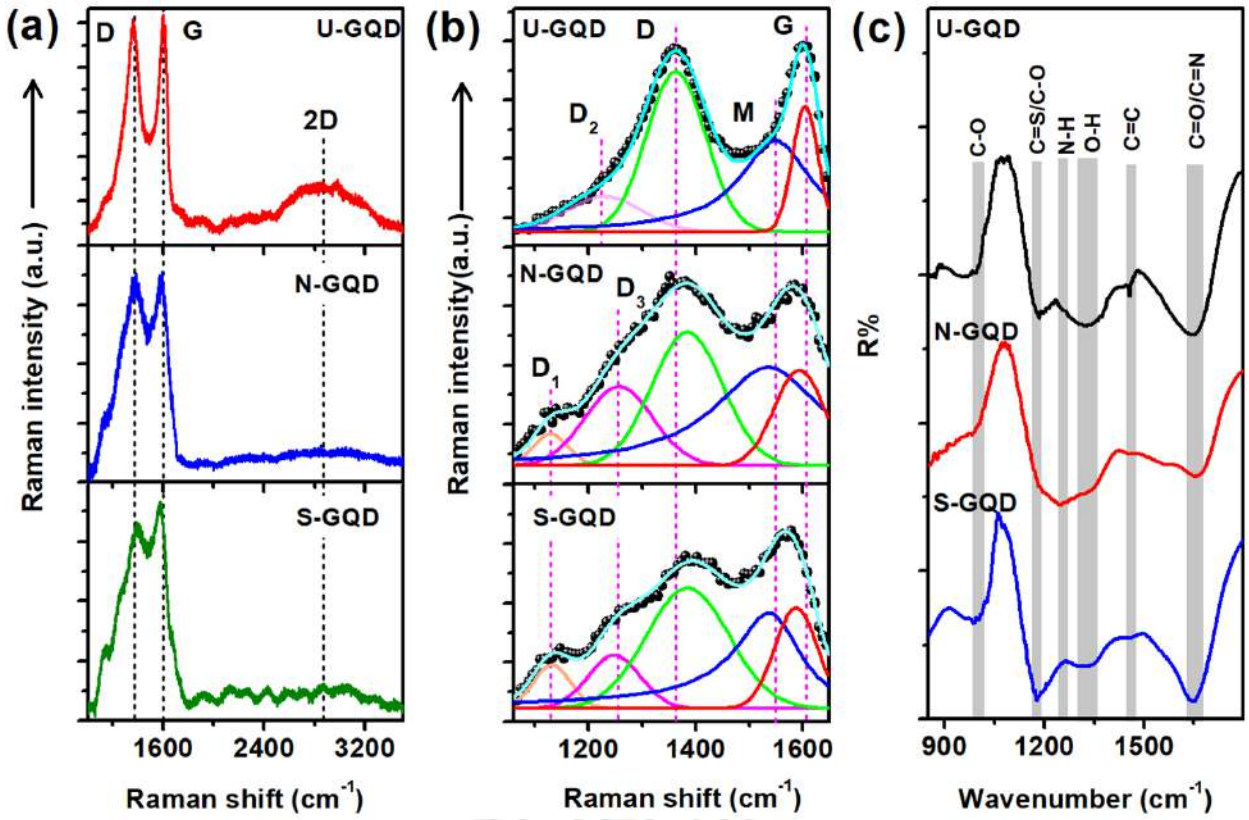

Fig. 3.4. (a) Comparative Raman spectra of U-GQDs, N-GQDs, and S-GQDs with 488 nm laser excitation. The vertical dashed lines indicate the positions of D, G, and 2D bands in U-GQDs. (b) Deconvolution of Raman spectrum of different samples with Gaussian peaks and a BWF peak (M) in the range 1060–1650 cm^{-1}. The symbol corresponds to the experimental data, and the solid curves represent the fitted peaks in each case. The vertical lines indicate the shift of the peak positions in different samples. (c) Comparison of the FTIR spectra of U-GQDs, N-GQDs, and S-GQDs.

in the lattice planes by the doped atoms. In addition, the doping of electron-rich N or S atoms increases the electronic charge in N-GQDs, and S-GQDs, as confirmed from C 1s XPS spectrum,

may result in the redshift of G band. Moreover, from **Fig. 3.4(a)**, the reduction of the intensity ratio of the 2D band to G band (I_{2D}/I_G) in doped GQDs is attributed to the enhancement of the electron concentration by N or S doping. In the deconvoluted spectrum of U-GQDs, the D band appears at 1363 cm^{-1} due to the presence of defective sites. In the present case, the values of I_D/I_G are obtained as 1.16, 1.40, and 1.19 for U-GQDs, N-GQDs, and S-GQDs, respectively. The highest value of I_D/I_G in N-GQD reveals the highest density of Raman active edge sites and a reduction in the crystallinity of the N-GQDs as compared to U-GQDs. Besides the characteristic G and D bands, the deconvolution of Raman spectra shows few additional Raman active bands corresponding to different functional groups named as D_1, D_2, and D_3, as listed in **Table 3.2**. The

Table 3.2. *The peak position of the deconvoluted Raman spectra in the region 1060–1650 cm^{-1} for the different types of GQDs.*

Sample	***Raman bands (cm^{-1})***					
	D_1	D_2	D_3	D	M	G
GQDs	-	1230	-	1363	1550	1604
N-GQDs	1130	-	1257	1384	1535	1593
S-GQDs	1132	-	1248	1385	1537	1586
Peak Identity	***sp^2-sp^3 carbon/C-S***	***C-O-C***	***C-N/SO***	***Edge states***	***Metallic***	***C=C***

D_2 band in U-GQDs represents the C-O vibration, whereas D_1 and D_3 bands in doped GQDs correspond to the N or S doping as well as several functional groups attached at the time of synthesis. The presence of the D_1 band in N-GQDs and S-GQDs comes to an agreement with a higher contribution of sp^3 carbon in the C1s XPS spectrum. Interestingly, as compared to U-GQDs, a gradual blue shift of the D bands is observed from N-GQDs to S-GQDs, caused by the compressive strain, which is consistent with XRD analysis of (100) and (101) planes. In addition to the defect bands, the presence of M band with BWF line shape for each sample represents the metallic component of GQDs.[1] Interestingly, the relative contribution of the M band in N-GQDs (~34%) is observed to be higher than that of S-GQDs (~31%) and U-GQDs (~32%) which is due to the presence of higher electronic charge in the graphitic network of N-GQDs caused by N doping.

The FTIR spectra of different types of GQDs are presented in **Fig. 3.4(c)**. The absorption band at ~1650 cm^{-1} and 1240 cm^{-1} correspond to C=N and N-H vibrations, confirming the N doping and presence of N-functional groups in N-GQDs.[33, 34] For S-GQDs, the strong absorption band at ~1180 cm^{-1} is attributed to the stretching vibration of C=S, indicating the successful doping of S atoms in the carbon network.[28, 29, 35] The strong absorption at ~1456 cm^{-1} in U-GQDs is the characteristics of the stretching vibration of C=C in the aromatic skeleton,[34] which is very weak for S-GQDs and N-GQDs perhaps due to the incorporation doping effect. The absorption peaks at ~1000 cm^{-1} and ~1356 cm^{-1} in all samples are attributed to the stretching vibration of C-O and bending vibration of O-H due to the presence of oxygen functional groups.[28, 34]

3.3.3. Optical Analysis

The optical properties of GQDs are investigated with the help of UV-vis absorption spectra, PL spectra at room temperature as well as low temperature (80 K) and TRPL spectra.

3.3.3.1. UV-vis Absorption Study

Fig. 3.5(a) shows the comparative absorption spectra of U-GQDs, N-GQDs, and S-GQDs. A deep UV absorption peak centered at ~265 nm in U-GQDs is assigned to the characteristic π–π^* transition within sp^2 hybridized carbon domains.[1] Note that in the doped samples, the intensity of this characteristic peak becomes intense as well as broader. As compared to U-GQDs, stronger absorption in doped GQDs implies the enhancement of the π–π^* transitions in the core as the result of doping with electron-donating S and N atoms. The absorption tail in the range 350–600 nm is assigned to the n–π^* transition for the non-bonding electrons of O (C=O), N (C-N), and S (C-S). The Tauc plot in **Fig. 3.5(b)** shows that the indirect bandgap for N-GQDs (~2.08 eV) is much smaller than that of U-GQDs (~3.48 eV). Jin et al. reported a reduction in the bandgap of N-GQDs with the increasing number of $-NH_2$ due to the donation of their lone pair electrons to the antibonding state in the benzene ring.[36] In the present case, the synthesis of N-GQDs in DMF solvent introduces electron-donating -NH groups in N-GQDs, which helps to reduce their bandgap. For the case of S-GQDs, due to the presence of electron-withdrawing S=O functional groups, C-S/C=S are not able to enhance the electronic charge in sp^2 carbon efficiently. Thus, S-GQDs exhibit a higher bandgap than that of N-GQDs.

3.3.3.2. Photoluminescence Excitation Spectra Study

The normalized PL excitation (PLE) spectra of all samples are presented in **Fig. 3.5(c)**, which shows the position of the excitation maxima for different types of GQDs. U-GQDs and S-GQDs show the PLE peak at ~338 nm, while that of N-GQDs is at ~360 nm. A weak shoulder peak at ~272 nm in all samples is associated with the π−π* transition. Thus, the dominance of the 338/360 nm peak indicates a substantial contribution of the functional groups/defects/dopants in the PL emission of all GQDs.

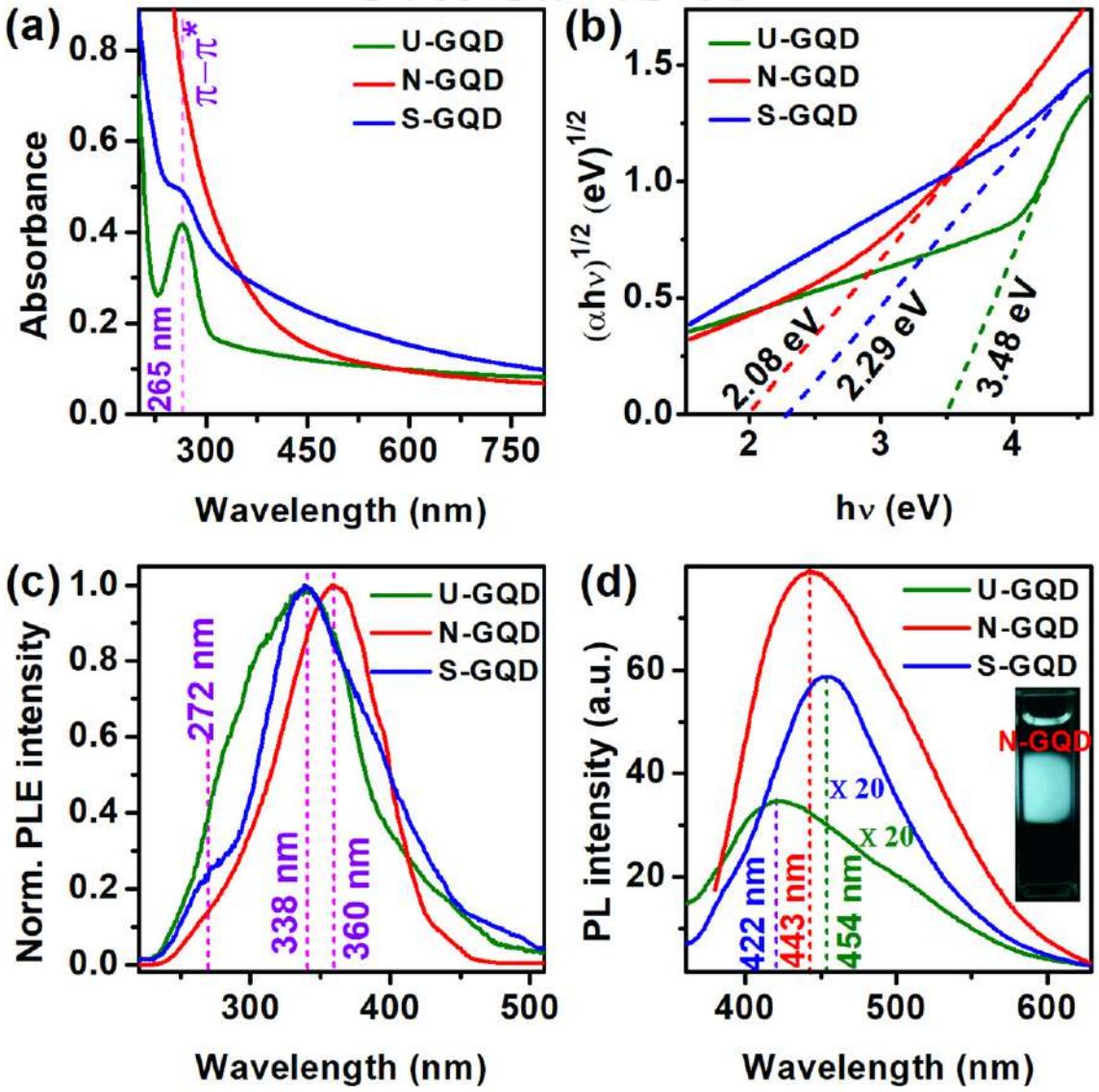

Fig. 3.5. (a) Comparative absorption spectra of U-GQDs, N-GQDs, and S-GQDs, and (b) the corresponding Tauc plots with indirect bandgaps indicated in respective cases. (c) The normalized PLE spectra of undoped, N and S doped GQDs for emissions at 422 nm, 443 nm, and 453 nm, respectively. (d) Comparative PL spectra of undoped and doped GQDs with the excitations at respective PLE maxima. The spectra of GQDs and S-GQDs are scaled up by a factor 20 to enable better comparison. The inset shows the digital photograph of N-GQDs dispersion with 360 nm excitation.

3.3.3.3. Room Temperature Photoluminescence Study

Based on the PLE spectra, the PL spectra of undoped and doped GQDs are acquired and presented in **Fig. 3.5(d)**. Note that the PL intensity of N-GQDs is much higher than that of U-GQDs and S-GQDs. Hence the spectra are appropriately scaled to enable a better comparison. N-GQDs with an emission peak at ~443 nm show ~25 times stronger PL intensity than that of S-GQDs, and the S-GQDs exhibit ~2 times higher PL intensity (at ~454 nm) than that of U-GQDs. A digital photograph of N-GQDs with the illumination of ~360 nm light is presented in the inset of **Fig. 3.5(d)**, which shows strong bluish-green emission. The relative QY (ϕ) of various types of GQDs was calculated using eqn. (2.3) of **Chapter 2**. For U-GQDs, N-GQDs, and S-GQDs, ϕ values are

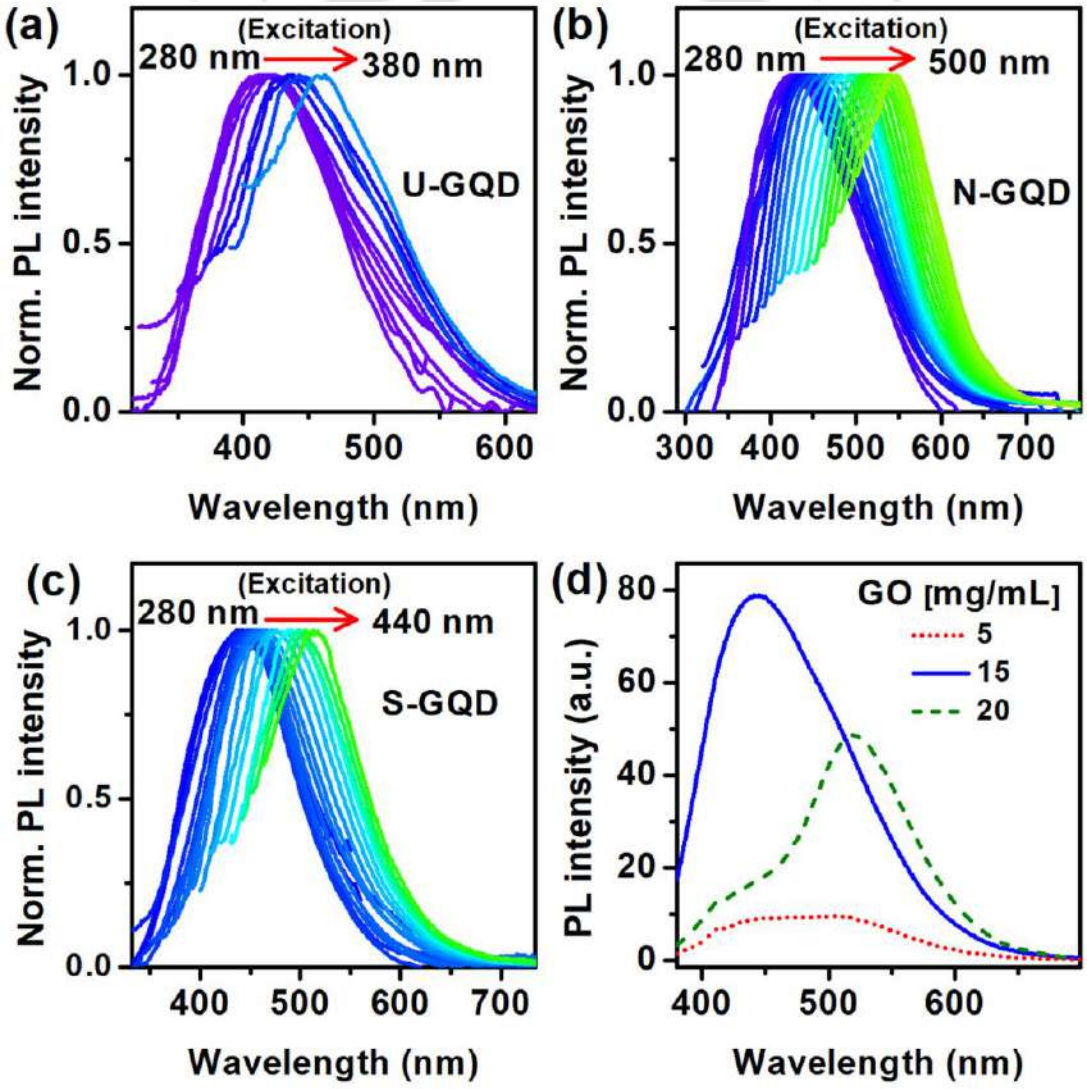

Fig. 3.6. Normalized PL spectra of (a) U-GQDs, (b) N-GQDs, and (c) S-GQDs with different excitation wavelengths. (d) PL spectra of N-GQDs synthesized with varying proportions of GO precursor; excitation wavelength 360 nm.

calculated as ~2%, 34%, and 1%, respectively. As compared to U-GQDs, despite highly intense PL in S-GQDs, low QY in S-GQDs may be due to higher absorption in S-GQDs. One the other hand, for the case of N-GQDs, the large PL enhancement is owing to the presence of electron-donating N atoms and radiative surface functional groups, which will be confirmed later. To investigate the origin of PL emission in different types of GQDs, the excitation wavelength-dependent PL spectra were acquired for all samples, as presented in **Fig. 3.6(a-c)**. With increasing excitation wavelengths, all types of GQDs show a systematic redshift of the emission maxima due to the presence of multi-emission centers, which is a common feature of fluorescent carbon materials. Moreover, the PL spectra of different types of N-GQDs (synthesized with 5, 15, and 20 mg/mL GO precursor in DMF medium) are shown in **Fig. 3.6(d)** to investigate the source of highly fluorescent emitting sites in N-GQDs. For a detailed analysis of the origin of emissive states in different types of GQDs, normalized PL spectra at excitations 300 nm and 370 nm are deconvoluted with multiple Gaussian peaks, as shown in **Fig. 3.7(a, b)**. The details of the deconvoluted peaks are presented in **Table 3.3**. For U-GQDs, the PL spectrum under the excitation of 300 nm shows a dominating contribution of zigzag edge states at ~410 nm,[37] whereas, for doped GQDs, a large contribution is observed from the doping states at ~440 nm/450 nm. Thus, the deconvoluted peaks at ~440 nm and 450 nm attributes to the electron-hole recombination of C-N/C=N and C-S/C=S states in N-GQDs and S-GQDs, respectively. Along with the zigzag edge states, the presence of COOH and C=O functional groups in U-GQDs show emission peak at ~480 nm and 530 nm, respectively.[37, 38] As we have observed the absence of COOH groups in XPS analysis for doped GQDs, no PL emission related to COOH groups in N-GQDs, and S-GQDs again confirms the above assignment of PL peak. In the case of higher λ_{ex} (λ_{ex} =370 nm), the contribution of zigzag edge states diminishes, and the doping states/functional groups dominate, which results in the overall redshift of the PL peak. As the epoxy and carboxylic groups in GQDs induce non-radiative recombination of localized electron-hole pairs,[2, 6] the presence of C-O-C/COOH surface functional groups in U-GQDs might be the main reason for low intense PL of U-GQDs. Qu et al. reported the transformation of non-radiative COOH groups to radiative C-N/C=N centers with the N doping.[39] So, the doping of N/S could decrease the non-radiative sites in doped GQDs. Along with the reduction of non-radiative sites, the solvothermal reaction helps in the formation of radiative carbonyl (C=O) groups in N-GQDs and S-GQDs, as revealed from the XPS analysis. The presence of C=O groups and the absence of COOH groups in N-GQDs

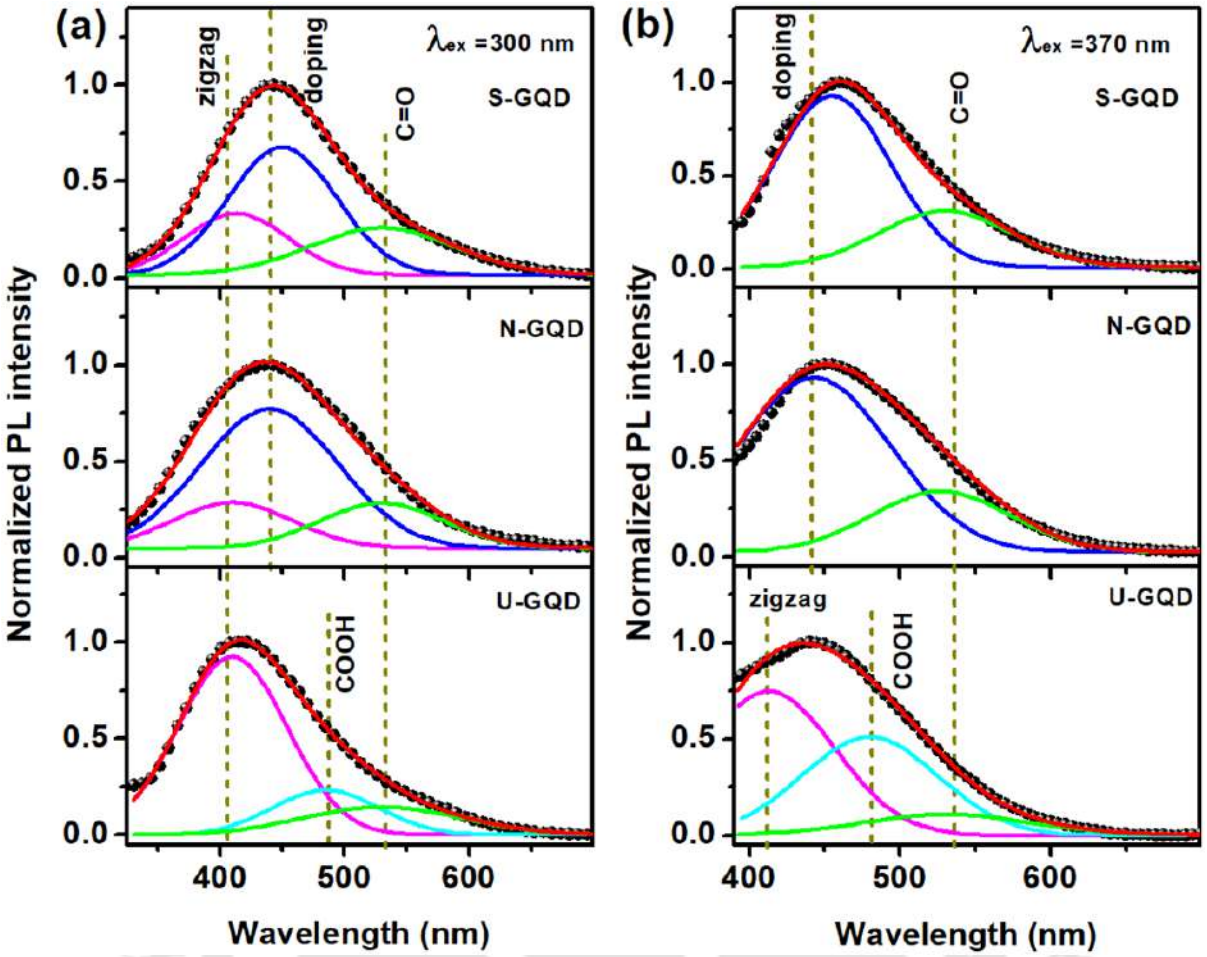

Fig. 3.7. Deconvolution of normalized PL spectra of U-GQDs, N-GQDs, and S-GQDs at the excitations 300 nm and 370 nm. The vertical dashed lines indicate the peak positions. The symbols stand for the experimental data, and the solid lines are for the fitted curves.

result in the extensive radiative recombination and thus high PL yield, while the existence of S=O functional groups in S-GQDs reduces the effective n–π* transition. According to **Fig. 3.6(d)**, with a low concentration of GO precursor, the PL intensity of N-GQDs is very low with the dominating contribution of oxygen-rich functional groups. At low GO concentration, the unreacted DMF could be attached to the surface of N-GQDs and increases the oxygen-related surface functional groups, which may reduce the electronic charge in the graphitic domains resulting in lower PL intensity. At a higher concentration of GO, the doping of N is not sufficient, which again results in lower PL intensity. Thus, the synthesis of N-GQDs with 15 mg/mL GO is optimized for efficient doping and strong PL emission.

Table 3.3. *Details of deconvoluted PL spectra and the corresponding identity of emission peaks of U-GQDs, N-GQDs, and S-GQDs at excitation 300 nm and 370 nm.*

λ_{ex} (nm)	Sample	Zigzag	FWHM (nm)	Doping	FWHM (nm)	COOH	FWHM (nm)	C=O	FWHM (nm)
300	GQDs	410	103	-	-	485	102	530	151
	N-GQDs	410	114	440	130	-	-	530	119
	S-GQDs	413	98	450	103	-	-	530	137
370	GQDs	413	103	-	-	480	107	531	135
	N-GQDs	-	-	443	120	-	-	527	109
	S-GQDs	-	-	455	92	-	-	530	105
Peak identity		***Zigzag edge state***		***Impurity/doping related***		***COOH functional group***		***C=O functional group***	

3.3.3.4. Low-Temperature Photoluminescence Study

To gain further insight into the emission mechanism, temperature-dependent PL spectra were acquired in the temperature range 80–300 K for different GQDs after drop-casting them on Si substrate. The temperature-dependent PL spectra of undoped and doped samples are shown in **Fig. 3.8(a-c)**. As the temperature goes down from 300 K to 80 K, a monotonic increase in the PL intensity is observed in U-GQDs and N-GQDs, indicating the positive thermal quenching (PTQ) phenomena.[26] At low temperatures, most of the carriers are frozen at the ground state, and thus the photogenerated carriers can recombine radiatively. With increasing temperature, the carriers acquire enough energy for escaping to higher energy levels, and the possibility of the transition of these carriers in the non-radiative states increases, which results in PTQ. The changes of the integrated PL intensity with the inverse of temperature are shown in **Fig. 3.8(d-f)** for all samples. A quantitative analysis of the PTQ is carried out with the well-known Arrhenius equation given by [40, 41]

$$I(T) = \frac{I_0}{1 + Ae^{-\frac{E_a}{K_B T}}} \qquad (3.1)$$

where I(T) and I_0 are integrated PL intensities at temperatures T K and 0 K, respectively. 'A' is a constant, E_a is the activation energy for the non-radiative process, K_B is the Boltzmann constant. To estimate the E_a value for U-GQDs and N-GQDs, the experimental data are fitted with eqn. (3.1)

in a higher temperature region (210–300 K), as shown at the corresponding inset of **Fig. 3.8(d, e)**. The obtained values of E_a are ~97 meV and 171 meV for U-GQDs and N-GQDs, respectively. These results indicate that the required energy to activate the non-radiative channels in N-GQDs

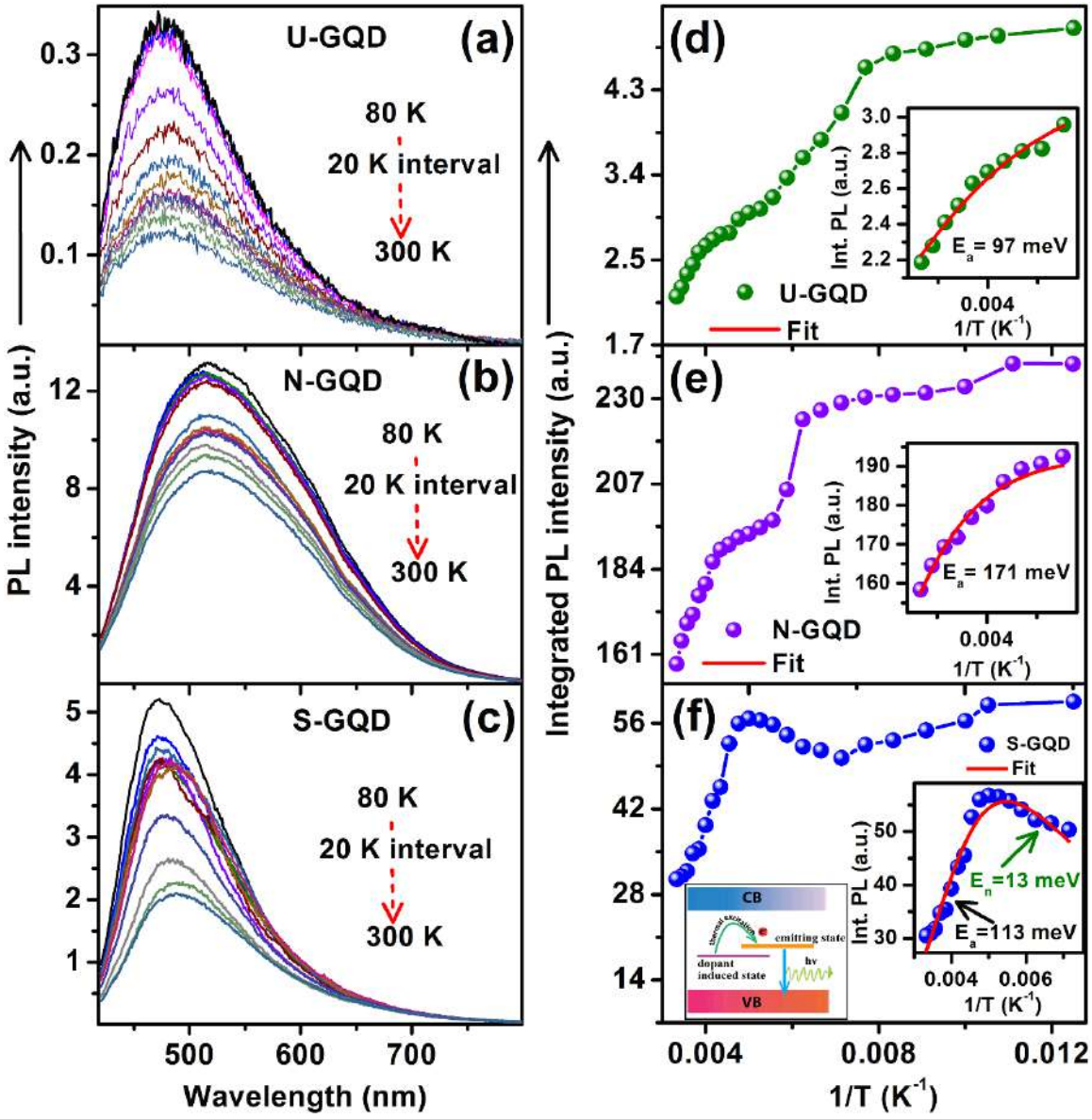

Fig. 3.8. Temperature-dependent PL spectra of (a) U-GQDs, (b) N-GQDs, and (c) S-GQDs. (d-f) The corresponding variation of the integrated intensity of PL as a function of the inverse of temperature. The insets in (d) and (e) show the Arrhenius fitting in the higher temperature region (210–300 K) for U-GQDs and N-GQDs. The inset in (f) shows modified Arrhenius fitting in the temperature range 140–300 K to show PTQ in cooperation with NTQ phenomena in S-GQDs. A band diagram is shown in the inset of (f) to represent the NTQ process.

is very high as compared to U-GQDs, which suppresses the transition to non-radiative channels and most of the photogenerated carriers recombine through radiative channels with subsequent

enhancement of the PL intensity in N-GQDs, consistent with the temperature-dependent intensity results. On the other hand, due to the low value of E_a, the transfer of photogenerated carriers to non-radiative states (defect, functional groups) are highly favorable in U-GQDs. Noticeably, with the change of the temperature from 80 K to 300 K, the PL intensity of U-GQDs and N-GQDs is reduced by ~3.3 and 1.48 times, respectively. This result indicates that the high intense PL in N-GQDs is not only for the high activation energy but also for the presence of a smaller number of non-radiative channels. Interestingly, for S-GQDs, PTQ behavior is observed in the range of 80–130 K and 220–300K. In the intermediate temperature region (140–210 K), the PL intensity of S-GQDs increases with increasing temperature, which is known as negative thermal quenching (NTQ). PTQ along with NTQ can be explained by Shibata model.[42] In the present case, we observed the NTQ behavior in the intermidate to room temperature region,where the Shibata model is reduced to the following equation with the approximation of $E_n << k_BT << E_a$ for single intermidate level:[43]

$$I(T) = \frac{I_0}{1+Ae^{-\frac{E_a}{K_BT}}} \times e^{-\frac{E_n}{K_BT}} \qquad (3.2)$$

The additional term in the numerator of eqn. (3.2) arises due to the NTQ effect, and E_n is the corresponding activation energy. The variation of integrated PL intensity with the inverse of 'T' is fitted with a modified Arrhenius equation for S-GQDs in the region 140–300 K, as shown in the inset of **Fig. 3.8(f)** and the value of E_a and E_n are obtained as ~113 meV and 13 meV, respectively. In the present case, for S-GQDs, the small activation energy (E_n ~13 meV) in NTQ could be assigned as the intersystem barrier for S doped atoms. The NTQ phenomena can be understood from the band diagram in the inset of **Fig. 3.8(f)**. The charge carriers of the dopant induced states migrate to the nearby emitting states with thermal excitation, which produce the radiative emission resulting in higher PL with increasing temperature. Moreover, we have observed that in spite of the presence of electron-donating S atoms in S-GQDs, S-GQDs cannot emit high intense PL like N-GQDs. Thus, we conclude that the presence of a large number of defect states and dopant atoms create a high density of non-radiative sites that are mainly responsible for the low intense PL of S-GQDs at room temperature. Moreover, the low value of E_a in S-GQDs helps easy activation of the non-radiative process as compared to N-GQDs. As compared to U-GQDs, the large value of E_n in S-GQDs may be due to the absence of COOH/OH functional groups in S-GQDs, which are marked as non-radiative sites.

3.3.3.5. Time-Resolved Photoluminescence Study

To investigate the recombination dynamics, each TRPL decay profile is fitted with a bi-exponential decay function, as discussed in **Chapter 2, Section 2.3.3.3**. **Fig. 3.9** shows the TRPL spectra of various samples and the corresponding fitted curve. The values of average lifetimes (τ_{avg}) for U-GQDs, N-GQDs, and S-GQDs are estimated to be ~3.36 ns, 7.58 ns, and 4.53 ns, respectively. The decay components (τ_1 and τ_2) and the corresponding amplitudes along with τ_{avg} of all samples are shown in the inset of **Fig. 3.9**. These two decay components in each sample corresponding to the emission from two energy states, consistent with the steady-state PL analysis (see **Fig. 3.7(b)**). The fast decay component (τ_1) with a lower amplitude can be assigned to the functional groups, and the slow component (τ_2) with higher amplitude is attributed to doping induced states or edge states. Since the doping induced state contributes the maximum in N-GQDs emission, it shows the highest amplitude (~75%) in the TRPL profile.

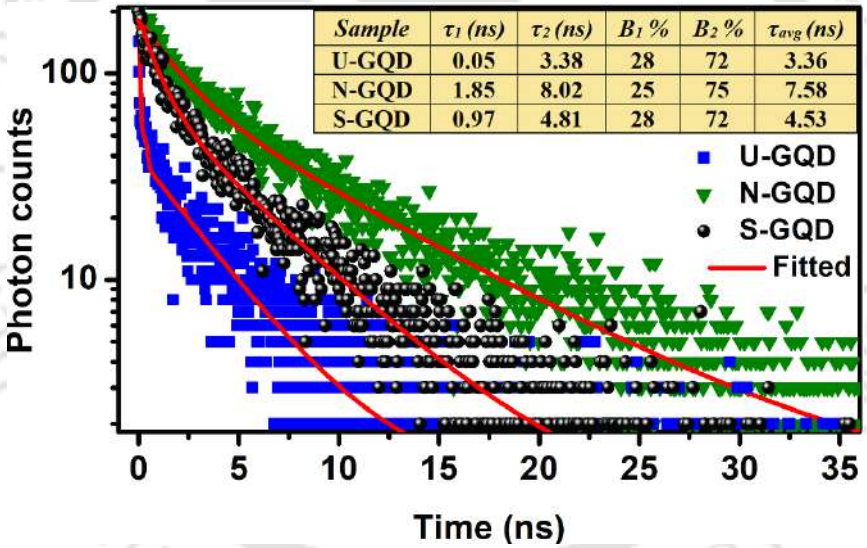

Fig. 3.9. Comparison of the TRPL spectra of U-GQDs, N-GQDs, and S-GQDs with 405 nm laser excitation. The fitted parameters and τ_{avg} value of each spectrum are shown in the inset.

3.3.4. Application of N-GQDs

3.3.4.1. N-GQDs as SERS Substrate

Next, we analyze the performance of the undoped and doped GQDs as SERS substrates for the detection of the ultra-low concentration of RhB in nM level. The SERS effects on U-GQDs, N-GQDs, and S-GQDs substrates are first measured with 514 nm laser excitation in the presence of 10^{-4} M RhB, as shown in **Fig. 3.10(a)**. Interestingly, a significant enhancement in Raman peaks of

RhB at ~1648 cm^{-1}, 1507 cm^{-1}, 1359 cm^{-1}, 1188 cm^{-1}, and 766 cm^{-1} are observed on N-GQDs substrate, and a tiny signal appears at ~1648 cm^{-1} and 1507 cm^{-1} with U-GQDs substrate, while S-GQDs do not show any measurable SERS signal. Different Raman modes of bare RhB (10^{-2} M) on Si substrate are shown in **Fig. 3.10(b).** Based on the high SERS signal, N-GQDs coated on Si substrate are optimized with different laser excitation for better result. **Fig. 3.10(c)** shows the Raman signal of RhB (10^{-4} M) at laser excitations 488 nm, 514 nm, and 633 nm, demonstrating

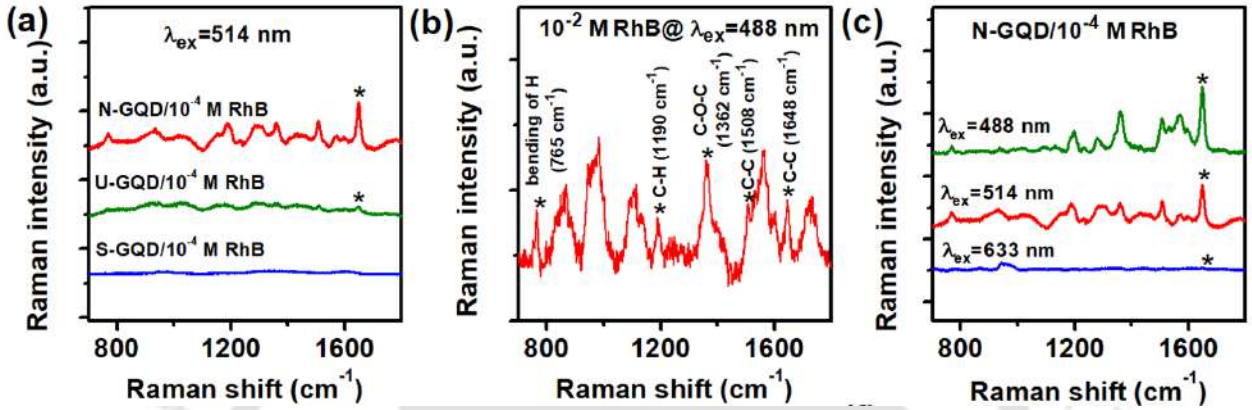

Fig. 3.10. (a) Raman spectra of RhB (10^{-4} M) using U-GQDs, N-GQDs, and S-GQDs as SERS substrates with laser excitation 514 nm, where '*' symbol indicates the SERS enhanced peak of RhB at 1648 cm^{-1}. (b) Raman spectrum of RhB (concentration 10^{-2} M) with different Raman active modes under laser excitation 488 nm. (c) SERS effect at different laser excitation wavelengths for 10^{-4} M RhB on N-GQDs substrate.

the highest enhancement of the SERS signal with 488 nm laser excitation. As a reference at 488 nm laser excitation, the enhancement factor (EF) for N-GQDs is calculated with the following equation:

$$EF = \frac{I_{SERS}}{I_R} \times \frac{C_R}{C_{SERS}} \times \frac{P \times t}{P_{SERS} t_{SERS}} \qquad (3.3.1)$$

where, I_{SERS} and I_R are the Raman intensity at ~1648 cm^{-1} of RhB with and without the presence of N-GQDs at the known concentration of RhB C_{SERS} and C_R, respectively. 'P' represents the laser power, and 't' is the accumulation time. For the present case, 'P' and 't' are the same for Raman and SERS measurement. As the SERS process depends on the effective number of the adsorbed analyte molecules, the eqn. (3.3.1) is modified as

$$EF = \frac{I_{SERS}}{I_R} \times \frac{N_R}{N_{SERS}} \qquad (3.3.2)$$

where N_R is the number of RhB molecules contributing to bulk Raman signal, and N_{SERS} is the number of absorbed RhB molecules contributing to SERS Raman signal. The number of RhB molecules is estimated as:

$$N = \frac{A_{laser}}{A_{substrate}} \times MVN_A \qquad (3.3.3)$$

A_{laser} is the area of the laser spot, and $A_{substrate}$ is that of the substrate. 'V' is the volume of the RhB solution, and 'M' is the molar concentration. For our case, the laser spot (1 μm diameter) and the size of the substrate (0.5cm × 0.5 cm) are identical for SERS and Raman measurements. For both measurements, the volume of the RhB solution is used as 20 μL. Assuming the uniform distribution of the RhB solution on the substrate,

$$\frac{N_R}{N_{SERS}} = \frac{M_R}{M_{SERS}} \qquad (3.3.4)$$

where, M_R and M_{SERS} are the molar concentration of RhB for Raman and SERS measurement, respectively. For the calculation of EF in the present case, the values of M_R and M_{SERS} are 10^{-2} M and 10^{-4} M, respectively. Thus,

$$EF = \frac{I_{SERS}}{I_R} \times \frac{M_R}{M_{SERS}} \qquad (3.3.5)$$

With I_{SERS}/I_R ~3.2 at ~1648 cm^{-1}, the value of EF is obtained as ~3.2×10^3 for 488 nm excitation. A comparison of the SERS performance of different carbon-based substrates with the present work is presented in **Table 3.4**. Thus, the enhancement factor for this N-GQDs substrate is the highest among the reported values without plasmonic components.

Table 3.4. *Comparison of SERS performance of different carbon-based substrates with the present work.*

SERS Substrate	*Laser excitation (nm)*	*Value of EF*	*Mechanism of Enhancement*	*LOD (nM)*	*Ref.*
GQDs	532	4.3×10^2	CM	1	[3]
GQD assembled Nanotubes	633	6.9×10^1	CM	1	[23]
Oxidized graphene	514	1.7×10^3	CM	-	[20]
Au NP–graphene–Ag NP hybrid	532	1.0×10^9	EM & CM	0.0001	[44]
Ag-RGO	633	1.0×10^7	EM & CM	0.1	[45]
N-GQDs	488	3.2×10^3	CM and FRET	0.1	***This work***

3.3.4.1.1. Mechanism of SERS Enhancement

The SERS enhancement mechanisms are reported mainly to be contributed by the electromagnetic enhancement (EM) and CM factors, where EM arises due to the localized electromagnetic field mainly in the presence of metallic components and CM involves the charge transfer phenomena. [3, 23] For GQDs, large surface area with accessible edges and dangling bonds can lead to effective adsorption of target molecules. In the present case, the possible reasons for the performance of N-GQDs as efficient SERS substrate are as follows. The π–π staking between the graphene and absorbed molecules could shorten the distance between the molecules and the substrate, which could facilitate an efficient charge transfer from substrate to target molecules.[46] Among all types of synthesized GQDs, the sp^2 domain in N-GQDs acquires the highest electronic charge contents, which facilitate maximum charge transfer to the target molecules by π–π interaction. Due to the high absorption of RhB, the strongest SERS signal was observed previously with 514 nm laser excitation.[47] In the present case, 488 nm laser excitation shows higher efficiency than 514 nm excitation for SERS enhancement. This is very likely to be related to the FRET process from N-GQDs to RhB. To clarify the contribution of the FRET process with RhB, the MB target (concentration 10^{-3} M) is also tested on the different types of GQDs for the SERS enhancement effect, as shown in **Fig. 3.11(a)** with 488 nm excitation. Although MB has aromatic structure, a low EF of SERS signal is observed with all kinds of the GQDs substrates, which reveals that the π–π interaction is not the only mechanism for the SERS signal in N-GQDs. Interestingly, the PL emission peak of N-GQDs (at excitation 488 nm) coincides with the absorption peak of RhB, while the absorption of MB is far away, as shown in **Fig. 3.11(b)**. Thus, due to overlap of the emission energy of donor (N-GQDs) with the absorption energy of acceptor molecule (RhB), and their close interaction, FRET is most likely to take place between N-GQDs and RhB. Thus, 488 nm excitation shows the highest EF in this donor-acceptor pair, and the EF mechanism is essentially of chemical nature, i.e., CM type. Note that among differently prepared N-GQDs substrates, N-GQDs prepared with 15 mg/mL GO concentration shows the maximum enhancement (see **Fig. 3.11(c)**). Interestingly, the same sample shows the highest PL intensity as well. This reveals the excited-state charge/energy transfer from N-GQDs to target molecules (RhB) is primarily responsible for the SERS enhancement in the present case, and this could be due to the radiative functional groups in N-GQDs. However, the contribution of EM enhancement, if any, cannot be ruled out entirely from the above observation. To ascertain the contribution of the functional groups in the SERS

enhancement, N-GQDs substrates are subjected to vacuum annealing at different temperatures (~200 °C, 400 °C and 600 °C) for 2 h to systematically control and eliminate only the functional groups.[37, 48] Remarkably, with increasing annealing temperature of N-GQDs substrate, the EF of 10^{-4} M RhB for 1648 cm^{-1} peak goes down systematically under 488 nm laser excitation, as shown in **Fig. 3.11(d)**. The inset shows the corresponding SERS spectra on annealed N-GQDs substrates at different temperatures. The reduction of the functional groups from N-GQDs by vacuum annealing reduces the energy transfer from N-GQDs to RhB in the FRET process. Thus, in the

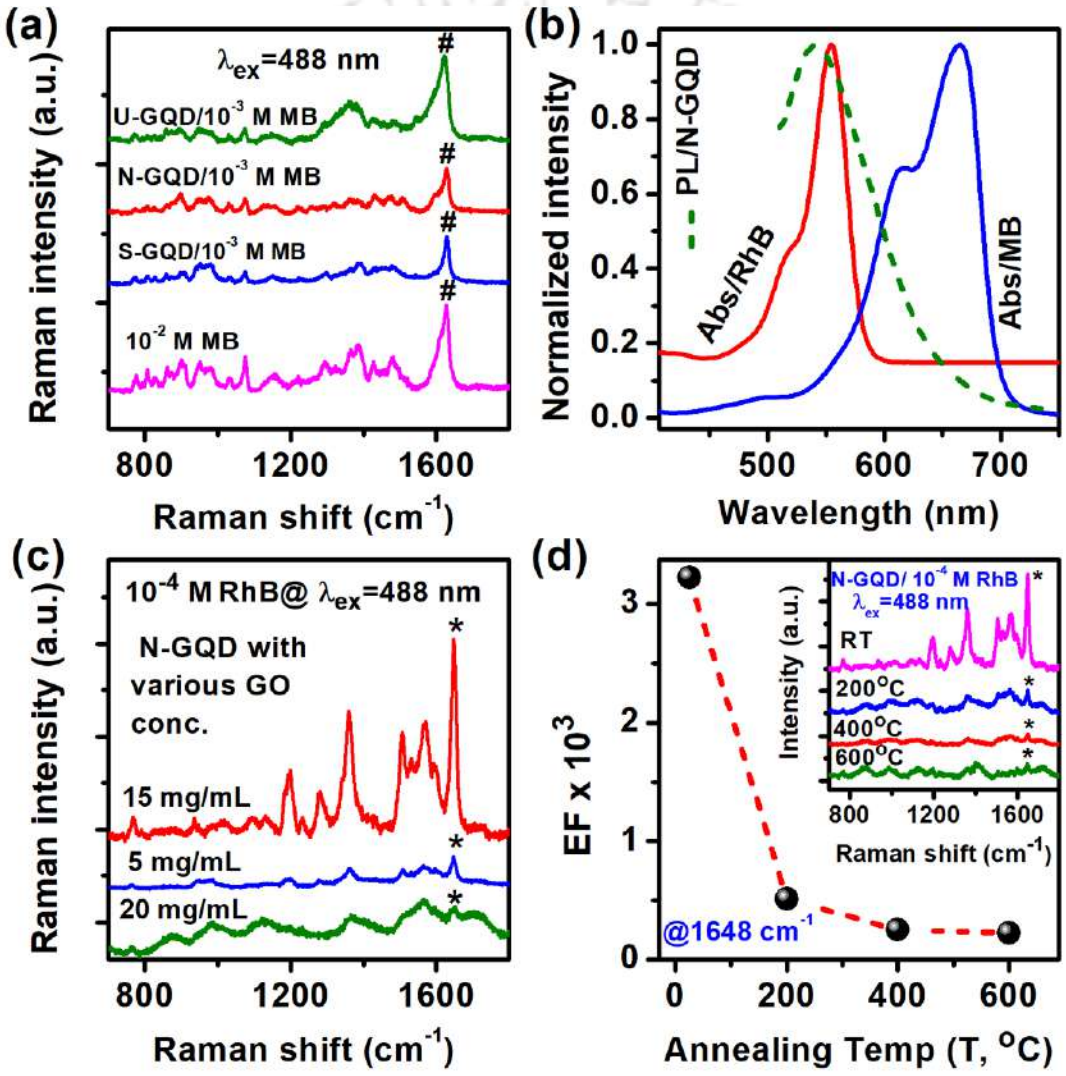

Fig. 3.11. (a) SERS effect with 10^{-3} M concentration of MB target using U-GQDs, N-GQDs, and S-GQDs as SERS substrates. '#' indicates the SERS peak of MB being monitored with 488 nm excitation. (b) Normalized PL spectrum of N-GQDs (0.2 mg/mL) with excitation 488 nm and the absorption spectra of RhB and MB with concentration 10^{-5} M. The overlap of spectra indicates the possibility of FRET between N-GQDs and RhB. (c) Comparison of SERS enhancement on N-GQDs substrate prepared with different proportions of GO precursor. (d) The change of the EF value as a function of annealing temperatures for N-GQDs substrates; the corresponding Raman spectra are shown in the inset.

present case, the π–π interaction and the functional groups both contribute to the SERS enhancement on N-GQDs substrate with the RhB target. With 633 nm laser excitation (see **Fig. 3.10(c)**), EF is calculated as ~10^2 for 10^{-4} M concentration of RhB at 1648 cm^{-1} peak, which is ~32 times lower than that of the 488 nm excitation. As there is no possibility of FRET between N-GQDs and RhB at 633 nm excitation, the SERS enhancement with 633 nm excitation must be only due to the π–π interaction. Thus, the contribution of FRET to SERS enhancement is only ~32, and that of CM is 10^2 yielding an overall enhancement of ~3.2x10^3. This confirms the combined contribution of CM interaction and FRET for the observed SERS enhancement with N-GQDs. In the case of U-GQDs and S-GQDs, due to the low PL intensity, the FRET process is less efficient, and hence overall SERS enhancement is low. Note that due to the semiconducting nature and spherical shape of GQDs, electromagnetic contribution to the observed SERS in the visible region of wavelength is negligible.[49]

3.3.4.1.2. N-GQDs SERS Substrate as Sensor

Based on the above discussion, the N-GQDs substrate is implemented to detect a very low concentration of RhB in nM level. **Fig. 3.12(a)** shows the systematic enhancement of the

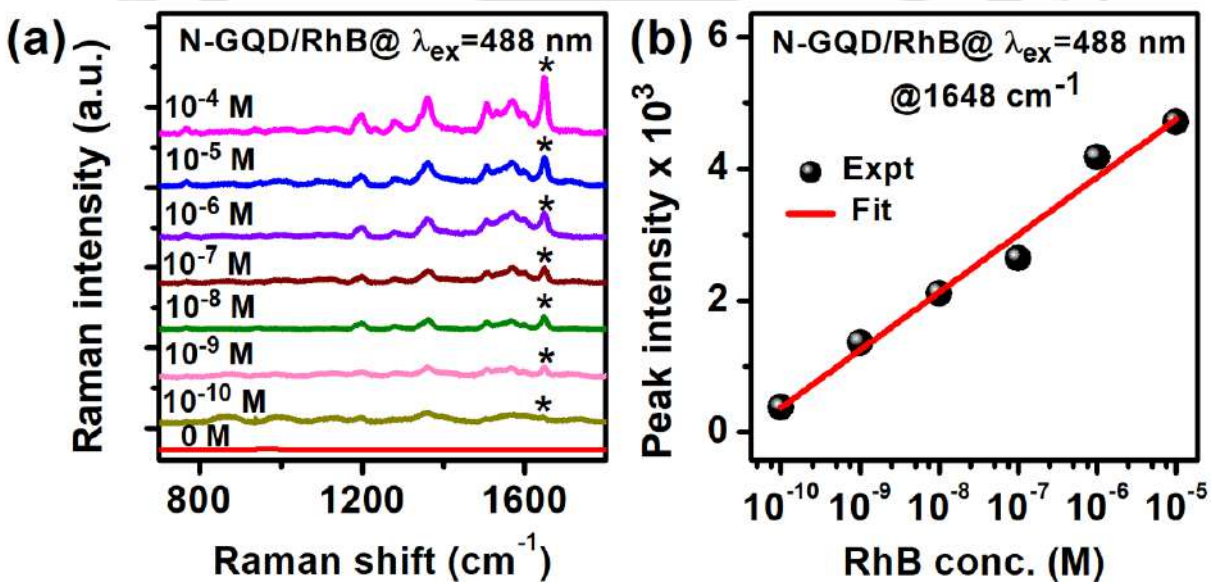

Fig. 3.12. (a) Concentration-dependent changes in the SERS signal intensity of RhB target on N-GQDs substrate, where '*' symbol indicates the SERS enhanced peak of RhB at 1648 cm^{-1}. (b) The variation of Raman intensity of 1648 cm^{-1} peak with the logarithm of RhB concentration shows a linear variation in the range 10^{-10}–10^{-5} M.

characteristic Raman peaks of RhB with increasing concentration of RhB in the range10^{-10}–10^{-4} M. The variation of Raman peak intensity at ~1648 cm^{-1} follows a linear nature with the log of

RhB concentration, as presented in **Fig. 3.12(b)**. We achieve a detection limit down to 0.1 nM, which is superior to the previous reports with GQDs substrate, as presented in **Table 3.4**.

3.3.4.2. N-GQDs for Liquid Phase White LED Fabrication

Since the N-GQDs exhibit strong bluish-green emission with high QY, N-GQDs are demonstrated here as an excellent light convertor. In the literature, GQDs was used as a light converter in the form of a layer coating.[4, 50] The coating of the GQD layer usually gives rise to aggregation-induced quenching of the fluorescence during the deposition of the GQDs solution on to a substrate, and the resulting intensity of light emission are low. To avoid the quenching effect, we consider the fabrication of the liquid phase WLED with N-GQDs and then go on to demonstrate WLED with

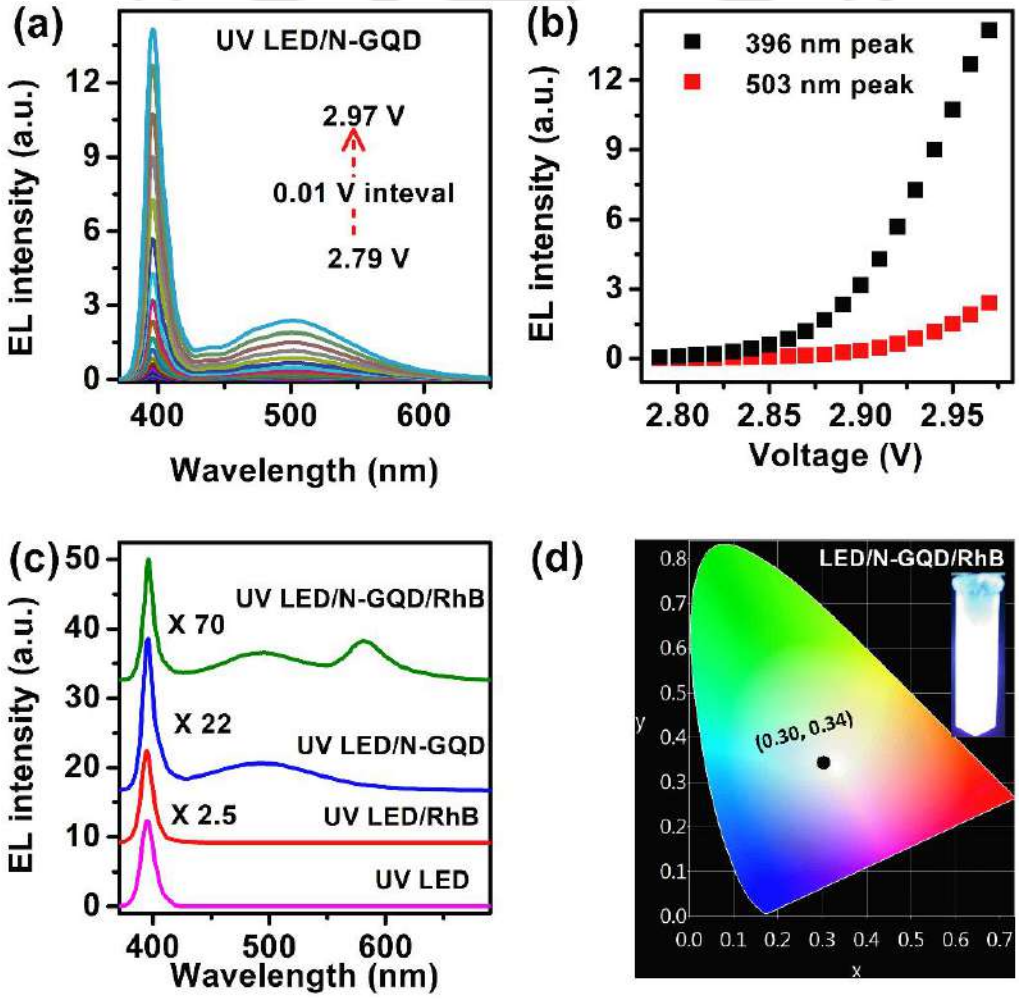

Fig. 3.13. (a) EL spectra of N-GQDs with the incorporation of low-cost UV LED under different bias voltages (2.79-2.97 V) and (b) the corresponding variation of EL intensity as a function of bias voltage for emission peaks at ~396 nm and 503 nm, which follow a nonlinear nature. (c) The comparison of the EL spectra of UV LED/N-GQDs in the absence and presence of 50 μM RhB at ~2.85 V. (d) CIE coordinate of UV LED/N-GQDs/RhB system and a digital photograph of liquid phase WLED in the inset.

high color purity by combining pink luminescent RhB. The EL spectra of the as-prepared UV LED/N-GQDs were recorded at different bias voltages in the range ~2.79–2.97 V, as shown in **Fig. 3.13(a)**. With increasing bias voltage, the variation of the EL intensity of UV LED centered at ~396 nm and the broad EL spectrum of N-GQDs with a peak at ~503 nm both follow a nonlinear nature (see **Fig. 3.13(b)**) in the liquid phase. **Fig. 3.13(c)** represents the comparative EL spectra of N-GQDs with the addition of 50 μM RhB at a constant voltage of ~2.85 V. **Fig. 3.13(d)** represents the CIE chromaticity coordinates and a digital photograph of liquid WLED with UV LED/N-GQDs/RhB system. With N-GQDs, the CIE coordinate of UV LED change from (0.17, 0.01) to (0.18, 0.26), demonstrating the light converting capability of N-GQDs. For the demand of WLED, the addition of RhB with the above system change the CIE coordinate from (0.18, 0.26) to (0.30, 0.34). Hence UV LED is successfully converted into pure WLED with a mixed solution. With the externally applied voltage, the emission of UV LED transfers to N-GQDs, which is confirmed from the reduction in the EL intensity at ~396 nm by ~12.3 times at the applied bias ~2.85 V (see **Fig. 3.13(c)**). The addition of RhB in the solution of N-GQDs reduces the EL intensity ~50 times at ~396 nm and increases the visible light emission. Moreover, the EL intensity of N-GQDs at ~503 nm is also decreased ~3 times by the FRET process. Thus, a series of energy transfer takes place in the following sequence: UV LED to N-GQDs and then to RhB, which establishes N-GQDs as an efficient color converter. By further tuning the mixing ratio of N-GQDs and RhB, the high purity WLED with CIE coordinate (0.33, 0.33) could be achieved in the liquid phase.

3.4. Summary and Conclusions

In this chapter, we presented a thorough discussion on the origin of PL emission in GQDs with a comparative study of structural and optical features of U-GQDs, N-GQDs, and S-GQDs synthesized by the solvothermal method. Next, N-GQDs was utilized as an efficient SERS substrate for the detection of RhB in nM level and light converting material for the fabrication of liquid phase WLED. The essential findings of this chapter are summarized below.

1. N-GQDs yield the highest PL QY due to the presence of electron-donating N atoms, while a comparatively low-intensity PL in S-GQDs is due to the presence of electron-withdrawing S=O functional groups.

2. N-GQDs substrate show SERS enhancement factor ~3.2×10^3 with 10^{-4} M RhB target molecule under 488 nm laser excitation with a limit of detection 0.1 nM due to combined effect of π–π interaction and FRET process.
3. The quantitative analysis of the individual contribution of both π–π interaction and FRET process are evaluated by comparing different target molecules, laser excitation wavelengths, and controlling the functional groups of N-GQDs through vacuum annealing.
4. Due to light converting ability, highly fluorescent N-GQDs are successfully utilized for the fabrication of a liquid phase WLED with the help of a low-cost UV LED and fluorescent RhB.

References

1. R. Das, G. Rajender and P. K. Giri, *Phys. Chem. Chem. Phys.*, 2018, **20**, 4527-4537.
2. S. Yang, J. Sun, X. Li, W. Zhou, Z. Wang, P. He, G. Ding, X. Xie, Z. Kang and M. Jiang, *J. Mater. Chem. A*, 2014, **2**, 8660-8667.
3. D. Liu, X. Chen, Y. Hu, T. Sun, Z. Song, Y. Zheng, Y. Cao, Z. Cai, M. Cao and L. Peng, *Nat. Commun.*, 2018, **9**, 193.
4. L. Tang, R. Ji, X. Cao, J. Lin, H. Jiang, X. Li, K. S. Teng, C. M. Luk, S. Zeng and J. Hao, *ACS Nano*, 2012, **6**, 5102-5110.
5. S. Li, Y. Li, J. Cao, J. Zhu, L. Fan and X. Li, *Anal. Chem.*, 2014, **86**, 10201-10207.
6. S. Zhu, J. Zhang, S. Tang, C. Qiao, L. Wang, H. Wang, X. Liu, B. Li, Y. Li and W. Yu, *Adv. Funct. Mater.*, 2012, **22**, 4732-4740.
7. Y. Yang, X. Wang, G. Liao, X. Liu, Q. Chen, H. Li, L. Lu, P. Zhao and Z. Yu, *J. Colloid Interface Sci.*, 2018, **509**, 515-521.
8. Z. Chen, C. Wu, Z. Zhang, W. Wu, X. Wang and Z. Yu, *Chin. Chem. Lett.*, 2018, **29**, 1601-1608.
9. P. Zhao, Q. Xu, J. Tao, Z. Jin, Y. Pan, C. Yu and Z. Yu, *WIREs Nanomed Nanobiotechnol*, 2018, **10**, e1483.
10. S. Lu, G. Xiao, L. Sui, T. Feng, X. Yong, S. Zhu, B. Li, Z. Liu, B. Zou and M. Jin, *Angew. Chem. Int. Ed.*, 2017, **56**, 6187-6191.
11. S. Lu, L. Sui, J. Liu, S. Zhu, A. Chen, M. Jin and B. Yang, *Adv. Mater.*, 2017, **29**, 1603443-1603449.
12. Q. Wang, S. Zhang, B. Wang, X. Yang, B. Zou, B. Yang and S. Lu, *Nanoscale Horiz.*, 2019, **4**, 1227-1231.
13. Y. Wang and A. Hu, *J. Mater. Chem. C*, 2014, **2**, 6921-6939.
14. R. Das, K. K. Paul and P. K. Giri, *Appl Surf Sci*, 2019, **490**, 318-330.

15. F. A. Permatasari, A. H. Aimon, F. Iskandar, T. Ogi and K. Okuyama, *Sci. Rep.*, 2016, **6**, 21042.
16. S. Khan, A. Gupta, N. C. Verma and C. K. Nandi, *Nano Lett.*, 2015, **15**, 8300-8305.
17. X. Niu, Y. Li, H. Shu and J. Wang, *Nanoscale*, 2016, **8**, 19376-19382.
18. R. Sekiya, Y. Uemura, H. Naito, K. Naka and T. Haino, *Chem.: Eur. J.*, 2016, **22**, 8198-8206.
19. G. Rajender, U. Goswami and P. K. Giri, *J. Colloid Interface Sci.*, 2019, **541**, 387-398.
20. S. Huh, J. Park, Y. S. Kim, K. S. Kim, B. H. Hong and J.-M. Nam, *ACS Nano*, 2011, **5**, 9799-9806.
21. P. Wang, M. Xia, O. Liang, K. Sun, A. F. Cipriano, T. Schroeder, H. Liu and Y.-H. Xie, *Anal. Chem.*, 2015, **87**, 10255-10261.
22. J. Ju, W. Liu, C. M. Perlaki, K. Chen, C. Feng and Q. Liu, *Sci. Rep.*, 2017, **7**, 6917.
23. H. Cheng, Y. Zhao, Y. Fan, X. Xie, L. Qu and G. Shi, *Acs Nano*, 2012, **6**, 2237-2244.
24. R. Ghosh, K. Imakita, M. Fujii and P. K. Giri, *Phys. Chem. Chem. Phys.*, 2016, **18**, 7715-7727.
25. J. W. Suk, R. D. Piner, J. An and R. S. Ruoff, *ACS nano*, 2010, **4**, 6557-6564.
26. T. Dey, S. Mukherjee, A. Ghorai, S. Das and S. K. Ray, *Carbon*, 2018, **140**, 394-403.
27. J. Feng, H. Dong, B. Pang, F. Shao, C. Zhang, L. Yu and L. Dong, *Phys. Chem. Chem. Phys.*, 2018, **20**, 15244-15252.
28. X. Li, S. P. Lau, L. Tang, R. Ji and P. Yang, *Nanoscale*, 2014, **6**, 5323-5328.
29. D. Qu, Z. Sun, M. Zheng, J. Li, Y. Zhang, G. Zhang, H. Zhao, X. Liu and Z. Xie, *Adv. Opt. Mater.*, 2015, **3**, 360-367.
30. Q. Liu, B. Guo, Z. Rao, B. Zhang and J. R. Gong, *Nano Lett.*, 2013, **13**, 2436-2441.
31. J.-L. Li, K. N. Kudin, M. J. McAllister, R. K. Prud'homme, I. A. Aksay and R. Car, *Phys. Rev. Lett.*, 2006, **96**, 176101.
32. D. Yang, A. Velamakanni, G. Bozoklu, S. Park, M. Stoller, R. D. Piner, S. Stankovich, I. Jung, D. A. Field and C. A. Ventrice Jr, *Carbon*, 2009, **47**, 145-152.
33. C. Zhu, S. Yang, G. Wang, R. Mo, P. He, J. Sun, Z. Di, N. Yuan, J. Ding and G. Ding, *J. Mater. Chem. C*, 2015, **3**, 8810-8816.
34. H. Ren, D. D. Kulkarni, R. Kodiyath, W. Xu, I. Choi and V. V. Tsukruk, *ACS Appl. Mater. Interfaces*, 2014, **6**, 2459-2470.
35. J. Gliniak, J. H. Lin, Y. T. Chen, C. R. Li, E. Jokar, C. H. Chang, C. S. Peng, J. N. Lin, W. H. Lien and H. M. Tsai, *ChemSusChem*, 2017, **10**, 3260-3267.
36. S. H. Jin, D. H. Kim, G. H. Jun, S. H. Hong and S. Jeon, *ACS Nano*, 2013, **7**, 1239-1245.
37. G. Rajender and P. K. Giri, *J. Mater. Chem. C*, 2016, **4**, 10852-10865.
38. R. Zhang, J. R. Adsetts, Y. Nie, X. Sun and Z. Ding, *Carbon*, 2018, **129**, 45-53.
39. D. Qu, M. Zheng, J. Li, Z. Xie and Z. Sun, *Light Sci. Appl.*, 2015, **4**, e364.
40. S. Parveen, K. K. Paul, R. Das and P. K. Giri, *J. Colloid Interface Sci.*, 2019, **539**, 619-633.
41. A. Bora, L. P. Mawlong, R. Das and P. K. Giri, *J. Colloid Interface Sci.*, 2019, **561**, 519-532.
42. Shibata, Hajime, *Jpn. J. Appl. Phys., (1998), 37, 550*.
43. T. Makino, K. Tamura, C. Chia, Y. Segawa, M. Kawasaki, A. Ohtomo and H. Koinuma, J. Appl. Phys., 2003, 93, 5929-5933.
44. Y. Zhao, W. Zeng, Z. Tao, P. Xiong, Y. Qu and Y. Zhu, *ChemComm*, 2015, **51**, 866-869.

45. Z.-X. Yan, Y.-L. Zhang, W. Wang, X.-Y. Fu, H.-B. Jiang, Y.-Q. Liu, P. Verma, S. Kawata and H.-B. Sun, *ACS Appl. Mater. Interfaces*, 2015, **7**, 27059-27065.
46. X. Ling, L. Xie, Y. Fang, H. Xu, H. Zhang, J. Kong, M. S. Dresselhaus, J. Zhang and Z. Liu, *Nano Lett.*, 2009, **10**, 553-561.
47. R. Ghosh, J. Ghosh, R. Das, L. P. Mawlong, K. K. Paul and P. K. Giri, *J. Colloid Interface Sci.*, 2018, **532**, 464-473.
48. S. Samanta, S. Singh and R. R. Sahoo, *New J. Chem.*, 2019, **43**, 2624-2639.
49. A. Polubotko and V. Chelibanov, *Optics and Spectroscopy*, 2017, **122**, 937-943.
50. G. S. Kumar, U. Thupakula, P. K. Sarkar and S. Acharya, *RSC Adv.*, 2015, **5**, 27711-27716.

भारतीय प्रौद्योगिकी संस्थान गुवाहाटी
Indian Institute of Technology Guwahati

Chapter 4

Quantitative Understanding of the Ultra-Sensitive and Selective Detection of Dopamine Using Graphene Oxide/WS_2 Quantum Dot Hybrid

In this present chapter, we report on the highly sensitive and selective detection of dopamine (DA) at pico-molar (pM) level by a low-cost sensing platform based on graphene oxide (GO) sheets anchored with tungsten disulfide quantum dots (WS_2 QDs). The liquid phase exfoliated WS_2 QDs are mostly bilayer type with an average particle size ~2.0, while the GO sheets are of few-layer thickness. The WS_2 QDs are highly luminescent with PL QY of ~15%, and they exhibit an excitation wavelength-dependent spectral shift in the PL emission due to the high degree of edge/defect states. In the presence of GO, the PL intensity of WS_2 QDs partially quenches due to the van der Waals interaction and excited-state charge transfer from WS_2 QDs to GO. However, in the presence of DA, a drastic quenching of the PL intensity occurs in GO/WS_2 hybrid, and this enables selective detection of DA as low as 10 pM, which is the lowest among the reported values. We present a new model to quantitatively explain the GO mediated efficient charge transfer and anomalous quenching of the PL intensity as the function of DA concentration. Finally, the GO/WS_2 based sensor is utilized for the detection of DA in the river water and blood serum with a satisfactory recovery, which establishes its practical utility as an efficient environmental and biochemical sensor.

4.1. Introduction

Dopamine, an organic compound of the catecholamine group and an important neurotransmitter, plays a vital role in many behavioral responses and functions of the mammalian central nervous system, metabolism, cardiovascular, renal, and hormonal systems.[1-4] As a chemical messenger, DA is involved in various neural signaling pathways as well as brain functions. The normal level of DA in the human body lines in the range 10–1000 nM, which maintains blood pressure, excellent motor activity, inspiration, intuition, and focus, while the presence of abnormal or insufficient DA causes severe neural diseases, such as Huntington's disease, Parkinson's disease, and schizophrenia.[1, 2, 5-8] Excess concentration of DA in the human body is responsible for

schizophrenia, addiction, difficulty in sleeping, hallucinations, etc. On the other side, deficiency of DA is one of the main reasons for Parkinson's disease, depression, less motivation, and enthusiasm, poor coordination, etc. For example, Phung et al. reported 86% lower concentration of DA than that of the healthy human body, who was suffering from antipsychotic drug-induced Parkinson's disease.[9] Thus, for the diagnosis of the DA deficiency symptoms, reliable and selective detection of DA in the human blood sample with pM level sensitivity is very important. Recently several analytical methods have been developed for the detection of DA, such as high-performance liquid chromatography,[10] capillary electrophoresis,[11] electrochemical,[2, 3] fluorescence sensors,[1, 7, 12] colorimetric sensors,[1, 6] SERS spectroscopy,[13] etc. Although several reports have been published to date on DA detection,[4, 14-16] ultra-high level of sensitivity and high selectivity in DA sensing along with a proper insight into the mechanism of sensing are still lacking in the literature. A quantitative understanding of the sensing performance is imperative to develop a practical DA sensor for everyday use.

WS_2 QDs, the semiconducting material with atomically thin layers in the group of transition metal dichalcogenides, are drawing enormous research attention due to their unique electronic structures and optical properties.[4, 14, 17] Fundamentally, WS_2 consists of the covalently bonded 2D building of S-W-S layers, where each of these layers is weakly bonded to each other via van der Waals forces. When 2D WS_2 nanosheets are confined into 0D by mechanical or chemical treatments,[17, 18] they exhibit a tunable optical bandgap together with high PL yield due to the quantum confinement of carriers and edge effects.[4, 14, 17] Owing to the tunable bandgap with defective states and functional groups, WS_2 QDs are reported to exhibit excitation wavelength-dependent PL emission with high QY.[4, 17, 19]As a consequence of their excellent luminescent property and non-toxic nature,[20] WS_2 QDs have been recently recognized as a promising material for optical imaging and fluorescence sensing in the biomedical field.[4, 14, 20, 21] However, the sensitivity of DA sensing by WS_2 QDs so far has been rather low.[4, 14] Developing biosensors that can discriminate DA from DA derivatives, such as epinephrine and norepinephrine with high sensitivity and selectivity continues to be a challenge.

GO is a 2D hexagonal lattice of carbon atoms with the presence of high density of oxygen functional groups in the basal planes and edges.[21-23] Due to the aromatic structure, GO is reported as an efficient adsorbent of other aromatic molecules through π–π interaction,[23, 24] and the high

density of its oxygen functional groups helps in the hydrogen bond interactions.[24] Recently, the strong interaction between active sites of SWCNTs and the defect states of WS_2 QDs has been reported.[17] GO, being a defect rich layered structure, can interact with WS_2 QDs in a similar manner. Based on the above, we study the interaction between the GO and WS_2 QDs and exploit the GO/WS_2 hybrid for the detection of DA with ultra-high sensitivity and selectivity by PL quenching of the hybrid. Therefore, the unusual nature of the PL quenching of GO/WS_2 hybrid is explained for a wide range of concentrations of DA (1 nM–10 μM) through the combined process of non-fluorescence complex formation and charge transfer dynamic. Furthermore, the sensing of the spiked DA in the Brahmaputra river water and the human blood serum is successfully achieved with the newly proposed GO/WS_2 hybrid sensor.

4.2. Experimental Details

4.2.1. Sample Preparation

4.2.1.1. Synthesis of Graphene Oxide

The synthesis of GO was carried out by the modified Hummers' method, as discussed in **Chapter 2, Section 2.2.1.1**. Briefly, 3 g expandable graphite flakes and 1.5 g $NaNO_3$ were mixed with 70 mL concentrated H_2SO_4 under continuous stirring for 2 h. Then, 9 g of $KMnO_4$ was added slowly in the above mixture for the oxidation of the graphite flakes. Afterward, MQ water was added at 98 °C, and then the solution was quenched with H_2O_2. MQ water was further added with the mixture to dilute the acidic parts. Finally, the GO was separated by centrifugation at 10,000 rpm.

4.2.1.2. Synthesis of WS_2 QDs

WS_2 QDs were synthesized by a simple top-down liquid-phase exfoliation method following the protocol reported earlier.[17] In brief, 80 mg WS_2 powder (Sigma Aldrich, 99 %) was mixed with 80 mL N-methyl-2-pyrrolidinone (NMP, Alfa Aesar, 95%). For the exfoliation of WS_2, the mixed solution was kept under tip-sonication (Sonic Ruptor 250, Omni International) for 15 h. Thereafter, the supernatant part of the solution was collected as WS_2 QDs by centrifugation at 12,000 rpm for 30 min in two cycles. After the evaporation of the solvent, the WS_2 QDs were re-dispersed in the water at a concentration of 1 mg/mL for further experiments.

4.2.2. Sensing of Dopamine with GO/WS_2 Hybrid

The detection of DA (Sigma Aldrich, 98%) was performed in a PBS buffer solution at pH 12. For the preparation of GO/WS_2 hybrid, WS_2 QDs aqueous solution (8.4 μg/mL) was mixed with different concentrations of GO solutions (0.05–0.5 mg/mL) under ultrasonication process in a 1:1 ratio to monitor the nature of PL quenching of WS_2 QDs caused by the GO. Next, for the sensing of DA, the quenching efficiency was optimized for GO/WS_2 hybrid by varying the GO concentration with 8.4 μg/mL WS_2 QDs solution and a fixed concentration of DA. In a typical run, 1 mL of stock solution of GO/WS_2 hybrid and 1 mL of DA solution of different concentrations, ranging from 10^{-5}–10^{2} μM, are mixed. All PL spectra are recorded under the excitation of 400 nm. Repeated measurements were carried out to check the reproducibility of the results.

4.2.3. Characterization Techniques

FESEM, TEM, XRD, Raman, UV-vis, PL, TRPL techniques have been described in **Chapter 2, Section 2.2.3**. For Raman analysis, 488 nm laser excitation was used in the present work, and TRPL spectra were recorded with 405 nm pulse laser excitation. The details of the AFM and XPS techniques have been discussed in **Chapter 3, Section 3.2.4**.

4.3. Results and Discussion

4.3.1. Morphology Studies

To study the morphology of the as-synthesized GO, at first TEM analysis of GO sheets is performed. In the TEM image shown in **Fig. 4.1(a)**, GO appears as a thin sheet-like structure. **Fig. 4.1(b)** shows the lattice fringes with interplanar spacing ~0.41 nm corresponding to (002) plane of GO. Interestingly, the lattice spacing here is a bit higher than that of the conventional (002) planes of graphitic structure, which is due to the high density of oxygen functional groups on the surface of GO sheets along with the displacement of the carbon atoms from original graphitic planes.[25, 26] The presence of oxygen in GO sheet is confirmed from EDX analysis, as discussed in **Chapter 2, Section 2.3.1**. For the investigation of the layer thickness of the synthesized GO sheets, the AFM image of GO is monitored carefully, as shown in **Fig. 4.1(c)**. In the inset of **Fig. 4.1(c)**, the height profile of the large area GO sheet reveals the layer thickness of ~4 nm corresponding to 3–4 layers of GO.[25] As compared to the graphene sheet, a higher thickness of GO sheet is expected due to the presence of oxygen functional groups.[25, 26] For the case of WS_2 QDs, the uniform distribution of the QDs with the particle size of ~2–4 nm is observed from the TEM image in **Fig. 4.1(d)**. The

average particle size is obtained as ~2.0 ± 0.3 nm with a lognormal size distribution of the QDs, as shown in the inset of **Fig. 4.1(d)**. **Fig. 4.1(e)** shows the HRTEM lattice fringes with an interplanar spacing of ~0.27 nm, representing (101) plane of WS_2.[27, 28] The AFM image of the synthesized WS_2 QDs are presented in **Fig. 4.1(f)** with the corresponding height profile in the inset

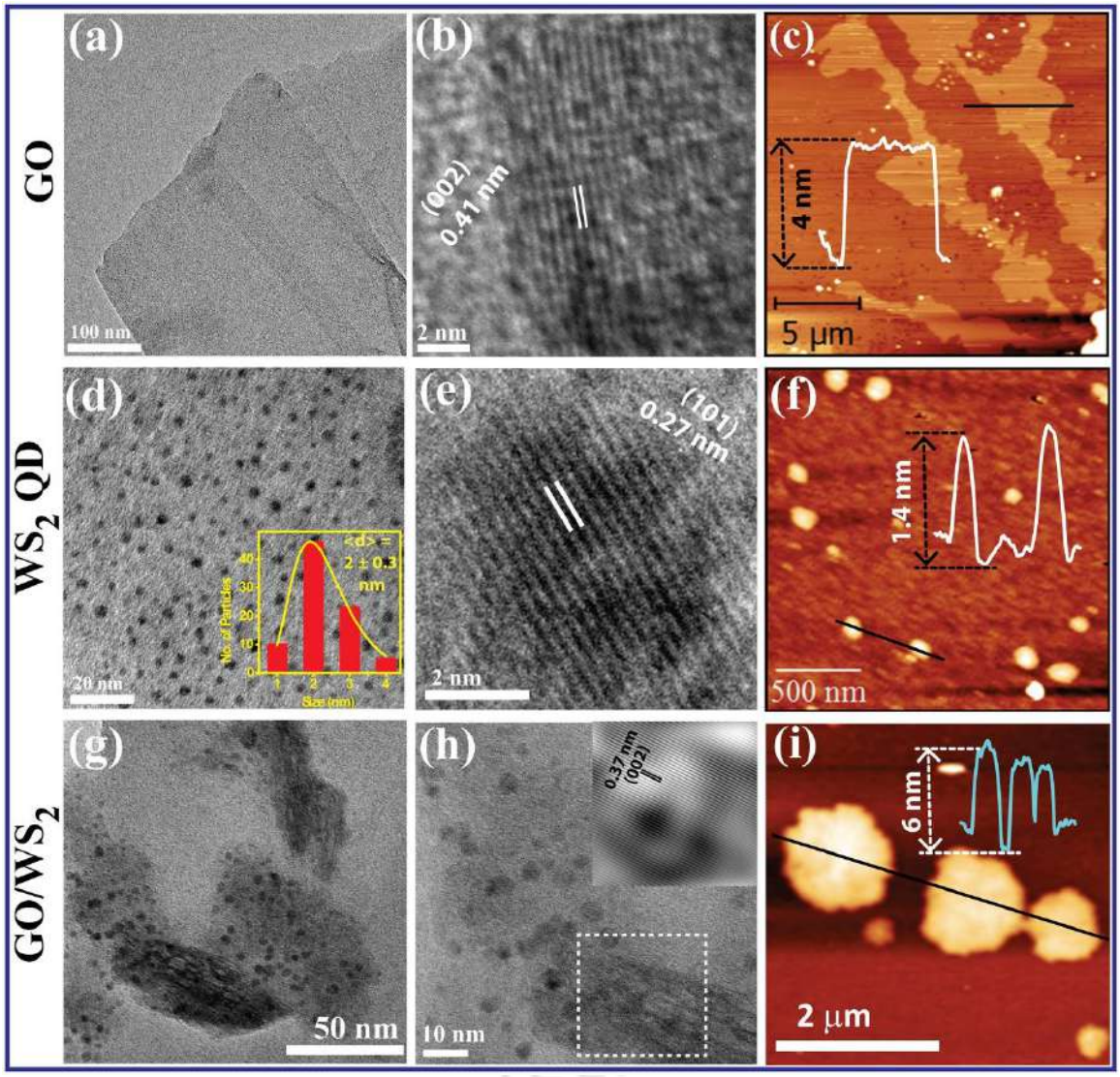

Fig. 4.1. (a) TEM image of GO sheet, and (b) HRTEM image of GO sheet with lattice fringes of (002) graphitic planes. (c) AFM image of the GO sheet with a layer thickness of ~4 nm observed from the height profile, shown as an inset. (d) TEM image of as-prepared WS_2 QDs; the inset shows the size distribution of the QDs with lognormal fitting (solid line). (e) HRTEM lattice fringe image of WS_2 QD showing an interplanar spacing of ~0.27 nm. (f) AFM image of WS_2 QDs with the height profile (inset) showing a bilayer thickness. (g, h) HRTEM image of GO/WS_2 hybrid showing the decoration of WS_2 QDs on GO sheets in different magnifications. The inset of (h) shows the inverse fast Fourier transform (IFFT) image of the lattice fringes of GO in GO/WS_2 hybrid. (i) AFM image of GO/WS_2 hybrid with the corresponding height profile shown in the inset.

and the layer thickness of WS_2 QDs is observed as ~1.4 nm, which confirms that most of the QDs are of bilayer thickness.[17] After the hybrid formation of GO and WS_2 QDs, the morphology of GO/WS_2 hybrid is extensively studied by TEM and AFM images. The HRTEM image of GO/WS_2 hybrid is shown in **Fig. 4.1(g, h)** in different magnifications, which demonstrate a nearly uniform decoration of WS_2 QDs on the GO sheets. The size of the QDs are found to be ~2–4 nm, consistent with the particle size of bare WS_2 QDs, shown in **Fig. 4.1(d)**. Moreover, the inset of **Fig. 4.1(h)** shows the lattice fringes of GO sheet (decorated with WS_2 QDs) with a lattice spacing ~0.37 nm, which corresponds to (002) plane of GO. The AFM image and the corresponding height profile of GO/WS_2 hybrid in **Fig. 4.1(i)** shows the layer thickness of ~5–6 nm, which indicates the combined thickness of bilayer WS_2 QDs on few-layer GO sheets.

4.3.2. Structural Analysis

4.3.2.1. XRD and Raman Analysis

For the structural analysis, the powder XRD patterns of the as-synthesized GO, WS_2 QDs, and their hybrid were recorded, as shown in **Fig. 4.2(a)**. The XRD pattern of GO shows a sharp, intense peak at 2θ ~10.5° corresponding to the characteristic (002) plane of GO.[26] Thus, the interplanar spacing ~0.84 nm, calculated from the XRD pattern of GO, is much higher than that of the precursor graphite flakes (~0.34 nm), as presented in the inset. The high degree of oxidation of graphite flakes introduces a vast number of oxygen functional groups in the graphitic planes, which assist in increasing the interplanar spacing in GO.[26, 29] The appearance of the new diffraction peaks for (100) and (004) planes is attributed to the defective states or functional groups in graphitic materials.[1, 30] In WS_2 QDs, the characteristic peak at 2θ ~14.3° for (002) planes confirms their hexagonal crystalline nature.[27, 31] As compared to (004) planes of WS_2 at 2θ ~27.0°, the low intense peak of (002) planes indicates the formation of the ultrathin structure of WS_2 QDs.[31] Along with the hexagonal planes, the appearance of (006) planes in the XRD pattern signifies the presence of the rhombohedral structure of WS_2.[31] Moreover, (102) and (106) peaks in the XRD pattern are also the signatures of WS_2 content. The XRD pattern of GO/WS_2 hybrid confirms the presence of the graphitic component together with WS_2 in the hybrid. In the hybrid structure, (002) plane of GO appears at 2θ ~12.2° and (004) plane of WS_2 is at 2θ ~25.9°. Interestingly, as compared to the bare GO and WS_2 QDs, the change of the peak position of (002) plane of GO and (004) plane of WS_2 indicate the close contact of GO and WS_2 QDs in GO/WS_2 hybrid.

The comparative Raman spectra of bare GO, WS_2 QDs, and GO/WS_2 hybrid are presented in **Fig. 4.2(b)**. In the as-synthesized GO sample, the characteristic D and G bands at ~1360 cm^{-1} and 1594 cm^{-1}, respectively, are observed in the Raman spectrum.[1, 32] The intensity ratio of D band to G

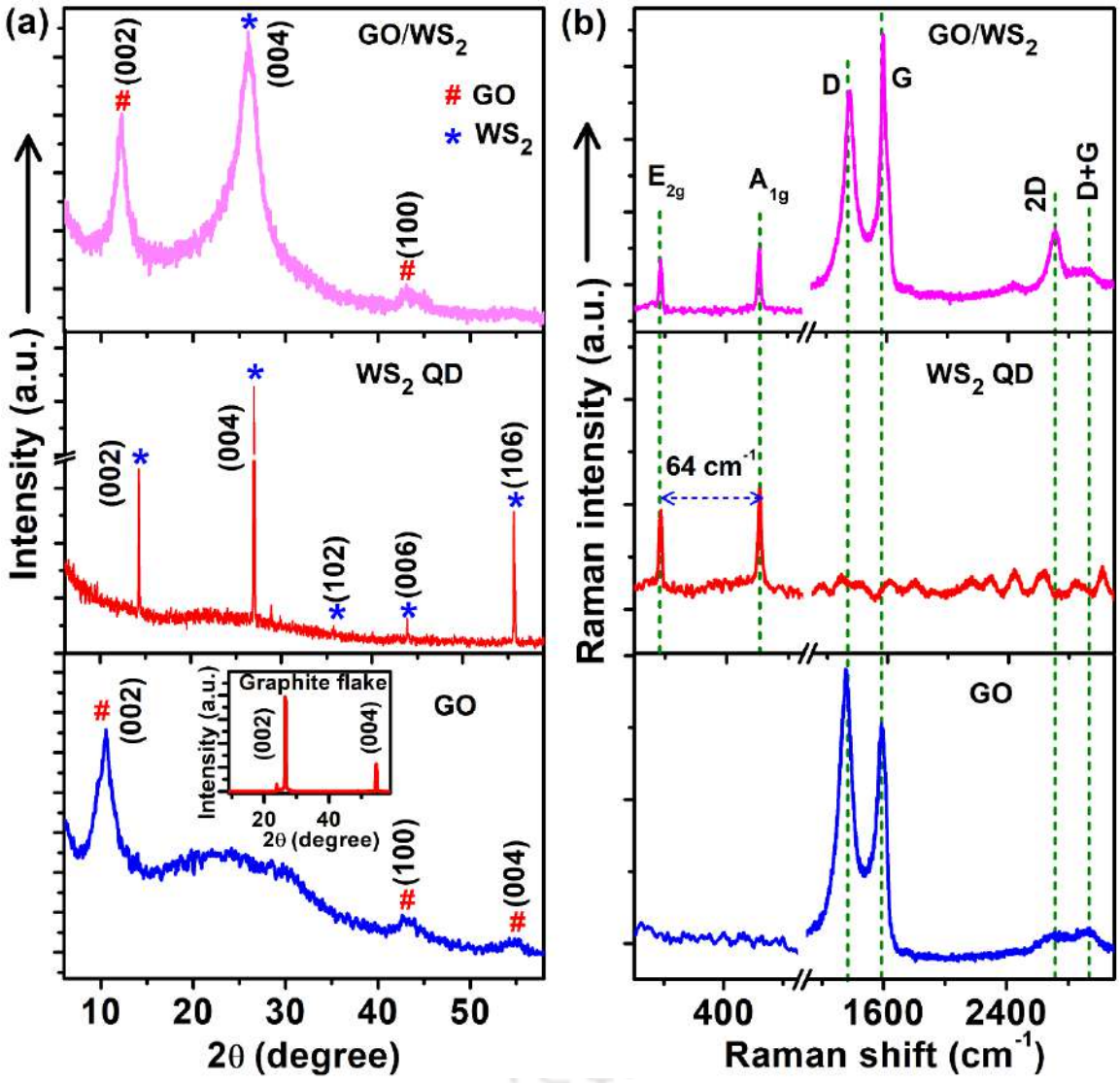

Fig. 4.2. (a) XRD pattern and (b) Raman spectra of as-synthesized GO sheet, WS_2 QDs, and GO/WS_2 hybrid. The inset in (a) shows the XRD pattern of graphite flakes for comparison with GO. The vertical dashed lines indicate the respective peak positions.

band, I_D/I_G ~1.2 is attributed to the high content of defects in the GO sheet.[32] A broad 2D band at ~2743 cm^{-1} alongside the D+G band at ~2938 cm^{-1} is also observed in the Raman spectrum of GO. The broad 2D band indicates the few-layered structure of GO,[33] which is in agreement with the AFM analysis. For the case of WS_2 QDs, two characteristic Raman modes, E_{2g} (~357.0 cm^{-1}) and

A_{1g} (~421.0 cm^{-1}) correspond to the in-plane and out-of-plane vibration of the W-S bond of the hexagonal WS_2, respectively.[17, 34] Notably, the frequency difference between E_{2g} and A_{1g} modes is ~64.0 cm^{-1}, which corresponds to the bilayer structure of WS_2,[35] and it is consistent with our AFM analysis. The appearance of the sharp Raman modes confirms the highly crystalline nature of the as-prepared WS_2 QDs. For the case of GO/WS_2 hybrid, the appearance of the characteristic peaks for both WS_2 and GO is clearly observed. In the hybrid structure, the value of I_D/I_G decreases from ~1.2 to ~1.0, indicating the reduction of defect density/functional groups due to the attachment of WS_2 QDs at the defect sites/functional groups of GO, as discussed in **Chapter 2, Section 2.3.2** for the interaction of U-GQDs and SWCNTs. In the present case, the existence of various oxygen functional groups and the vacancy/defect states in GO act as the active sites for the efficient interaction of WS_2 QDs in GO/WS_2 hybrid formation. Noticeably, the 2D Raman band in GO/WS_2 hybrid becomes stronger as compared to that of the GO, which indicates the reduction of the functional groups of GO.[36]

4.3.2.2. XPS Analysis

To acquire the details of various chemical states and the corresponding binding energy, we analyze the high-resolution XPS spectra of bare WS_2 QDs, GO, and their hybrid, as presented in **Fig. 4.3**. **Fig. 4.3(a)** shows the W 4f core-level XPS spectrum of WS_2 QDs, which is deconvoluted into six

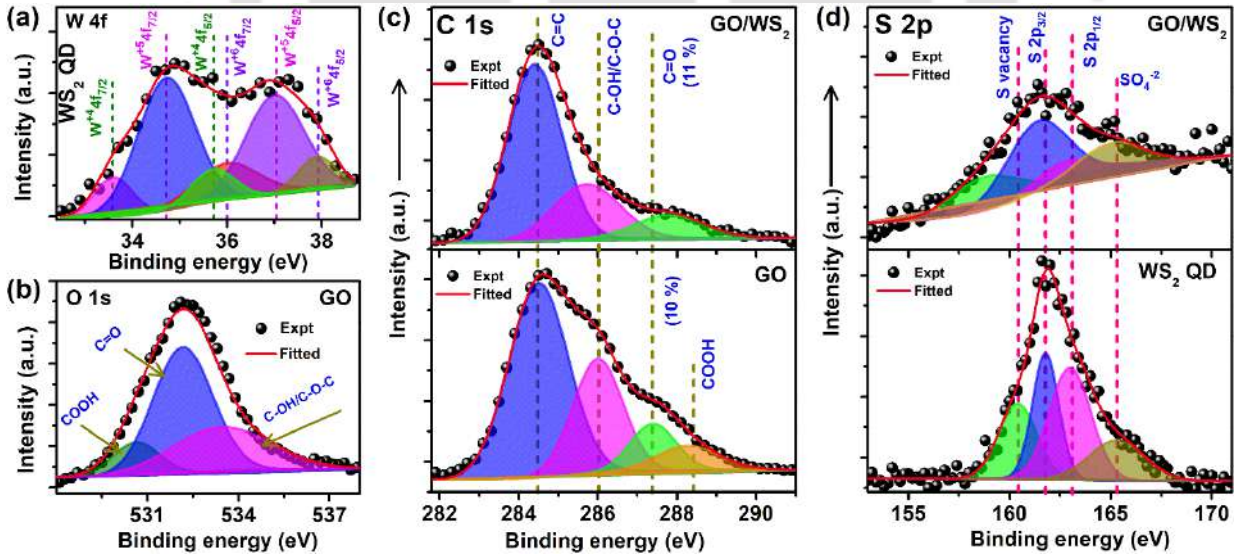

Fig. 4.3. Deconvolution of the high-resolution XPS spectra of (a) W 4f of WS_2 QDs and (b) O 1s of GO. Comparison of the high-resolution XPS spectra of (c) C 1s in GO, and GO/WS_2 hybrid and (d) S 2p in WS_2 QDs, and GO/WS_2 hybrid. Each spectrum is fitted with a Shirley baseline.

Gaussian peaks with a Shirley baseline. The deconvoluted peaks with binding energy ~33.6 eV and 35.7 eV are assigned to W^{+4} $4f_{7/2}$ and W^{+4} $4f_{5/2}$ states in WS_2 QDs, respectively.[37, 38] In the W 4f XPS spectrum, the presence of the defect states as W^{+5} (W^{+5} $4f_{7/2}$ ~34.7 eV and W^{+5} $4f_{5/2}$ ~37.0 eV) and W^{+6} (W^{+6} $4f_{7/2}$ ~36.0 eV and W^{+6} $4f_{5/2}$ ~37.9 eV) states are observed in WS_2 QDs, which are believed to arise from the edge states of WS_2 QDs due to the solution exfoliation process.[21, 38, 39] For the case of GO, O 1s spectrum consists of three different peaks at ~530.6 eV, 532.2 eV, and 533.4 eV, which are assigned to COOH, C=O, and C–OH/C–O–C functional groups of GO, respectively (see **Fig. 4.3(b)**).[40-42] The comparison of the deconvoluted C 1s spectrum of GO and GO/WS_2 hybrid are presented in **Fig. 4.3(c)**. The deconvoluted C 1s spectrum of GO shows the existence of graphitic sp^2 hybridized carbon (C=C) at ~284.5 eV together with various oxygen functional groups, such as C–C/C–OH/C–O–C at ~286.0 eV, C=O at ~287.4 eV and COOH at ~288.3 eV.[40, 42] Interestingly, COOH functional groups of GO is absent in GO/WS_2 hybrid, while the contribution C=O increases, as observed from **Fig. 4.3(c)**.[40] The deconvoluted S 2p XPS spectra of WS_2 QDs and GO/WS_2 hybrid are also compared in **Fig. 4.3(d)**. In bare WS_2 QDs, the appearance of a peak at ~160.4 eV is due to the sulfur (S) vacancy in WS_2 QDs, which is in agreement with the presence of +6 and +5 oxidation states of W.[39] Meanwhile, the peaks at ~161.8 eV and 163.0 eV are attributed to the co-existence of the characteristic S $2p_{3/2,}$ and S $2p_{1/2}$ states, respectively. Another prominent peak at ~165.3 eV indicates the presence of SO_4^{-2} states in S 2p XPS spectrum of WS_2 QDs.[37] Thus, the XPS analysis confirms the abundance of edge related defects in WS_2 QDs. Moreover, the deconvoluted S 2p XPS spectrum of WS_2 shows a change of the binding energy of the vacancy states after GO/WS_2 hybrid formation. Thus, the XPS analysis of C 1s and S 2p spectra reveals that the chemical interaction between GO and WS_2 QDs is mainly driven by the interaction between oxygen-rich functional groups GO and S-vacancy states of WS_2 QDs. These results clearly indicate the chemical bonding and hybrid formation between the GO and WS_2 QDs.

4.3.3. Optical Analysis

To study the optical properties of fluorescent WS_2 QDs, UV-vis absorption, photoluminescence excitation spectra (PLE), and PL spectra are analyzed systematically.

4.3.3.1. UV-vis Absorption Study

The absorption spectrum of WS_2 QDs shows an absorption band at ~265 nm in the deep UV region due to the bound exciton transitions from deep level valence band states to the conduction band, as shown in **Fig. 4.4(a)**.[43] Additionally, the appearance of the broad absorption tail in the range of 350–700 nm is due to the defect states in WS_2 QDs.[17] The Tauc plot in the inset of **Fig. 4.4(a)** shows a direct bandgap of ~4.08 eV for WS_2 QDs, which corresponds to the deep valance band to conduction band transition.[17] For the case of GO, the maximum absorption is observed at ~260 nm due to the characteristic π–π* transition with an indirect bandgap of ~3.75 eV.

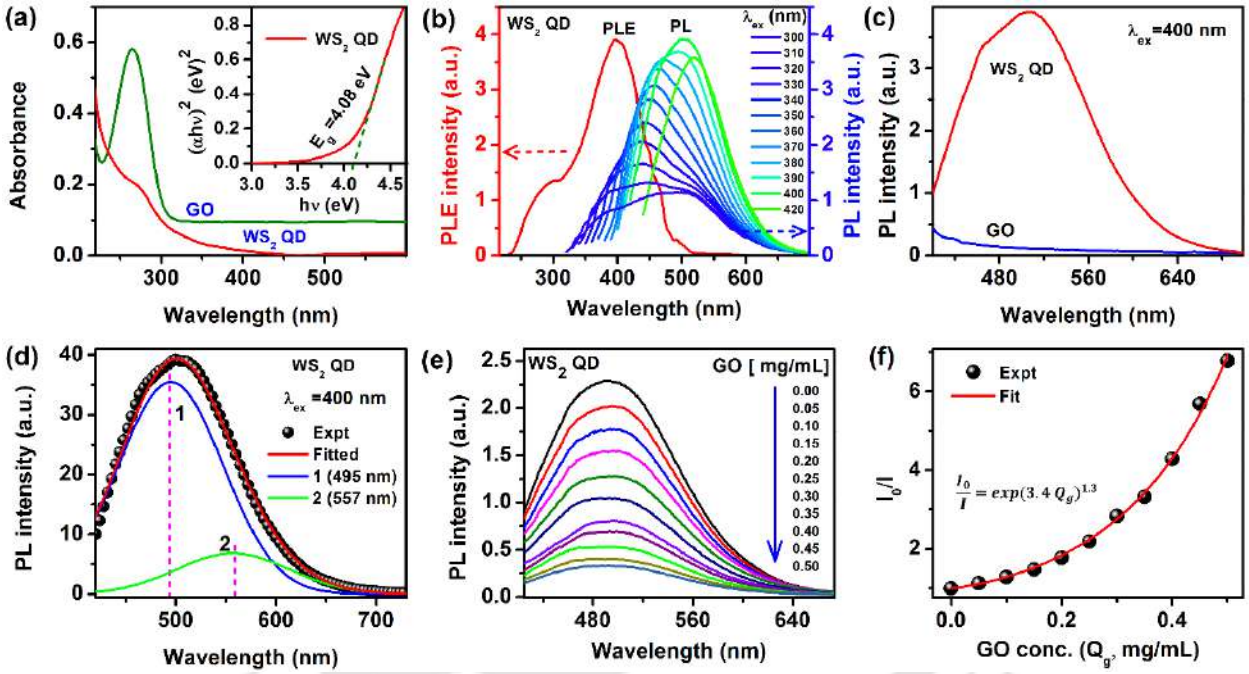

Fig. 4.4. (a) Absorption spectra of WS_2 QDs and GO sheets. The inset shows the Tauc plot for WS_2 QDs, considering the direct bandgap. (b) PLE spectrum of WS_2 QDs together with their excitation wavelength-dependent PL spectra. (c) Comparison of the PL spectra of bare WS_2 QDs and GO sheets under 400 nm excitation. (d) The Gaussian deconvolution of the PL spectrum of WS_2 QDs at λ_{ex} =400 nm. (e) The change of the PL intensity of WS_2 QDs with the addition of different concentrations of GO (0.05–0.5 mg/mL) and (f) the corresponding non-linear Stern-Volmer plot of I_0/I with GO concentration.

4.3.3.2. Photoluminescence Study

Due to the long absorption tail, the excitation wavelength-dependent PL spectral shift is expected in WS_2 QDs. The PLE spectrum of WS_2 QDs is presented together with the excitation wavelength-dependent PL spectra in **Fig. 4.4(b)**. The PLE spectrum exhibits a strong peak at ~400 nm along with a sideband at ~290 nm. By changing the excitation wavelengths (λ_{ex}) in the range of 300–420 nm, WS_2 QDs shows a redshift of the emission peaks. Interestingly, the QDs exhibit a relatively

broad emission spectrum for low wavelength excitation (λ_{ex}), which gradually becomes narrower with the increase of λ_{ex}.[4, 17] Among different excitations, the maximum intensity of the PL peak is observed at λ_{ex} =400 nm, which is consistent with the PLE spectrum. Note that under 400 nm excitation, GO does not show any significant PL emission as compared to that of WS_2 QDs (see **Fig. 4.4(c)**). The Gaussian deconvolution of the PL spectrum of WS_2 QDs at λ_{ex} =400 nm shows two peaks at ~495 nm, and 557 nm, as shown in **Fig. 4.4(d).** These peaks are due to the defects in the surface and in-plane defects arising from the S-vacancy (absence of S atoms) in the hexagonal lattice of WS_2.[17, 44] Note that the S 2p XPS spectrum of WS_2 confirmed the presence of S-vacancy, and thus the PL result is consistent with the XPS analysis.

To study the PL behavior of GO/WS_2 hybrid, the change of PL intensity of WS_2 QDs is monitored at ~496 nm as a function of the concentration of GO (Q_g) under λ_{ex} =400 nm. **Fig. 4.4(e)** shows the systematic quenching of the PL intensity of WS_2 QDs with the increasing concentration of GO in the range of 0.05–0.5 mg/mL. In **Fig. 4.4(f)**, the variation of I_0/I with GO concertation is observed to follow a non-linear Stern-Volmer equation, as used in equ. (2.5) of **Chapter 2**, given by:

$$\frac{I_0}{I} = exp(b\,Q_g)^m \qquad (4.1)$$

where I_0 and I are the PL emission intensities of WS_2 QDs before and after the addition of GO. 'b', and 'm' are the constants with the values of 3.4 mL/mg and 1.3, respectively. Such a deviation from the linear Stern-Volmer equation indicates the large extent of the quenching in the well-known 'Sphere of action' model.[45] With λ_{ex} =400 nm, as the PL contribution is mainly due to the defect states of WS_2 QDs (see **Fig. 4.4(d)**), the PL quenching can be attributed to the attachment of GO at the defect sites of QDs together with the van der Waals interaction.[17, 23] The details of the interaction mechanism of GO and WS_2 QDs are discussed later. The stability of GO/WS_2 is monitored with respect to pH and time, and the results are shown in **Fig. 4.5(a-c)**. With the variation of pH from neutral to basic, the normalized PL spectra of GO/WS_2 and the corresponding change of the maximum PL peak position with pH are shown in **Fig. 4.5(a, b)**. The negligible change in the PL spectra, as well as the maximum PL peak position with the variation of pH, reveal the high stability of GO/WS_2 in the aqueous medium. The intensity of the PL spectra of GO/WS_2 is observed to be constant for 1 h at pH 12, as shown in **Fig. 4.5(c)**.

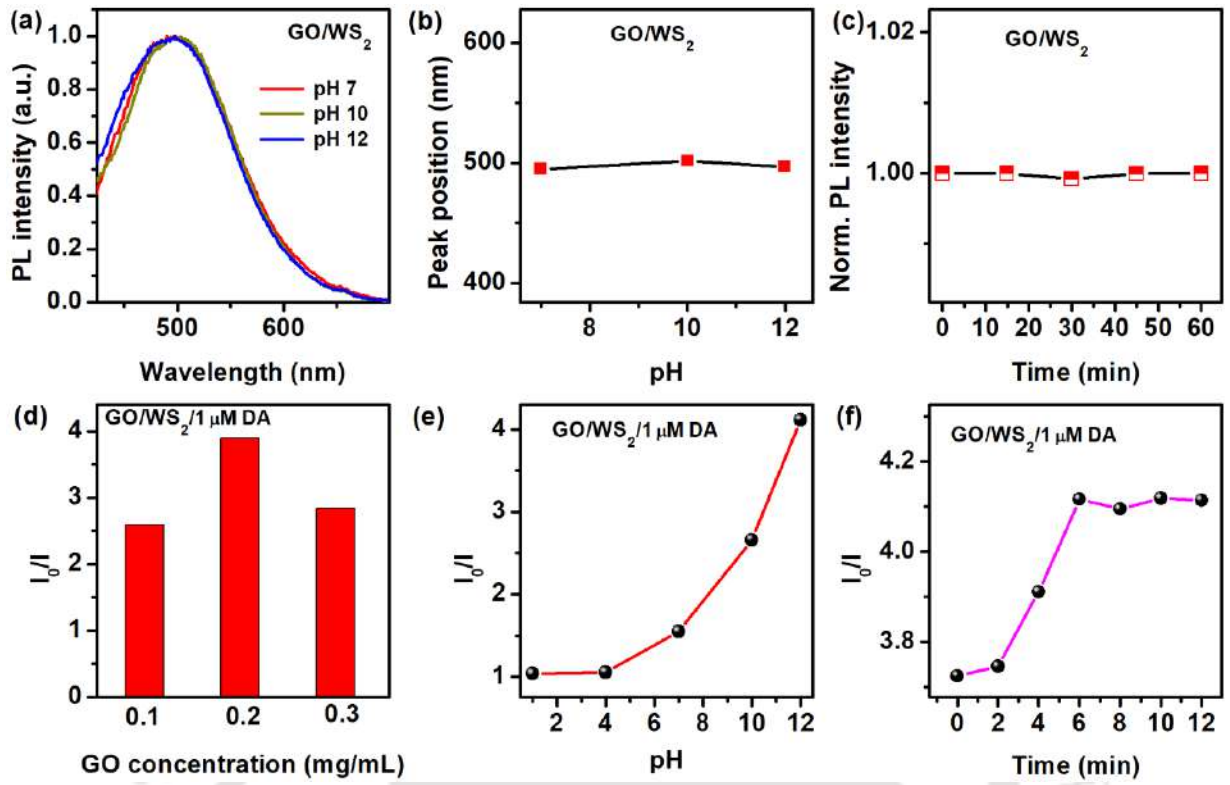

Fig. 4.5. (a) Normalized PL spectra of GO/WS_2 hybrid at different pH, and (b) the corresponding variation of the PL peak position with pH. (c) Stability of the GO/WS_2 hybrid with time. Optimization of DA sensing parameters with the variation of (d) GO concentration, (e) pH value, and (f) the reaction time for a fixed concentration of WS_2 QDs and DA.

4.3.4. Dopamine Sensing with GO/WS_2 Hybrid

For the DA sensing with GO/WS_2 hybrid, different concentrations of DA (Q) in the range of 10 pM–10 μM are added with a fixed concentration of GO/WS_2 hybrid solution. The change of the PL intensity with DA is monitored carefully for the emission peak at ~496 nm under λ_{ex} =400 nm. For the efficient sensing of DA, crucial experimental parameters, e.g., GO/WS_2 concentration, pH, and reaction time, are optimized for a fixed concentration of DA, as shown in **Fig. 4.5(d-f)**. Based on the optimization, GO/WS_2 hybrid with 8.4 μg/mL WS_2 QDs, and 0.2 mg/mL GO at pH 12 shows maximum quenching efficiency after 6 min of reaction with DA. At the optimized condition, the changes of the PL intensity with various concentration of DA is shown in **Fig. 4.6(a)**. The relative change in the PL intensity, $(1- I/I_0)$, (where I_0 and I are the PL intensity of GO/WS_2 before and after the addition of the DA) with Q is shown in **Fig. 4.6(b)**. Obviously, the PL quenching does not follow any of the known Stern-Volmer equations. It does not follow even the

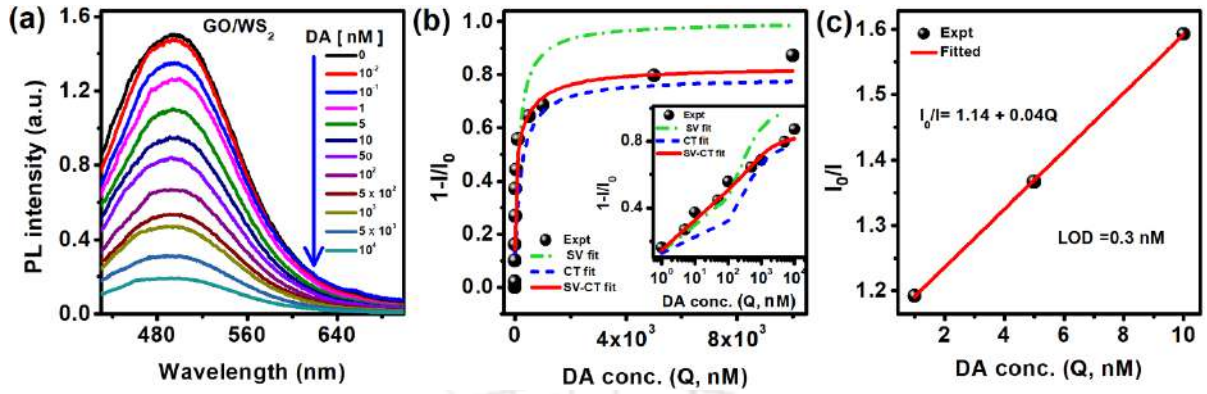

Fig. 4.6. (a) PL spectra of GO/WS_2 hybrid before and after the addition of different concentrations of DA (10 pM–10 μM). (b) The variation of the relative change in the PL intensity (1- I/I_0) as the function of DA concentration (Q) is fitted with different models (SV, CT, and SV-CT) in the DA concentration range 1 nM–10 μM. For better visualization of the deviation from the well-known SV and CT model, the inset shows the variation of (1- I/I_0) vs. log(Q). (c) The linear variation of I_0/I with DA concentration of 1–10 nM with LOD 0.3 nM.

dynamic quenching behavior or the 'Sphere of action' model discussed earlier. To explain the nature of the quenching in the present case in a wide concentration range of DA (10 pM–10 μM), we need to incorporate surface adsorption of DA followed by charge transfer phenomena and ground-state complex formation. Note that in the conventional models of quenching, surface adsorption is not taken into consideration. However, this seems to be obvious and important for the present case, as the defect sites can readily act as the sites for adsorption. For the consideration of ground-state complex formation, the well-known linear Stern-Volmer (SV) equation can be used:

$$I(Q) = \frac{I_0}{1+K_{sv}Q} \qquad (4.2)$$

where I_0 is the initial intensity of PL, and K_{sv} is a constant. Unfortunately, the experimental data does not follow the linear SV equation, particularly at the higher concentration region of DA, as shown by the dashed line in **Fig. 4.6(b)** and the corresponding inset. Note that only over a small range of concentration (1–10 nM), a linear variation of I_0/I with Q is observed with a limit of detection (LOD) of 0.3 nM, as shown in **Fig. 4.6(c)**. However, over a wide range of concentrations, it is highly non-linear. To account for the nonlinearity, we incorporate the surface adsorption of the quencher and the charge transfer at the interface between two species. To describe the photo-excited charge transfer process in semiconducting materials, the first-order rate equation can be introduced as follows: [42]

$$\frac{dM}{dt} = G - [K_1 + K_2(Q)]M \qquad (4.3.1)$$

Here, 'M' is the number of excitons in GO/WS_2 hybrid at any time 't'. 'G' is the generation rate, K_1 is the decay rate constant of excitons, 'Q' is the concentration of the quencher, and the concentration-dependent decay rate $K_2(Q)$ is the rate of charge transfer from an excited state to the quencher (DA). For the case of steady-state ($t \to \infty$),

$$M(Q) = \frac{G}{K_1 + K_2(Q)} \qquad (4.3.2)$$

Considering the surface adsorption of DA on GO/WS_2, $K_2(Q)$ is assumed to follow the relation,[39, 49]

$$K_2(Q) = K_2(0)\left(1 - \frac{S}{\alpha Q + 1}\right) \qquad (4.3.3)$$

where $K_2(0)$ is the rate of charge transfer in the absence of DA, 'S' is the charge transfer efficiency, and 'α' is the adsorption probability of DA on GO/WS_2 hybrid. By using the value of $K_2(Q)$ in eqn. (4.3.2), the PL intensity I(Q) being proportional to M(Q) is expressed as:

$$I(Q) = PM(Q) = \frac{\frac{PG}{K_1 + K_2(0)}}{1 - \left(\frac{K_2(0)S}{K_1 + K_2(0)} \times \frac{1}{\alpha Q + 1}\right)}$$

or,
$$I(Q) = \frac{E}{1 - \frac{F}{\alpha Q + 1}} \qquad (4.3.4)$$

where, $E = \frac{PG}{K_1 + K_2(0)}$, and $F = \frac{K_2(0)S}{K_1 + K_2(0)}$ are the constants, 'P' is the collection efficiency of PL. Interestingly, the charge transfer equation seems to be followed quite well in the PL quenching behavior in higher concentration range of DA, as shown in **Fig. 4.6(b)**. Thus, for a comprehensive understanding of the quenching process, the combined equation of the linear SV eqn. (4.2) and the charge transfer (CT) equation eqn. (4.3.4) need to be considered as follows:

$$I(Q) = \frac{I_0}{1 + BQ} + \frac{E}{1 - \frac{F}{\alpha Q + 1}} \qquad (4.4)$$

where, 'B', 'E' and 'F' are the constants. This combined model is termed as SV-CT model and at Q =0, right-hand side of eqn. (4.4) is taken as I_0. Interestingly, the variation of (1- I/I_0) vs. Q nicely follows the SV-CT model in the wide concentration region (1 nM–10 μM), as shown in **Fig. 4.6(b)**. The inset of **Fig. 4.6(b)** shows the concentration data in the logarithmic scale, indicating a strong deviation of the SV and the CT model from the experimental data. In contrast, our data follows the SV-CT model of PL quenching over the entire range of concentration. Additionally, the value of fitting parameter α =0.7 confirms the high adsorption probability of DA on GO/WS_2. Thus, it can be concluded that the ground state complex formation followed by charge transfer from WS_2

QDs to GO and then to DA leads to unusual quenching of PL in the GO/WS_2 hybrid. It is evident from the experimental data that using the newly developed DA sensor, we able to detect as low as 10 pM concentration of DA. Note that a comparative analysis of the reported works and this work is presented in **Table 4.1**, which shows that the GO/WS_2 hybrid system achieves ~four orders of

Table 4.1. *Comparative performance of fluorescence-based dopamine sensors using WS_2 QDs and GO based 2D materials.*

System	***Detection Range***	***LOD***	***Ref.***
WS_2 QDs	5.0 – 50 μM	3.3 μM	[4]
WS_2 QDs/Au^{+3}	240 nM – 0.78 μM	230 nM	[14]
Fluorescent GO	250 nM – 20 μM	94 nM	[15]
WS_2 QDs	100 nM – 10 μM	100 nM	***This work***
GO/WS_2 QDs	10 pM – 10 μM	10 pM	***This work***

magnitude higher sensitivity than the reported systems for DA sensing. The change of the PL intensity of bare WS_2 QDs is shown in **Fig. 4.7(a)** with DA concentration 0.1–10 μM. Further, for the comparative study of the quenching efficiency of various systems, the PL spectra of bare WS_2 QDs and GO/WS_2 are shown before and after the addition of 10 μM DA under identical conditions (see **Fig. 4.7(b)**). Interestingly, for the WS_2 QDs alone, barely ~35% quenching is achieved with DA, while for the GO/WS_2 hybrid system, ~87% quenching is observed after the addition of 10 μM DA. A comparative study of the PL quenching of WS_2 QDs hybrid with U-GQDs and S-GQDs in the presence of DA is shown in **Fig. 4.7(c, d)**. With U-GQDs or S-GQDs as mediators, the quenching efficiency is much smaller (~29% and 4%) than that of GO. Thus, GO plays a crucial role in the ultrasensitive detection of DA.

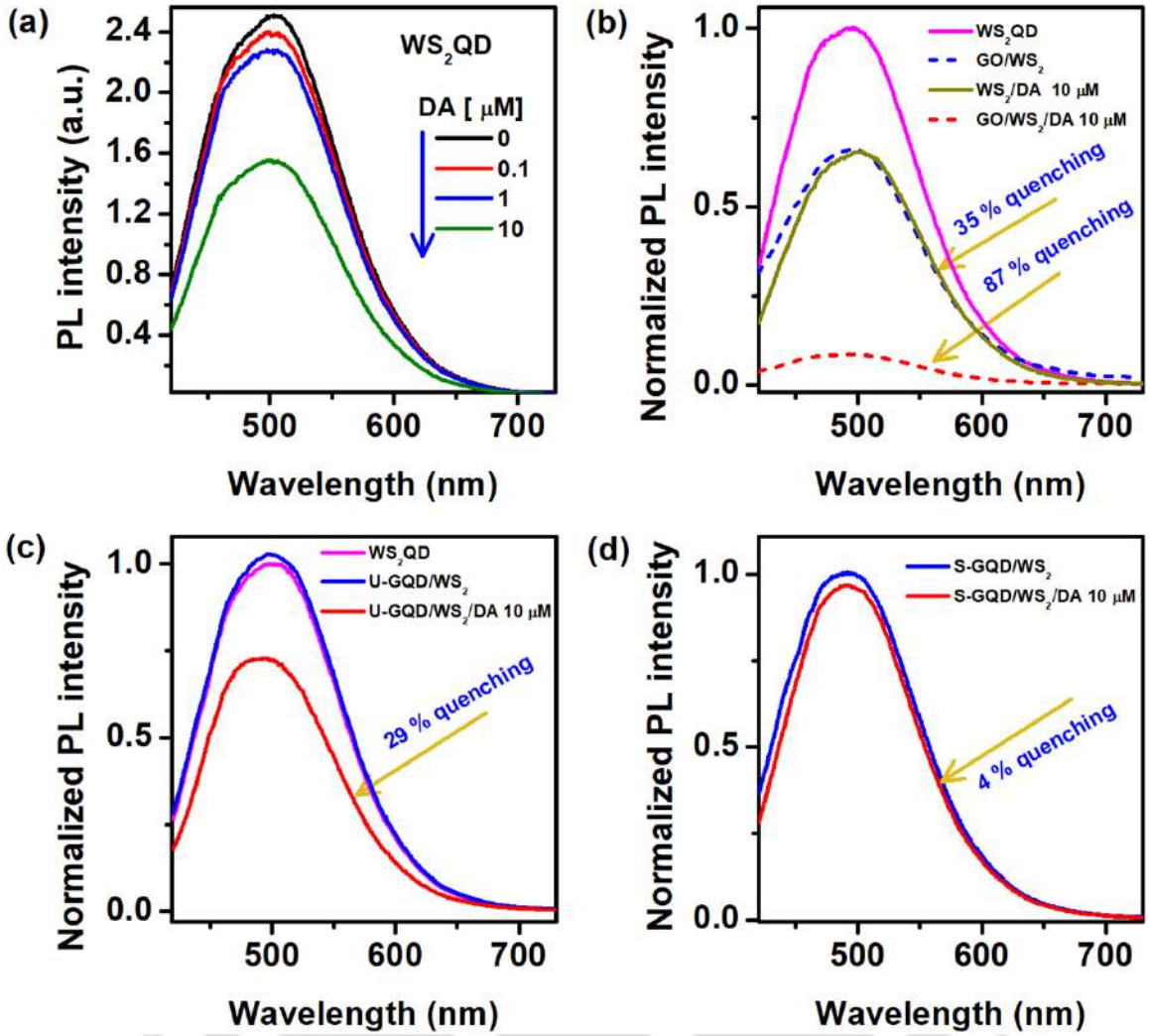

Fig. 4.7. (a) The change of the PL intensity of bare WS_2 QDs in the presence of a different concentration of DA. Comparison of PL quenching efficiency of (b) GO, (c) U-GQDs, and (d) S-GQDs with a fixed concentration of WS_2 QDs and 10 μM DA.

4.3.5. Mechanism of Superior Dopamine Sensing with GO/WS_2 Hybrid

To elucidate the mechanism of DA sensing with GO/WS_2 hybrid, it is imperative to analyze the nature of the interaction between WS_2 QDs and GO. A comparative analysis of the deconvoluted O 1s spectra in GO, GO/WS_2, and GO/WS_2/DA is shown in **Fig. 4.8(a)**, and the corresponding details of the fitting parameters are tabulated in **Table 4.2**, which reveals the reduction of COOH functional groups and the increase in the contribution of C=O groups in GO after interacting with the WS_2 QDs. This is consistent with the change in C 1s spectrum in **Fig. 4.3(c)**. Moreover, from **Table 4.2**, it is observed that the binding energy of the various chemical states in O 1s spectra becomes lower in GO/WS_2 hybrid than that of GO. As the electronegativity of O (3.50) is higher

than that of S (2.51),[40] after the interaction of WS_2 with the oxygen functional groups of GO, the electronic charge increases around O, and subsequently, in the oxygen functional groups of GO.

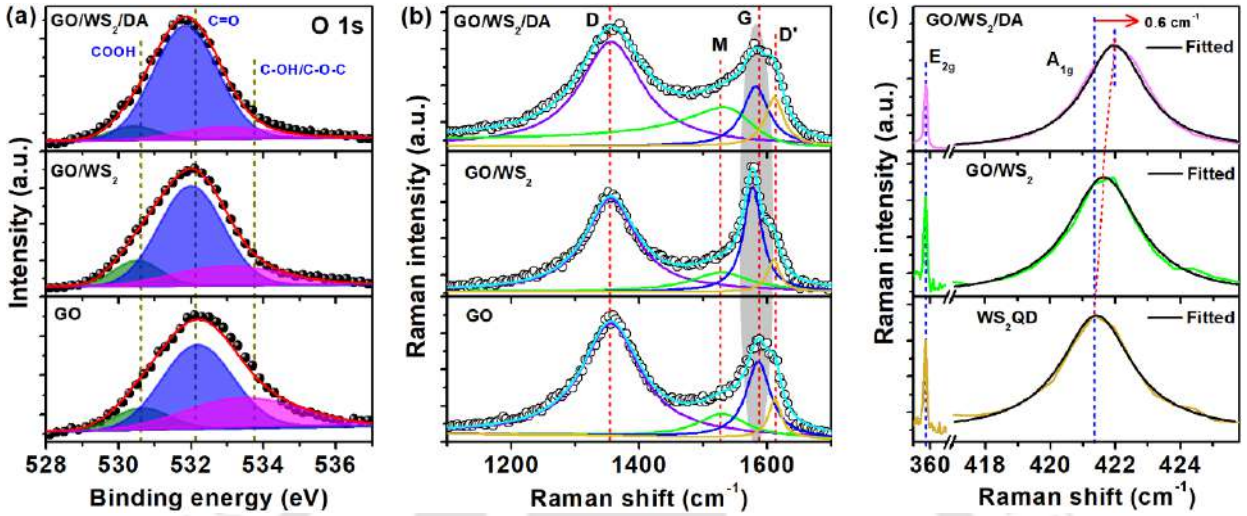

Fig. 4.8. (a) Comparison of the high-resolution XPS spectra of O 1s in GO, GO/WS_2, and GO/WS_2/DA hybrids. Each spectrum is fitted with a Shirley baseline. (b) Deconvolution of the Raman spectra of GO, GO/WS_2, and GO/WS_2/DA in the frequency range of ~1050–1700 cm^{-1}. In each case, the symbols denote the experimental data, and the solid lines show the fitted curves. The respective peak positions in different samples are indicated by the vertical dashed lines. (c) Comparison of the Raman spectra of WS_2 and GO/WS_2 hybrids showing a gradual blue shift of the A_{1g} Raman mode of WS_2 QDs with the addition of GO, GO/DA, respectively, while the E_{2g} peak remains unchanged (excitation: 488 nm).

This difference in electronegativity essentially allows the charge transfer from WS_2 to GO. In **Fig. 4.8(b, c)**, the Raman spectra of GO, WS_2, GO/WS_2, and GO/WS_2/DA are deconvoluted for a better understanding of the complex formation and charge transfer processes. The fitting parameters are

Table 4.2. *Details of the deconvoluted high-resolution XPS spectra of O 1s for GO, GO/WS_2, and GO/WS_2/DA.*

Sample	*Peak position (eV)*	*Peak identity*	*% of contributions*
GO	530.6	COOH	12
	532.2	C=O	55
	533.4	C-OH/C-O-C	33
GO/WS_2	530.5	COOH	12
	532.0	C=O	66
	533.0	C-OH/C-O-C	22
GO/WS_2/DA	530.4	COOH	8
	531.8	C=O	81
	532.9	C-OH/C-O-C	11

tabulated in **Table 4.3**. In **Fig. 4.8(b)**, the deconvoluted Raman spectra show the presence of D, M, G, and D' bands. M and D' band are assigned to the metallic contribution and structural disorder/edges states in GO, respectively.[30, 46] As compared to GO, GO/WS_2 hybrid shows a redshift of G peak by ~11 cm^{-1}, while other peak positions remain almost unchanged. This is indicative of the charge transfer from WS_2 to GO, which enhances the overall electronic charge in

Table 4.3. *Details of the Raman modes for GO, GO/WS_2, and GO/WS_2/DA.*

Sample	***Raman bands (cm^{-1})***					
	D	***M***	***G***	***D'***	***E_{2g}***	***A_{1g}***
GO	1356	1528	1586	1612	-	-
WS_2 QD	-	-	-	-	357.3	421.4
GO/WS_2	1356	1529	1577	1610	357.3	421.6
GO/WS_2/DA	1356	1531	1582	1611	357.3	422.0
Peak identity	*Defects (GO)*	*Metallic (GO)*	*In-plane vibration of C=C bond (GO)*	*Structural disorder /edges (GO)*	*In-plane vibration of W-S bond (WS_2)*	*Out-of-plane vibration of W-S bond (WS_2)*

the graphitic domain.[42] On the other hand, the A_{1g} peak of WS_2 QDs shows a blueshift of ~0.2 cm^{-1} in the GO/WS_2 hybrid (see **Fig. 4.8(c)**, while the E_{2g} mode remains unchanged, which is the indication of the charge deficiency in WS_2 QDs, after its interaction with the GO.[17] Further, the unchanged position of E_{2g} mode confirms that GO interacts with WS_2 QDs mainly in the out-of-plane direction. The charge transfer from the WS_2 QDs to GO is also energetically favorable considering the relative band gaps of the two components. Since WS_2 QDs have a high bandgap of ~4.08 eV, while the GO has a lower bandgap (~3.75 eV), the electrons can be easily transferred from WS_2 QDs to GO, which is consistent with the Raman analysis. Next, we consider the interaction of DA with GO/WS_2 hybrid. It is well known that DA has an aromatic structure with two catechol groups. Due to the aromatic structure of DA, it can easily attach with GO by the π–π interactions.[1] Ren et al. reported strong adsorption of DA on GO surface by the formation of strong hydrogen bonding between GO and DA, in addition to non-covalent π–π interaction in the aqueous medium.[24] It is well known that in the basic medium, DA is oxidized to dopamine-o-quinone (DQ) by the conversion of –OH groups of DA to C=O groups.[1, 47] As we have observed a higher quenching efficiency at higher pH (see **Fig. 4.5(e)**), the interaction of GO and DA via hydrogen bond formation is very unlikely in the basic medium. Note that after the interaction of DA with

GO/WS_2 hybrid, the O 1s XPS spectrum of the composite reveals a higher concentration of C=O, confirming the oxidation of catechol groups of DA (see **Fig. 4.8(a)** and **Table 4.3**). Remarkably, the adsorption of DA molecules into the GO surface is observed to follow the Freundlich isotherm, as shown in **Fig. 4.9(a)**. Freundlich isotherm is expressed as:[15, 45]

$$log\frac{[Q]}{dI} = m\ log\frac{[Q]}{dI_{max}} + c \qquad (4.5)$$

where dI is the change of the PL intensity of GO/WS_2 at PL maxima, dI_{max} is the change of the PL

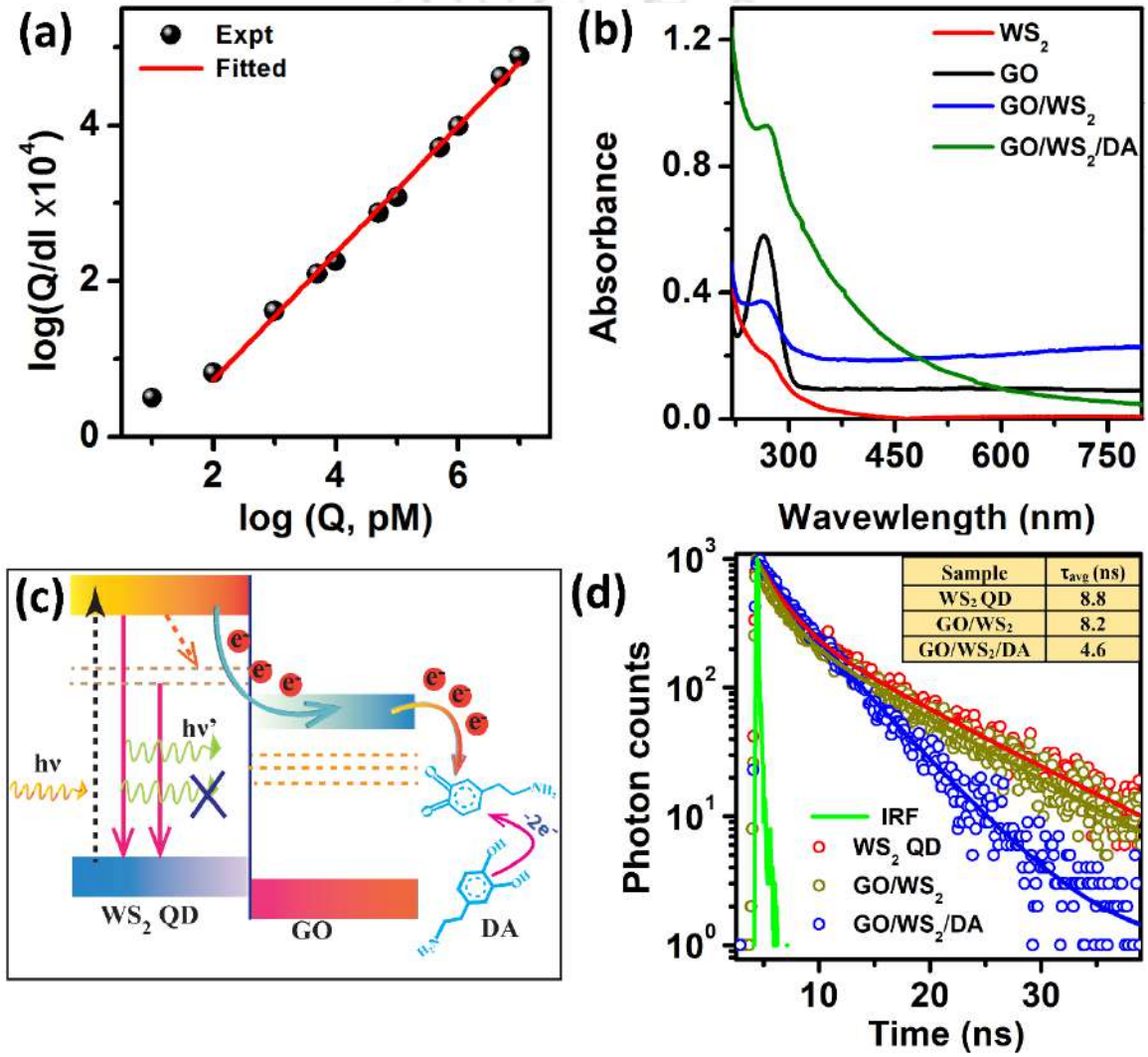

Fig. 4.9. (a) Freundlich isotherm model fitting for the multilayer adsorption of DA on GO sheets. (b) The change of the absorption spectra of WS_2 QDs after the composite formation with GO and DA. (c) An illustration of the energy band diagram of GO/WS_2 hybrid and the charge transfer process from WS_2 QDs to DA via GO. The horizontal dashed lines indicate defect states in WS_2 QDs and GO. (d) Time-resolved PL spectra of WS_2 QDs, GO/WS_2, and GO/WS_2/DA; the corresponding average decay times are shown in the inset.

intensity at saturation, 'm' and 'c' are the constants. Thus, in the present case, the multilayer adsorption of DA occurs on the GO/WS_2 hybrid platform. Note that a higher absorbance of the GO/WS_2/DA system shown in **Fig. 4.9(b)** is consistent with the above. In the present case, as the non-covalent π–π interaction between GO and DA is more likely than the interaction between WS_2 QDs and DA, the absorption is mainly governed by the adsorption of DA on the GO surfaces. Moreover, DQ being a strong electron acceptor by nature,[17, 48] there is a possibility of charge transfer from GO to DA. Xu et al. described DA as a reducing agent for the preparation of reduced GO from GO.[49] From **Fig. 4.8(a)**, the reduction of the contribution of COOH functional groups from ~12% to 8% in the presence of DA in the O 1s spectrum confirms the same. Punckt et al. demonstrated the high electrical conductivity of reduced GO.[50] Thus, in the presence of DA, the reduction of GO also facilitates the charge transportation from WS_2 to DA via GO sheets. A schematic of the charge transfer process from WS_2 QDs to DA through GO is illustrated in **Fig. 4.9(c)**. For the quantitative analysis of the charge transfer process, the TRPL spectra of WS_2 QDs are analyzed before and after the formation of various hybrids. In **Fig. 4.9(d)**, it is observed that the change of the lifetime (τ_{avg} ~8.8 ns) of WS_2 QDs is only ~0.6 ns after GO/WS_2 hybrid formation, while with the addition of DA, the composites exhibit very fast decay (τ_{avg} ~4.6 ns). Note that a negligible change of τ_{avg} for the WS_2/DA system discards the possibility of direct charge transfer from WS_2 QDs to DA. Thus, the excited state charge transfer from WS_2 QDs to DA through the GO layer causes a strong PL quenching. In presence of DA, the charge transfer phenomenon is consistent with the Raman spectral analysis, shown in **Fig. 4.8(b, c)**. In **Fig. 4.8(b)**, the G peak of GO/WS_2/DA blue shifts by ~5 cm^{-1} as compared to that of GO/WS_2, confirming the reduction of electronic charge in the graphitic domain of GO due to its interaction with DA. Additionally, the gradual blue shift of the A_{1g} peak of WS_2 QDs by ~0.2 cm^{-1} and 0.6 cm^{-1} in GO/WS_2 and GO/WS_2/DA, respectively, is consistent with the charge transfer from WS_2 QDs to GO to DA. The excited states charge transfer from WS_2 QDs to GO increases the electronic charge in GO, which produces a strong in-plane vibration of sp^2 bonded carbon of GO, and after the attachment of DA with GO via π–π interactions, the strong electron acceptor DQ takes out the electrons from GO. As a result, in the presence of DA, the electronic charge density in GO is reduced. Note that the direct charge transfer from WS_2 to DA is insignificant compared to the charge transfer via GO, as we have observed from the PL quenching efficiency in **Fig. 4.7(a, b)**. As compared to bare WS_2 QDs, GO/WS_2 hybrid causes very efficient charge separation and charge

transfer to DA due to the π–π interaction of DA and GO, resulting in the ultra-high sensitive detection of DA. Note that with U-GQDs or S-GQDs mediator, we have observed negligible quenching of WS_2 QDs PL intensity in the presence of DA. Due to the presence of abundant functional groups and small size of U-GQDs and S-GQDs, their conductivity is very low. Thus, in the present case, GO not only helps in the π–π interaction with DA but also behaves like a good charge transport medium from WS_2 QDs to DA and thus leads to an efficient quenching of PL intensity, finally leading to the ultrasensitive detection of DA.

4.3.6. Selectivity in Dopamine Sensing

Selectivity is a very crucial parameter in sensing performance. For the use of GO/WS_2 hybrid as an efficient DA sensor in the real samples, the interference species, such as organic compounds, metal ions, solvents, should be tested under identical experimental conditions. In the present case, glucose (GL), uric acid (UA), ascorbic acid (AA), L-cysteine (L-Cys), glycine (Gly), and thiourea (thio) at a concentration of 10 μM are used as organic compounds, and Na^+, Cu^{2+}, Ca^{2+}, Al^{3+}, Cd^{2+}, Hg^{2+}, Pb^{2+} are used as metal ions. H_2SO_4, HCl, DMF, and DMSO are used as the interfering solvents. **Fig. 4.10(a)** represents the relative change of the PL intensity (I_0/I) of GO/WS_2 hybrid with the addition of different species. Interestingly, a strong quenching of PL intensity is observed only with the presence of DA, and no significant quenching is found by the addition of other solvents/samples. Here, the π–π interaction between DA and GO helps to select only DA among all other interfering agents. Thus, the GO/WS_2 hybrid system performs as a highly sensitive and selective sensor of DA.

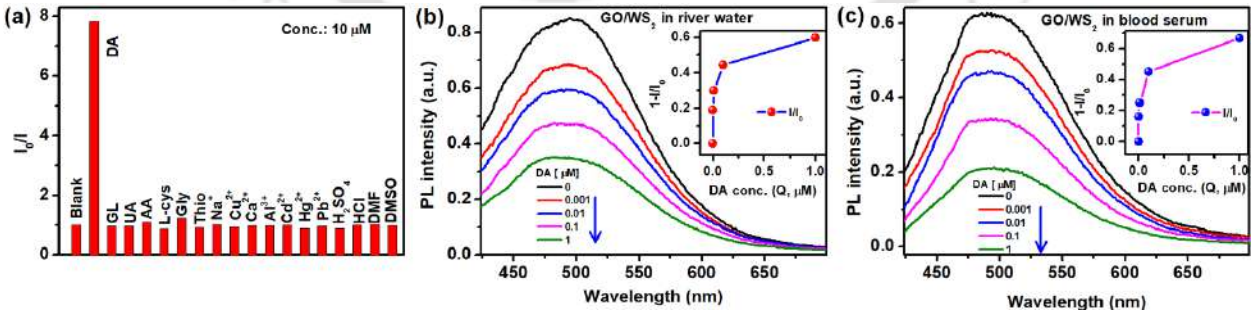

Fig. 4.10. (a) The selectivity of DA sensing by GO/WS_2 hybrid in the presence of different interfering species (concentration 10 μM). (b, c) The evolution of PL intensity of GO/WS_2 with varying concentrations of spiked DA in the Brahmaputra River water and the human blood serum, respectively. The corresponding inset shows the relative change of the PL intensity ($1-I/I_0$) with spiked DA concentrations.

4.3.7. Analysis of Real-life Samples

For assessing the practical utility of the GO/WS_2 hybrid as an efficient DA sensor, different concentrations of DA were spiked into real-life samples. The concentration of DA is determined by the standard addition method. The developed hybrid sensor is utilized for the detection of DA in the Brahmaputra river water as an environmental sensor and the human blood sample as a biosensor. The water sample was simply filtered with a 0.22 μm membrane without any further processing. For the detection of DA in the river water, the detecting aqueous solution (GO/WS_2 hybrid) was prepared after 20 times dilution of filtered water, maintaining a pH of 12. The change of the PL intensity with the spiked DA concentration in the river water sample is presented in **Fig. 4.10(b)**. The inset of **Fig. 4.10(b)** shows the relative change in the PL intensity ($1-I/I_0$) against the spiked DA in the river water, which follows a non-linear behavior, as discussed before. To test the GO/WS_2 hybrid-based sensor in the human serum for the detection of spiked DA, the human blood serum was diluted (100 times) with a buffer solution of pH 12. The change of the PL intensity is monitored at different concentrations of spiked DA (1 nM–1.0 μM), as shown in **Fig. 4.10(c)**. The variation of ($1- I/I_0$) with DA concentration is shown in the inset of **Fig. 4.10(c)**. A satisfactory recovery of DA concentration is observed in real samples with our GO/WS_2 hybrid sensor, as presented in **Table 4.4**. Thus, the hybrid sensor reported here has great potential as an environmental sensor as well as a biosensor.

Table 4.4. *Detection of dopamine spiked in the Brahmaputra river water and blood serum samples.*

Sample	***Added concentration of DA (nM)***	***Found concentration of DA (nM)***	***Recovery (%)***
Brahmaputra river water	1	1 ± 0.007	100
	10	15 ± 0.09	150
	100	81 ± 0.60	81
	1000	720 ± 2.0	72
Blood serum	1	1 ± 0.001	100
	10	10 ± 0.010	100
	100	80 ± 0.2	80
	1000	760 ± 4.0	76

4.4. Summary and Conclusions

In this chapter, the role of GO in the sensitive and selective detection of DA by the GO/WS_2 hybrid is elucidated through an in-depth study. The important findings of this chapter are summarized below.

1. The interaction between highly fluorescent WS_2 QDs and GO via van der Waals interaction, and the defect states and functional groups lead to the excited state charge transfer from WS_2 to GO in the GO/WS_2 hybrid, resulting in the PL quenching of WS_2 QDs with a non-linear SV plot following 'sphere of action' model.
2. The GO/WS_2 hybrid is used for the ultrasensitive and selective detection of DA at a concentration of 10 pM, which is the lowest among the reported values.
3. Strong π–π interaction between DA and GO, and in the basic medium, the conversion of DA to DQ (a strong electron acceptor) promotes the efficient electron transfer from GO to DA, which facilitate more rapid quenching of the PL intensity of WS_2 QDs.
4. The nature of PL quenching in a wide concentration range of DA (10 pM–10 μM) is described by developing a modified model with the combined effect of the excited-state charge transfer and the ground-state complex formation, following the Freundlich isotherm.

These results pave the way for the development of a practical sensor for the ultrasensitive detection of DA using heterojunctions of 2D layered materials.

References

1. R. Das, K. K. Paul and P. K. Giri, *Appl Surf Sci*, 2019, **490**, 318-330.
2. M. Keerthi, G. Boopathy, S.-M. Chen, T.-W. Chen and B.-S. Lou, *Sci. Rep.*, 2019, **9**, 1-12.
3. M. A. Kafi, A. Paul, A. Vilouras and R. Dahiya, *Biosens. Bioelectron.*, 2020, **147**, 111781.
4. X. Zhao, D. He, Y. Wang and C. Fu, *Mater. Chem. Phys.*, 2018, **207**, 130-134.
5. H. Su, B. Sun, L. Chen, Z. Xu and S. Ai, *Anal. Methods*, 2012, **4**, 3981-3986.
6. Y. Lin, C. Chen, C. Wang, F. Pu, J. Ren and X. Qu, *ChemComm*, 2011, **47**, 1181-1183.
7. X. Zhou, P. Ma, A. Wang, C. Yu, T. Qian, S. Wu and J. Shen, *Biosens. Bioelectron.*, 2015, **64**, 404-410.
8. L. Wu, L. Feng, J. Ren and X. Qu, *Biosens. Bioelectron.*, 2012, **34**, 57-62.

9. V.-D. Phung, W.-S. Jung, T.-A. Nguyen, J.-H. Kim and S.-W. Lee, *Nanoscale*, 2018, **10**, 22493-22503.
10. B. Guadarrama-Flores, M. Rodríguez-Monroy, F. Cruz-Sosa, F. García-Carmona and F. Gandía-Herrero, *J. Agric. Food Chem.*, 2015, **63**, 2741-2749.
11. A.-J. Wang, J.-J. Feng, W.-J. Dong, Y.-H. Lu, Z.-H. Li and M.-L. Riekkola, *J. Chromatogr. A*, 2010, **1217**, 5130-5136.
12. X. Chen, S. Chen and Q. Ma, *Anal. Methods*, 2017, **9**, 2246-2251.
13. F. Gao, L. Liu, G. Cui, L. Xu, X. Wu, H. Kuang and C. Xu, *Nanoscale*, 2017, **9**, 223-229.
14. M.-J. Kim, S.-J. Jeon, T. W. Kang, J.-M. Ju, D. Yim, H.-I. Kim, J. H. Park and J.-H. Kim, *ACS Appl. Mater. Interfaces*, 2017, **9**, 12316-12323.
15. J.-L. Chen, X.-P. Yan, K. Meng and S.-F. Wang, *Anal. Chem.*, 2011, **83**, 8787-8793.
16. S. Kulchat, W. Boonta, A. Todee, P. Sianglam and W. Ngeontae, *Spectrochimica Acta Part A: Molecular and Biomolecular Spectroscopy*, 2018, **196**, 7-15.
17. A. Bora, L. P. Mawlong, R. Das and P. K. Giri, *J. Colloid Interface Sci.*, 2019, **561**, 519-532.
18. W. Yin, X. Zhang, X. Bai, D. Xue, X. Zhuang, H. Song and W. W. Yu, *ChemPlusChem*, 2018, **83**, 1052-1056.
19. W. Yin, X. Bai, P. Chen, X. Zhang, L. Su, C. Ji, H. Gao, H. Song and W. W. Yu, *ACS Appl. Mater. Interfaces*, 2018, **10**, 43824-43830.
20. J. H. Appel, D. O. Li, J. D. Podlevsky, A. Debnath, A. A. Green, Q. H. Wang and J. Chae, *ACS Biomater Sci Eng*, 2016, **2**, 361-367.
21. Y. Yan, C. Zhang, W. Gu, C. Ding, X. Li and Y. Xian, *J. Phys. Chem. C*, 2016, **120**, 12170-12177.
22. J. W. Suk, R. D. Piner, J. An and R. S. Ruoff, *ACS nano*, 2010, **4**, 6557-6564.
23. C. Lu, Y. Liu, Y. Ying and J. Liu, *Langmuir*, 2017, **33**, 630-637.
24. H. Ren, D. D. Kulkarni, R. Kodiyath, W. Xu, I. Choi and V. V. Tsukruk, *ACS Appl. Mater. Interfaces*, 2014, **6**, 2459-2470.
25. F. Thema, M. Moloto, E. Dikio, N. Nyangiwe, L. Kotsedi, M. Maaza and M. Khenfouch, *J. Chem*, 2012, **2013**.
26. S. Park, J. An, J. R. Potts, A. Velamakanni, S. Murali and R. S. Ruoff, *Carbon*, 2011, **49**, 3019-3023.
27. A. Ghorai, A. Midya and S. K. Ray, *New J. Chem.*, 2018, **42**, 3609-3613.
28. M. O. Valappil, A. Anil, M. Shaijumon, V. K. Pillai and S. Alwarappan, *Chem.: Eur. J.*, 2017, **23**, 9144-9148.
29. D. C. Marcano, D. V. Kosynkin, J. M. Berlin, A. Sinitskii, Z. Sun, A. Slesarev, L. B. Alemany, W. Lu and J. M. Tour, *ACS nano*, 2010, **4**, 4806-4814.
30. R. Das, G. Rajender and P. K. Giri, *Phys. Chem. Chem. Phys.*, 2018, **20**, 4527-4537.
31. S. Sharma, S. Bhagat, J. Singh, R. C. Singh and S. Sharma, *J. Mater. Sci.*, 2017, **52**, 11326-11336.
32. X. Díez-Betriu, S. Álvarez-García, C. Botas, P. Álvarez, J. Sánchez-Marcos, C. Prieto, R. Menéndez and A. De Andrés, *J. Mater. Chem. C*, 2013, **1**, 6905-6912.
33. A. Kaniyoor and S. Ramaprabhu, *Aip Advances*, 2012, **2**, 032183.
34. A. Berkdemir, H. R. Gutiérrez, A. R. Botello-Méndez, N. Perea-López, A. L. Elías, C.-I. Chia, B. Wang, V. H. Crespi, F. López-Urías and J.-C. Charlier, *Sci. Rep.*, 2013, **3**, 1755.
35. L. Yuan and L. Huang, *Nanoscale*, 2015, **7**, 7402-7408.

36. R. Arul, R. N. Oosterbeek, J. Robertson, G. Xu, J. Jin and M. C. Simpson, *Carbon*, 2016, **99**, 423-431.
37. F. Perrozzi, S. Emamjomeh, V. Paolucci, G. Taglieri, L. Ottaviano and C. Cantalini, *Sens. Actuators B: Chem.*, 2017, **243**, 812-822.
38. G. Leftheriotis, S. Papaefthimiou, P. Yianoulis and A. Siokou, *Thin solid films*, 2001, **384**, 298-306.
39. S. H. Choi, S. Boandoh, Y. H. Lee, J. S. Lee, J.-H. Park, S. M. Kim, W. Yang and K. K. Kim, *ACS Appl. Mater. Interfaces*, 2017, **9**, 43021-43029.
40. R. Das, S. Parveen, A. Bora and P. K. Giri, *Carbon*, 2020, **160**, 273-286.
41. D. Yang, A. Velamakanni, G. Bozoklu, S. Park, M. Stoller, R. D. Piner, S. Stankovich, I. Jung, D. A. Field and C. A. Ventrice Jr, *Carbon*, 2009, **47**, 145-152.
42. R. Das, H. Sugimoto, M. Fujii and P. K. Giri, *ACS Appl. Mater. Interfaces*, 2020, **12**, 4755-4768.
43. A. Bayat and E. Saievar-Iranizad, *J. Lumin.*, 2017, **185**, 236-240.
44. P. K. Chow, R. B. Jacobs-Gedrim, J. Gao, T.-M. Lu, B. Yu, H. Terrones and N. Koratkar, *ACS nano*, 2015, **9**, 1520-1527.
45. D. K. Singh, P. K. Iyer and P. K. Giri, *Carbon*, 2012, **50**, 4495-4505.
46. G. Rajender and P. K. Giri, *J. Mater. Chem. C*, 2016, **4**, 10852-10865.
47. J. Zhao, L. Zhao, C. Lan and S. Zhao, *Sens. Actuator B-Chem.*, 2016, **223**, 246-251.
48. P. Bhawal, S. Ganguly, T. Chaki and N. Das, *RSC Adv.*, 2016, **6**, 20781-20790.
49. L. Q. Xu, W. J. Yang, K.-G. Neoh, E.-T. Kang and G. D. Fu, *Macromolecules*, 2010, **43**, 8336-8339.
50. C. Punckt, F. Muckel, S. Wolff, I. A. Aksay, C. A. Chavarin, G. Bacher and W. Mertin, *Appl. Phys. Lett.*, 2013, **102**, 023114.

भारतीय प्रौद्योगिकी संस्थान गुवाहाटी
Indian Institute of Technology Guwahati

Chapter 5

Mechanistic Insights into Highly Sensitive and Selective Label-free Detection of Dopamine in Human Serum with Nitrogen-Doped Graphene Quantum Dots Decorated on Au Nanoparticles

In the present chapter, a rapid, facile, and label-free dual-mode sensing strategy of dopamine (DA) in the real samples is developed with a metal-semiconductor hybrid by integrating nitrogen-doped graphene quantum dots (N-GQDs) decorated on Au nanoparticles (Au@N-GQDs). Based on the systematic change of the UV-vis absorption intensity of Au@N-GQDs with DA concentration, the well-known Hill equation is introduced for the sensing of DA in the range of 0–10 μM with a detection limit of 40 nM. Additionally, the strong blue fluorescence of Au@N-GQDs is observed to be drastically quenched with the addition of DA in the neutral aqueous medium by following the well-known linear Stern-Volmer equation. The mechanistic insight into the sensing mechanism is explored here by careful monitoring of the evolution of the interaction of Au NPs, and N-GQDs with DA at different conditions through the electron microscopic and spectroscopic investigation. The highly sensitive and selective detection of DA over a wide range is attributed to the unique core-shell structure formation with Au@N-GQDs as well as the electron transfer from N-GQDs. The presence of Au NPs in Au@N-GQDs hybrids accelerates the sensing process (~14 fold higher than that of bare N-GQDs) by the formation of stable dopamine-o-quinone (DQ) in this present detection scheme. The quenching of Au@N-GQDs fluorescence intensity makes it possible to detect the spiked DA in the human serum in a linear range from 0–80 μM with the limit of detection (LOD) of 590 nM. This sensing scheme is also successively applied to trace DA in the Brahmaputra river water sample with a satisfactory recovery (~95–112%). Our studies reveal a mental-semiconductor based novel sensing system for DA following the core-shell structure formation, which is highly promising for the design of the efficient biological and environmental sensor.

5.1. Introduction

In the previous chapter, the effective fluorometric sensing of DA by a hybrid system consisting of semiconducting graphene oxide and WS_2 QDs has been discussed. Various sensing methods have been developed for the detection of DA, including the high-performance liquid chromatography,[1] capillary electrophoresis,[2] electrochemical,[3] fluorescent sensors,[4, 5] and colorimetric sensor[6]. Among these, colorimetric and fluorescence sensing methods are regarded as the simplest as well as the cost and time effective methods with appreciably lower detection limit. In **Chapter 3**, we have discussed the synthesis of nitrogen-doped GQDs (N-GQDs) and observed the creation of structural defects and more active sites along with the improved optical properties in N-GQDs. Chen et al. reported the sensing of DA with N-GQDs up to 1 μM concentration with the change of their optical property.[4] For the detection of DA, metallic nanoparticles (NPs) were also used as a promising detector, and mainly aggregation of the NPs in the presence of DA was reported as the key factor of the sensing.[6-8] Au NPs combined with graphitic materials have been studied as highly promising heterostructures for sensing applications. The oxygen-rich functional groups on the surface of graphene provide active sites for the nucleation of Au NPs instead of the use of conventional reducing agents.[9, 10] Following the unique synthesis method, the GQD functionalized Au NPs were prepared for various sensing applications including metal ion sensing,[11] H_2O_2 sensing,[12] etc. Recently, reduced GQDs with Au NPs core-shell structure has been used for the colorimetric detection of cysteine by aggregation.[9] Though a variety of sensing methods were developed for DA with high sensitivity and selectivity, an in-depth understanding of the sensing mechanism is still lacking in the literature.

In the present work, we develop a rapid, stable, sensitive, and highly selective sensor with Au@N-GQDs for the optical detection of DA in the neutral aqueous medium with low technical demands. The oxygen-rich functional groups of N-GQDs facilitate the formation of the composites with DA, which leads to the formation of a core-shell structure with DA as the shell over Au NPs core. Based on the phenomenon of the composite formation, the newly developed sensor is used for the efficient detection of DA through the measurement of UV-vis absorption as well as the fluorescence quenching. Additionally, this sensor is applied for the detection of spiked DA in the real samples, such as Brahmaputra river water, and human serum, with high selectivity as well as recovery.

5.2. Experimental Details

5.2.1. Sample Preparation

5.2.1.1. Synthesis of Graphene Oxide

GO is synthesized from graphite flakes by a well-known modified Hummers' method, as discussed in **Chapter 2, Section 2.2.1.1**. First, graphite flakes and $NaNO_3$ were mixed in 2:1 ratio with concentrated H_2SO_4 under continuous stirring for 2 h. Subsequently, $KMnO_4$ was added in the acid mixture at 4 °C. After the addition of $KMnO_4$, the stirring was continued at 35 °C for 4 h for proper oxidation. After that, MQ water was slowly added to the prepared mixture at 98 °C, and then the solution was quenched with 15 mL of 30% H_2O_2. Finally, GO was collected by centrifugation.

5.2.1.2. Synthesis of Nitrogen-doped GQDs

N-GQDs were synthesized by the top-down method in DMF solvent using GO as precursor, discussed in **Chapter 3, Section 3.2.1.3**. In brief, 600 mg of GO powder was dispersed in 40 mL DMF and then the solution was heated at 220 °C for 7h into the Teflon lined autoclave. After cooling down at room temperature, the yellow suspension was collected as N-GQDs.

5.2.1.3. Synthesis of Au@N-GQDs

At first, 14 mg of as-synthesis N-GQDs was dispersed in 20 mL of MQ water by using the ultra-sonication process. Then the solution was heated at 110 °C with stirring for 10 min. Afterward, 2 mL of $HAuCl_4$, 4 H_2O solutions (5 mM, 99.9%, Alfa Aesar) was added dropwise into the above N-GQDs solution, and the yellow color of N-GQDs solution was observed to be changed into a light pink color, which indicated the formation of Au@N-GQDs. After the natural cooling to room temperature, the Au@N-GQDs was collected as the precipitate part by centrifugation at 13,000 rpm for 10 min. The concentration of the obtained Au@N-GQDs solution is 0.63 mg/mL. Au@N-GQDs aqueous solution at a concentration of 0.09 mg/mL has been used for most of the experiments, and the sample is termed as A2. For comparison, a higher and a lower concentration of Au@N-GQDs aqueous solution was also used, and these are termed as A1, and A3 for the concentrations of 0.07 mg/mL, and 0.13 mg/mL, respectively. Further, Au@N-GQDs was prepared with different ratio of N-GQDs (i.e., 4, 6, 10, and 20 mg) under identical conditions, and the treatment procedure is same as above. Note that N-GQDs with a concentration of 0.09 mg/mL have been used for comparative studies.

5.2.2. Detection of Dopamine

The detection of DA was performed in PBS buffer solution at pH 7. For the efficient sensing of DA, different concentrations of stock solution of Au@N-GQDs were used to find out the optimum concentration, and repeatability for the sensing. In a typical run, 0.5 mL of stock solution of Au@N-GQDs, and 2.0 mL of DA solutions at different concentrations, ranging from 0.01 to 100 μM, are added into a cuvette and incubated for 4 min at 30 °C temperature before taking the absorption, and PL spectra. All PL spectra are recorded under the excitation at 300 nm. All the measurements were repeated thrice to ensure the reproducibility of results. For the comparison, UV-vis absorption and PL spectra of bare N-GQDs were also recorded.

5.2.3. Characterization Techniques

The detailed characterization techniques, such as TEM, XRD, Raman, UV-vis, PL, etc., used to study the present system were described in **Chapter 2, Section 2.2.3**. Raman spectra were recorded with 488 nm laser excitation. For the TRPL measurements, a 308 nm LED source was used as the excitation source. FTIR measurements were performed in PerkinElmer, Spectrum BX spectrophotometer in the reflectance mode.

5.3. Results and Discussion

5.3.1. Morphology Studies

Fig. 5.1(a) shows the TEM image of as-prepared N-GQDs with a homogeneous dispersion, and the average size of N-GQDs is observed as ~4.9 nm using the lognormal fitting of the corresponding size distribution, as shown in the inset. In addition, a well-resolved lattice fringe pattern with an interplanar spacing of ~0.19 nm is observed from the HRTEM image of the N-GQDs (see **Fig. 5.1(b)**), corresponding to (101) hexagonal lattice plane of graphite. **Fig. 5.1(c)** shows the TEM image of hexagonal Au NPs successfully grown using N-GQDs as a reducing agent, resulting in the Au@N-GQDs hybrid formation. The inset of **Fig. 5.1(c)** shows the HRTEM lattice fringes of Au NPs with a lattice spacing of ~0.22 nm, and 0.20 nm, corresponding to Au(111), and Au(002) planes, respectively.[13] The sizes of as-synthesized Au@N-GQDs are observed in the range of ~10–40 nm. Further, the presence of N-GQDs (size ~2–5 nm) on (111) facet of Au NP is observed in the HRTEM image of Au@N-GQDs, as shown in **Fig. 5.1(d),** confirming the good decoration of N-GQDs on Au NP surface. **Fig. 5.1(e, f)** show the high-resolution TEM images of Au@N-GQDs/DA after the addition of a very low concentration of DA

(0.06 µM), where DA nicely wraps on Au@N-GQDs. At relatively higher concentration of DA (0.4 µM), N-GQDs are observed to be detached partially from the Au NPs, and decorated uniformly over the surrounding DA cloud, as shown in **Fig. 5.1(g)**. This may be due to the reduced

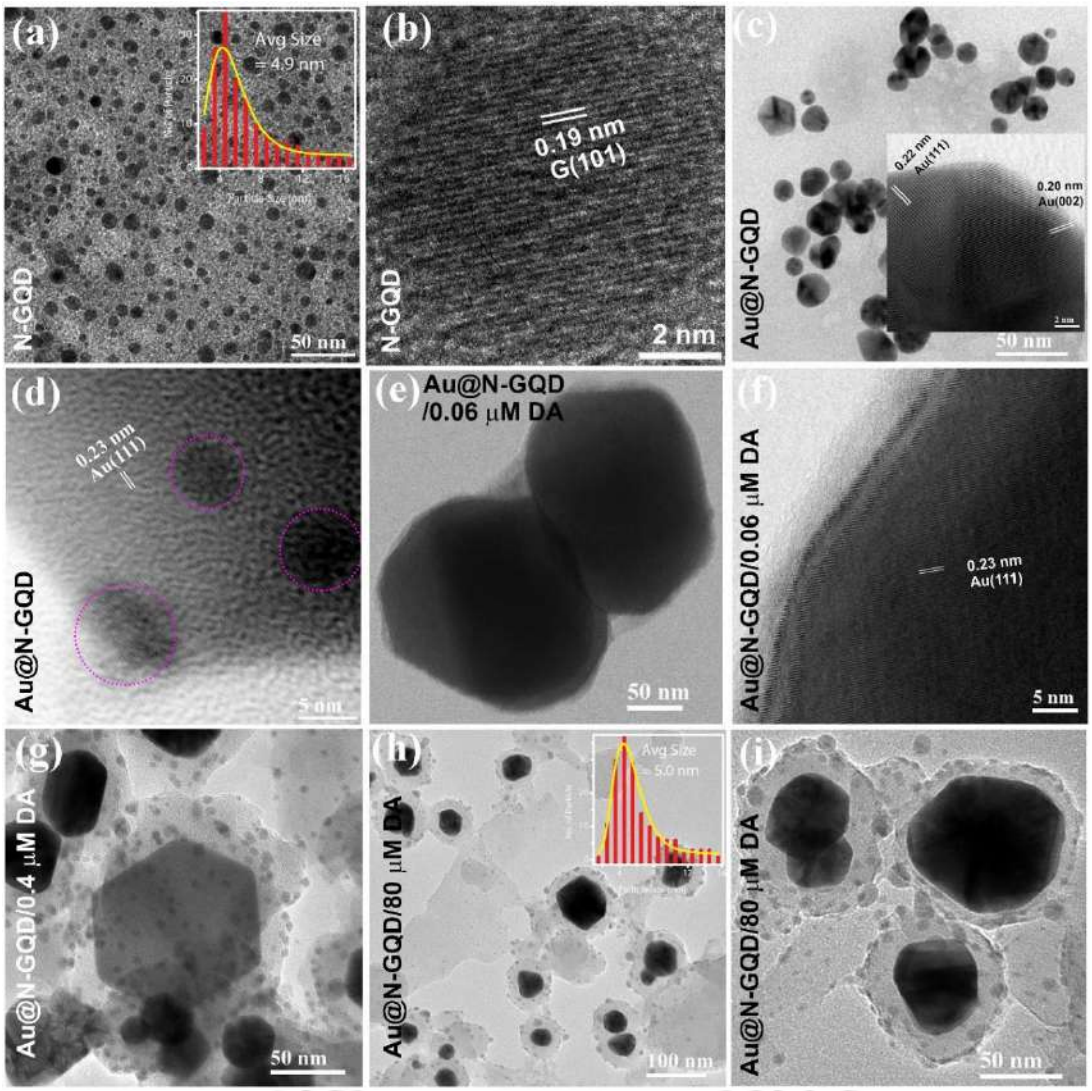

Fig. 5.1. (a) TEM image of N-GQDs with uniform size distribution, shown as an inset. (b) HRTEM of N-GQD with lattice spacing ~0.19 nm. (c) TEM image of Au@N-GQDs hybrids with the lattice fringes of Au NP facets in the inset. (d) HRTEM of Au@N-GQDs, showing the decoration of N-GQDs on Au NP surface with dotted circles. TEM, and HRTEM images of Au@N-GQDs with different DA concentrations: (e, f) 0.06 µM, (g) 0.40 µM, and (h, i) 80 µM. The inset of (h) shows the size distribution of N-GQDs at the periphery of the core-shell structure.

interaction between Au NP and N-GQDs in the presence of DA. **Fig. 5.1(h, i)** show the TEM images of Au@N-GQDs with DA concentration of 80 µM at different magnifications. Interestingly, at such a high DA concentration, Au NP and DA form a core-shell structure, where Au NP and DA act as core and shell, respectively, as shown in **Fig. 5.1(h, i)**. Interestingly, N-

GQDs are observed to be completely detached from the Au NP surfaces and accumulate at the periphery of the DA shell. Note that in some regions, N-GQDs and DA clouds are found together quite away from the Au NPs (see **Fig. 5.1(i)**), though it is very less compared to core-shell structures. The size distribution of N-GQDs in Au@N-GQDs/DA composite is shown in the inset

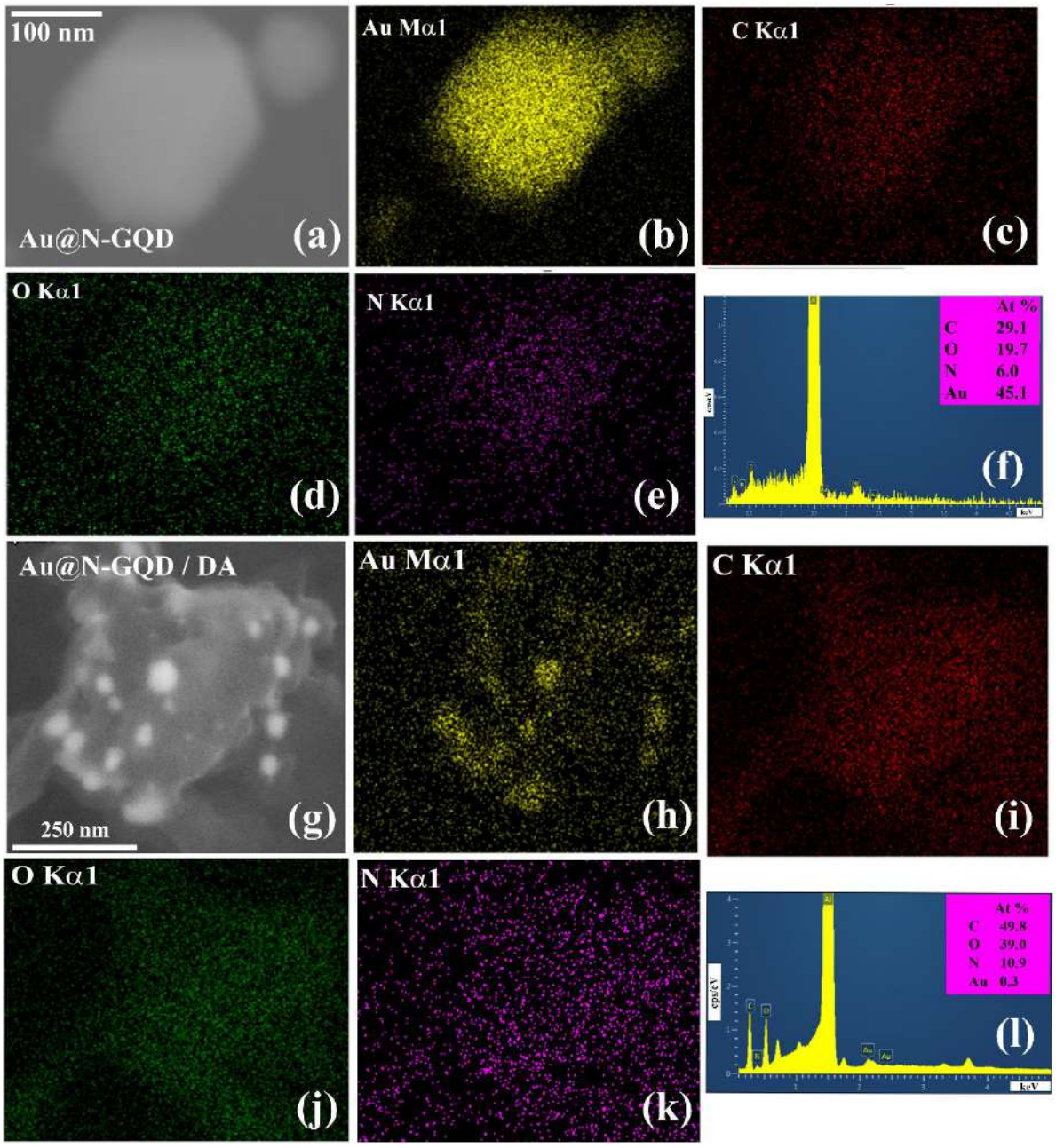

Fig. 5.2. (a) FESEM image of Au@N-GQDs, and (b-e) the corresponding elemental mapping is showing the spatial distribution of various elements. The scale bar is the same in all cases. (f) EDX spectrum showing the elemental compositions of Au@N-GQDs. (g) FESEM image of Au@N-GQDs/DA and (h-k) the corresponding elemental mapping of Au@N-GQDs/DA showing the spatial distribution of various elements. The scale bar is the same in all cases. (l) EDX spectrum showing the elemental composition of Au@N-GQDs/DA.

of **Fig. 5.1(h)**, which shows an average particle size of ~5 nm, consistent with the size of bare N-GQDs. For the analysis of the spatial distribution, and atomic percentage of the elementals present, FESEM image and the corresponding EDX mapping of Au@N-GQDs and Au@N-GQDs/DA are presented here. **Fig. 5.2(a)** shows the FESEM image of Au@N-GQDs on which the elemental mapping was performed. **Fig. 5.2(b-e)** exhibit the spatial distribution of the elements Au, C, O, and N, respectively. The EDX elemental mapping of Au@N-GQDs reveals that the Au NPs are uniformly decorated with N-GQDs, which is consistent with the TEM analysis. **Fig. 5.2(g-k)** show the FESEM image of Au@N-GQDs/DA and the corresponding spatial distribution of the elements Au, C, O, and N, respectively. Au NPs are observed to be decorated over the DA clouds. Note that DA and N-GQDs both contain carbon atoms. Further, the EDX spectra corresponding to Au@N-GQDs, and Au@N-GQDs/DA are shown in **Fig. 5.2(f, l)**, respectively, confirming the elemental compositions.

5.3.2. Structural Analysis

5.3.2.1. XRD Analysis

The XRD patterns of pristine DA, N-GQDs, Au@N-GQDs, and Au@N-GQDs/DA are shown in **Fig. 5.3(a)** to evaluate their crystalline structure and the changes in the crystalline planes after the hybrid formation. A broad diffraction peak at 2θ ~26.2° along with a small peak at 2θ ~43.0° correspond to (002), and (100) planes of N-GQDs, which has been discussed in **Chapter 3, Section 3.3.2.1**. The XRD pattern of Au@N-GQDs shows the diffraction peaks at 2θ ~38.2°, 44.5°, and 64.7°, which correspond to (111), (002), and (220) planes of face-centered-cubic (fcc) Au, respectively.[14] Interestingly, in Au@N-GQDs, (002) planes of N-GQDs is detected at a slightly higher angle (2θ ~26.5°), which is attributed to the contraction of the interplanar spacing of N-GQDs after attachment with Au NPs. Additionally, the XRD peak of (100) planes of N-GQDs becomes very weak after the attachment with Au NPs, while (101) peak appears significantly strong, as shown in the XRD pattern of Au@N-GQDs. With the addition of DA in Au@N-GQDs, (002) diffraction peak of N-GQDs is not clearly observed, which may be due to the passivation by the DA clouds. In addition, all the Au diffraction peaks are detected with slight peak broadening, indicating the formation of the Au@N-GQDs/DA composites.

5.3.2.2. Raman and FTIR Spectral Analysis

Results of micro-Raman studies on different samples are shown in **Fig. 5.3(b)**. To acquire detailed information about the change in the crystallinity and the attached functional groups, Raman spectrum of each sample is deconvoluted in the range of 1000–1725 cm^{-1} with multiple Lorentz

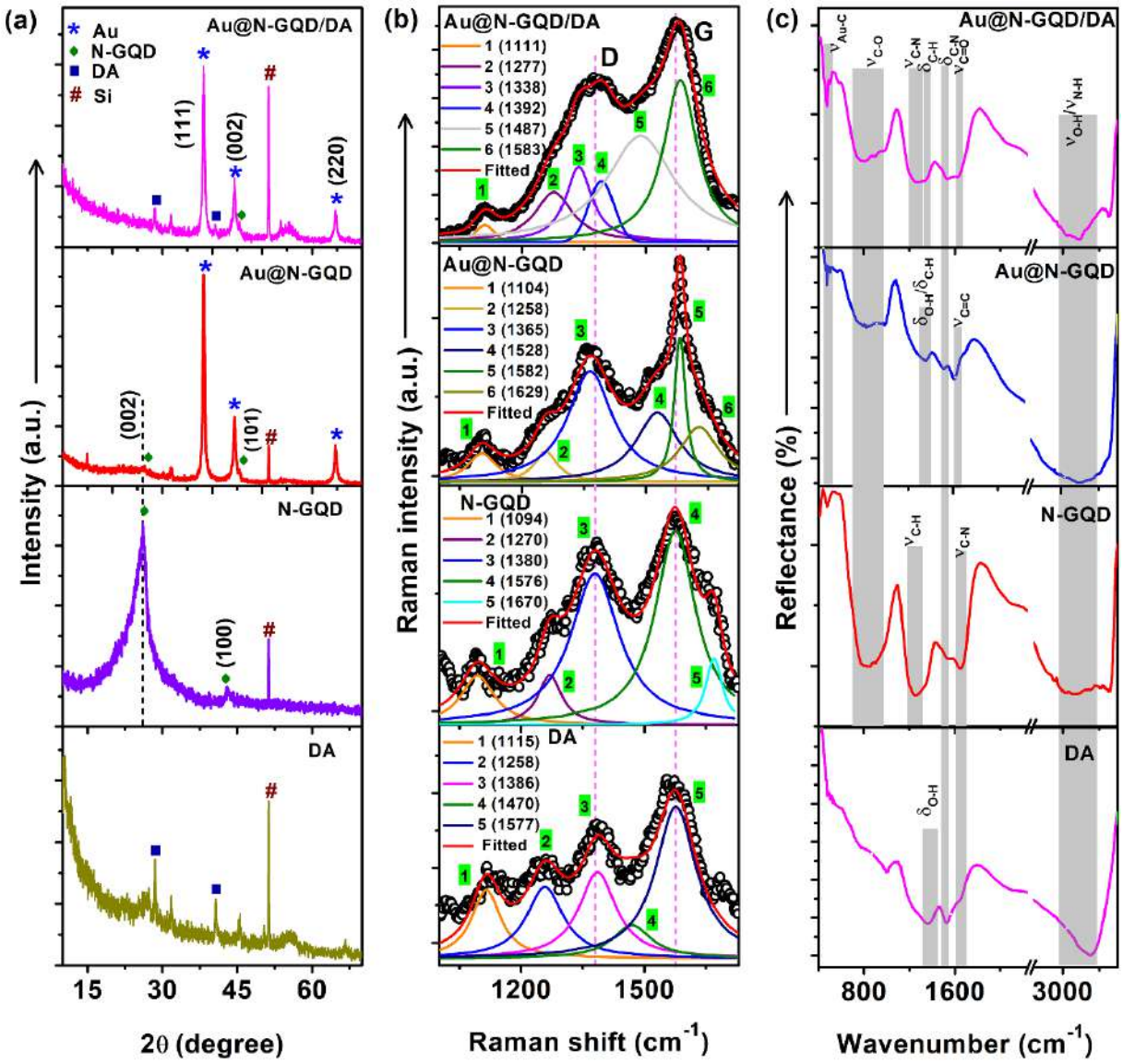

Fig. 5.3. A comparison of the (a) XRD pattern, (b) Raman spectra, and (c) FTIR spectra of pristine DA, N-GQDs, Au@N-GQDs, and Au@N-GQDs/DA. Each Raman spectrum is fitted with Lorentz peaks in the range of 1000–1725 cm^{-1}.

peaks. In the case of bare N-GQDs, the deconvoluted peak at ~1576 cm^{-1} shows the characteristic G band, which is associated with the in-plane phonon vibration of sp^2 carbon, and D band at ~1380 cm^{-1} confirms the lattice distortions/defects. The appearance of the other peaks in N-GQDs at

~1094 cm^{-1}, 1270 cm^{-1}, and 1670 cm^{-1} is due to the attached functional groups, associated with the stretching vibration of the C-C bond, tertiary dimethyl amines (C-N) group, and amide C=O bond, respectively.[15] As compared to N-GQDs, D band position in Au@N-GQDs is redshifted to ~1365 cm^{-1} due to the lattice distortion in N-GQDs caused by the local intensive plasmonic electromagnetic (EM) field induced by the Au NPs.[16] In contrast, G peak of Au@N-GQDs is blueshifted by ~6 cm^{-1} with a drastic reduction of FWHM (~87 cm^{-1}) attributed to the strong vibration of C=C bond in graphitic components by the influence of Au NPs. In comparison to N-GQDs, the blueshift in G band in Au@N-GQDs is attributed to the creation of compressive strain in sp^2 network of N-GQDs in the presence of Au NPs, which is consistent with the XRD analyses. Besides the characteristic D, and G band, the deconvoluted Raman spectrum of Au@N-GQDs shows the presence of Raman peaks at ~1104 cm^{-1}, and 1258 cm^{-1} with two new Raman active modes at ~1528 cm^{-1}, and 1629 cm^{-1}. The new peak at ~1528 cm^{-1} may be due to the lattice distortions in the sp^2 plane of N-GQDs caused by the formation of Au-C bonds.[17] The other peak at ~1629 cm^{-1} in Au@N-GQDs is assigned to the stretching vibration of C=N-OH, which confirms the additional functionalization of N-GQDs with O-H groups in the course of reduction of gold salt.[15] Additionally, the Raman peak at ~1258 cm^{-1} in Au@N-GQDs is attributed to the C-H bond vibration. The Raman mode at ~1670 cm^{-1} of N-GQDs is found to disappear after their interaction with Au NP surfaces, which may be due to the change of amines groups at the time of gold salt reduction. For Au@N-GQDs/DA, the deconvoluted Raman spectrum shows the D band and G band position at ~1392 cm^{-1}, and 1583 cm^{-1}, respectively. Interestingly, the appearance of Raman modes at ~1338 cm^{-1} (stretching vibration of C-O bond), and 1487 cm^{-1} (phenyl C=C stretching mode) only in Au@N-GQDs/DA confirm the attachment of DA with Au@N-GQDs.[18-20] The D band position in Au@N-GQDs/DA is observed to be upshifted from 1365 cm^{-1} to 1392 cm^{-1} as compared to the Au@N-GQDs, which is due to the detachment of N-GQDs from Au NPs. This is further confirmed from the disappearance of the Au-C bond vibration (~1528 cm^{-1}) in Au@N-GQDs/DA. Note that the value of I_G/I_D is ~2.5 for Au@N-GQDs/DA, while that for N-GQDs, and Au@N-GQDs are found to be ~1.3. The enhancement in G band intensity with DA addition may be due to the π-π interaction, and chemical bonding between N-GQDs, and DA due to the presence of aromatic rings in both the systems.[20, 21] The deconvoluted Raman spectrum of DA is also presented for comparison and it shows peaks similar to that of GQDs. In Au@N-GQDs/DA, the Raman peak for C-C stretching vibration mode appears at ~1111 cm^{-1}, while C-N bending

vibration mode of N-GQDs reappears at ~1277cm^{-1} with a blue shift of ~7 cm^{-1}, confirming the partial detachment of N-GQDs from Au NPs.

The FTIR spectra were recorded to know the changes in the vibrational modes and the chemical bonds before and after the addition of DA in Au@N-GQDs. In the FTIR spectra shown in **Fig. 5.3(c)**, the broad absorption peak in the region ~3000–3500 cm^{-1} for different samples is the characteristic band of the N-H stretching vibration and free hydroxyl group (O-H) vibration.[22, 23] In case of N-GQDs, the strong peaks detected at ~1651 cm^{-1}, and 1535 cm^{-1} correspond to the stretching, and in-plane bending vibrations of the C-N bond, respectively, and these confirm the successful doping as well as the functionalization of GQDs with nitrogen. The additional band at ~1253 cm^{-1} can be assigned as C-H_2 wagging vibration, while the other band in the region ~900–1100 cm^{-1} is due to the stretching vibration of C-O group, confirming the presence of oxygen-rich functional groups in N-GQDs.[15, 23] For Au@N-GQDs composite, a strong and sharp vibrational mode, corresponding to C=C bond, appears at ~1609 cm^{-1} due to the influence of surface plasmon resonance (SPR) in Au NPs, consistent with the Raman analysis. As compared to N-GQDs, C-N bending mode in Au@N-GQDs is observed to be downshifted from ~1535 cm^{-1} to 1521 cm^{-1}, implying the attachment of N-GQDs with Au NPs by the C-N related functional groups. Additionally, a peak at ~1355 cm^{-1} corresponding to C-H/O-H bending vibration is observed in Au@N-GQDs, which is in agreement with the Raman analysis. The presence of a strong, and sharp band at ~475 cm^{-1} is due to the Au-C bond formation, which confirms the strong attachment of Au with N-GQDs.[15, 24] The FTIR spectrum of Au@N-GQDs/DA shows two distinct peaks at ~1535 cm^{-1}, and 1682 cm^{-1} within a broad absorption band corresponding to C-N bending vibration, which is probably due to the CONH or CNH composite formation.[15] The absorption peak at ~1363 cm^{-1} arises from the vibration of O-H functional groups in DA, and it disappears entirely after the attachment with Au@N-GQDs, while the appearance of an absorption peak at ~1682 cm^{-1} corresponding to C=O vibration in Au@N-GQDs/DA implies the conversion of catechol groups of DA into C=O bond in the presence of Au@N-GQDs. Interestingly, the reappearance of the absorption peak for C-N bending vibration in Au@N-GQDs/DA at the identical position to that of N-GQDs (~1535 cm^{-1}) confirms the detachment of N-GQDs from Au NPs through the influence of DA, and it is consistent with the TEM analysis. Note that in Au@N-GQDs/DA, two absorption bands for C-O, and C-H bond vibrations at ~1270 cm^{-1}, and 1343 cm^{-1}, respectively, show peak broadening due to the influence of DA.

5.3.3. Optical Analysis

In the present work, DA is detected in dual mode with Au@N-GQDs. First, colorimetric sensing of DA by UV-vis absorption and then fluorescence based sensing of DA with the change of PL intensity of Au@N-GQDs are presented here.

5.3.3.1. Colorimetric Sensing of Dopamine

Fig. 5.4(a) shows the comparison of UV-visible absorption spectra of as-prepared N-GQDs and Au@N-GQDs. The optical absorption of N-GQDs is mainly dominant in the UV region with a hump at ~274 nm due to the π-π* transition of sp^2 hybridized carbon components, while an extended tail up to 650 nm is attributed to the n-π* transition, as discussed in **Chapter 3, Section 3.3.3.1**. For the case of Au@N-GQDs, two strong characteristic absorption peaks at ~300 nm and 543 nm are attributed to the characteristic absorption peaks of N-GQDs and Au NPs, respectively. It is reported that the Au NPs with size ~10–40 nm exhibit the SPR absorption band peaked at ~530 nm.[25] However, in the present case the SPR absorption peak of Au NPs in Au@N-GQDs is observed to be redshifted by ~13 nm, which may be due to the hybrid formation of metallic Au NPs with N-GQDs.[26] For the synthesis of Au@N-GQDs, the ratio of $HAuCl_4$, and N-GQDs was optimized based on SPR absorption wavelength maxima. In each case, the amount of N-GQDs was varied, keeping $HAuCl_4$ concentration fixed (5 mM). The variation of the SPR absorption peak position with the amount of N-GQDs is shown in the inset of **Fig. 5.4(a)** and it reveals that the smallest size Au NPs is formed with 0.7 mg/mL of N-GQDs. Since sensing mechanism in the present case is related to the surface interactions, the smallest size of Au@N-GQDs is preferred due to its high surface area. Thus, 0.7 mg/mL N-GQDs with 5 mM $HAuCl_4$ is chosen as the optimum ratio for further experiments. For DA, the characteristic absorption peak for aromatic carbon (C=C) appears at ~277 nm. Note that no signature of oxidation of DA was observed in our sample does due to the absence of any peak at ~350 nm (see **Fig. 5.4(b)**)[27, 28]. After the addition of DA with Au@N-GQDs (sample A2), a systematic enhancement in the absorption intensity, and the broadening of the absorption peak at ~300 nm is observed with increasing concentration of DA, as shown in **Fig. 5.4(c)**, which may be due to the formation of a composite of N-GQDs with DA. The enlarged view of the SPR absorption peak (~510–580 nm) in Au@N-GQDs with different concentrations of DA is presented in the inset of **Fig. 5.4(c)**. The N-GQDs/DA composite formation is supported by the shift in the absorption peak of Au@N-GQDs from 300–306 nm, as shown in **Fig. 5.4(b)**. Due to the formation of a composite with DA, the reduction of charge density

in N-GQDs forces the detachment of N-GQDs/DA from Au NP surfaces. Thus, with the increasing concentration of DA, electron density in Au NPs and the corresponding SPR absorption intensity

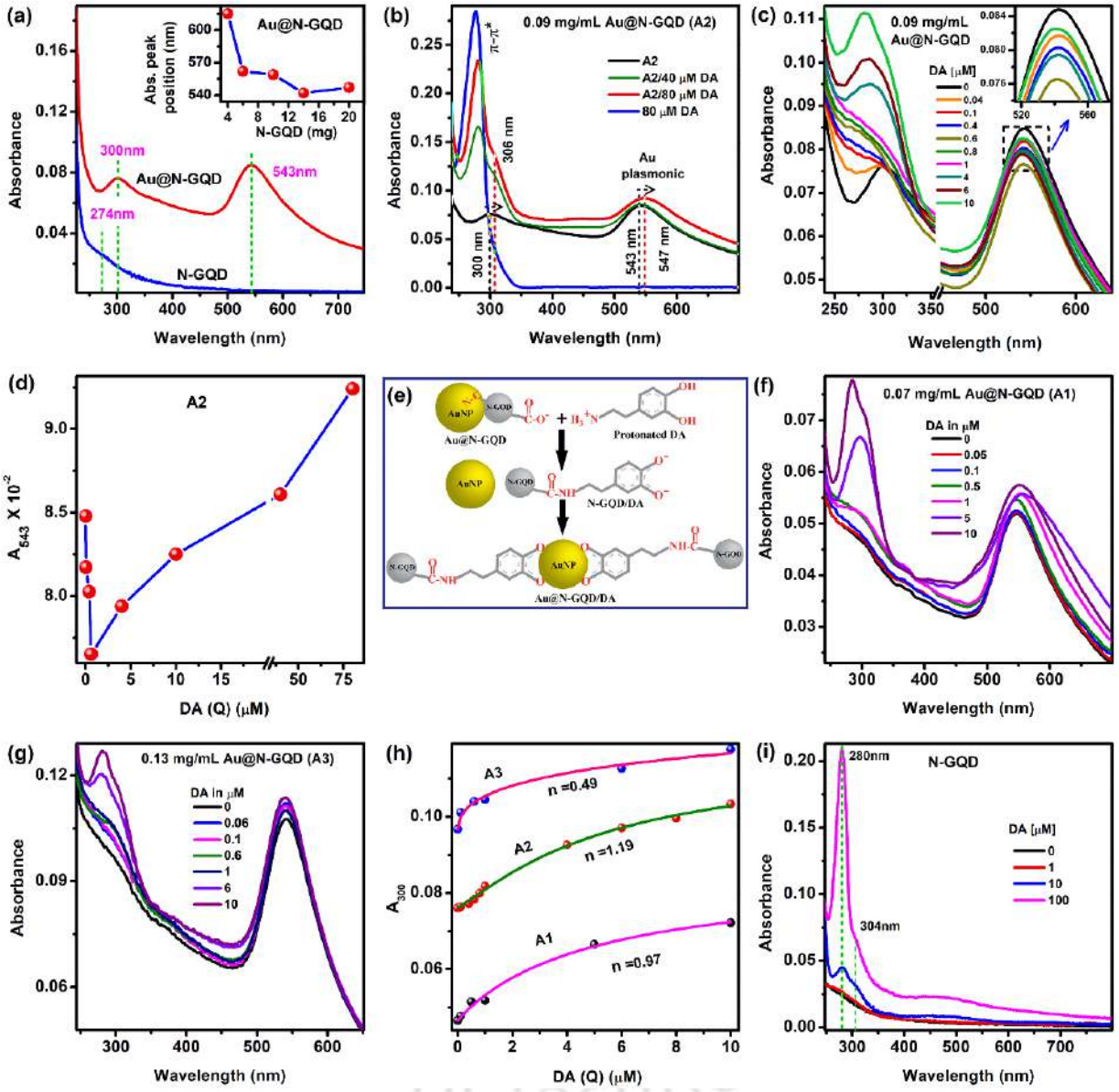

Fig. 5.4. (a) Comparison of UV-vis absorption spectra of N-GQDs, and Au@N-GQDs. The inset shows the change in absorption peak position with N-GQDs concentration for the optimization of the growth of Au@N-GQDs. (b) Comparison of the absorption spectra of DA, Au@N-GQDs, and their composite; the redshift in the absorption peak of N-GQDs with the addition of DA is indicated with a vertical dashed line. (c) The change of the UV-vis absorption of Au@N-GQDs (A2) with various concentrations of DA (0–10 μM). The inset shows the enlarged view of the SPR absorption in the range of ~510–580 nm. (d) The change in SPR absorption intensity of Au@N-GQDs at ~543 nm with DA concentration. (e) A schematic of the stepwise interaction of DA with Au@N-GQDs. The change in the absorption spectra of (f) A1, and (g) A3 with different concentrations of DA. (h) Comparison of the change in the absorption intensity of Au@N-GQDs at ~300 nm with different concentrations of DA for A1, A2, and A3. Experimental data in each case is well fitted with the Hill equation, and the corresponding 'n' value is shown in each case. (i) Evolution of the absorption spectra of N-GQDs with different concentrations of DA (0, 1, 10, and 100 μM).

reduce, while the absorption intensity of N-GQDs (~300 nm) increases monotonically. Interestingly, a further increase of DA concentration leads to the enhancement in intensity and a redshift of the SPR absorption peak. The redshift of the SPR absorption peak may be due to the interaction of Au NPs with DA, while the increased SPR absorption indicates the migration of electrons towards Au NPs.[29] **Fig. 5.4(d)** shows the change in the SPR absorption intensity at ~543 nm (A_{543}) with the variation of DA concentration. After the detachment of N-GQDs from Au NP surfaces, Au NPs become more active to recover the reduced electron density, and as a result, they can actively attach with electron-rich phenoxide-enolate, following further ground state composite formation between N-GQDs, and DA, resulting in the enhancement of the absorption intensity at ~300 nm. A schematic of the interaction mechanism of DA with Au@N-GQDs is shown in **Fig. 5.4(e)**. Before the addition of DA, there is a strong coupling/bonding between Au NPs, and N-GQDs possibly through Au-C/C-N bonds. At low concentrations of DA, N-GQDs make N-GQDs/DA composites, and eventually, they are detached from Au NPs. With further increase of the DA concentration, N-GQDs/DA makes a shell-like structure surrounding the Au NPs. It is reported that DA has a good ionizing property due to two acidic protons with a value of ~9 pK.[30] In a neutral medium, DA behaves like a positively charged particle with ($-NH_3^+$) groups (known as protonated DA), while in N-GQDs, oxygen-rich functional groups, such as COOH, C=O, C-O-C, OH behave as negatively charged terminals.[6, 31, 32] Thus, high content of oxygen-rich functional groups at the edge as well as at the basal plane of N-GQDs can easily form a composite by neutralizing the amine group of protonated DA (CONH, CNH bond formation), whereas, the aromatic ring of N-GQDs and DA can also be attached by noncovalent interaction with π-π stacking.[20, 32, 33] Due to the interaction of DA with N-GQDs, N-GQDs/DA composite is forced to detach from Au NP surfaces, and after the detachment the electron density of Au NPs reduces. Consequently, Au NPs become more active to accept electrons for recovering their electron density. Since DA is converted to protonated DA (NH_3^+) in the neutral medium, the formation of stable dopamine-o-quinone (DQ) structure is not favorable for it.[31] After its attachment with N-GQDs, protonated DA becomes neutralized, and may leave acidic protons of the catechol groups to get a stable structure of DQ via phenoxide-enolate formation.[30] Due to the high electron affinity, Au NPs readily accept the phenoxide-enolate through their negative charge terminals, forming a core-shell structure with DA, keeping N-GQDs at the periphery of the shell (see **Fig. 5.1(i)**). Note

that the detachment of the N-GQDs from Au NPs surfaces makes Au NPs more active as an electron acceptor, accelerating composite formation between N-GQDs, and DA.

Further, the change in absorption with DA concentrations are also repeated with two other stock solution of Au@N-GQDs (A1, and A3), and the similar results are obtained, as shown in **Fig. 5.4(f, g)**. Based on the change in the absorption intensity at ~300 nm, a novel sensor is proposed here for the detection of DA, following the well-known Hill equation. The Hill equation is a very useful tool in biochemistry and pharmacology to describe the binding of a ligand to a macromolecule. The Hill equation was originally formulated by Archibald Hill in 1910 to study the O_2 binding with hemoglobin.[34] Afterwards, Hill equation was well studied for analyzing the degree of cooperativity from Hill coefficient of ligand binding.[35, 36] According to the literature, the Hill equation is formally equivalent to Langmuir isotherm, while the Hill coefficient was reported as the interaction coefficient.[37, 38] In order to study the detection of DA by Au@N-GQDs hybrid system, the absorption intensity at ~300 nm (A_{300}) for various DA concentration (Q) is fitted with the following Hill equation,

$$A_{300} = S + \frac{(E-S)Q^n}{Q^n+K^n} \qquad (5.1)$$

where 'E', 'S', and 'K' are the constants. and 'n' is the interaction coefficient. If n >1, the system shows positive cooperativity, i.e., an increase in the affinity of a binding site due to the previous binding of a ligand to another site.[39] It is also reported that due to the multiple binding sites, n <1 is also possible for the binding of a ligand.[40] In the case of strong interaction, n >1 is observed. The plot of A_{300} vs. Q for each concentration of Au@N-GQDs is well fitted by the Hill equation in the concentration region 0.1–10.0 μM and the corresponding value of interaction coefficient are found to be n_{A1} =0.97, n_{A2} =1.19, and n_{A3} =0.49 for A1, A2, and A3, respectively, as shown in **Fig. 5.4(h)**. It is evident from the 'n' values that the interaction is stronger in the case of A2. As compared to earlier reports, efficient detection of DA with Au@N-GQDs is carried out here in a wider concentration range (0.04–10 μM), as listed in **Table 5.1**. The value of interaction coefficient (n) from the fitting with the Hill equation can be used for the prediction of optimum condition (concentration of Au@N-GQDs stock solution) to achieve efficient DA sensing. For A1, as N-GQDs are less in amount, the absorption intensity corresponding to N-GQDs/DA composite at ~300 nm is low (see **Fig. 5.4(f)**), while for A3 the corresponding absorption is higher due to

high content of N-GQDs. Despite a lower concentration of N-GQDs in A1, a larger value of interaction coefficient (n_{A1} =0.97) in A1 than that of A3 (n_{A3} =0.49) indicates the possible interaction between DA and Au NPs, besides the interaction between DA and N-GQDs. In the dilute solution, as the amount of Au@N-GQDs is less, these are well separated from each other,

Table 5.1. *Comparison of different colorimetric and fluorometric sensors reported for dopamine detection.*

Sensing platform	*Sensing mechanism*	*Method of detection*	*Detection range*	*LOD (nM)*	*Ref.*
Au NP	Aggregation	Absorption	1.0 nM−1.0 μM	5000.0	[32]
Citrate cap-Ag NP	Aggregation	Absorption	0−0.6 μM	60.0	[6]
Au NP with Cu^{+2}	Aggregation	Absorption	0.5-10 μM	200.0	[7]
Beta-cyclodextrin modified Au NP	Aggregation	Absorption	20−250 nM and 350−1600 nM	3.0	[8]
Au@N-GQDs	Core-shell formation	Absorption	0.04−80 μM	40.0	***This work***
GQDs	Charge transfer	PL quenching	0.01−60 μM	8.0	[41]
GQDs	Charge transfer	PL quenching	0.25−50 μM	90.0	[33]
N-GQDs	Charge transfer	PL quenching	1−200 μM	70.0	[4]
Polypyrrole/GQDs	Charge transfer	PL quenching	5−8000 nM	0.01	[5]
Dopamine modified Carbon NP with Fe^{+3}	Charge transfer	PL recovery	0.1−10 μM	68.0	[42]
Carbon Dot, and Au NP	Aggregation of Au NP	PL recovery	0.5−3 μM	37.0	[43]
Au@N-GQDs	Core-shell formation	PL quenching	0−100 μM	430.0	***This work***

and DA may easily separate N-GQDs from the Au NP surfaces by the formation of N-GQDs/DA composite even at a lower concentration of DA. On the other hand, at higher concentrations of Au@N-GQDs, metallic Au NP surface is highly crowded with N-GQDs, and thus higher concentration of DA is further involved in the N-GQDs/DA composite formation than the interaction with Au NP surfaces. Thus, for A2 and A3, a higher absorption intensity at ~300 nm

indicates that the absorption at ~300 nm arises from the interaction between DA and N-GQDs. Though 'n' value decreases with increasing concentration of Au@N-GQDs stock solution, an intermediate concentration (A2) shows a high interaction coefficient (n_{A2} =1.19) indicating a high affinity of DA towards Au@N-GQDs with an optimum concentration of Au@N-GQDs (0.09 mg/mL). The highest value of n_{A2} confirms that Au NPs play an energetic role in the interaction between DA and N-GQDs. For A1, and A2, the SPR absorption peak of Au@N-GQDs becomes broader and redshifted, whereas for A3, the SPR absorption intensity increases without any shift. This may be explained on the basis of better interaction of DA with Au NPs for A1, and A2, while for A3, mainly free metallic Au NP surfaces are responsible for the enhanced SPR absorption. Thus, to achieve efficient detection of DA, the optimum concentration of Au@N-GQDs is essential, and in the present case, A2 is observed to be the optimum concentration. To support the role of Au NPs, the change in absorption of bare N-GQDs in presence of DA at different concentrations is shown in **Fig. 5.4(i)**. Relatively higher absorption intensity and the broadening is observed for Au@N-GQDs, confirming the significant effect of the metallic Au NPs for a higher fraction of N-GQDs/DA composite formation.

5.3.3.2. Fluorescence Sensing of Dopamine

The efficient detection of DA based on the quenching of the fluorescence intensity of Au@N-GQDs is also carried out here. The PL spectra of N-GQDs and Au@N-GQDs are shown in **Fig. 5.5(a)** under 300 nm excitation. As compared to N-GQDs, the high intense PL with an emission peak at ~414 nm of Au@N-GQDs is due to the high absorption of N-GQDs in presence of Au NPs. Before detecting DA, a series of experiments were performed to find the most appropriate conditions for the effective sensing of DA in the proposed scheme. The PL intensity of as-prepared Au@N-GQDs stored at room temperature is monitored at certain intervals, as shown in **Fig. 5.5(b)**. The fluorescence response of Au@N-GQDs is stable, with only ~1.8% reduction of the PL intensity at the end of four weeks period. This indicates the high stability of Au@N-GQDs hybrid for sensing applications. To get the best quenching efficiency in the hybrid system, different concentrations of stock solution of Au@N-GQDs are tested with 10 μM concentration of DA. The bar diagram of the relative change of the PL intensity (I_0/I) (where I_0 and I are the PL intensity at ~414 nm before and after the addition of DA with Au@N-GQDs, respectively) with different stock solutions of Au@N-GQDs (see **Fig. 5.5(c)**) reveals that A2 achieves maximum quenching efficiency. The sensitivity of the developed method for DA detection is strongly influenced by the

pH value of the sensing environment. The pH of the solution is the key factor for the sensitivity of the system since the pH affects the generation of protonated DA (NH_3^+), and consequently, the composite formation. The change in the PL intensity is presented in **Fig. 5.5(d)** before and after

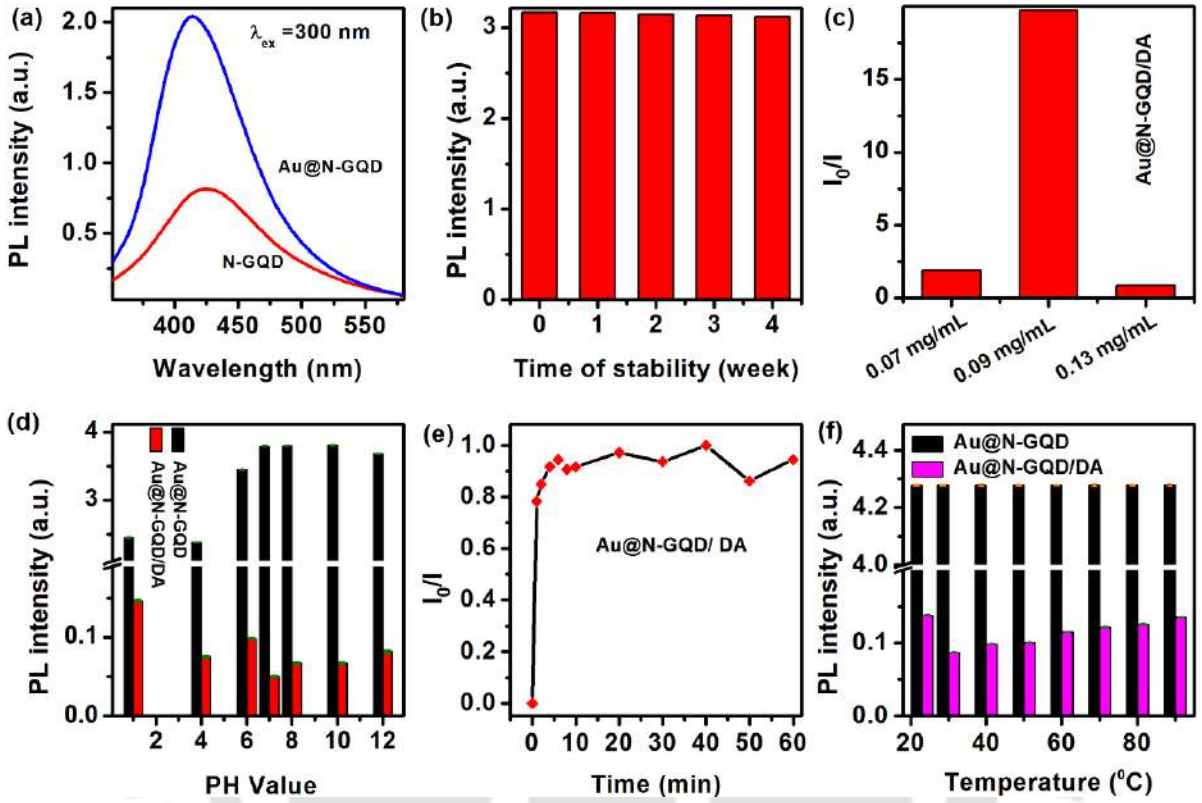

Fig. 5.5. (a) Comparison of PL spectra of N-GQDs, and Au@N-GQDs. (b) The photostability of Au@N-GQDs based on PL intensity at the excitation of 300 nm. Optimization of the DA sensing parameters: (c) various concentrations of Au@N-GQDs, (d) pH value of the solution, (e) reaction time, and (f) temperature.

the addition of DA into Au@N-GQDs solution with the variation of the reacting buffer (pH =1–12). The fluorescence intensity of Au@N-GQDs is found to be pH-dependent, and it remains stable in the pH range of 7–12, but decreases below pH 7. When pH <6, COOH functional groups of N-GQDs act as neutral, and they hardly interact with the NH_3^+ group of protonated DA. With increasing pH values of the medium, the COOH group acts as COO^- , while DA is converted to DQ through the formation of phenoxide-enolate for pH >9 (pk_a ~9 for DA). In alkaline medium, the possibility of the composite formation between N-GQDs and DA is less, since the negatively charged carboxylic groups and phenoxide-enolate repulse each other. In the pH range 6–9, the ground state composite formation between COO^- of N-GQDs, and NH_3^+ group of protonated DA can take place. The maximum PL quenching is observed at pH 7, and thus pH 7 is considered as

the optimum pH for the sensitive detection of DA. The reaction time of the sensing was also investigated under the optimal pH and the concentration of the stock solution. **Fig. 5.5(e)** shows the normalized value of the relative change of PL intensity (I_0/I) with reaction time. The fluorescence intensity drops rapidly, and it is almost constant after 4 min. Therefore, 4 min is chosen as an optimum reaction time for further analysis. The effect of temperature on the efficient PL quenching was also studied. As shown in **Fig. 5.5(f)**, the degree of quenching is the highest at 30 °C and hence this temperature is the optimal temperature for efficient sensing. Thus, our sensor is most sensitive for room temperature operation, which is always desirable. Under the optimized conditions, the comparative PL spectra of A2 at various concentrations of DA (0.0–0.4 μM, and 0.6–100.0 μM) is monitored carefully, as presented in **Fig. 5.6(a-d)**. At a very low concentration of DA, the PL intensity is found to be quenched, and then PL intensity of the system is partially recovered with DA concentration in the range of 0.08–0.40 μM, as shown by the dashed/dotted lines in **Fig. 5.6(a)**. **Fig. 5.6(b)** shows the corresponding calibration graph of the fluorescence intensity ratio I_0/I vs. DA concentration (in μM). Interestingly, at a higher concentration of DA (0.6–100.0 μM), a monotonic decrease in the PL intensity is observed in **Fig. 5.6(c)**, and this region of concentration is considered for DA sensing application. **Fig. 5.6(d)** depicts the corresponding variation of I_0/I with DA concentration for the detection of DA in the concentration (Q) range of 1.0–100.0 μM and it shows a linear variation of I_0/I with Q given by

$$\frac{I_0}{I} = 1 + 0.51Q \qquad (5.2)$$

The value of LOD, determined by the 3σ/b (σ is the standard deviation of the lowest signal, and b is the slope of eqn. (5.2)), is calculated to be ~430 nM, which is comparable with the reported values using fluorescence method, as presented in **Table 5.1**. The calculated LOD value is consistent with the experimental observations, since the non-monotonic nature extends up to 0.40 μM DA concentration, and beyond it, the linear region of sensing starts. To verify the unusual behavior of the PL intensity of Au@N-GQDs in the presence of DA, the different stock solutions of Au@N-GQDs (A1 and A3) are also studied, as shown in **Fig. 5.6(e-h)**. In each case, similar behavior is observed in the change of PL intensity with DA concentration. For A2 and A3, initially the PL intensity reduces systematically, and then partially recovered, followed by the reduction in the PL intensity with increasing DA concentration. When the concentration of DA is low, the formation of covalent bond between the NH_3^+ group of DA and oxygen coupled functional groups

of N-GQDs facilitate a systematic reduction in the PL intensity by the ground state complex formation. Due to the N-GQDs/DA composite formation, N-GQDs are partially detached from Au NP surfaces, as discussed in **Section 5.3.3.1**. Thus, the exposed surface area of the functionalized

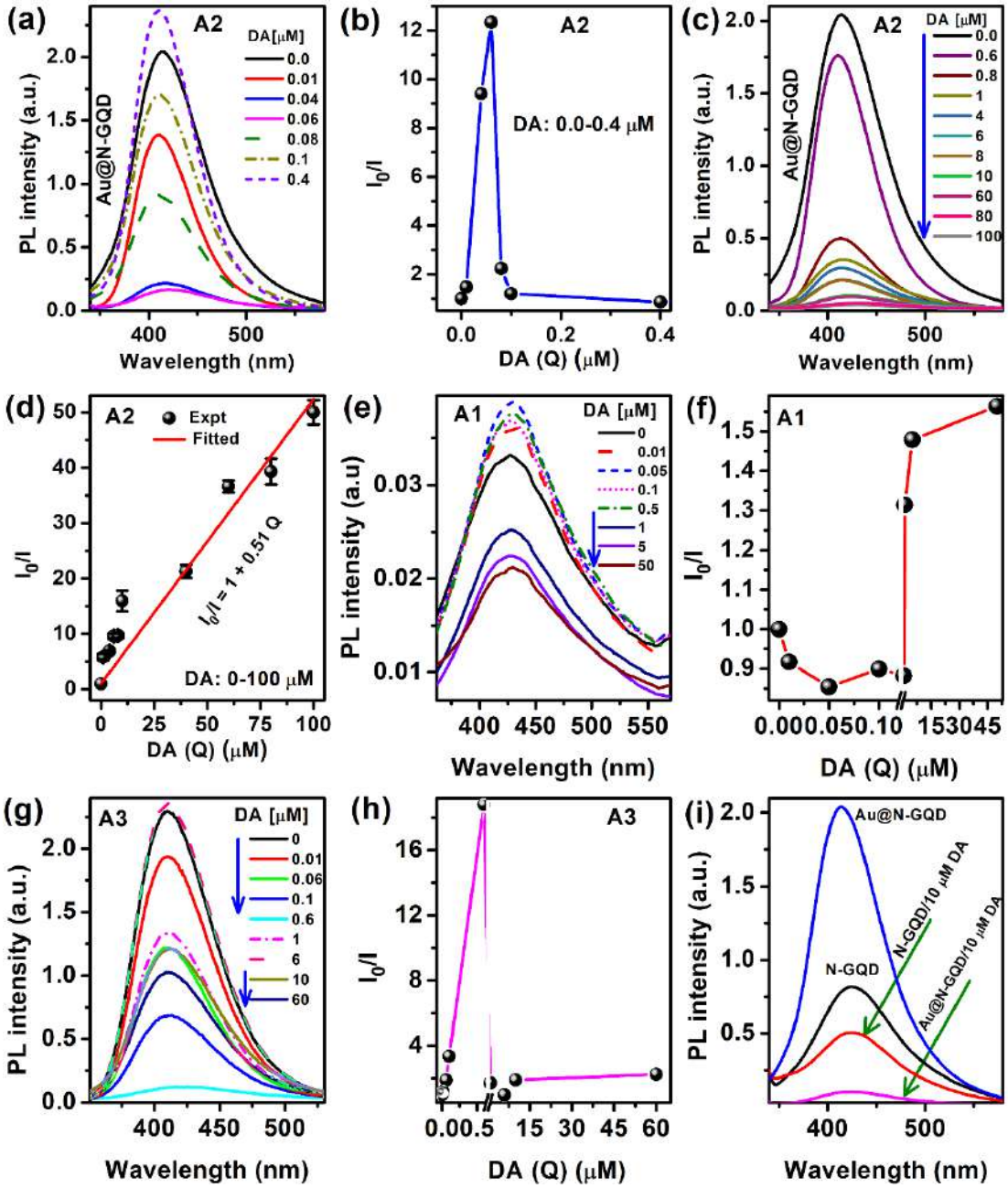

Fig. 5.6. (a) The evolution of the PL spectra of Au@N-GQDs (A2) with the addition of DA in the concentration range of 0.0–0.4 μM, and (b) the corresponding variation of I_0/I with DA concentration following a non-monotonic behavior. (c) The change of the PL intensity of A2 at higher concentration of DA (0.6–100.0 μM) showing systematic quenching of PL. (d) PL intensity (I_0/I) as a function of DA concentration, showing a linear Stern-Volmer plot in the concentration range of 1–100 μM. (e) The change in the PL spectra of A1, and (f) the corresponding relative change in the PL intensity as a function of DA concentration; (g, h) the same for A3. (i) Comparison of the PL quenching of N-GQDs, and Au@N-GQDs after the addition of 10 μM DA.

N-GQDs increases naturally, and the PL starts to recover partially in the concentration region of 0.08–0.4 μM for A2. Besides the N-GQDs/DA ground state complex formation, Au NPs and DQ, being good electron acceptors, may extract electrons from N-GQDs, which may quench the PL intensity further in a higher DA concentration region. In the case of A1, due to the low concentration of N-GQDs, initially the PL intensity recovers by the detachment of N-GQDs from Au NP surfaces and then it quenches at a higher concentration of DA. For A3, despite more ground state complex formation, more DA is involved to make the surface of Au NPs free and thus a lower interaction of Au NPs and phenoxide-enolate occurs in A3. Further, **Fig. 5.6(i)** shows the PL spectra of N-GQDs and Au@N-GQDs before and after the addition of 10 μM DA. Quenching in PL intensity is measured to be ~1.57 times, and ~20.4 times for N-GQDs, and Au@N-GQDs, respectively. Therefore, an enormous quenching in PL intensity is achieved in the presence of Au@N-GQDs, which enables it as a superior fluorometric sensor for DA.

5.3.3.3. Time-Resolved Photoluminescence Study

For the confirmation on the contribution of the charge transfer process in the PL quenching of Au@N-GQDs with DA, a comparative study of the TRPL spectra is presented in **Fig. 5.7**. TRPL spectra of N-GQDs, and Au@N-GQDs before and after the addition of different concentrations of DA were monitored at their respective emission peaks. Each spectrum is fitted with the bi-exponential decay function, as discussed in **Chapter 2, Section 2.3.3.3**. The bi-exponential decay behavior of the PL intensity suggests the presence of two emissive sites, which are usually attributed to the sp^2 domains, and functional groups at the edge of Au@N-GQDs.[44] For N-GQDs, τ_{avg} is calculated to be ~6.0 ns, while that of Au@N-GQDs is ~5.1 ns, as shown in **Fig. 5.7(a, b)**, respectively. In the case of Au@N-GQDs, electrons are transferred from N-GQDs to Au NPs due to the higher electron affinity of Au NPs. The overlap of the emission spectrum of N-GQDs with the SPR absorption spectrum of Au NPs supports the possible electron transfer from N-GQDs to Au NPs.[45] In Au@N-GQDs, the quenching of the PL intensity due to the electron transfer is possible only when the radiative excitons of the system are transferred to other material or suffer from non-radiative recombination. At a low concentration of DA (0.06 μM), there is a negligible change in the decay time (τ_{avg} ~5.9 ns) of Au@N-GQDs/DA as compared to that of N-GQDs, and it confirms that the quenching in lower concentration region is only due to the ground state N-GQDs/DA complex formation (see **Fig. 5.7(c)**). At higher concentrations of DA, the high electron

affinity of Au NPs, and DQ facilitate the electron transfer from N-GQDs, which in turn results in the fast decay (τ_{avg} ~4.4 ns) for Au@N-GQDs/4 μM DA, as shown in **Fig. 5.7(d)**. Thus, the presence of Au NPs accelerates the fast electron transfer, resulting in the high rate of composite formation, and PL quenching.

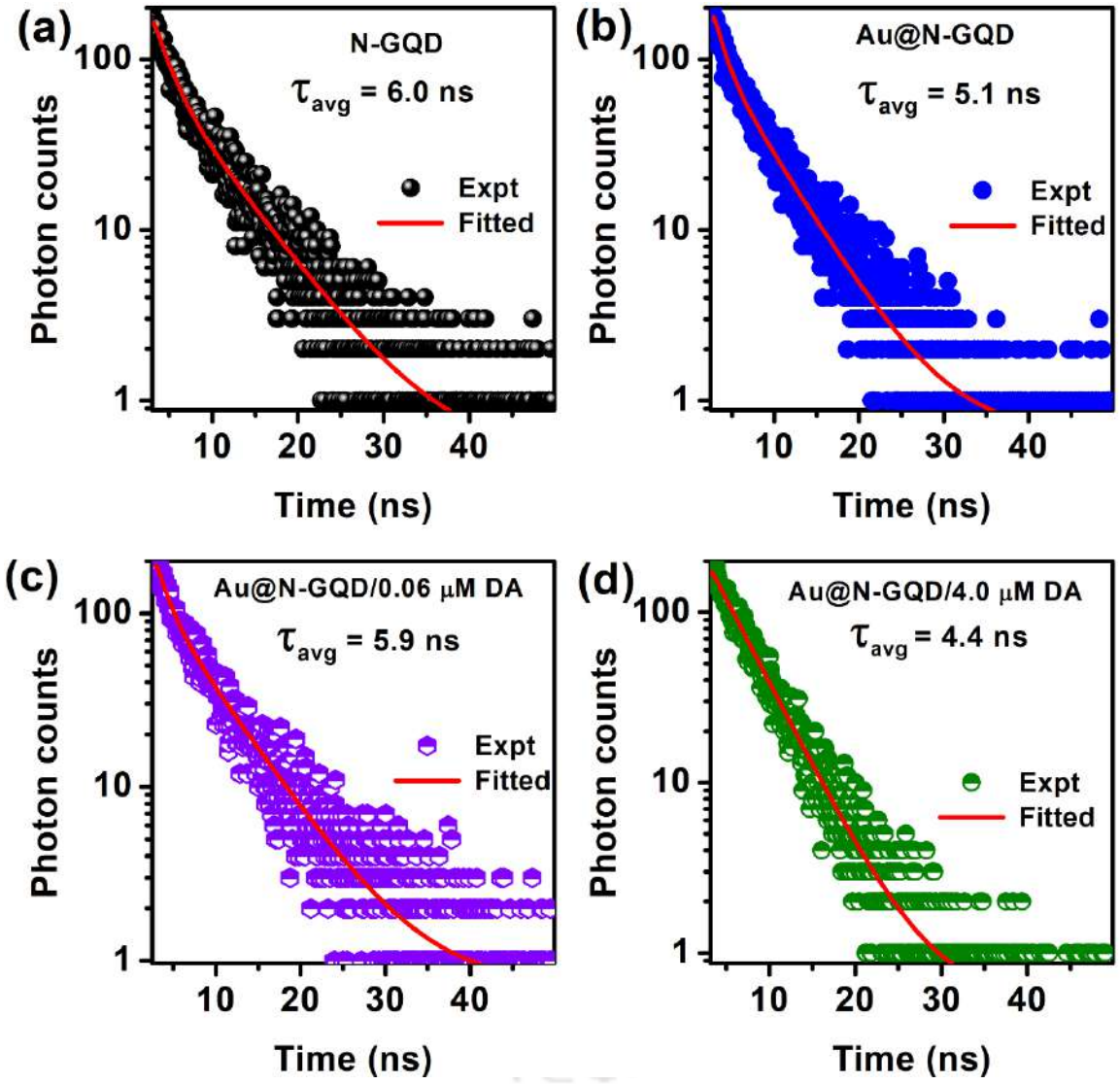

Fig. 5.7. TRPL spectra of (a) N-GQDs, (b) Au@N-GQDs, (c) Au@N-GQDs/0.06 μM DA, and (d) Au@N-GQDs/4.0 μM. DA.

5.3.4. Selectivity of Dopamine Sensing

For the detection of DA in the real samples, not only the sensitivity but also the selectivity is very important because of the possible interference from different metal ions and other biomolecules. In order to investigate the selectivity of the sensing, i.e., PL quenching, and the change in

absorption intensity of Au@N-GQDs with DA, common interference species, such as metal ions (Ag^{+}, Co^{+2}, Cu^{+2}, Hg^{+2}, Pb^{+2}, Cr^{+3}, Al^{+3}, Cd^{+2}, Mg^{+2}, Mn^{+2}, Ni^{+2}, Fe^{+2}, Na^{+}, K^{+}, and Zn^{+2}), and biomolecules (ascorbic acid (AA), uric acid (UA), hydroquinone (HQ), glucose (Gls), glycine (Gly), thiourea (thio), L-cysteine (L-Cys), and glutamic acid (Glu)) at a concentration of 10 μM are considered here under the identical experimental conditions. **Fig. 5.8(a)** shows the relative change of the PL intensity (I_0/I) of Au@N-GQDs with different species. The strong PL quenching

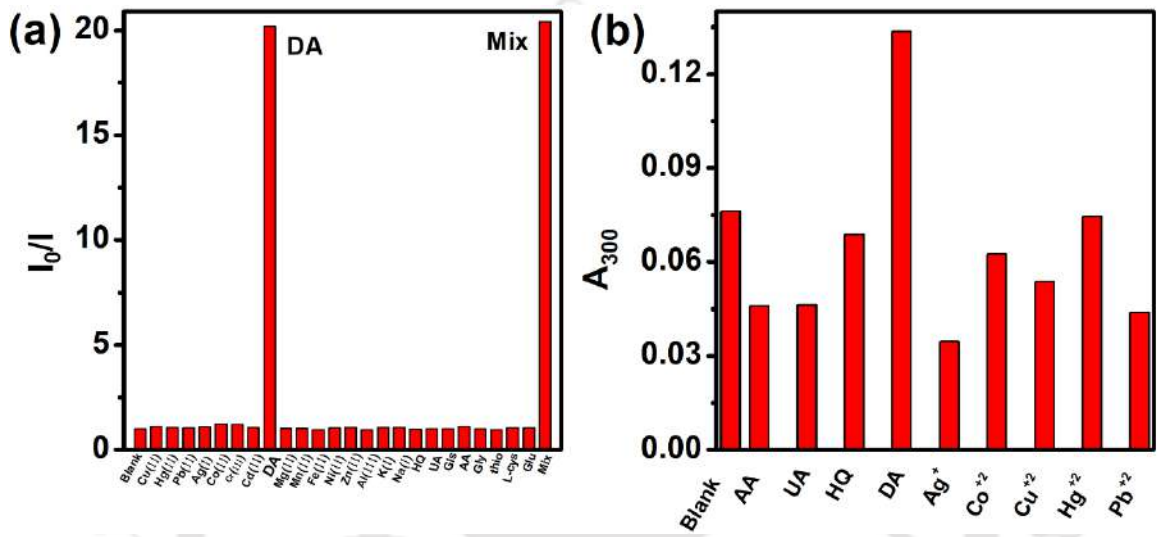

Fig. 5.8. The selectivity of DA sensing in (a) fluorometric, and (b) colorimetric methods in presence of different interference species at 10 μM concentration.

occurs only with the addition of DA, and no significant quenching is observed by other molecules and ions. A mixture of all interfering species with DA also shows a quenching effect similar to that with only DA. The selectivity of this hybrid system is also investigated by the change in the intensity of the absorption at ~300 nm, as shown in **Fig. 5.8(b)**. These observations confirm that the proposed sensing platform is highly selective towards the detection of DA.

5.3.5. Analysis of Real Samples

For the investigation of the practical feasibility of Au@N-GQDs based DA sensor, different concentrations of DA in the range of 0–80 μM were spiked into the real samples, and the concentrations of DA in the samples were determined by the standard addition method in Brahmaputra river water, and the human serum, as discussed in **Chapter 4, Section 4.3.7**. **Fig. 5.9(a, b)** shows the change in the normalized PL spectra of Au@N-GQDs with different concentrations of spiked DA in the river water and the human serum samples. For both the cases,

the variation of I_0/I with DA concentration is observed to follow a linear Stern-Volmer equation, as shown in **Fig. 5.9(c, d)**. The calculated LODs of DA concentration are ~480 nM and 590 nM

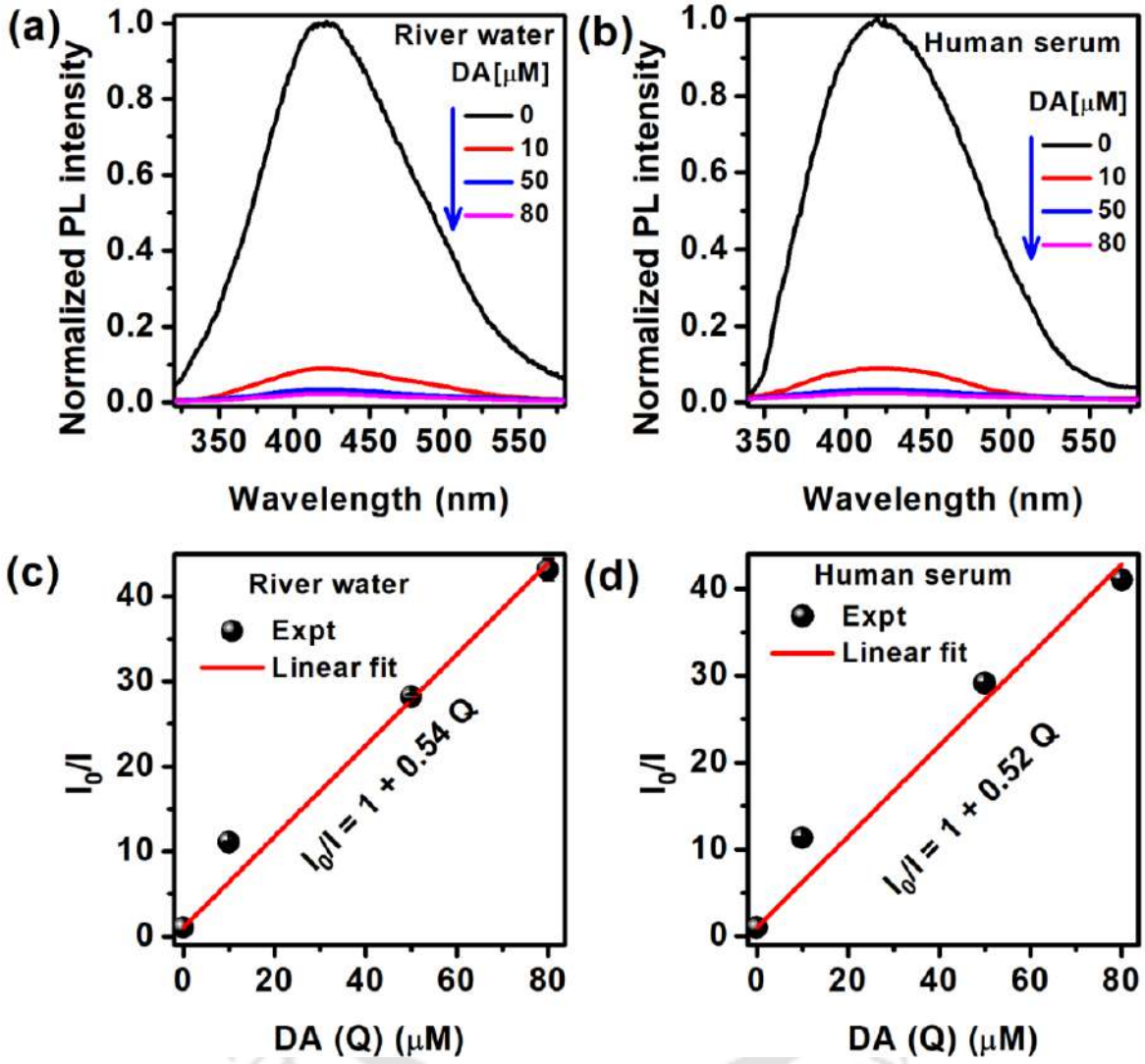

Fig. 5.9. The change in the normalized PL spectra of Au@N-GQDs with the spiked DA concentration (0–80 μM) in (a) the Brahmaputra River water, and (b) the human serum sample. The relative change of the PL intensity (I_0/I) of Au@N-GQDs at ~414 nm in the presence of different concentrations of DA spiked in (c) the Brahmaputra river water, and (d) the human serum.

for the river water and the human serum sample, respectively. The recovery of DA in the river water is ~96.3–102.1%, and that for the human serum is ~94.5–112.3%, as presented in **Table 5.2**. Thus, the recovery of DA is satisfactory in both cases.

Table 5.2. *Detection of dopamine spiked in real samples, e.g. Brahmaputra river water and human serum.*

Sample	*Added concentration of DA (μM)*	*Measured concentration of DA (μM)*	*Recovery (%)*	*RSD (%)*
Brahmaputra river water	10.0	10.7±0.1	107.0	0.9
	50.0	48.2±0.5	96.3	1.0
	80.0	81.6±2.0	102.1	2.5
Human serum	10.0	11.2±0.2	112.3	1.8
	50.0	49.8±0.03	99.6	0.1
	80.0	75.6±0.1	94.5	0.1

5.4. Summary and Conclusions

This chapter presents simple photometric and colorimetric method for detecting DA below the normal level of DA in the human serum and investigate the mechanism of sensing. This proposed sensor is efficient, and it holds the potential for DA detection in the environmental and biological samples in a fast and reproducible way. The important conclusions of this chapter are:

1. Highly sensitive and selective, low-cost and straightforward DA sensor is demonstrated here based on the Au@N-GQDs through the formation of a unique core-shell structure with DA as a shell over the Au NPs core.
2. Primarily electrostatic interaction and π-π stacking facilitate the N-GQDs/DA ground state complex formation, and the presence of Au NPs accelerates the ground state complex formation by making a core-shell structure with phenoxide-enolate.
3. Au NPs are successfully demonstrated to play a vital role in the N-GQDs/DA composite formation, proving Au@N-GQDs as a more efficient sensor than bare N-GQDs.
4. In the colorimetric sensing, the well-known Hill equation is introduced to explain the nature of the change of the absorption intensity of Au@N-GQDs in the presence of DA with LOD 40 nM.

5. In the photometric sensing strategy, the relative change of the PL intensity of Au@N-GQDs follows a linear Stern-Volmer equation due to the combined effect of ground-state complex formation, and efficient charge transfer from N-GQDs to the core-shell structure.

References

1. B. Guadarrama-Flores, M. Rodríguez-Monroy, F. Cruz-Sosa, F. García-Carmona and F. Gandía-Herrero, *J. Agric. Food Chem.*, 2015, **63**, 2741-2749.
2. A.-J. Wang, J.-J. Feng, W.-J. Dong, Y.-H. Lu, Z.-H. Li and M.-L. Riekkola, *J. Chromatogr. A*, 2010, **1217**, 5130-5136.
3. L. Yang, N. Huang, Q. Lu, M. Liu, H. Li, Y. Zhang and S. Yao, *Anal. Chim. Acta*, 2016, **903**, 69-80.
4. X. Chen, S. Chen and Q. Ma, *Anal. Methods*, 2017, **9**, 2246-2251.
5. X. Zhou, P. Ma, A. Wang, C. Yu, T. Qian, S. Wu and J. Shen, *Biosens. Bioelectron.*, 2015, **64**, 404-410.
6. Y. Lin, C. Chen, C. Wang, F. Pu, J. Ren and X. Qu, *ChemComm*, 2011, **47**, 1181-1183.
7. H. Su, B. Sun, L. Chen, Z. Xu and S. Ai, *Anal. Methods*, 2012, **4**, 3981-3986.
8. D. Wen, W. Liu, A. K. Herrmann, D. Haubold, M. Holzschuh, F. Simon and A. Eychmüller, *Small*, 2016, **12**, 2439-2442.
9. X. Hai, X. Lin, X. Chen and J. Wang, *Sens. Actuator B-Chem.*, 2018, **257**, 228-236.
10. G. Goncalves, P. A. Marques, C. M. Granadeiro, H. I. Nogueira, M. Singh and J. Gracio, *Chem. Mater.*, 2009, **21**, 4796-4802.
11. S. L. Ting, S. J. Ee, A. Ananthanarayanan, K. C. Leong and P. Chen, *Electrochim. Acta*, 2015, **172**, 7-11.
12. J. Ju and W. Chen, *Anal. Chem.*, 2015, **87**, 1903-1910.
13. T. J. Macdonald, K. Wu, S. K. Sehmi, S. Noimark, W. J. Peveler, H. Du Toit, N. H. Voelcker, E. Allan, A. J. MacRobert and A. Gavriilidis, *Sci. Rep.*, 2016, **6**, 39272.
14. G. Rajender, B. Choudhury and P. K. Giri, *Nanotechnology*, 2017, **28**, 395703.
15. G. Socrates, *Infrared and Raman characteristic group frequencies: tables and charts*, John Wiley & Sons, 2004.
16. C.-E. Cheng, C.-Y. Lin, H.-Y. Chang, C.-H. Huang, H.-Y. Lin, C.-H. Chen, C.-C. Hsu, C.-S. Chang and F. S. S. Chien, *Opt. Express*, 2013, **21**, 6547-6554.
17. R. K. Biroju and P. K. Giri, *J. Phys. Chem. C*, 2014, **118**, 13833-13843.
18. S. Sánchez-Cortés and J. Garcia-Ramos, *J. Colloid Interface Sci.*, 2000, **231**, 98-106.
19. L. Qin, X. Li, S.-Z. Kang and J. Mu, *Colloids Surf. B Biointerfaces*, 2015, **126**, 210-216.
20. P. Wang, M. Xia, O. Liang, K. Sun, A. F. Cipriano, T. Schroeder, H. Liu and Y.-H. Xie, *Anal. Chem.*, 2015, **87**, 10255-10261.
21. X. Ling, L. Xie, Y. Fang, H. Xu, H. Zhang, J. Kong, M. S. Dresselhaus, J. Zhang and Z. Liu, *Nano Lett.*, 2009, **10**, 553-561.
22. K. K. Paul, N. Sreekanth, R. K. Biroju, T. N. Narayanan and P. K. Giri, *Sol. Energy Mater Sol. Cells*, 2018, **185**, 364-374.

23. H. Ren, D. D. Kulkarni, R. Kodiyath, W. Xu, I. Choi and V. V. Tsukruk, *ACS Appl. Mater. Interfaces*, 2014, **6**, 2459-2470.
24. H.-T. Liu, X.-G. Xiong, P. D. Dau, Y.-L. Wang, D.-L. Huang, J. Li and L.-S. Wang, *Nat. Commun.*, 2013, **4**, 2201.
25. Y. Q. He, S. P. Liu, L. Kong and Z. F. Liu, *Spectrochim. Acta A*, 2005, **61**, 2861-2866.
26. R. Gone, C. Biswajit and P. K. Giri, *Nanotechnology*, 2017, **28**, 395703.
27. Q. Wei, F. Zhang, J. Li, B. Li and C. Zhao, *Polym. Chem.*, 2010, **1**, 1430-1433.
28. Y. Liu, K. Ai, J. Liu, M. Deng, Y. He and L. Lu, *Adv. Mater.*, 2013, **25**, 1353-1359.
29. K. Pashangeh, M. R. Hormozi-Nezhad, M. Akhond and G. Absalan, *Plasmonics*, 2018, **13**, 1409-1415.
30. S. Govindaraju, S. R. Ankireddy, B. Viswanath, J. Kim and K. Yun, *Sci. Rep.*, 2017, **7**, 40298.
31. A. N. Pham and T. D. Waite, *J. Inorg. Biochem.*, 2014, **137**, 74-84.
32. Y. Leng, K. Xie, L. Ye, G. Li, Z. Lu and J. He, *Talanta*, 2015, **139**, 89-95.
33. J. Zhao, L. Zhao, C. Lan and S. Zhao, *Sens. Actuator B-Chem.*, 2016, **223**, 246-251.
34. A. V. Hill, *j. physiol.*, 1910, **40**, 4-7.
35. M. W. Pantoliano, E. C. Petrella, J. D. Kwasnoski, V. S. Lobanov, J. Myslik, E. Graf, T. Carver, E. Asel, B. A. Springer and P. Lane, *J. Biomol. Screen.*, 2001, **6**, 429-440.
36. R. Mattera, B. Pitts, M. Entman and L. Birnbaumer, *J. Biol. Chem.*, 1985, **260**, 7410-7421.
37. J. N. Weiss, *The FASEB Journal*, 1997, **11**, 835-841.
38. I. Langmuir, *J. Am. Chem. Soc.*, 1918, **40**, 1361-1403.
39. D. I. Cattoni, O. Chara, S. B. Kaufman and F. L. G. Flecha, *PloS one*, 2015, **10**, e0146043.
40. F. J. Ruzicka and P. A. Frey, *J. Phys. Chem. B*, 2010, **114**, 16118-16124.
41. S. Weng, D. Liang, H. Qiu, Z. Liu, Z. Lin, Z. Zheng, A. Liu, W. Chen and X. Lin, *Sens. Actuator B-Chem.*, 2015, **221**, 7-14.
42. K. Qu, J. Wang, J. Ren and X. Qu, *Chem. Eur. J.*, 2013, **19**, 7243-7249.
43. F. Qu, W. Huang and J. You, *Colloids Surf. B Biointerfaces*, 2018, **162**, 212-219.
44. Y. Zhao, X. Wu, S. Sun, L. Ma, L. Zhang and H. Lin, *Carbon*, 2017, **124**, 342-347.
45. S. Huang, L. Wang, C. Huang, B. Hu, W. Su and Q. Xiao, *Microchim. Acta*, 2016, **183**, 1855-1864.

Chapter 6

Quantitative Understanding of Charge Transfer Mediated Fe^{3+} Sensing and Fast Photoresponse by Nitrogen-Doped Graphene Quantum Dots Decorated on Plasmonic Au Nanoparticles

The formation of heterostructure with plasmonic nanoparticles drastically alters the optoelectronic properties of graphene quantum dots (GQDs), resulting in exceptional properties. In this chapter, an in depth analysis and the applications of the extraordinary fluorescence and photoresponse characteristics of the Au@N-GQDs hybrid are presented. The as-prepared Au@N-GQDs show more than one order of magnitude enhancement in the fluorescence intensity compared to the bare N-GQDs, which is attributed to hot electron generation and improved absorption in N-GQDs by the local field enhancement and the modification of the edge functional groups. Due to the selective coordination to Fe^{3+} ions, the Au@N-GQDs exhibit extraordinary quenching of fluorescence with ultrahigh sensitivity for the detection of Fe^{3+} (<1 nM). Further, a new model for the charge transfer dynamics is developed involving the Langmuir's law of adsorption to explain the unusual quenching, which strongly deviates from the known models of static/dynamic quenching. The proposed sensor is successfully implemented for the ultrasensitive detection of Fe^{3+} ions in human serum and Brahmaputra river water samples, representing its high potential applications in the clinical as well as environmental diagnosis. Additionally, due to the high absorption in the UV-Vis-NIR region and high charge density with long life excitons, the Au@N-GQDs are utilized as a photodetector with ~10^4 times faster response than that of the bare N-GQDs. The Au@N-GQDs based photodetector possesses a high responsivity of ~1.36 A/W and a remarkably high external quantum efficiency of ~292.2%, which are much superior to the GQDs based photodetectors reported till date. The underlying mechanism of fast photoresponse is ascribed to the transfer of hot electrons along with the tunneling of the electrons from Au NPs to N-GQDs as well as the defect reduction of N-GQDs by the incorporation of Au NPs., The outstanding performance of N-GQDs based plasmonic photodetector, without the use of any charge transporting layer, opens up unique opportunities for future high-speed optoelectronic devices.

6.1. Introduction

In the previous chapter, we have discussed on the synthesis of Au@N-GQDs and their application as the dual-mode optical sensor for the detection of dopamine biomolecule with high selectivity and sensitivity. Being a promising hybrid structure, Au@N-GQDs are further implemented in multipurpose applications of various fields. Fe^{3+} is one of the essential metal ions in the human body system, and it plays a vital role in cellular metabolism, oxygen transport, enzyme catalysis as well as nucleic acid synthesis processes.[1-3] The dysfunction of Fe^{3+} in the human body can cause several diseases, such as anemia, Parkinson's illness, malaria, Alzheimer's disease, cancer, etc.[3, 4] Therefore, effective sensing of Fe^{3+} ion is highly desirable for healthy living. Considerable research has been devoted to constructing different analysis methods for the quantitative and quantitative detection of Fe^{3+} ions. Earlier, the detection of Fe^{3+} was accomplished by ion-exchange chromatography[5] and spectrophotometric detection using organic dyes.[6] However, the difficulties in sample preparation and pre-treatment procedures, the requirement of the sophisticated instrumentation, and finally the low sensitivity encouraged the researchers to find out the alternatives for efficient, rapid, and easy sensing of Fe^{3+} ions. Fluorometric methods have been established as the time effective, simple, low cost, selective, and sensitive for the detection of metal ions. Being a fluorescent material, both un-doped and doped GQDs were widely used for the fluorometric sensing applications.[7, 8], Different types of functionalization of GQDs were also reported previously for Fe^{3+} sensing, though the sensitivity is not appreciable.[3, 9] In this chapter, the Au@N-GQDs grown by a green method is demonstrated as a fluorescence-based sensor for Fe^{3+} ions over a wide range (1 nM to 10 μM) in the human serum and the Brahmaputra river water samples. We provide an in-depth and quantitative understanding of the quenching mechanism by introducing a new model for charge transfer dynamics and quenching.

Despite its fascinating properties, the zero band gap of graphene limits its applications in optoelectronic devices due to the low optical absorption, short carrier lifetime, low spectral responsivity, small difference in dark and light signal, etc.[10, 11] Interestingly, GQDs with high surface area, tunable bandgap, high optical absorption, and efficient multiple carrier generation properties extend the potential of graphitic materials in the optoelectronic devices.[12, 13] Due to lower carrier density, weak conductivity, higher trapping states and defect states, the performance of the GQD based photodetectors have not achieve the desired level of performance needed for

commercial application. Subsequently, the doped GQDs were introduced to increase the conductivity and carrier density for the improvement in the photocurrent.[14, 15] Among these, N-GQDs attracted certain attention as a good photodetector due to their n-type conductivity.[15] Lately, due to the adjustable bandgap, strong quantum confinement and the ability of the electron-hole pair formation, GQDs were implemented in the graphene-based layer staking device as a charge generating layer and significant improvement of the device performances were observed.[16-18] Nguyen et al. recently reported an enhanced photoresponsivity of monolayer WSe_2 by the incorporation of N-GQDs as a transporting layer.[19] On the other hand, with a shell of GQDs on Si nanowire core, a large photocurrent was achieved due to the charge transfer from GQDs.[20] Its noteworthy that the performance of the graphene-based photodetectors has been improved with the aid of surface plasmon effects.[21-23] On the contrary, the improvement of the GQDs based photodetector has been overlooked. Herein, we demonstrate a major improvement in the performance of the N-GQDs based photodetector by the incorporation of Au NPs by an in-situ growth along with the fast photoresponse, and we investigate the underlying mechanism thoroughly. Note that we do not use any charge transporting layer in the N-GQDs based photodetector device reported here.

6.2. Experimental Details

6.2.1. Sample Preparation

6.2.1.1. Synthesis of Graphene Oxide

The synthesis of GO was carried out by a modified Hummers' method, discussed in **Chapter 2, Section 2.2.1.1**. In a typical synthesis, 3 g expandable graphite flakes and 1.5 g $NaNO_3$ were mixed with 70 mL concentrated H_2SO_4 under continuous stirring. Afterward, 9 g of $KMnO_4$ was mixed slowly in the above mixture at 4 °C and then the mixture was stirred for 4 h for proper oxidation. MQ water was added to the acid mixture at 98 °C, and then the solution was quenched with H_2O_2. Further, MQ water was added into the mixture to dilute the acidic parts and finally, GO was separated out from the unreacted flakes and impurities by centrifugation.

6.2.1.2. Synthesis of Nitrogen-doped GQDs

The top-down synthesis of N-GQDs was carried out by a solvothermal route in DMF solvent, as discussed in **Chapter 3, Section 3.2.1.3**. Briefly, 600 mg of GO powder was dispersed in 40 mL

DMF under ultra-sonication and then the solution was heated at 220 °C for 7h into the Teflon lined autoclave. Finally, the yellow suspension was collected as N-GQDs.

6.2.1.3. Synthesis of Au@N-GQDs

After the synthesis of N-GQDs, Au@N-GQDs was prepared by an in-situ method using N-GQDs as the reducing agent, discussed in **Chapter 5, Section 5.2.1.3**. In brief, 0.7 mg/mL aqueous solution of N-GQDs was prepared by the ultra-sonication process. Then the solution was heated at 110 °C under continuous stirring for 10 min. Next, 2 mL of $HAuCl_4$, 4 H_2O solutions was added dropwise into the aqueous solution of N-GQDs for the synthesis of Au@N-GQDs. The stirring was further continued for 30 min for proper reduction.

6.2.2. Detection of Fe^{3+} Ions

For the detection of Fe^{3+} ions by Au@N-GQDs, different concentrations of $FeCl_3$ (Merck) stock solutions were prepared with MQ water. Typically, 1 mL of each concentration of $FeCl_3$ was mixed with 0.5 mL of Au@N-GQDs (101 μg/mL) aqueous solution, and consequently, 1 mL of buffer solution (pH 6) was added into the above solution to fix the pH value. In the course of comparison of the sensitivity, the effect of Fe^{3+} with bare N-GQDs and N-GQDs mixed with c-Au NPs (synthesized by standard citrate reduction method) (N-GQDs/c-Au NPs) were also considered.

6.2.3. Device Fabrication for Photocurrent Measurements

In the present case, the Au@N-GQDs Schottky junction photodetector device architecture was adopted with a symmetric structure with two Al electrodes (each of width 1 mm) with a gap of 136 μm for the top contact measurement. At first, a thick uniform layer of Au@N-GQDs was deposited on 400 nm SiO_2/Si substrate by the repeated spin-coating process followed by heating at 70 °C in each step. Afterward, Al electrodes were deposited through a mask on top of the Au@N-GQDs layer by thermal evaporation at a base pressure of $\sim 1\times10^{-6}$ Torr. For comparison, a similar device was also prepared with bare N-GQDs.

6.2.4. Characterization Techniques

The details of the characterization techniques TEM, AFM, XPS, UV-vis, PL, TRPL, etc., were described in **Chapter 2, Section 2.2.3** and **Chapter 3, Section 3.2.4**. In this study, Raman spectra were recorded with 514 nm laser excitation. For TRPL measurements, a 375 nm pulsed laser source was used for excitation. To characterize the electrical behavior of the photodetector,

current-voltage (I-V) measurements were carried out using a microprobe station (ECOPIA EPS-500) connected to a source measure unit (Keithley 2400, USA) controlled by LabTracer software. During the measurements, the photodetector was mounted in the dark, electrically, and optically sealed chamber on the optical table to reduce vibrational noise. For the measurement of the photocurrent, 405 nm laser and 250 W xenon lamp (Newport, USA) along with a monochromator (Oriel Instruments, USA) were aligned for the illumination. The light pulse was generated using a chopper (SRS, USA). For the measurement of the fast photoresponse in Au@N-GQDs, the device was illuminated with 405 nm pulsed laser driven by a high-frequency pulse generator, and the photocurrent was measured across a 100 kΩ load resistor to record the voltage drop by a digital storage oscilloscope (Tektronix, TDS2012). This enabled high-speed recording of the photocurrent, which was not possible using the source-measure unit alone.

6.3. Results and Discussion

6.3.1. Morphology Studies

The morphology of the as-grown N-GQDs and Au@N-GQDs are studied with TEM and AFM analyses. **Fig. 6.1(a)** shows the well-dispersed N-GQDs of circular shape, synthesized by the solvothermal method. The statistical size distribution of the N-GQDs is shown in the inset of **Fig. 6.1(a)**. The average size (diameter) of the N-GQDs is obtained as ~3.6 nm using the lognormal fitting, as shown in the upper inset of **Fig. 6.1(a)**. The AFM height profile analysis in the lower inset of **Fig. 6.1(a)** shows that the N-GQDs are mostly of monolayer type. The HRTEM image of N-GQDs is shown in **Fig. 6.1(b)**. The HRTEM lattice fringes of a single N-GQD is shown in the inset of **Fig. 6.1(b)** with a lattice spacing of ~0.24 nm, which corresponds to the (1120) plane of the hexagonal structure of N-GQDs, confirming their crystalline nature.[13] The TEM image in **Fig. 6.1(c)**, including a high-resolution image in the inset, shows Au@N-GQDs with mostly hexagonal shape and some with pentagonal, triangular and spherical shapes, as discussed in **Chapter 5, Section 5.3.1**. The size distribution of Au@N-GQDs with the average particle size of ~23.4 nm is shown as the inset of **Fig. 6.1(c)**. In **Fig. 6.1(d)**, a nice decoration of N-GQDs on the surface of Au NPs is visualized from the HRTEM image. Note that the size of the N-GQDs on Au NP is identical to that of the size of bare N-GQDs shown in **Fig. 6.1(a),** and this is consistent with the discussion of **Chapter 5, Section 5.3.1**. Further, the inset of **Fig. 6.1(d)** shows the lattice fringes

of (111) facet of Au NP with the interplanar spacing of ~0.235 nm, which is consistent with the previous analysis.[24]

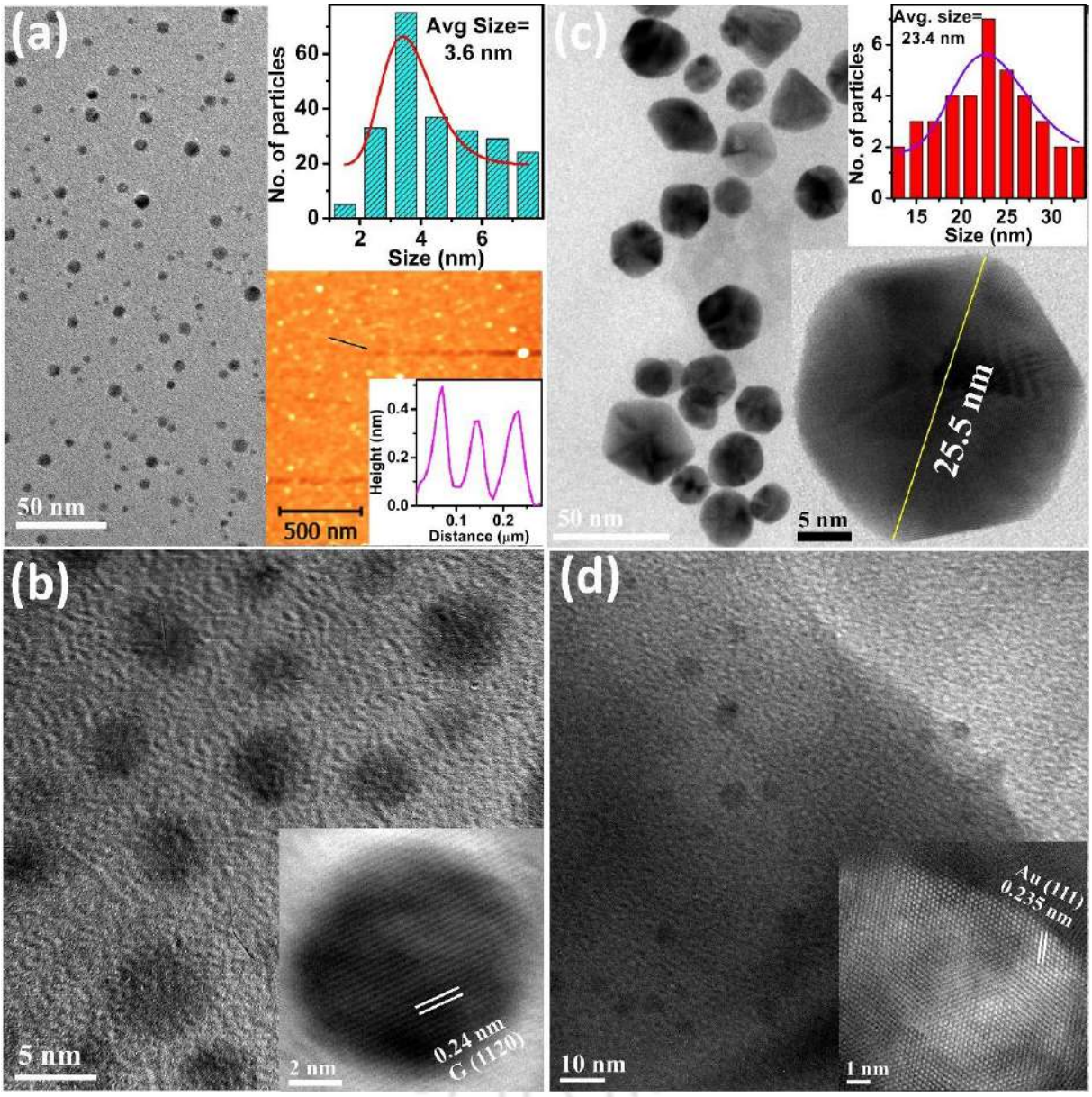

Fig. 6.1. (a) TEM image of N-GQDs; the corresponding size distribution with lognormal fitting is shown in the upper right inset. AFM image of N-GQDs with the height profile is presented in the lower right inset. (b) The HRTEM image of N-GQDs. The inset shows a single N-GQD with a lattice spacing of ~0.24 nm corresponding to (1120) hcp planes. (c) The TEM image of as-synthesized Au@N-GQDs with mostly of hexagonal shape and some with pentagonal, triangular, and spherical shapes. The upper right inset shows the particle size distribution and the corresponding lognormal fitting. A hexagonal-shaped Au NP with size ~25.5 nm is shown in the magnified scale in the lower right inset. (d) The HRTEM image of the Au@N-GQDs showing the decoration of N-GQDs on an Au NP. The inset shows the HRTEM lattice fringes of an Au NP.

6.3.2. Chemical and Structural Analysis

6.3.2.1. XPS Analysis

An overview of the chemical composition of N-GQDs and Au@N-GQDs is presented in **Fig. 6.2(a)** using the XPS survey scan. Three characteristic peaks at ~284 eV, 399 eV, and 531 eV are observed in both N-GQDs and Au@N-GQDs for C 1s, N 1s, and O 1s, respectively,[25] while the characteristic peak at ~84 eV for Au 4f appears only in Au@N-GQDs,[26] as expected. For the

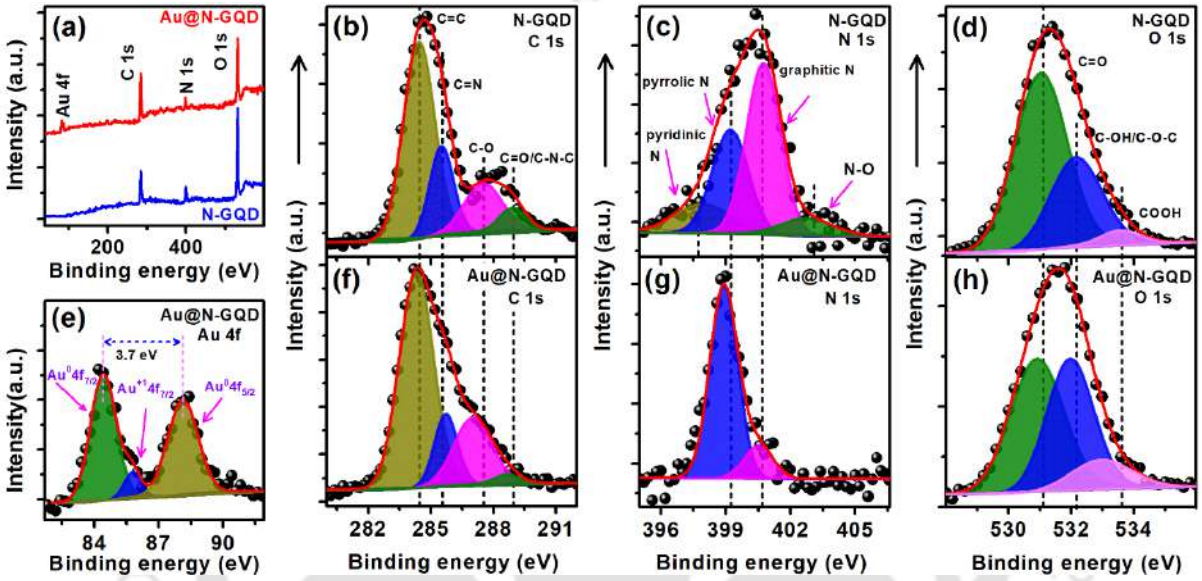

Fig. 6.2. (a) XPS survey scan spectra of N-GQDs and Au@N-GQDs. (b-d) High-resolution XPS spectra of C1s, N 1s, and O 1s, respectively, of N-GQDs. (e-h) Au 4f, C1s, N 1s, and O 1s XPS spectra of Au@N-GQDs, respectively. Each spectrum is fitted with a Shirley baseline. The symbols represent the experimental data, and the filled areas correspond to the Gaussian fits of different energy states.

detailed analysis of the chemical states in N-GQDs and Au@N-GQDs, the high-resolution XPS spectra corresponding to C 1s, N 1s, O 1s, and Au 4f are deconvoluted with multiple Gaussian peaks, as shown in **Fig. 6.2(b-h)**. In the deconvoluted C 1s spectrum in N-GQDs (see **Fig. 6.2(b)**), the peak at ~284.3 eV refers to the graphite-like sp^2 hybridized state (C=C) and the other peaks at ~285.5 eV, 287.5 eV and 288.9 eV are assigned to C=N, C-O, and C=O/ C-N-C functional groups, respectively.[25] For N 1s spectrum of N-GQDs, the binding energy at ~397.9 eV, 399.2 eV, 400.7 eV, and 402.7 eV (see **Fig. 6.2(c)**) are assigned to pyridinic N, pyrrolic N, graphitic N and oxidized state of N as N-O, respectively.[27, 28] The pronounced peaks at ~399.2 eV and 400.7 eV confirm the doping of N atom in N-GQDs. In **Fig. 6.2(d)**, three different peaks at ~531.0 eV, 532.1 eV and 533.5 eV in O 1s spectrum endorse the existence of oxygen-rich functional groups C=O, C-OH/C-O-C and COOH, respectively, in N-GQDs.[25, 27] In the case of Au@N-GQDs, the characteristic Au

4f doublet is deconvoluted with two peaks at ~84.4 eV and 88.1 eV, corresponding to Au $4f_{7/2}$, and Au $4f_{5/2}$ states, respectively, with a spin-orbit splitting of ~3.7 eV, as shown in **Fig. 6.2(e)**.[26] Along with the pure metallic Au, the appearance of a peak at ~85.8 eV is due to the Au^{+} $4f_{7/2}$ state endorsing the bonding of Au with N-GQDs.[26] In Au@N-GQDs, four different peaks of C 1s appear at ~284.3 eV, 285.7 eV, 287.0 eV, and 288.6 eV, as shown in **Fig. 6.2(f)**. As compared to N-GQDs, the contribution of C=C peak increases from ~57% to 63%, while the contribution of N, O related functional groups decreases. This confirms the reduction of defects from the graphitic array after the attachment of Au NPs. It is noteworthy that the reduction in the binding energy of each state of C 1s in Au@N-GQDs, except C=N state, confirms the increase of the electron density in the Au@N-GQDs hybrid. The upshift in the binding energy of C=N from ~287.5 eV to 287.7 eV is attributed to the electron donation to Au^{3+} ions at the time of reduction reaction. For N 1s spectrum in Au@N-GQDs (see **Fig. 6.2(g)**), only pyrrolic N (~398.9 eV) and graphitic N (~400.5 eV) peaks appear. The disappearance of the pyridinic N and N-O peak in Au@N-GQDs revels that these functional groups play a vital role in the reduction of Au^{3+}. The lone pair electrons of the pyridinic N help in the attachment of the Au NPs with N-GQDs and as a result, the discontinuity in the graphitic network is filled up leading to the reduction of the defect in N-GQDs, while the presence of substantial pyrrolic N (~85%) can increase the n-type conductivity[15] and higher density of states. In Au@N-GQDs, the modification of the oxidation states of C=O (~530.9 eV), C-OH/C-O-C (~531.9 eV) and COOH (~532.9 eV) functional groups is observed from the deconvoluted O 1s spectrum. The lowering in the binding energy of these functional groups reveals the high electronic charge density in Au@N-GQDs (see **Fig. 6.2(h)**). The overall increase of the relative atomic % of C 1s and the reduction of N 1s and O 1s contribution in the Au@N-GQDs hybrid, as listed in **Table 6.1**, confirm the reduction of defects and impurities in the graphene structure. Moreover, the deconvoluted high-resolution spectra confirm the modification of the functional groups.

Table 6.1. *Comparison of the atomic concentration (%) of C, N, O, Au in N-GQDs and Au@N-GQDs, as revealed from the XPS analysis.*

Characteristic peaks	*N-GQDs*	*Au@N-GQDs*
C 1s	54.0%	66.8%
N 1s	10.0%	5.2%
O 1s	36.0%	27.5%
Au 4f	-	0.5%

6.3.2.2. XRD Analysis

To study the structure and crystallinity of N-GQDs and Au@N-GQDs, the XRD patterns are presented in **Fig. 6.3(a)**. In the case of N-GQDs, a broad diffraction peak centered at 2θ ~24.6° corresponds to (002) graphitic plane. The nanoscale size of the particles and the presence of an excess amount of functional groups and defects are responsible for the broadening of the diffraction peak in N-GQDs.[4, 29] On the other hand, the diffraction corresponding to (002) graphitic planes for Au@N-GQDs is detected at a higher 2θ value (~26.1°) as compared to bare N-GQDs. Due to the higher electron density, the functional groups in the basal plane of N-GQDs mainly participate for the reduction of the Au^{3+} ions, and as a result, Au NPs are mostly attached on the surface of N-GQDs instead of edge sites.[30] Thus, due to the attachment of Au NPs, the functional groups are partly eliminated from the basal plane, and as a result, the interplanar spacing may be reduced, giving rise to a peak at a higher 2θ value. The reduction of the linewidth of this (002) graphitic peak also indicates the reduction/passivation of the defective sites and functional groups from the graphitic structure. For Au@N-GQDs, two additional diffraction peaks occur at 2θ ~38.3° and 44.6° correspond to (111) and (002) facets, respectively, of fcc Au NPs.

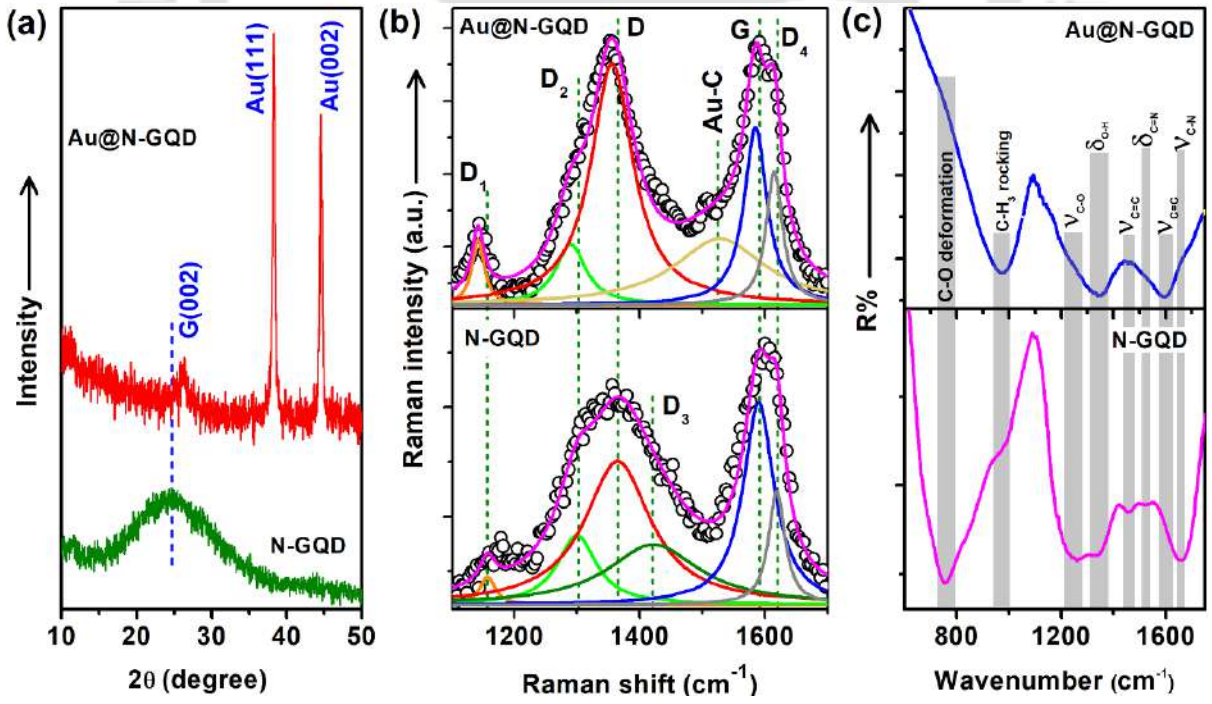

Fig. 6.3. A comparison of the (a) XRD pattern, (b) Raman spectra, and (c) FTIR spectra of N-GQDs and Au@N-GQDs. In (b) the symbol indicates the experimental data and the solid lines represent the fitted curves. The deconvoluted Raman peaks are labeled as D_1, D_2, D, D_3, G, and D_4, and the respective peak positions are indicated with vertical dashed lines.

6.3.2.3. Raman Spectral Analysis

For further endorsement of the structural characteristics, Raman spectra of as-synthesized N-GQDs and Au@N-GQDs are presented in **Fig. 6.3(b)**. To acquire insight into the edge states and functional groups, each spectrum is fitted with six Lorentz peaks in the range of ~1100–1700 cm^{-1}. The vertical dashed lines on the deconvoluted spectra indicate the positions of D and G bands in N-GQDs at ~1365 cm^{-1} and 1590 cm^{-1}, respectively. The D band arises from the structural defects in the sp^2 domain of N-GQDs, whereas the G band in N-GQDs is due to the in-plane phonon vibration of C=C carbon components, as mentioned in **Chapter 3, Section 3.3.2.2**. The appearance of additional Raman bands in N-GQDs and Au@N-GQDs are labelled as D_1, D_2, D_3, and D_4, as shown in **Fig. 6.3(b)**. In particular, the Raman peak at ~1300 cm^{-1} (D_2) is attributed to the O=C-N bond vibration,[31] and that at ~1422 cm^{-1} (D_3) corresponds to the vibration of C=O/C-O groups,[32] and this confirm the presence of N and O functional groups in N-GQDs. Also, the Raman band at ~1528 cm^{-1} in Au@N-GQDs is attributed to the Au-C bond formation due to the strong coupling between N-GQDs and Au NPs in Au@N-GQDs. Its noteworthy that as compared to N-GQDs, a redshift of the G band in Au@N-GQDs from ~1590 cm^{-1} to 1585 cm^{-1} is due to the charge transfer from Au NPs to N-GQDs [33]. The enhancement of electron density in N-GQDs is attributed to the increasing polarizability of the Raman active species. This improvement of the polarizability facilitates the redshift of the Raman bands. Interestingly, after the interaction of N-GQDs with Au NPs, an enhancement in the intensity ratio of I_D to I_G (I_D/I_G) from ~0.73 to 1.33 is observed, accompanied by the reduction of the FWHM of D band and the disappearance of D_3 band. The enhancement in intensity of D band is primarily due to the preferential attachment of Au NPs at the defect sites of N-GQDs and the local enhancement of field due to the plasmonic absorption by Au NPs.[34] In presence of the Au NPs, the intensity of both the G and D bands increase, with a higher enhancement factor for D band particularly due to the attachment of Au NPs at the defect sites.[34] Thus, the enhancement in D band intensity here does not necessarily mean the increase in the defect density. Further, the improvement of D_4 band (~1615 cm^{-1}), corresponding to C=N-OH stretching vibration in Au@N-GQDs,[31] indicates the modification of the functional groups with –OH contributions. Moreover, a drastic reduction in the FWHM of G band from ~60 cm^{-1} to ~44 cm^{-1} is ascribed to the strong vibration of C=C bond in Au@N-GQDs through the enhancement of the local EM field by the SPR absorption of Au NPs, as discussed in **Chapter 5, Section 5.3.2.2**. The Raman analysis confirms the modification of the defect states in N-GQDs as well as the

increase of the charge density in N-GQDs as a result of metal-carbon composites formation, consistent with the XPS analysis.

Due to the attachment of Au NPs with N-GQDs, the change of the functional groups and modification of different bond vibration are also confirmed from FTIR analysis. The characteristics FTIR spectra of the N-GQDs and Au@N-GQDs are presented in **Fig. 6.3(c)**. The absorption band corresponding to stretching vibration and in-plane bending vibration of C-N and C=N appear at ~1660 cm^{-1} and 1522 cm^{-1}, respectively, which confirm the successful functionalization of GQDs with nitrogen.[31] An absorption peak at ~1455 cm^{-1} arises due to the stretching vibration of phenyl groups in N-GQDs.[31] Moreover, the absorption band at ~1335 cm^{-1} and 1260 cm^{-1} are assigned to the bending vibration of O-H and stretching vibration of C-O bond, respectively, suggesting the presence of abundant oxygen-containing functional groups in N-GQDs.[31] Additionally, the absorption band at ~976 cm^{-1} and 764 cm^{-1} are due to the C-H_3 rocking vibration and C-O deformation in N-GQDs.[31] In Au@N-GQDs, strong absorption of C=C stretching vibration at ~1598 cm^{-1} is due to the influence of the local EM field enhancement of Au NPs, consistent with the Raman analysis. Noteworthy, the absorption band corresponding to C-N and C=N at ~1660 cm^{-1} and 1522 cm^{-1}, respectively, diminish in Au@N-GQDs as a result of the metal-carbon hybrid formation, again confirming the removal of defect states from N-GQDs. Interestingly, an absorption band at ~1345 cm^{-1} corresponding to O-H vibration becomes sharper as well as stronger in Au@N-GQDs due to the modification of the functional groups, and this is consistent with XPS and Raman analyses.

6.3.3. Optical Analysis

6.3.3.1. UV-vis Absorption Study

The absorption spectra of N-GQDs and Au@N-GQDs are presented in **Fig. 6.4(a).** N-GQDs show a sharp absorption peak at ~262 nm for π-π* transition with an extended tail from 300–800 nm due to the functionalization of N-GQDs with N, O associated functional groups. For the case of Au@N-GQDs, the absorption spectrum exhibits two characteristic absorption peaks, one at ~262 nm for the absorption by N-GQDs and the other at ~547 nm due to the contribution of the surface plasmon resonance (SPR) absorption of Au NPs in the hybrids, as discussed in **Chapter 5, Section 5.3.3.1**. Note that due to the incorporation of Au NPs, there is a reduction in the indirect bandgap

of N-GQDs from ~3.56 eV to 2.53 eV, which suggests a higher electron density in N-GQDs due to the strong coupling of Au NPs with N-GQDs, as shown in the inset of **Fig. 6.4(a)**.

6.3.3.2. Photoluminescence Excitation Spectra Study

Fig. 6.4(b) shows the photoluminescence excitation (PLE) spectra of N-GQDs and Au@N-GQDs with a broad peak centered at ~345 nm for both N-GQDs and Au@N-GQDs, and the PLE peak intensity of Au@N-GQDs is observed to be ~12 times higher than that of the bare N-GQDs. To acquire more information on the various factors contributing to the high intensity PLE spectrum of Au@N-GQDs, it is deconvoluted with three Gaussian peaks, as shown in **Fig. 6.4(b)**. The peak at ~266 nm corresponds to the π-π* transition, and the peaks at ~326 nm and 375 nm are assigned for the contribution of the surface functional groups and the doped atoms in Au@N-GQDs.

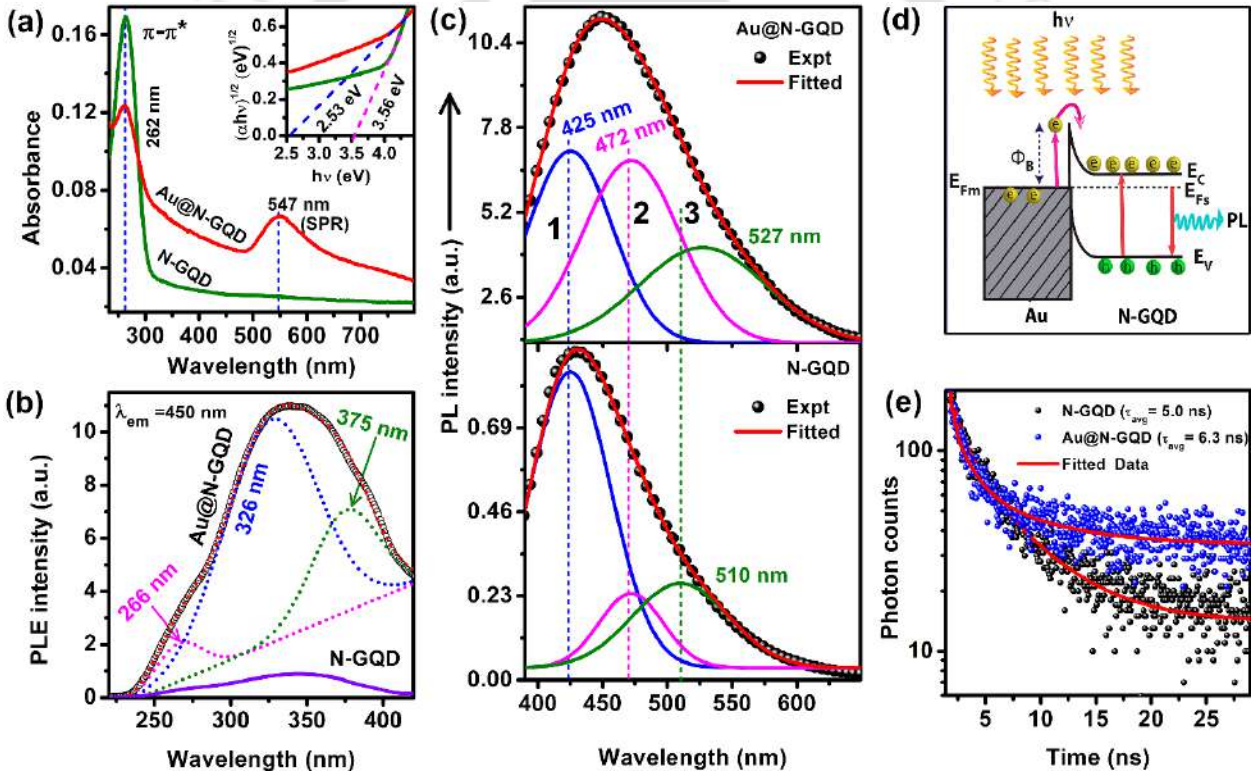

Fig. 6.4. (a) Comparison of the UV-vis absorption spectra of N-GQDs and Au@N-GQDs. The vertical dashed lines show the absorption peaks corresponding to N-GQDs (~262 nm) and plasmonic Au NPs (~547 nm). The inset shows the Tauc plot for the estimation of the indirect bandgap of N-GQDs and Au@N-GQDs. (b) The PLE spectra of N-GQDs and Au@N-GQDs monitored at the emission position 432 nm and 450 nm, respectively. The PLE spectra of Au@N-GQDs is deconvoluted with three Gaussian peaks. The dashed curves represent the fitted peaks, and the symbol corresponds to the experimental data of Au@N-GQDs. (c) A comparison of the deconvoluted PL spectra of N-GQDs and Au@N-GQDs. (d) Schematic illustration of the band diagram and the electron transfer in Au@N-GQDs under light irradiation giving rise to an enhanced PL intensity. (e) Comparison of the TRPL spectra of N-GQDs and Au@N-GQDs.

6.3.3.3. Photoluminescence Spectra Study

Under the excitation of 350 nm, the PL spectra of N-GQDs and Au@N-GQDs are presented in **Fig. 6.4(c)** with the PL emission maxima at ~432 nm and 450 nm, respectively. In the case of Au@N-GQDs, the maximum emission intensity is ~12.1 times stronger than that of the bare N-GQDs, which is consistent with the PLE spectra. To understand the origin of large enhancement of the PL intensity in Au@N-GQDs, the PL spectrum of both N-GQDs and Au@N-GQDs are deconvoluted with three different Gaussian peaks, as presented in **Fig. 6.4(c)**. In N-GQDs, peak 1 at ~425 nm is attributed to the free zigzag edge states,[35] peak 2 (~472 nm) is contributed by the COOH/OH and CN-OH functional groups at the edge sites and peak 3 (~510 nm) is due to the presence of oxygen-rich C=O/C-O-C groups, as discussed in **Chapter 3, Section 3.3.3.3**. No change in the center of peak 1 and peak 2 for Au@N-GQDs implies that Au NPs do not interact with the free zigzag edge states and COOH/OH groups of N-GQDs, while ~17 nm redshift of peak 3 in Au@N-GQDs indicates the interaction of Au NPs with epoxy groups. Thus, it may be concluded that the modification of the functional groups is not responsible for the PL enhancement in Au@N-GQDs. The key factor, which is responsible for the PL enhancement in Au@N-GQDs, is the attachment of plasmonic Au NPs with N-GQDs. Owing to the plasmon-enhanced absorption, Au NPs can absorb incident photons and produce coherent collective oscillation of electrons, which decay non-radiatively by the generation of high kinetic energy (~3 eV) hot electrons.[36, 37] Note that the interaction of metallic Au NPs and semiconducting N-GQDs produces a Schottky barrier (Φ_B) at the interface of Au@N-GQDs,[12] as illustrated in **Fig. 6.4(d)**. The energy of the hot electrons is generally higher than the local Schottky barrier height,[37] and as a result, the hot electrons are easily transferred to the conduction band of the semiconductor N-GQDs. Since the N-GQDs have lower electron density than the metallic Au NPs, N-GQDs can simply accept the hot electrons. Further, the work function of GO/GQD (~5.86 eV) is reported to be higher than that of the Au NPs (~5.20 eV).[38] It has been reported that the presence of functional groups increases the work function of GQD.[39] Hence, due to the lower work function of Au NPs, the electron would be transferred from Au NPs to N-GQDs. The redshift of the G band, as observed from Raman spectra analysis, clearly indicates the charge (electron) transfer from Au NPs to N-GQDs. Note that the presence of strong electronegative nitrogen atoms further enhances the electron-accepting capability of N-GQDs.[40] **Fig. 6.4(d)** shows a schematic of the band diagram and the hot electron transfer process in Au@N-GQDs under light illumination. Here, E_{Fs} and E_{Fm} are the Fermi energy

levels of N-GQDs and Au, respectively, which align to single energy level in Au@N-GQDs. E_C and E_V are the conduction and valance band energy level of N-GQDs. Along with the generation of hot electrons in Au NPs, electron-hole pairs are also generated in N-GQDs by the enhancement of the overall absorption of N-GQDs with the local field enhancement in the presence of plasmonic Au NPs. Thus, the developed electron density in the conduction band of N-GQDs causes higher recombination and yields a higher intensity of PL in Au@N-GQDs. Despite the charge separation at the metal-semiconductor junction, there is a net increase in the PL intensity, implying that the plasmonic effect surpasses the charge separation effect. For a quantitative analysis of the PL enhancement, the absolute QY was measured by using an integrating sphere. The measured PL QY are of ~7.9% and 12.3% for N-GQDs and Au@N-GQDs, respectively.

6.3.3.4. Time-Resolved Photoluminescence Study

For the investigation of the charge transfer phenomena, a comparison of the TRPL spectra of N-GQDs and Au@N-GQDs is shown in **Fig. 6.4(e)**, which shows the average carrier lifetime of ~5.0 ns and 6.3 ns for N-GQDs and Au@N-GQDs, respectively. With the incorporation of Au NPs, a higher lifetime or slower decay of PL in Au@N-GQDs is consistent with the plasmonic-based system reported earlier.[36] The TRPL spectrum for each sample is fitted well with a tri-exponential function. The faster decay component, τ_1 (~0.16 ns) in N-GQDs is due to the band to band transition, while τ_2 (~1.19 ns) and τ_3 (~5.21 ns) are attributed to the interstates to band transitions in N-GQDs.[41] Interestingly, τ_1 (~0.06 ns) and τ_2 (~1.09 ns) turned out to be very fast in Au@N-GQDs as compared to that of the bare N-GQDs. Since the time constant is inversely proportional to the density of carriers, the decay of the excited state electrons will be faster if the electron density is higher. Thus, faster decays in Au@N-GQDs endorse the transfer of hot electrons from Au NPs to the excited state of N-GQDs and the subsequent increase in electron density. In contrast, though the electron density increases in the excited states, the decay time τ_3 (~6.70 ns) increases in Au@N-GQDs. This is primarily due to the charge separation at the Au/N-GQDs junction that reduces the recombination probability. The formation of the Schottky barrier at the interface of Au NPs and N-GQDs produces a space charge region in the N-GQDs.[36] This may cause a charge separation in N-GQDs, resulting in higher exciton stability. Despite the charge separation, we observe an overall increase in the PL intensity with Au NPs due to the reasons discussed above. It is very interesting

to note that both faster and slower decay components are present in Au@N-GQDs, which can be beneficial for multi-purpose applications.

6.3.4. Applications of Au@N-GQDs

6.3.4.1. Au@N-GQDs as Metal Ion Sensor

6.3.4.1.1. Detection of Fe^{3+} Ions

According to the above discussion, a high PL QY in Au@N-GQDs is observed with the effective contribution of OH/COOH functional groups and plasmonic enhancement. Noteworthy, due to the high electron donating tendency of OH groups, they can efficiently interact with Fe^{3+} ions.[3, 42] Based on the above, we investigate the Au@N-GQDs as a fluorometric sensor for Fe^{3+} sensing with ultrahigh sensitivity and, consequently, implemented them for the detection of Fe^{3+} ions in the human serum and different water samples.

Before the detection of Fe^{3+} ions with Au@N-GQDs, a set of experiments was performed to find out the optimum condition for efficient sensing based on PL quenching, as presented in **Fig. 6.5**. To get the best quenching efficiency in the present sensing system, different concentrations of stock solution of Au@N-GQDs are tested with 10 μM concentration of Fe^{3+}. The bar diagram of the PL intensity of different concentrations of Au@N-GQDs (83, 101, and 130 μg/mL) is shown in **Fig. 6.5(a)** before and after the addition of 10 μM concentration of Fe^{3+}, where 101 μg/mL concentration of Au@N-GQDs shows the maximum quenching efficiency. Self-agglomeration of Au@N-GQDs may be responsible for less sensitivity at higher concentration, while at lower concentration there may be insufficient sites for efficient interaction with Fe^{3+} ions. Thus, the intermediate concentration is chosen as the optimum concentration of Au@N-GQDs for an effective sensing performance. The effect of pH is investigated with different buffer solutions, keeping the Fe^{3+} concentration unchanged (5 μM). The change of the PL intensity of Au@N-GQDs with pH values of the reacting buffer is presented in **Fig. 6.5(b)** before and after the addition of Fe^{3+} solution. Bu et al. reported that at pH<5, the surface charge density of Au NPs decreases,[43] while in the basic medium, there is a possibility of Fe^{3+} ions to interact with the OH^- groups of the basic solution resulting in the ineffective quenching of the PL intensity of Au@N-GQDs by Fe^{3+} ions. In the present study, most proficient quenching is achieved at pH 6, which is thus chosen as an optimized pH for further experiments. The reaction time is also observed to influence the sensing performance. With the addition of 5 μM Fe^{3+} solution with Au@N-GQDs, systematic

reduction of the PL intensity is observed, and it reaches a kind of plateau after 11 min of reaction (see **Fig. 6.5(c)**). Considering this, 12 min is chosen as the optimum reaction time in the experiments. To optimize the reaction temperature, the relative change in PL intensity, I_0/I (I_0 and I are the PL intensity of the system before and after the addition of Fe^{3+} solution) for Au@N-GQDs

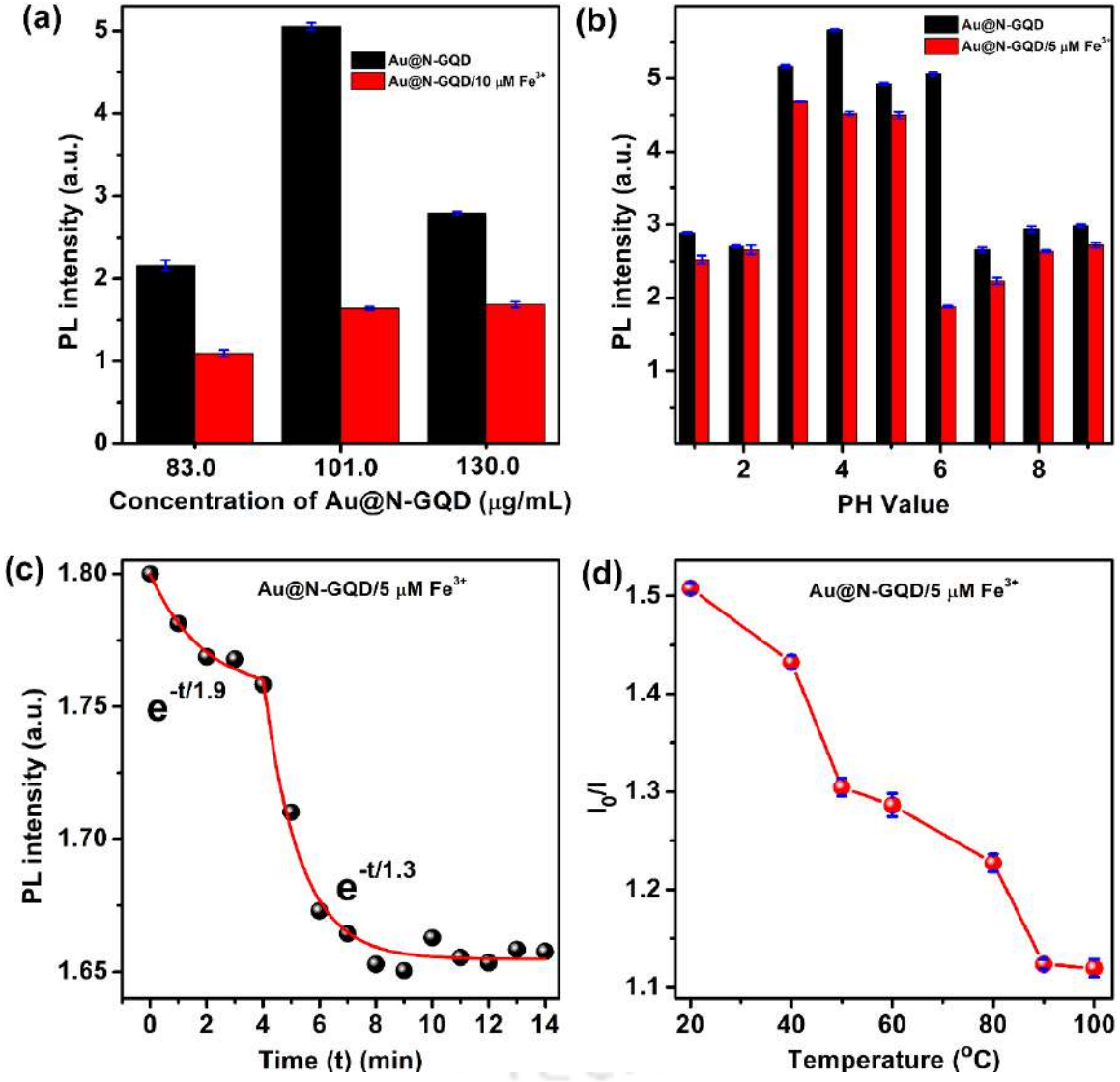

Fig. 6.5. Optimization of sensing parameters: (a) concentration of Au@N-GQDs, (b) pH values of buffer solution, (c) reaction time, and (d) temperature. The temporal variation of the PL intensity in the presence of Fe^{3+} shown in (c) is fitted with two sequential exponentials.

at different temperatures is shown in **Fig. 6.5(d)**. Here, 20°C temperature (room temperature) is showing the highest quenching of the PL intensity of Au@N-GQDs. At higher temperature, low efficiency of the PL quenching may be due to the aggregation as well as instability of Au NPs.[44] Thus, all experiments were carried out at room temperature. Therefore, Au@N-GQDs with a

concentration of 101 μg/mL is chosen as an optimum concentration at pH 6 for 12 min of reaction with Fe^{3+} at 20 °C temperature under the excitation of 350 nm. The PL spectra of Au@N-GQDs before and after the addition of different concentrations of Fe^{3+} solution was recorded in a wide range of concentration (0.001–10 μM) under optimized condition, as shown in **Fig. 6.6(a)**. The

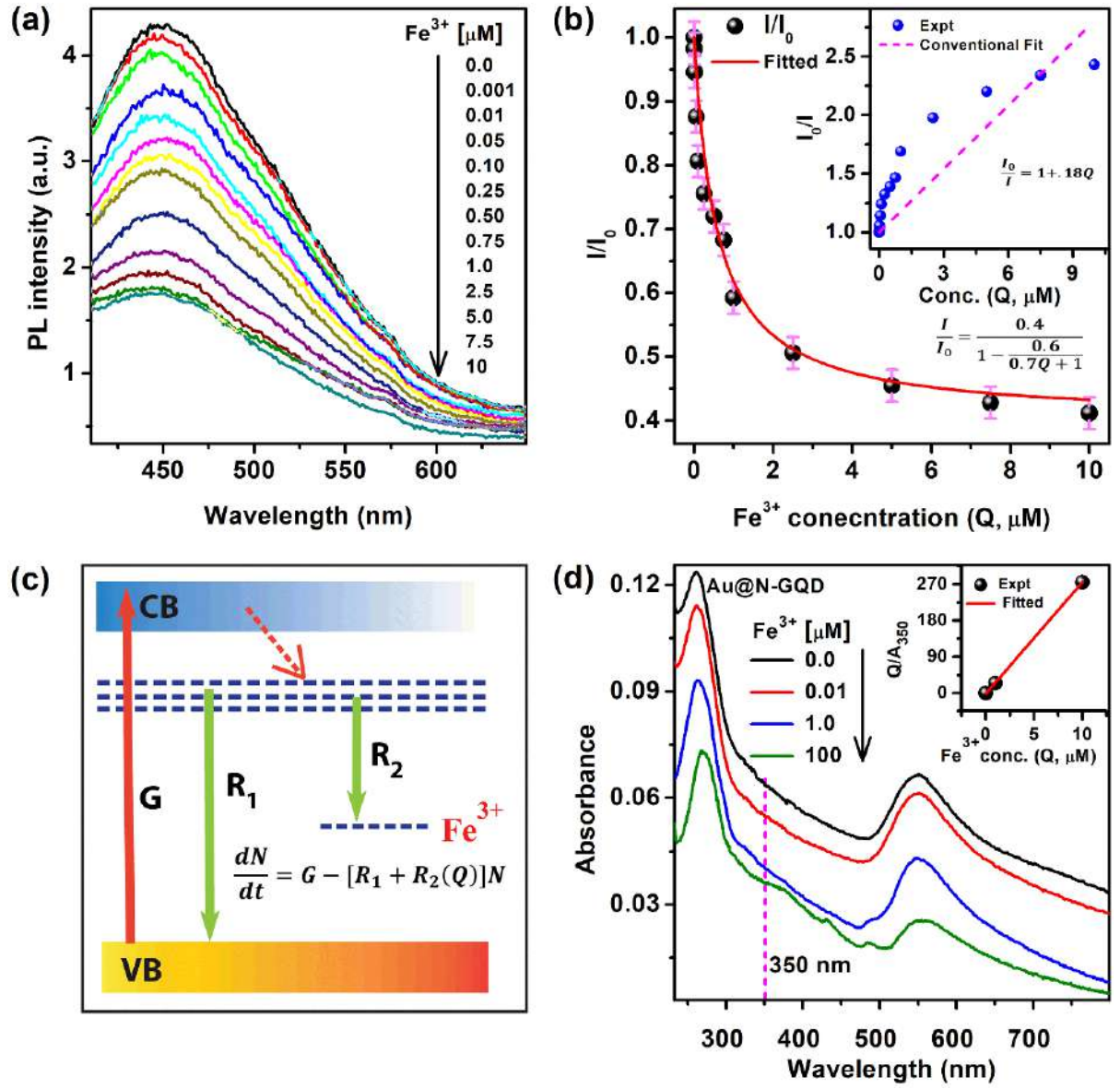

Fig. 6.6. (a) The PL spectra of Au@N-GQDs before and after the addition of Fe^{3+} (0.001–10 μM) with the excitation of 350 nm. (b) The relative change in PL intensity (I/I_0) as a function of Fe^{3+} concentration. The inset shows the variation of I_0/I vs. Q, which strongly deviates from the conventional Stern-Volmer plot (dashed line). (c) The energy band diagram showing the generation (G), and recombination (R_1, R_2) pathways for carriers in the presence of Fe^{3+}. The horizontal dashed lines represent the defect levels in Au@N-GQDs. (d) The change in the UV-vis absorption spectra of Au@N-GQDs after the addition of different concentrations of Fe^{3+} ion. The inset shows the Langmuir isotherm plot for Fe^{3+} adsorption on Au@N-GQDs (at ~350 nm).

variation of the relative change in the PL intensity, in the form of (1- I/I_0), as a function of the concentration of Fe^{3+} ions is shown in **Fig. 6.6(b)**. Note that in the present case, the change of the PL intensity of Au@N-GQDs with Fe^{3+} addition does not follow the conventional linear Stern-Volmer equation, as shown by the dashed line fit to the experimental data in the inset of **Fig. 6.6(b)**. However, over a small concentration range from 0.10–0.75 μM, a linear variation of I_0/I with Fe^{3+} gives a limit of detection (LOD) 30 nM. A quantitative understanding of the non-linearity and insight into the mechanism of quenching via charge transfer is rarely addressed in the literature. The exciton decay process in different semiconductors was reported previously with the first-order rate equation.[45, 46] Herein, for an in-depth analysis of the quenching phenomena of the PL intensity of Au@N-GQDs with a wide concentration range of Fe^{3+} ions, we use the first-order rate equations to model the charge transfer dynamics as the following:

$$\frac{dN}{dt} = G - [R_1 + R_2(Q)]N \qquad (6.1.1)$$

'N' is the population of excitons in Au@N-GQDs at any time 't'. 'G' and R_1 represent the generation rate and decay rate of excitons, respectively. 'Q' represents the concentration of Fe^{3+} ions. $R_2(Q)$ is the rate of charge transfer to Fe^{3+} ions, which is concentration-dependent. **Fig. 6.6(c)** shows a schematic illustration of different recombination pathways, including the charge transfer in Au@N-GQDs from defect levels to Fe^{3+} ions. Due to the sub-bandgap excitation used in the present case, the recombination/decay from the impurity/defect levels are also considered here. By solving the rate equation, we obtain

$$N(Q,t) = \frac{1}{R_1+R_2(Q)}\left(G - e^{-(R_1+R_2(Q))t}\right) \qquad (6.1.2)$$

For the steady-state PL measurement, as $t \to \infty$, eqn. (6.1.2) turns out to be

$$N(Q) = \frac{G}{R_1+R_2(Q)} \qquad (6.1.3)$$

Since the absorption intensity of Au@N-GQDs follows Langmuir's isotherm model with the concentration of Fe^{3+} ions (see **Fig. 6.6(d)** and the corresponding inset), we use the concentration dependent rate of charge transfer[45] to Fe^{3+} ions as,

$$R_2(Q) = R_2(0)\left(1 - \frac{S}{\alpha Q+1}\right) \qquad (6.1.4)$$

where 'S' is the charge transfer efficiency and 'α' is the adsorption probability of Fe^{3+} ions on Au@N-GQDs. $R_2(0)$ is the rate of charge transfer at Q =0. In the Langmuir adsorption model, the adsorbent (in this case, Au@N-GQDs) is assumed to be an ideal solid surface composed of a series

of distinct sites capable of binding the adsorbate (Fe^{3+}). Note that in the conventional model of quenching, adsorption of molecules is not considered. However, the adsorption of molecules and concentration dependent charge transfer rate are the key factors that distinguishes the present case from the conventional analysis of quenching phenomena. Now, the PL intensity of the system is expressed as:

$$I(Q) = AN(Q) = \frac{\frac{AG}{R_1+R_2(0)}}{1-\left(\frac{R_2(0)S}{R_1+R_2(0)}\times\frac{1}{\alpha Q+1}\right)} = \frac{B}{1-\frac{C}{\alpha Q+1}} \qquad (6.1.5)$$

where 'B' and 'C' are constants defined as:

$$B = \frac{AG}{R_1+R_2(0)} \qquad (6.1.6) \qquad \text{and} \quad C = \frac{R_2(0)S}{R_1+R_2(0)} \qquad (6.1.7),$$

and 'A' is the collection efficiency of luminescence. In the present case, the plot of (1- I/I_0) vs. Q clearly follows the above eqn. (6.1.5) (see **Fig. 6.6(b)**) with fitting constant B =0.4, C =0.6 and α =0.7, as obtained through iterations. This result reveals that the quenching of the PL intensity of Au@N-GQDs due to the charge transfer to Fe^{3+} ions follows the first-order rate equation. Additionally, the high value of the adsorption probability (α =0.7) found from the fitting confirms the strong interaction between Fe^{3+} ions and Au@N-GQDs. Next, using the value of 'B' and 'C' in eqn. (6.1.6) and (6.1.7), we obtain $R_2(0) \approx 2R_1$. Thus, the rate of charge transfer to Fe^{3+} is stronger than any other decay process, including radiative recombination. Additionally, with the help of the eqn. (6.1.6) and (6.1.7) and fitting parameters, we can conclude that the charge transfer efficiency (S) is >60% that leads to the high quenching in the presence of Fe^{3+} ions. Note that high efficiency of charge transfer is enabled by the high quality of the interface between the two species due to

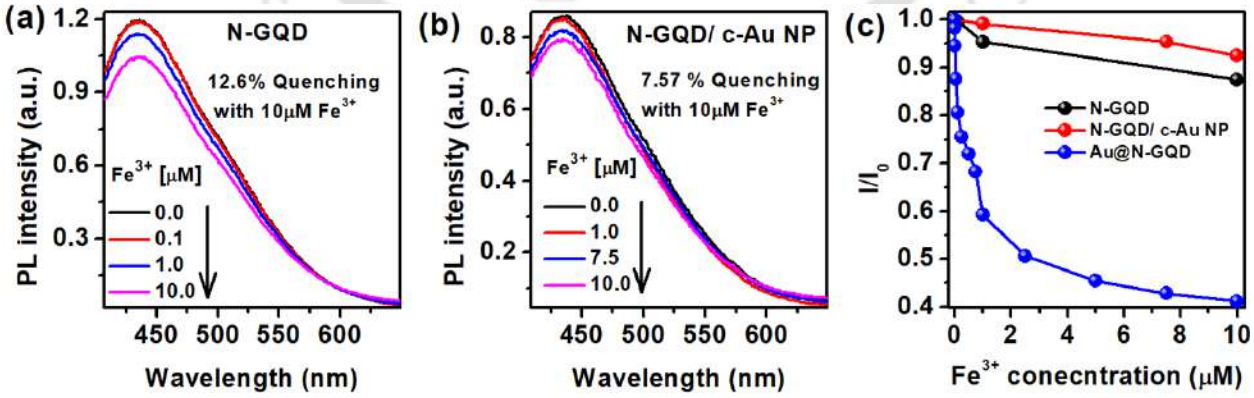

Fig. 6.7. A comparison of the PL spectra of (a) bare N-GQDs and (b) N-GQDs/c-Au NPs with different concentrations of Fe^{+3}. (c) The relative change in PL intensity (I/I_0) as a function of Fe^{3+} concentration for different samples.

the in-situ growth of the hybrid. For comparison, the PL spectra of bare N-GQDs and N-GQDs/c-Au NPs mixture were also considered for Fe^{3+} sensing in the range 0.1–10.0 μM (see **Fig. 6.7(a, b)**). In the presence of 10 μM Fe^{3+} solution, N-GQDs and N-GQDs/c-Au NPs systems show much lower quenching of the PL intensity only by ~13% and 8%, respectively, while the Au@N-GQDs show a very high quenching of ~60%. A comparison of the relative change in the PL intensity, I/I_0 vs. Fe^{3+} concentration in the case of N-GQDs, N-GQDs/c-Au NPs, and Au@N-GQDs is shown in **Fig. 6.7(c)**. These results demonstrate that the rate of the fluorescence quenching is much higher for Au@N-GQDs with remarkably high sensitivity (1 nM), whereas the sensitivity of bare N-GQDs and N-GQDs/c-Au NPs system are 100 nM and 1000 nM, respectively. Further, as compared to other GQD-based fluorescence sensor, here we achieve as low as 1 nM LOD for the sensing of Fe^{3+} ion with Au@N-GQDs, as listed in **Table 6.2**.

Table 6.2. *Comparison of performance of GQD based sensors based on fluorescence quenching for Fe^{3+} sensing reported in the literature and the present work.*

Sensing Platform	*Detection Range (nM)*	*Limit of Detection (nM)*	*Ref.*
N-GQDs	3,320 - 32,260	746.2	[47]
N-GQDs	1000 - 19,45,000	90.0	[48]
N-GQDs	1000 - 70,000	80.0	[4]
Dopamine-GQDs	20 - 2,000	7.6	[49]
S, N-GQDs	12 - 1,000	1.7	[2]
Au@N-GQDs	1 - 10,000	1.0	***This Work***

6.3.4.1.2. Mechanism of Fe^{3+} Sensing with Au@N-GQDs

The possible mechanisms behind the ultrahigh sensitivity of Au@N-GQDs towards Fe^{3+} ions are discussed here based on the experimental evidences. The following may be the key factors behind the Fe^{3+} sensing with Au@N-GQDs. First, due to a higher affinity of Au NPs to the functional groups of the basal planes of N-GQDs, the edge functional groups of Au@N-GQDs are not only easily accessible but also well separated from each, which is beneficial for efficient and mass interaction with Fe^{3+}. Second, a higher contribution of –OH edge functional groups in Au@N-GQDs causes good coordination with Fe^{3+} ions. Third, due to the high electron-donating property

of –OH groups in Au@N-GQDs, electron-rich Au@N-GQDs transfer electrons to the half-filled 3d-orbit of Fe^{3+} ions for their neutralization. Fourth, the long-lived excitons in Au@N-GQDs can help in the efficient interaction and photoinduced charge transfer to Fe^{3+} ions. Through the strong coordination with –OH functional groups in Au@N-GQDs, N-GQDs transfer photoinduced electrons to Fe^{3+}, facilitating more charge separation and reduce radiative recombination in Au@N-GQDs. Due to the interaction of Fe^{3+} ions with the functional group of Au@N-GQDs, Au@N-GQDs get agglomerated after interfacing with Fe^{3+}, as visualized through the TEM imaging (see **Fig. 6.8(a, b)**). TEM elemental mapping and EDX analysis confirmed the presence

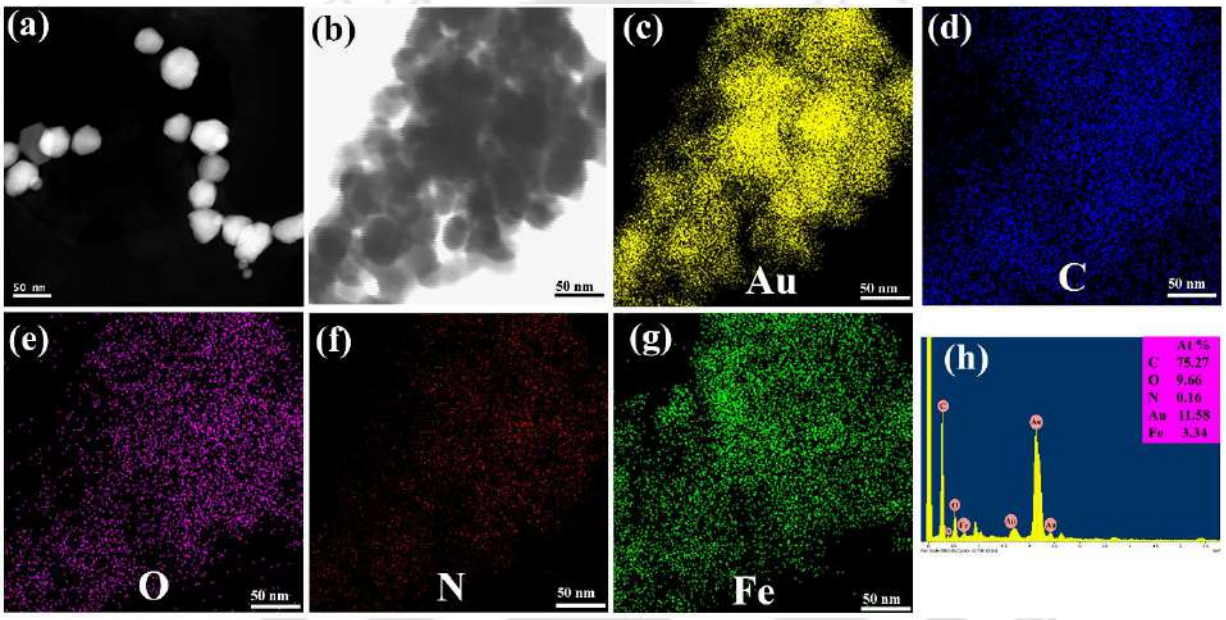

Fig. 6.8. (a) HAADF image of Au@N-GQDs assembly without Fe^{3+}, and (b) STEM image of Au@N-GQDs after the addition of Fe^{3+} ions. STEM elemental mappings of Au@N-GQDs/ Fe^{3+}: (c-g) elemental maps of Au, C, O, N and Fe, respectively. (h) EDX spectrum showing the atomic percentage of the respective elements in Au@N-GQDs/Fe^{3+}.

of Fe^{3+} in the Au@N-GQDs/Fe^{3+} composites (see **Fig. 6.8(c-h)**). Further, the FTIR analysis reveals the reduction of bending vibration related to –OH groups at ~1352 cm^{-1} (see **Fig. 6.9(a)**), due to the complex formation between Fe^{3+} ions and –OH groups in Au@N-GQDs. The systematic reduction of the N-GQDs absorption, consistent with the PL quenching, confirms the Au@N-GQDs/Fe^{3+} complex formation through N-GQDs, whereas, the diminution of the intensity of SPR absorption peak of Au@N-GQDs suggests the occurrence of charge transfer (see **Fig. 6.6(d)**). In the presence of Fe^{3+}, the PL lifetime is increased from ~6.3 ns to 12.0 ns, which implies a dynamic quenching process through a stronger charge separation (see **Fig. 6.9(b)**). From **Fig. 6.9(c),** it is also found that in the presence of Fe^{3+}, PL lifetime of N-GQDs increases from ~5.0 ns to 6.3 ns,

signifying the photoinduced charge separation via N-GQDs. For the case of Au@N-GQDs, a higher electron density with more stable exciton facilitates more interaction possibilities with Fe^{3+}, following the charge separation. Note that in the case of N-GQDs/c-Au NPs, no appreciable change in the lifetime is observed after the addition of Fe^{3+}. Interestingly, in the presence of Fe^{3+} ions, the photocurrent is reduced by ~5 times, as evident from **Fig. 6.9(d)**. With 405 nm laser

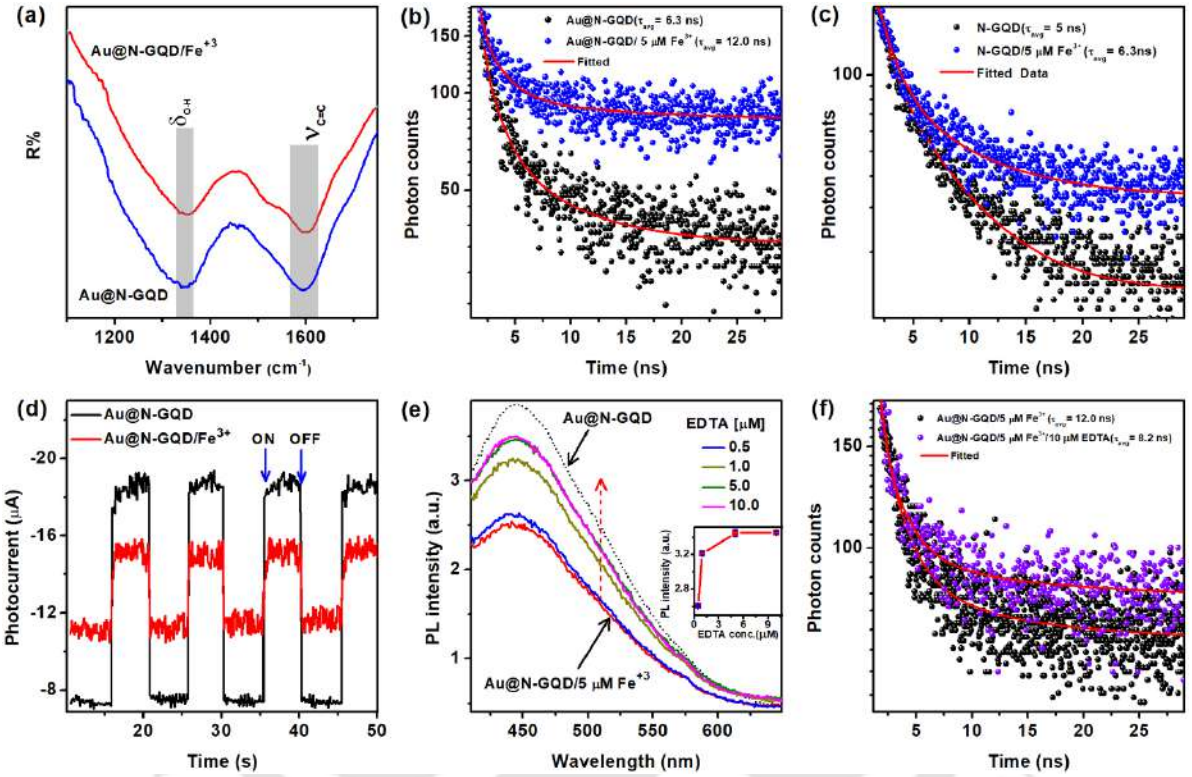

Fig. 6.9. (a) Comparison of the FTIR spectra of Au@N-GQDs before and after interaction with Fe^{3+}. TRPL decay spectra of (b) Au@N-GQDs, and (c) N-GQDs before and after the addition of Fe^{3+} with 375 nm laser excitation. (d) The photocurrent of Au@N-GQDs before and after the addition of Fe^{3+}. (e) EDTA concentration-dependent fluorescence intensity spectra for Au@N-GQDs in presence of 5 μM Fe^{3+} ions. The inset shows the change of the PL intensity with EDTA concentration. (f) The TRPL spectra of Au@N-GQDs/5 μM Fe^{3+} before and after the addition of 10 μM EDTA.

excitation, the photogenerated charge carriers are transferred from Au@N-GQDs to the unfilled orbits of Fe^{3+} ions before reaching the electrode, and consequently, the photocurrent is reduced. These results endorse that Fe^{3+} ions quench the PL intensity of Au@N-GQDs by capturing the photogenerated electrons and thus reducing their recombination probability. For a better understanding, the temporal change of the PL intensity with the reaction time (t) is fitted with two distinct sequential exponents, as shown in **Fig. 6.5(c)**. Just after the addition of Fe^{3+} with Au@N-GQDs, as there is insufficient time for Au@N-GQDs/Fe^{3+} complex formation, the inefficient

charge transfer causes a slower quenching ($e^{-t/1.9}$), while the fast temporal PL decay in the second region ($e^{-t/1.3}$) is attributed to an efficient charge transfer, accelerated by the Au@N-GQDs/Fe^{3+} complex formation. This analysis shows that the quenching of PL intensity of Au@N-GQDs is assisted by the photoinduced charge transfer to Fe^{3+} ions followed by Au@N-GQDs/Fe^{3+} complex formation. Further, to understand the nature of the complex formation between Fe^{3+} ions and Au@N-GQDs, the change of the PL intensity of the complex is investigated by the addition of ethylenediaminetetraacetic acid (EDTA, Sigma Aldrich) at different concentrations (0.5–10 μM), as shown in **Fig. 6.9(e)**. Interestingly, the PL intensity of Au@N-GQDs is observed to be recovered with the addition of EDTA. The inset of **Fig. 6.9(e)** shows the variation of the recovered PL intensity of Au@N-GQDs with EDTA concentration. With 10 μM concentration of EDTA, the PL intensity of Au@N-GQDs is recovered up to ~91% of its original value. Due to higher stability of Fe^{3+}–EDTA (log $K_{Fe\text{-}EDTA}$ =25),[50] Fe^{3+} makes chelation with EDTA triggering the disaggregation of Au@N-GQDs, and the PL intensity of Au@N-GQDs is restored. For further confirmation, the recovery of the lifetime (from ~12 ns to 8.2 ns) of Au@N-GQDs in the presence of 10 μM EDTA is also demonstrated with the addition of 5 μM Fe^{3+} (see, **Fig. 6.9(f)**). The recovery of each component of the decay time after the detachment of Fe^{3+} endorses that the PL quenching of Au@N-GQDs occurs due to the extraction of electrons from the excited state of Au@N-GQDs by Au@N-GQDs/Fe^{3+} complex formation. These studies confirm that the quenching of the PL of Au@N-GQDs is caused by the excited state electron transfer through the interaction with the edge functional groups of N-GQDs, resulting in the aggregation of Au@N-GQDs. It is worth mentioning that the reversibility of the fluorescent probe makes it extremely useful for practical applications.

6.3.4.1.3. Selectivity of Au@N-GQDs towards Fe^{3+} Ions

The ultra-high sensitivity of Au@N-GQDs towards Fe^{3+} ions encourages us to implement them for the analysis of real-life samples. However, the selectivity test is highly desirable before their use in real samples. For this purpose, several other possible co-existing ions of Fe^{3+}, such as Na^{+}, Mn^{2+}, Mg^{2+}, Cs^{+}, Cd^{2+}, Cr^{3+}, Sn^{2+}, Zn^{2+}, Ag^{+}, Co^{2+}, Cu^{2+}, Hg^{2+}, Pb^{2+} and Al^{3+} of 10 μM concentration were added to Au@N-GQDs solution under the identical experimental condition. **Fig. 6.10(a)** presents the relative change of the PL intensity (I_0/I) of Au@N-GQDs with different interfering species, where only Fe^{3+} shows the most proficient quenching of the PL intensity,

confirming its high selectivity towards Fe^{3+}. As compared to other metal ions, the overlap of the $FeCl_3$ absorption and the PL spectra of Au@N-GQDs at the excitation of 350 nm (see **Fig. 6.10(b)**) facilitate efficient photoinduced charge transfer leading to a higher selectivity towards Fe^{3+} ions.

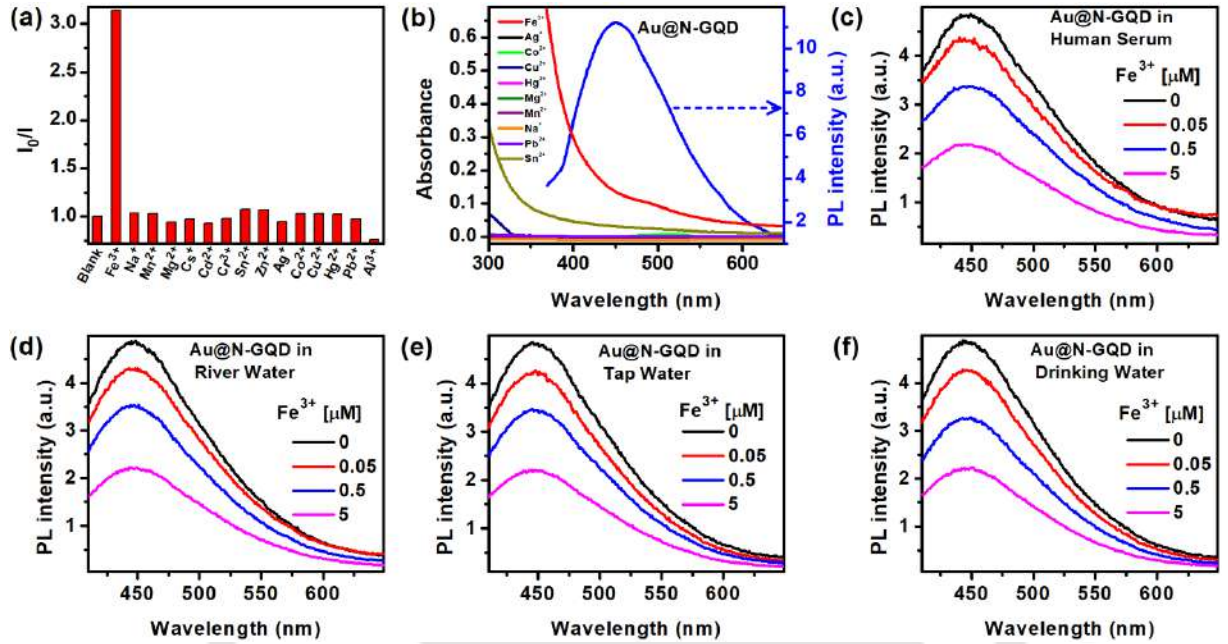

Fig. 6.10. (a) The selectivity of Au@N-GQDs for Fe^{3+} sensing measured by fluorescence quenching (I_0/I) of Au@N-GQDs with the presence of 10 μM concentration of different metal ions. (b) A comparison of the absorption spectra of various metal ions and the spectral overlap of the emission spectra of Au@N-GQDs with the absorption spectra of Fe^{3+} solution. Evolution of the PL spectra of Au@N-GQDs with the spiked Fe^{3+} concentration in (c) human serum, (d) Brahmaputra river water, (e) tap water, and (f) drinking water.

6.3.4.1.4. Sensing of Fe^{3+} in Real-life Samples

For the detection of spiked Fe^{3+} in the human serum and the river water samples at pH 6, the samples were prepared, similar to that discussed in **Chapter 4, Section 4.3.7**. The change in the PL intensity with spiked Fe^{3+} concentration (0.05, 0.5, 5 μM) in the serum sample and river water samples are shown in **Fig. 6.10(c, d)**. To evaluate the Au@N-GQDs based Fe^{3+} sensors in the tap water and drinking water, the samples were collected from the laboratory basin and RO water purifier (Kent), respectively. Each water sample was simply filtered with a 0.22 μm membrane without any further processing. Following a similar procedure for the serum sample preparation, Au@N-GQDs solutions in different water samples were prepared after 20 times dilution of each sample. **Fig. 6.10(e, f)** shows the change of the PL intensity with the spiked Fe^{3+} concentration in the tap water and drinking water samples. In each case, the sensing of Fe^{3+} ions is evident from the quenching of fluorescence. The recovery of Fe^{3+} ions in different real samples are as shown in

Table 6.3, which shows satisfactory recovery and it holds great potential for Au@N-GQDs as an efficient biosensor as well as an environmental sensor. Note that at very low concentration (0.05 *μM)* of Fe^{3+}, the recovery was high perhaps due to the intrinsic iron content in the water that was used for dilution.

Table 6.3. *Detection of Fe^{3+} spiked in the human serum and different aqueous samples.*

Sample	*Added concentration of Fe^{3+} (μM)*	*Found concentration of Fe^{3+} (μM)*	*Recovery (%)*
Human Serum	0.05	0.120±0.002	240
	0.5	0.600±0.003	120
	5	5.750±0.002	115
Brahmaputra river water	0.05	0.136±0.005	272
	0.5	0.490±0.008	98
	5	6.080±0.003	121
Tap water	0.05	0.143±0.004	286
	0.5	0.510±0.002	102
	5	5.600±0.004	112
Drinking water	0.05	0.153±0.003	306
	0.5	0.680±0.001	136
	5	5.600±0.002	112

6.3.4.2. Au@N-GQDs as High-Speed Schottky Junction Photodetector

The enhanced absorption in the entire UV-vis-NIR region and the high charge density with great exciton stability in Au@N-GQDs motivates us to explore their application in photodetector. Herein, Au@N-GQDs are utilized to demonstrate their efficacy as a fast Schottky junction photodetector. **Fig. 6.11(a)** illustrates the device configuration with an optical image of the patterned Al electrodes on top of Au@N-GQDs film. Here, the electrical characteristic of the device was measured at room temperature by applying a voltage (V) to the Al top contact. **Fig. 6.11(b)** shows the cross-sectional view of ~80 nm thick layer of Au@N-GQDs on the SiO_2/Si substrate. The semi-log scale plot of I-V characteristics of Au@N-GQDs shown in **Fig. 6.12(a)** reveals an asymmetric nonlinear behavior for the positive and negative bias voltages for both dark and light conditions, suggesting a back-to-back Schottky diode-like behavior. **Fig. 6.12(b)** depicts

the time-dependent photoresponses of Au@N-GQDs device upon the light on/off intervals of 2.67 ms under 405 nm laser excitation with an illumination power of ~3.68 mW/cm^2 at different bias voltages (-5V, -7V, and -10 V). The induced photocurrent is observed to be proportional to the applied bias voltage.

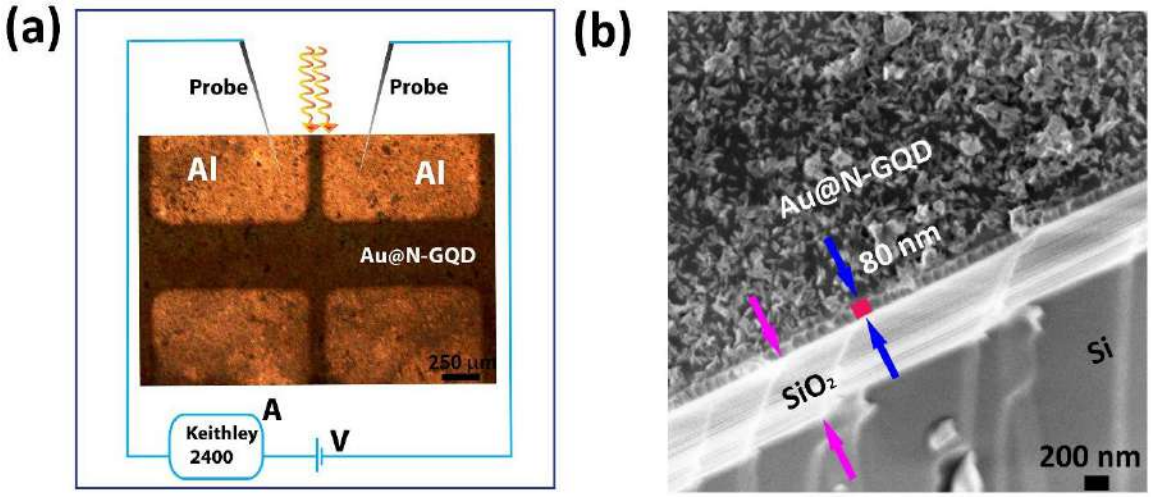

Fig. 6.11. (a) Schematic illustration of the photodetector measurement, with an optical image of patterned Al electrodes on top of the Au@N-GQDs film. (b) Cross-sectional FESEM image of uniform Au@N-GQDs film on SiO_2/Si substrate.

The fast reversibility of the on/off switching of Au@N-GQDs device over several cycles shows remarkable repeatability and robustness of the device. With the decoration of N-GQDs on Au NPs surface, a high-performance photodetector is achieved in the present work. Note that in N-GQDs, a minimum -5V bias is required to get an appreciable photocurrent (see **Fig. 6.12(c)**). In contrast, the Au@N-GQDs device can be operated with as low as -1 V bias, as shown in the inset of **Fig. 6.12(c)**, confirming the stronger intrinsic charge separation in Au@N-GQDs. Note that at zero bias, no measurable photocurrent is observed for Au@N-GQDs, even at the high excitation intensity. Despite the light-induced charge separation in Au@N-GQDs, an intrinsic property of metal/semiconductor junction, the charge carriers do not get sufficient energy to reach up to the electrodes under zero bias, while the photocurrent is appreciable for Au@N-GQDs photodetector at -1 V, which is superior to that of the N-GQDs based photodetectors reported earlier.[12, 13, 18] At -5 V, the photocurrent is reasonably high for Au@N-GQDs photodetector compared to that of N-GQDs device. As compared to N-GQDs, an enormous increase of the photocurrent in Au@N-GQDs can be attributed to the enhanced near field oscillation of electrons in Au NPs, which increases the carrier density in Au@N-GQDs by the hot electrons in Au NPs and electron-hole

separation in N-GQDs. One of the performance parameters of a photodetector is the photoresponse time/speed. The fast photoresponse of Au@N-GQDs was measured using a digital storage oscilloscope. The photoresponse data with higher time resolution is presented in **Fig. 6.12(d)** for Au@N-GQDs photodetector with a 405 nm pulsed laser excitation. The laser source could be

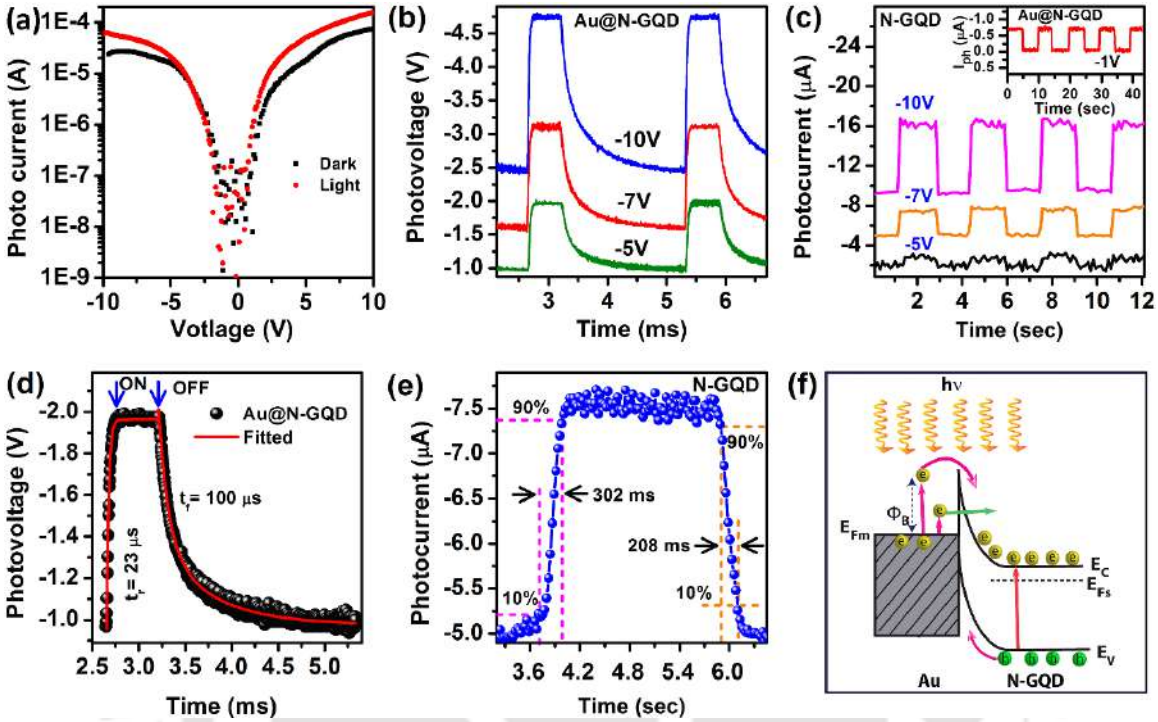

Fig. 6.12. (a) The typical I-V characteristic of the Au@N-GQDs layer measured under the dark and light (405 nm laser with power 3.68 mW/cm^2). Temporal response of the photodetector with (b) Au@N-GQDs and (c) bare N-GQDs at different bias voltages (-5 V to -10 V). The inset of (c) shows the photocurrent of Au@N-GQDs with -1 V bias. Single magnified photoresponse curve with 405 nm pulsed laser for estimating rise/fall times of (d) Au@N-GQDs and (e) N-GQDs based photodetector. (f) Schematic of the band diagram of Au@N-GQDs with illumination under reverse bias (V<0).

modulated up to a frequency of 10 kHz with an external TTL. To estimate the characteristic rise/fall time of the Au@N-GQDs photodetector, the photoresponse curve is fitted with the exponential rise and decay functions as:[51, 52]

$$I_r(t) = I_{0r} + A_1\left(1 - e^{-\frac{t}{t_r}}\right) \quad (6.2)$$

$$I_f(t) = I_{0f} + B_1 e^{-\frac{t}{t_f}}, \quad (6.3)$$

where $I_r(t)$ and $I_f(t)$ are the photocurrents with time 't' for rising and falling edges, respectively. I_{0r}, I_{0f}, A_1, and B_1 are constant. t_r and t_f are the rise and fall times, respectively. The values of t_r and

t_f for Au@N-GQDs are found as ~23 μs and 100 μs, respectively, through the exponential fitting. As compared to the performance of GQDs based photodetectors reported to date, our Au@N-GQDs based device shows a much faster response, as shown in **Table 6.4**. The fast rise time (23 μs) is due to the built-in potential at the Au NPs and N-GQDs junction. A comparatively slower

Table 6.4. *Comparison of the performance of GQDs based photodetectors reported in the literature and the present work.*

Sample/ Device structure	***Operating Voltage(V)***	***Responsivity (A/W)***	***Detectivity ($cm \cdot Hz^{1/2}/W$)***	***EQE (%)***	***Rise/fall time***	***Ref.***
GQDs	5.0	0.002	9.59×10^{11}	5.9	64 ms / 43 ms	[12]
Graphene/GQDs/ graphene	5.5	0.5	2.4×10^{11}	80	- / 30 μs	[18]
N-GQDs	5.0	0.103	1.5×10^{10}	24.4	302 ms / 208 ms	***This work***
Au@N-GQDs	5.0	1.36	2.03×10^{11}	292.2	23 μs /100 μs	***This work***

decay of the photocurrent with a fall time of 100 μs is attributed to defect states in N-GQDs of Au@N-GQDs. In contrast, the response time of bare N-GQDs is much slower, and it is calculated as t_r ~302 ms and t_f ~208 ms from the photoresponse data presented in **Fig. 6.12(e)**. A schematic illustration of the energy band diagram, explaining the generation of photocurrent in Au@N-GQDs junction, is presented in **Fig. 6.12(f)**. When a Schottky junction is formed between the metal and semiconductor, a built-in potential V_0 appears across the junction to the alignment of the Fermi levels. Correspondingly, an electric field directed from N-GQDs to Au NPs in the space charge region of the Schottky junction causes energy bands bending on the semiconductor side.[36] With the external reverse bias, V_{ex}, the potential increases to (V_0+V_{ex}), which enables further band bending in the semiconducting side along with an increase of the space charge region width and the electric field in the Schottky junction. Due to a higher band bending in N-GQDs under reverse bias, the Fermi level of N-GQDs goes down compared to that of the Au NPs (see **Fig. 6.12(f)**), which helps in the efficient transfer of hot electrons. Also, the enhancement of the electric field

drifts the charge carrier towards the opposite electrodes and causes a high photocurrent. Under reverse bias condition, the flow of electrons and holes are depicted in **Fig. 6.12(f)**. Thus, with the incident illumination, the probability of recombination of carriers is very low under external reverse bias, and it results in the high photocurrent in the Au@N-GQDs device. As compared to N-GQDs, the fast photoresponse of Au@N-GQDs is attributed to a faster charge separation at the Schottky junction. It is well known that for a moderate to high doping case, the depletion width is ~0.1 μm at the semiconductor side. In the present case, the thickness of the individual N-GQD is ~0.4 nm, as confirmed from the AFM height profile. Thus, due to the ultralow thickness of the semiconducting N-GQD region, the carriers can transfer from one side to another by tunneling, besides the hot-electron transfer at the Schottky junction. This tunneling is believed to contribute to the faster photoresponse in the Au@N-GQDs device. The attachment of Au NPs with N-GQDs also helps to reduce the defects in N-GQDs (as confirmed from XRD, XPS and Raman analysis) and the surface modification with the functional groups also help to reduce the trapping states and increase the mobility of the charge carrier in N-GQDs, resulting in the fast photoresponse. Furthermore, the large mean free path of electrons in Au NPs helps in efficient hot electron transfer to N-GQDs,[37] and in case of Au@N-GQDs, the plasmon-induced electromagnetic field causes an efficient separation of photogenerated charge carriers.[53] Additionally, the presence of oxygen-rich functional groups in Au@N-GQDs helps to produce a low resistance path by reducing the local Schottky barrier height at the metal/semiconductor interfaces.[54] It is noteworthy that the response speed of the Au@N-GQDs photodetector is much superior to that of the previously developed GQD based photodetector with and without the use of the transporting layer, as listed in **Table 6.4**. Further, the responsivity of Au@N-GQDs photodetector is much higher than that of the typical commercial photodetector based on Si.

To investigate the quantitative dependence of the photocurrent with the illumination intensity, the photocurrent of Au@N-GQDs device is measured for different powers of 405 nm laser, as shown in **Fig. 6.13(a)**. The dependence of photocurrent on the incident powder can be fitted by a simple power-law equation:[20]

$$I_{ph} = BP_{in}^{\alpha} \qquad (6.4)$$

where photocurrent I_{ph}, P_{in} is the incident light power density, 'B' is constant, and 'α' is the exponent. The power equation fits the experimental data with an exponent α =0.98, as shown in

the inset of **Fig. 6.13(a)**. This linear variation of the photocurrent with laser power for Au@N-GQDs photodetector reveals that the amount of photogenerated carriers is nearly proportional to the absorbed photon flux,[20] implying a low recombination probability in Au@N-GQDs.

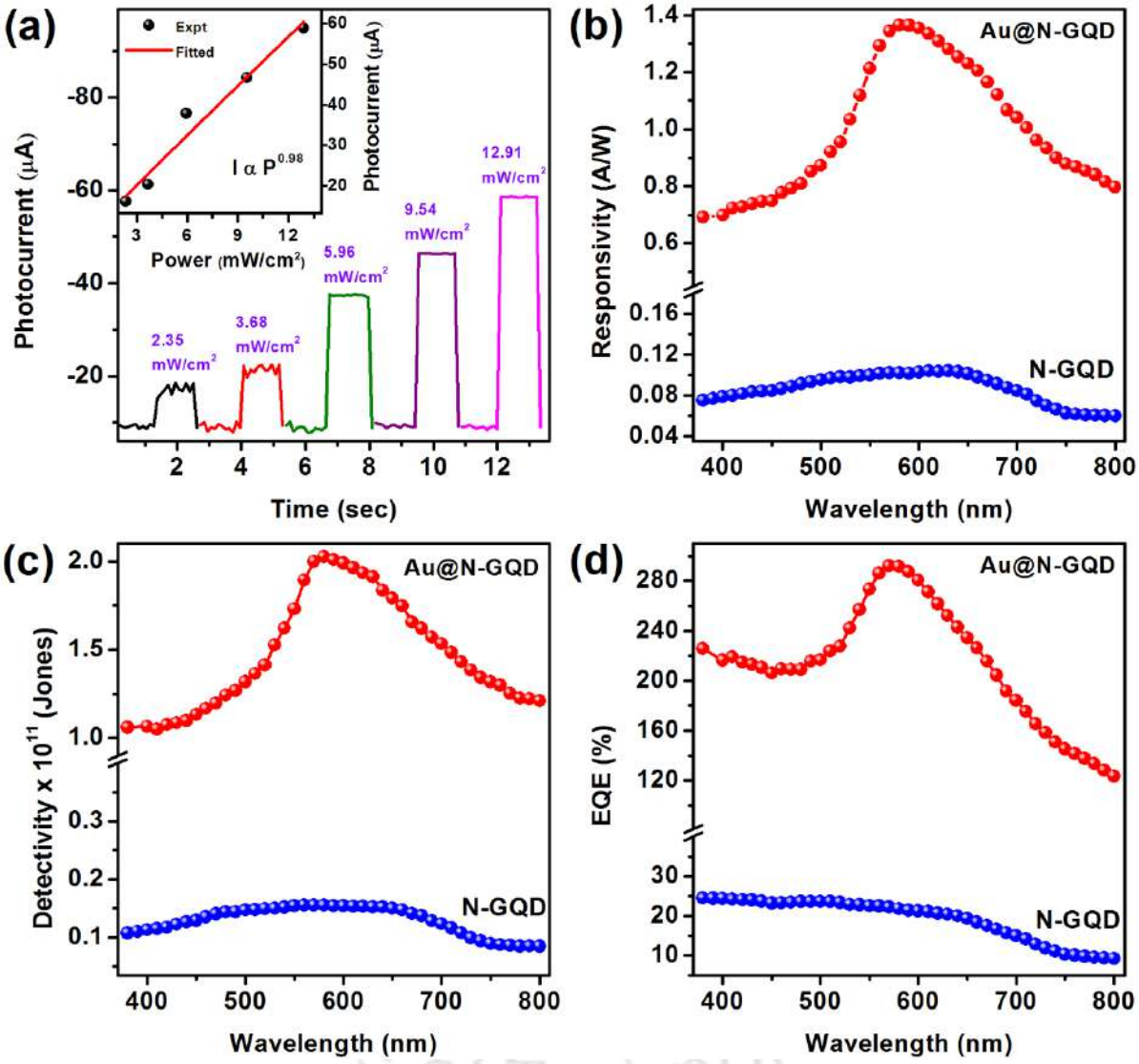

Fig. 6.13. (a) Excitation power-dependent temporal response of photocurrent in Au@N-GQDs with 405 nm pulsed laser excitation. The inset shows the corresponding dynamic response of the photodetector. A comparison of (b) responsivity, (c) detectivity, and (d) EQE of N-GQDs and Au@N-GQDs under 5 V bias.

To characterize the performance of the as-fabricated photodetectors, the figure of merit parameters of responsivity (R(λ)), detectivity (D), and external quantum efficiency (EQE) are evaluated in the spectral range of 380–800 nm at 5 V bias for both N-GQDs and Au@N-GQDs. R(λ) indicates the response efficiency of a detector with a specific optical signal, and it is estimated according to the following equation:[55]

$$R(\lambda) = \frac{I_{ph}}{P_{in}A} \qquad (6.5)$$

where 'A' is the effective illuminated area (in the present case, A =0.01 cm^2). The comparative spectral responsivity of N-GQDs and Au@N-GQDs is shown in **Fig. 6.13(b)**. Bare N-GQDs exhibit a broadband response (UV-vis region) with a responsivity ~0.103 A/W, while Au@N-GQDs shows the relatively high spectral response with a peak responsivity of ~1.36 A/W at 580 nm. Thus, the responsivity of Au@N-GQDs is ~14 times higher than that of bare N-GQDs. Note that the peak of the spectral response or photoresponsivity is near to the plasmonic absorption peak (~547 nm), which strongly suggests that the superior performance of Au@N-GQDs photodetector mainly originates from the plasmon resonance-enhanced absorption and subsequent hot electron generation. It's noteworthy that the present device without any charge transporting layer shows superior performance than the transporting layer-based GQDs system reported previously.[18]

Next, the detectivity of the photodetector was calculated using the relation:[20]

$$D = R(\lambda)\left(\frac{A}{2QqI_D}\right)^{1/2} \qquad (6.6)$$

where 'q' is the electronic charge (1.6×10^{-19} C). The I_D is the dark current. The detectivity of N-GQDs and Au@N-GQDs are estimated as ~1.5×10^{10} Jones and 2.03×10^{11} Jones, respectively, at 580 nm with 5V bias (see **Fig. 6.13(c)**). Thus, the detectivity of Au@N-GQDs based photodetector is ~13.5 times higher than that of the bare N-GQDs based device. Based on the literature reports, we find that Au@N-GQDs based photodetector processes superior performance in comparison to other GQD based photodetectors, as summarized in **Table 6.4**.

Similarly, the EQE is calculated using the relation:[20]

$$EQE(\%) = 100\,\frac{1240\,R(\lambda)}{\lambda} \qquad (6.7)$$

For N-GQDs, the highest value of EQE is ~24.4% at 420 nm, while that of Au@N-GQDs is ~292.2% at 580 nm, as shown in **Fig. 6.13(d)**. The large value of EQE larger than 100% is attributed to the tunneling of the electrons from Au NPs to N-GQDs through the thin depletion region at the Au/N-GQD interface. Further, under the reverse bias, as the holes of N-GQDs moves towards the metal/semiconductor interface, as illustrated in **Fig. 6.12(f)**, the hole trapping at the interface may thins down the depletion region[56] and causes more charge tunneling to N-GQDs.

6.4. Summary and Conclusions

In this chapter, we have demonstrated the usages of Au@N-GQDs hybrid as the superior metal ion sensor by a fluorometric method and the same hybrid as a high-speed photodetector in the visible region. The important findings of this works are summarized below.

1. Au@N-GQDs are implemented as a label-free sensor of Fe^{3+} ions with ultrahigh sensitivity (LOD with 1 nM) and selectivity, utilizing the unusual quenching of fluorescence of Au@N-GQDs in presence of Fe^{3+}.
2. The unusual quenching of fluorescence of Au@N-GQDs in the presence of Fe^{3+} ions is quantitatively analyzed, for the first time, by solving the analytical rate equations with the incorporation of Langmuir's law of adsorption and nonradiative charge transfer to the acceptor ions,
3. The developed sensor is successfully implemented for the detection of Fe^{3+} ions in the human serum and water samples from different sources, including Brahmaputra river water with satisfactory recovery.
4. The fabrication of Au@N-GQDs based Schottky-junction photodetector shows ~10^4 times faster photoresponse than that of the bare N-GQDs along with high photoresponsivity and detectivity.
5. The plasmonic Au NPs in the Au@N-GQDs system generates hot electrons and transfer these to N-GQDs by crossing the Schottky barrier as well as by the tunneling through the thin depletion region at the Au/N-GQD interface.

The manifold applications of Au@N-GQDs, grown by a green approach, open up the versatility of Au@N-GQDs in the biomedical and optoelectronic research fields.

References

1. S. Li, Y. Li, J. Cao, J. Zhu, L. Fan and X. Li, *Anal. Chem.*, 2014, **86**, 10201-10207.
2. X. Cui, Y. Wang, J. Liu, Q. Yang, B. Zhang, Y. Gao, Y. Wang and G. Lu, *Sens. Actuators B: Chem.*, 2017, **242**, 1272-1280.
3. Q. Ma, J. Song, S. Wang, J. Yang, Y. Guo and C. Dong, *Appl Surf Sci*, 2016, **389**, 995-1002.
4. H. Xu, S. Zhou, L. Xiao, H. Wang, S. Li and Q. Yuan, *J. Mater. Chem. C*, 2015, **3**, 291-297.

5. R. Ajlec and J. Štupar, *Analyst*, 1989, **114**, 137-142.
6. E. Chinoporos, *Anal. Chem.*, 1962, **34**, 437-438.
7. A. Ananthanarayanan, X. Wang, P. Routh, B. Sana, S. Lim, D. H. Kim, K. H. Lim, J. Li and P. Chen, *Adv. Funct. Mater.*, 2014, **24**, 3021-3026.
8. P. Wu, W. Li, Q. Wu, Y. Liu and S. Liu, *RSC Adv.*, 2017, **7**, 44144-44153.
9. R. Guo, S. Zhou, Y. Li, X. Li, L. Fan and N. H. Voelcker, *ACS Appl. Mater. Interfaces*, 2015, **7**, 23958-23966.
10. M. Long, P. Wang, H. Fang and W. Hu, *Adv. Funct. Mater.*, 2019, **29**, 1803807.
11. Z. Jin, P. Owour, S. Lei and L. Ge, *Curr. Opin. Colloid Interface Sci.*, 2015, **20**, 439-453.
12. Q. Zhang, J. Jie, S. Diao, Z. Shao, Q. Zhang, L. Wang, W. Deng, W. Hu, H. Xia and X. Yuan, *ACS nano*, 2015, **9**, 1561-1570.
13. T. Dey, S. Mukherjee, A. Ghorai, S. Das and S. K. Ray, *Carbon*, 2018, **140**, 394-403.
14. Y. Du and S. Guo, *Nanoscale*, 2016, **8**, 2532-2543.
15. C.-B. Ma, Z.-T. Zhu, H.-X. Wang, X. Huang, X. Zhang, X. Qi, H.-L. Zhang, Y. Zhu, X. Deng and Y. Peng, *Nanoscale*, 2015, **7**, 10162-10169.
16. S.-H. Cheng, T.-M. Weng, M.-L. Lu, W.-C. Tan, J.-Y. Chen and Y.-F. Chen, *Sci. Rep.*, 2013, **3**, 2694.
17. H. Tetsuka, A. Nagoya and S.-i. Tamura, *Nanoscale*, 2016, **8**, 19677-19683.
18. C. O. Kim, S. W. Hwang, S. Kim, D. H. Shin, S. S. Kang, J. M. Kim, C. W. Jang, J. H. Kim, K. W. Lee and S.-H. Choi, *Sci. Rep.*, 2014, **4**, 5603.
19. D. A. Nguyen, H. M. Oh, N. T. Duong, S. Bang, S. J. Yoon and M. S. Jeong, *ACS Appl. Mater. Interfaces*, 2018, **10**, 10322-10329.
20. I. Mihalache, A. Radoi, R. Pascu, C. Romanitan, E. Vasile and M. Kusko, *ACS Appl. Mater. Interfaces*, 2017, **9**, 29234-29247.
21. M. Kim, P. Kang, J. Leem and S. Nam, *Nanoscale*, 2017, **9**, 4058-4065.
22. Y. Liu, R. Cheng, L. Liao, H. Zhou, J. Bai, G. Liu, L. Liu, Y. Huang and X. Duan, *Nat. Commun.*, 2011, **2**, 579.
23. B. Du, L. Lin, W. Liu, S. Zu, Y. Yu, Z. Li, Y. Kang, H. Peng, X. Zhu and Z. Fang, *Laser Photonics Rev.*, 2017, **11**, 1600148.
24. R. Das, K. K. Paul and P. K. Giri, *Appl Surf Sci*, 2019, **490**, 318-330.
25. R. Parvizi, S. Azad, K. Dashtian, M. Ghaedi and H. Heidari, *Sci. Rep.*, 2019, **9**, 3798.
26. J. A. Sierra, C. R. Vanoni, M. A. Tumelero, C. C. P. Cid, R. Faccio, D. F. Franceschini, T. B. Creczynski-Pasa and A. A. Pasa, *New J. Chem.*, 2016, **40**, 1420-1429.
27. D. Qu, Z. Sun, M. Zheng, J. Li, Y. Zhang, G. Zhang, H. Zhao, X. Liu and Z. Xie, *Adv. Opt. Mater.*, 2015, **3**, 360-367.
28. X. Lu, D. Wang, L. Ge, L. Xiao, H. Zhang, L. Liu, J. Zhang, M. An and P. Yang, *New J. Chem.*, 2018, **42**, 19665-19670.
29. N. Suzuki, Y. Wang, P. Elvati, Z.-B. Qu, K. Kim, S. Jiang, E. Baumeister, J. Lee, B. Yeom and J. H. Bahng, *ACS Nano*, 2016, **10**, 1744-1755.
30. J. P. Melo, P. L. Ríos, P. Povea, C. Morales-Verdejo and M. B. Camarada, *ACS Omega*, 2018, **3**, 7278-7287.
31. G. Socrates, *Infrared and Raman characteristic group frequencies: tables and charts*, John Wiley & Sons, 2004.
32. G. Rajender and P. K. Giri, *J. Mater. Chem. C*, 2016, **4**, 10852-10865.
33. K. K. Paul, N. Sreekanth, R. K. Biroju, A. J. Pattison, D. Escalera-López, A. Guha, T. N. Narayanan, N. V. Rees, W. Theis and P. K. Giri, *J. Mater. Chem. A*, 2018, **6**, 22681-22696.

34. R. K. Biroju and P. K. Giri, *J. Phys. Chem. C*, 2014, **118**, 13833-13843.
35. J. Du, H. Wang, L. Wang, S. Zhu, Y. Song, B. Yang and H. Sun, *J. Mater. Chem. C*, 2016, **4**, 2235-2242.
36. K. K. Paul and P. K. Giri, *J. Phys. Chem. C*, 2017, **121**, 20016-20030.
37. J. Gosciniak, F. B. Atar, B. Corbett and M. Rasras, *Sci. Rep.*, 2019, **9**, 6048.
38. N. T. Khoa, S. W. Kim, D.-H. Yoo, E. J. Kim and S. H. Hahn, *Appl. Catal. Gen.*, 2014, **469**, 159-164.
39. Z. Ding, Z. Hao, B. Meng, Z. Xie, J. Liu and L. Dai, *Nano Energy*, 2015, **15**, 186-192.
40. S. H. Jin, D. H. Kim, G. H. Jun, S. H. Hong and S. Jeon, *ACS Nano*, 2013, **7**, 1239-1245.
41. G. S. Kumar, R. Roy, D. Sen, U. K. Ghorai, R. Thapa, N. Mazumder, S. Saha and K. K. Chattopadhyay, *Nanoscale*, 2014, **6**, 3384-3391.
42. X. Zhu, Z. Zhang, Z. Xue, C. Huang, Y. Shan, C. Liu, X. Qin, W. Yang, X. Chen and T. Wang, *Anal. Chem.*, 2017, **89**, 12054-12058.
43. Y. Bu and S. Lee, *J. Nanosci. Nanotechnol.*, 2013, **13**, 4178-4182.
44. Y. Leng, K. Xie, L. Ye, G. Li, Z. Lu and J. He, *Talanta*, 2015, **139**, 89-95.
45. Z. Li, R. Ye, R. Feng, Y. Kang, X. Zhu, J. M. Tour and Z. Fang, *Adv. Mater.*, 2015, **27**, 5235-5240.
46. L. P. Mawlong, A. Bora and P. K. Giri, *Sci. Rep.*, 2019, **9**, 1-14.
47. H. Qi, M. Teng, M. Liu, S. Liu, J. Li, H. Yu, C. Teng, Z. Huang, H. Liu and Q. Shao, *J. Colloid Interface Sci.*, 2019, **539**, 332-341.
48. J. Ju and W. Chen, *Biosens. Bioelectron.*, 2014, **58**, 219-225.
49. A. Dutta Chowdhury and R.-a. Doong, *ACS Appl. Mater. Interfaces*, 2016, **8**, 21002-21010.
50. M. Ganguly, C. Mondal, J. Pal, A. Pal, Y. Negishi and T. Pal, *Dalton Trans.*, 2014, **43**, 11557-11565.
51. G. Haider, P. Roy, C. W. Chiang, W. C. Tan, Y. R. Liou, H. T. Chang, C. T. Liang, W. H. Shih and Y. F. Chen, *Adv. Funct. Mater.*, 2016, **26**, 620-628.
52. J. Ghosh, R. Ghosh and P. K. Giri, *ACS Appl. Mater. Interfaces*, 2019.
53. Y.-C. Yen, J.-A. Chen, S. Ou, Y.-S. Chen and K.-J. Lin, *Sci. Rep.*, 2017, **7**, 42524.
54. P. Bampoulis, K. Sotthewes, M. H. Siekman and H. J. Zandvliet, *ACS Appl. Mater. Interfaces*, 2018, **10**, 13218-13225.
55. K. K. Paul, L. P. Mawlong and P. K. Giri, *ACS Appl. Mater. Interfaces*, 2018, **10**, 42812-42825.
56. S. Dhar, T. Majumder and S. P. Mondal, *ACS Appl. Mater. Interfaces*, 2016, **8**, 31822-31831.

Chapter 7

Summary and Outlooks

An overview of the important contributions and the highlights of the new findings of this thesis are presented in this chapter. Open questions and the scope for the future works are discussed at the end.

7.1. Summary and Highlights of the Thesis Contribution

In this thesis, the synthesis of undoped and doped GQDs are elucidated by the solvothermal method using graphene oxide (GO) as the precursor material to find out the origin of strong PL emission in various types of GQDs. The tuning of the PL intensity of undoped GQDs is shown by the functionalized with single-walled carbon nanotubes (SWCNTs) and the nature of the interaction between GQDs and SWCNTs is revealed from various spectroscopic and microscopic tools (**Chapter 2**). Next, we discussed about the exciting optical properties of nitrogen-doped GQDs (N-GQDs), and they are implemented as the efficient SERS substrate for the detection of RhB in nM level and a light converter for the fabrication of liquid phase white LED (**Chapter 3**). Next, the hybrid structure of graphitic material GO and WS_2 QDs (GO/WS_2) is implemented for the detection of dopamine (DA) in pM level by the fluorometric method in the human serum and the Brahmaputra river water. In the fluorometric method, the nature of the change of the PL intensity of GO/WS_2 is explained by the combined effect of the linear Stern-Volmer equation and the charge transfer dynamics, for the very first time. The DA sensing with the heterostructures of undoped $GQDs/WS_2$ and sulfur-doped $GQDs/WS_2$ is also compared with GO/WS_2 (**Chapter 4**). Next, the hybrid of N-GQDs and plasmonic Au NPs (Au@N-GQDs) is demonstrated as a dual-mode DA sensor by the formation of a unique core-shell structure (**Chapter 5**). Also, the synthesized Au@N-GQDs are used for the detection of Fe^{3+} ions in nM level by the quenching of PL intensity of fluorescent Au@N-GQDs, and the nature of this quenching is explained by considering the surface adsorption followed by concentration-dependent charge transfer dynamics, for the first time. Finally, Au@N-GQDs are explored for the fabrication of high-speed (rise time ~23 μs) photodetector without any charge transporting layer (**Chapter 6**). Our findings on doping and

functionalization of GQDs would stimulate further investigations for their applications in biomedical and optoelectronics fields in a larger scale.

The highlights of the present thesis are presented below.

A. Tuning of the photoluminescence intensity of GQDs through the functionalization with SWCNTs

Undoped GQDs with high PL quantum yield are prepared by a solvothermal approach. We demonstrated a new approach to tune of PL intensity of undoped GQDs (U-GQDs) through the functionalization with SWCNTs over a concentration range of 2–60 μg/mL. We reported an anomalous quenching behavior of U-GQDs in the presence of SWCNTs. In the very low concentration region (SWCNTs: 2–8 μg/mL), PL intensity of U-GQDs is observed to be enhanced systematically, while a systematic quenching of PL intensity of U-GQDs is monitored with the higher concentration of SWCNTs (≥10 μg/mL), following a non-linear Stern-Volmer equation. The enhancement of PL intensity of U-GQDs in the low concentration region is governed by the dominating metallic nature of SWCNTs at the low concentrations, which increases the incident local field on the U-GQDs by the plasmonic effect. On the other hand, faster than exponential quenching in the high concentration region is attributed to the combined effect of ground state composite formation and excited-state charge transfer from fluorescent U-GQDs to SWCNTs due to the dominating semiconducting nature of SWCNTs when they are bundled. This work has been published in "*Phys. Chem. Chem. Phys. 20 (2018), 4527-4537*".

B. Elucidating the origin of high photoluminescence quantum yield in N-GQDs and their applications as SESR sensor and white light convertor

We have presented a comparative study of the structural and optical features of various types of GQDs synthesized in water, DMF, and DMSO medium by a top-down approach with GO as the precursor. We proposed that in DMF and DMSO medium, N-GQDs and S-GQDs are formed mainly with the nucleophilic reaction, while in water the GO sheet is cut into pieces due to the strain caused by the epoxy groups on the basal planes. Among different types of GQDs, N-GQDs show the highest PL QY (~34%) due to the reduction of non-radiative sites at the time of solvent reaction and the presence of electron-donating N atoms. In contrast, the as-synthesized S-GQDs do not yield high PL intensity primarily due to the presence of electron-withdrawing S=O

functional groups, which act as a non-radiative trap center. Next, we demonstrated N-GQDs as a very efficient SERS substrate with a chemical enhancement factor (EF) of ~3.2×10^3 at 1648 cm^{-1} in the presence of 10^{-4} M RhB as a target molecule under 488 nm laser excitation, which is the highest among the reported values, and consequently, this SERS substrate is able to detect RhB as low as 0.1 nM. For the first time, the individual contributions of π–π interaction and FRET process in the SERS enhancement are evaluated by comparing with different target molecules, laser excitation wavelengths, and controlling the functional groups of N-GQDs through vacuum annealing. Besides, the highly fluorescent N-GQDs are successfully implemented in developing a liquid phase white LED with the help of a low-cost UV LED and RhB solution. This work has been published in "*Carbon 160 (2020), 273-286*".

C. Ultrasensitive Dopamine sensing in human serum by GO/WS_2 hybrid

We have explored a unique hybrid system of GO and WS_2 QDs for the ultrasensitive and selective fluorometric detection of DA as low as 10 pM in a basic medium, which is lowest among the reported values. In the GO/WS_2 hybrid, the interaction of WS_2 QDs with GO via van der Waals interaction, and the defect states/functional groups lead to the excited state charge transfer from fluorescent WS_2 QDs to GO. With the addition of DA in GO/WS_2, DA is first adsorbed on the GO surface due to the strong π–π interaction, enabling the easy charge transfer from GO to DA. Additionally, in the basic medium, the conversion of DA to DQ (a strong electron acceptor) promotes the efficient electron transfer from GO to DA, and as a result, the PL intensity of WS_2 QDs quenches more rapidly in the presence of DA. To explain the nature of PL quenching in a wide concentration range, here we have developed a modified model by considering the combined effect of surface adsorption in the ground-state complex formation following the Freundlich isotherm and excited-state charge transfer. From a comparative study, we have also experimentally elucidated that compared to GQD based hybrid systems, GO/WS_2 is highly efficient for the DA sensing due to a higher possibility of π–π interaction with DA and a high charge transporting ability of GO. Furthermore, the proposed fluorescence-based sensor is successfully implemented as an efficient DA sensor spiked in the Brahmaputra river water and the human serum samples. This work has been published in "*J. Mater. Chem. C 8 (2020), 7935-7946*".

D. Dual-mode dopamine sensing with Au@N-GQDs by the unique core-shell structure formation

We presented in-situ green synthesis of Au@N-GQDs hybrid and it is demonstrated as a dual-mode sensor of DA in the human serum through the formation of a unique core-shell structure with DA as a shell. In the presence of DA, the enhancement of UV-Vis absorption intensity and the quenching of PL intensity of Au@N-GQDs have been used for the colorimetric and fluorometric detection of DA, respectively, in the range of 0.04–100.0 μM. Primarily electrostatic interaction and π-π stacking between N-GQDs and DA facilitate the N-GQDs/DA ground state complex formation, and the presence of Au NPs accelerates this ground-state complex formation by making a core-shell structure with phenoxide-enolate. It is also highlighted that the core-shell structure helps in higher quenching of PL intensity of Au@N-GQDs through electron transfer. This work demonstrates the efficacy of Au@N-GQDs as a more efficient DA sensor than the bare N-GQDs. This work has been published in "*Appl. Surf. Sci. 490 (2019), 318-330*".

E. Implementation of Au@N-GQDs as a metal ion (Fe^{3+}) sensor and a high-speed photodetector

Besides a biomolecule sensor, we have also established Au@N-GQDs as an efficient metal ion sensor as well as fast photodetector without using any charge transporting layer. Au@N-GQDs are implemented as a label-free sensor of Fe^{3+} ions with ultra-high sensitivity (< 1 nM) and selectivity by exploring the PL quenching of Au@N-GQDs in presence of Fe^{3+} ions. The quenching behavior does not follow the known laws of quenching and the unusual quenching of the PL intensity of Au@N-GQDs in the presence of Fe^{3+} ions is modeled by solving the analytical rate equations, incorporating Langmuir's law of adsorption and non-radiative charge transfer to the acceptor ions, for the first time. Further, the newly developed sensor is successfully executed for the detection of spiked Fe^{3+} ions in human serum and real water samples, including Brahmaputra river water with satisfactory recovery.

Next, we have demonstrated the Au@N-GQDs film based planar photodetector with fast photoresponse and high photoresponsivity. With the incorporation of plasmonic Au NPs in the Au@N-GQDs system, Au NPs generate hot electrons and transfer these to N-GQDs to achieve high photocurrent. Additionally, through the attachment of the Au NPs on the basal plane of N-GQDs, the reduction of the defect states along with the modification of the edge functional groups

as well as the tunneling of electrons from Au NPs to N-GQDs through the thin depletion region produce the fast photoresponse (~10^4 times faster than bare N-GQDs) in Au@N-GQDs. A high spectral responsivity of ~1.36 A/W at 580 nm is achieved in Au@N-GQDs photodetector by the plasmonic effect, and it is ~14 times higher than that of the bare N-GQDs. This work has been published in "*ACS Appl. Mater. Interfaces 12 (2020), 4755-4768*".

7.2. Scope of Future Work

The present thesis focused on the study of the optical properties of various types of undoped and doped GQDs and their heterostructures with semiconducting nanomaterials (SWCNTs and WS_2 QDs) and plasmonic Au nanoparticles for their applications as SERS sensor, biomolecules and metal ion sensors in real-life samples, and as a high-speed photodetector. However, there are ample scopes for further work in this filed for more efficient and large-scale application of doped and functionalized GQDs. Some possible extensions of the current work are enumerated below.

1. As a fluorescent material, here we have achieved up to 34% PL QY in GQDs after nitrogen doping. For the biomedical applications, further improvement of the PL QY of GQDs and their biocompatibility at higher concentrations is an open challenge.
2. The upconversion PL study of various types of GQDs and the corresponding mechanism can be explored.
3. As a metal-free SERS substrate, N-GQDs have been demonstrated here to detect as low as 0.1 nM concentration of RhB. Differently modified GQDs can be implemented for the detection of other target molecules, such as glucose, DA, etc., for practical applications.
4. The use of GO/WS_2 hybrid for the sensing of serotonin can be further studied.
5. This thesis presented the applications of the hybrid structure of N-GQDs with metallic Au NPs only. The GQDs based bi-metallic hybrid structure such as Au/Ag, Au/Pt, etc., can be explored for improved performance in the sensing and optoelectronic applications.
6. Better control over the growth of GQDs with desired functional groups and optimization of the GQD based photodetectors with low dark current and high sensitivity can be explored for practical applications. Flexible and wearable photodetectors based on GQDs are promising for further exploration.